UNIVERSITY OF THESSALY

SCHOOL OF ENGINEERING

DEPARTMENT OF MECHANICAL ENGINEERING

Doctor of Philosophy Dissertation

STRUCTURAL BEHAVIOR AND STABILITY OF CYLINDRICAL STEEL SHELLS WITH LATERAL CONFINEMENT

by

DANIEL VASILIKIS

Diploma of Mechanical Engineering, U.Th., 2006

Master of Science (M.Sc.), Department of Mechanical Engineering, U.Th., 2008

Supervisor: Dr. Spyros A. Karamanos, Associate Professor

Submitted in partial fulfillment
of the requirements for the degree
of Doctor of Philosophy

Volos, 2012

ΠΑΝΕΠΙΣΤΗΜΙΟ ΘΕΣΣΑΛΙΑΣ

ΠΟΛΥΤΕΧΝΙΚΗ ΣΧΟΛΗ

ΤΜΗΜΑ ΜΗΧΑΝΟΛΟΓΩΝ ΜΗΧΑΝΙΚΩΝ

Διδακτορική Διατριβή

ΔΟΜΙΚΗ ΣΥΜΠΕΡΙΦΟΡΑ ΚΑΙ ΕΥΣΤΑΘΕΙΑ ΧΑΛΥΒΔΙΝΩΝ ΚΥΛΙΝΔΡΙΚΩΝ ΚΕΛΥΦΩΝ ΥΠΟ ΠΛΕΥΡΙΚΟΥΣ ΠΕΡΙΟΡΙΣΜΟΥΣ

Δανιήλ Βασιλικής

Διπλωματούχος Μηχανολόγος Μηχανικός, Π.Θ., 2006

Μεταπτυχιακό Δίπλωμα, Τμήμα Μηχανολόγων Μηχανικών, Π.Θ, 2008

Επιβλέπων: Δρ. Σπύρος Α. Καραμάνος, Αναπληρωτής Καθηγητής

Υπεβλήθη για την εκπλήρωση μέρους των
απαιτήσεων για την απόκτηση του
Διδακτορικού Διπλώματος

Βόλος, 2012

Examination Committee:

Dr. Spyros A. Karamanos (Supervisor), Associate Professor, Department of Mechanical Engineering, University of Thessaly

Dr. Philip C. Perdikaris, Professor, Dept. of Civil Eng., University of Thessaly

Dr. Dimitrios E. Beskos, Professor, Dept. of Civil Eng., University of Patras

Dr. Antonios E. Giannakopoulos, Professor, Dept. of Civil Eng., University of Thessaly

Dr. Alexis T. Kermanidis, Assistant Professor, Dept. of Mech. Eng., University of Thessaly

Dr. George N. Labeas, Associate Professor, Dept. of Mechanical & Aeronautics Engineering, University of Patras

Dr. Euripides S. Mistakidis, Professor, Dept. of Civil Eng., University of Thessaly

Εξεταστική Επιτροπή:

Δρ. Σπύρος Α. Καραμάνος (Επιβλέπων)
Αναπληρωτής Καθηγητής, Τμήμα Μηχανολόγων Μηχανικών, Πανεπιστήμιο Θεσσαλίας

Δρ. Φίλιππος Κ. Περδικάρης (Μέλος Τριμελούς)
Καθηγητής, Τμήμα Πολιτικών Μηχανικών, Πανεπιστήμιο Θεσσαλίας

Δρ. Δημήτριος Ε. Μπέσκος (Μέλος Τριμελούς)
Καθηγητής, Τμήμα Πολιτικών Μηχανικών, Πανεπιστήμιο Πατρών

Δρ. Αντώνιος Ε. Γιαννακόπουλος
Καθηγητής, Τμήμα Πολιτικών Μηχανικών, Πανεπιστήμιο Θεσσαλίας

Δρ. Αλέξιος Θ. Κερμανίδης
Επίκουρος Καθηγητής, Τμήμα Μηχανολόγων Μηχανικών, Πανεπιστήμιο Θεσσαλίας

Δρ. Γεώργιος Ν. Λαμπέας
Αναπληρωτής Καθηγητής, Τμήμα Μηχανολόγων & Αεροναυπηγών Μηχανικών, Πανεπιστήμιο Πατρών

Δρ. Ευριπίδης Σ. Μυστακίδης
Καθηγητής, Τμήμα Πολιτικών Μηχανικών, Πανεπιστήμιο Θεσσαλίας

Acknowledgements

Many people have contributed directly and indirectly to the completion of this dissertation. First of all, I would like to express my sincere gratitude to the supervisor of this thesis, Associate Professor Spyros A. Karamanos, for giving me the opportunity to obtain my PhD degree, and for his help with finding a PhD subject combining the academic environment with industry. His confidence in me, his support and guidance have contributed to the achievement of the scopes of this PhD project. I would like to acknowledge Shelter S.A Company and personally Prokopis Tsintzos for their funding during a significant part of this research.

Also, I am grateful to the other members of the examining committee for their remarks and suggestions that improved the study. Furthermore, I would like to express my sincere gratitude to A.M. (Nol) Gresnigt for his valuable suggestions on the experimental data and comments about the numerical results, and for giving me the possibility to visit the Stevin Laboratory at Delft University of Technology. I would like to thank the Professors, the PhD students and the engineers with whom I have collaborated, for their help during my PhD research. Especially, I would like to thank Sotira Houliara, Patricia Pappa, George Varelis, and Aglaia Pournara for their help and collaboration. Moreover, I am grateful to my friends and colleagues for their constant friendship and support during all the years of my studies in Volos.

This dissertation is dedicated to my family for their support all these years of my studies. Finally, I would also like to thank Anastasia for her support and encouragement.

Daniel Vasilikis

Ευχαριστίες

Για την πολύχρονη προσπάθεια ολοκλήρωσης αυτής της διατριβής, δεν θα μπορούσα να μην αναγνωρίσω την συνεισφορά, άμεση η έμμεση, διαφόρων προσώπων. Χωρίς την υποστήριξη τους, η εκπλήρωση των στόχων της διατριβής θα ήταν αδύνατη.

Πρώτα απ' όλα θα ήθελα να εκφράσω τις ευχαριστίες μου στον επιβλέποντα της έρευνας Αναπληρωτή Καθηγητή κ. Σπύρο Α. Καραμάνο για τη δυνατότητα που μου έδωσε να αποκτήσω τον τίτλο του διδάκτορα και την εμπιστοσύνη που μου επέδειξε καθ' όλη τη διάρκεια της συνεργασίας μας. Η πολύτιμη καθοδήγηση και ενασχόληση του συνέβαλαν καθοριστικά στην επίτευξη των στόχων της διατριβής. Τον ευχαριστώ επίσης για τις πολύτιμες γνώσεις και συμβουλές του σε ακαδημαϊκά και όχι μόνο θέματα καθώς και για την εξασφάλιση της χρηματοδότησης καθ' όλη τη διάρκεια της έρευνας. Θα ήθελα επίσης να ευχαριστήσω τον κ. Προκόπη Τσίντζο, διευθυντή της εταιρίας SHELTER ABEE, για την ευγενική του χρηματοδότηση κατά τη διάρκεια αυτής της έρευνας.

Στα μέλη της εξεταστικής επιτροπής εκφράζω τις ευχαριστίες μου για τις πολύτιμες παρατηρήσεις και υποδείξεις τους, οι οποίες συνέβαλαν στην βελτίωση του τελικού κειμένου. Επίσης θα ήθελα να ευχαριστήσω τον Αν. Καθ. A.M. (Nol) Gresnigt για τις πολύτιμες του συμβουλές σχετικά με τα πειραματικά δεδομένα και τα σχόλια του πάνω στα υπολογιστικά αποτελέσματα. Επίσης τον ευχαριστώ για τη δυνατότητα που μου έδωσε να επισκεφθώ το εργαστήριο StevinLab στο Πολυτεχνείο του Delft. Θα ήθελα επίσης να ευχαριστήσω όλους τους καθηγητές, διδακτορικούς φοιτητές και συναδέλφους μηχανικούς με τους οποίους συνεργάστηκα και με βοήθησαν κατά τη διάρκεια αυτής της έρευνας. Ιδιαίτερα ευχαριστώ τους συναδέλφους μου Σωτηρία Χουλιαρά, Πατρίτσια Παππά, Γιώργο Βαρέλη και Αγλαΐα Πουρνάρα για την βοήθεια και τη συνεργασία τους. Οφείλω επίσης να ευχαριστήσω όλους τους φίλους μου για την βοήθεια, την υποστήριξη και την ειλικρινή φίλια τους καθ' όλη τη διάρκεια των σπουδών μου στο Βόλο.

Η διατριβή αυτή αφιερώνεται στην οικογένεια και τους συγγενείς μου για την ηθική και υλική τους υποστήριξη όλα αυτά τα χρόνια των σπουδών μου. Τέλος, θα ήθελα να ευχαριστήσω την σύντροφο μου Αναστασία για την κατανόηση, την υποστήριξη και την ενθάρρυνση της.

Δανιήλ Βασιλικής

STRUCTURAL BEHAVIOR AND STABILITY OF CYLINDRICAL STEEL SHELLS WITH LATERAL CONFINEMENT

DANIEL VASILIKIS

University of Thessaly, Department of Mechanical Engineering, 2012

Supervisor: Dr. Spyros A. Karamanos, Associate Professor.

Abstract

Motivated by practical engineering applications, the present study investigates the structural behavior and stability of thin-walled steel cylindrical shells with lateral confinement under two main types of loading, namely external pressure and longitudinal bending, both resulting in structural failure. The present work emphasizes on structural stability in terms of buckling, post-buckling and imperfection sensitivity. The investigation is computational using advanced finite element tools through the employment of a general-purpose finite element program. The cylindrical shells under consideration and the corresponding confinements are simulated with nonlinear finite elements that account for both geometric and material nonlinearities. An extensive literature review on the examined mechanical issues is conducted for the evaluation and assessment of available analytical solutions and experimental data. A numerical simulation methodology is developed and verified in order to model the shell and the interaction with the confinement. Shells of elastic material are considered first, offering the possibility of comparing the numerical results with available closed-form or simplified analytical predictions. Subsequently, the buckling response of steel shells is examined and the results are compared with available experimental data.

For the case of external pressure loading, the numerical results are presented in the form of pressure-deformation equilibrium paths, and show an unstable post-buckling response beyond the point of ultimate pressure capacity, indicating significant imperfection sensitivity on the value of the maximum pressure. The effects of the diameter-to-thickness ratio (D/t), the yield stress, the interface friction, and the medium deformability on the structural response are examined. It is demonstrated that even for rigid confinement

medium, the maximum (buckling) pressure is well below the pressure that causes plastification of the entire cylinder (referred to as yield pressure). Finally, based on the numerical results, a simplified and efficient methodology is developed which is compatible with the recent general provisions of European design recommendations for shell buckling, and could be used for design purposes.

For the case of longitudinal bending loading of confined cylinders, the analysis refers to the case of the so-called lined pipes, focusing on the behavior of the thin-walled inner pipe (liner) which interacts with the outer pipe. Using a numerical simulation, the stresses and deformations in the compression zone are monitored, with emphasis on possible detachment of the liner from the confining medium, and on the formation of wrinkles. Furthermore, the development of liner ovalization, bending moment, local hoop curvature, axial stress, and hoop stress with increasing level of bending are investigated. The effects of liner thickness, friction, liner prestressing, and stiffness of the confining medium on the buckling curvature and wavelength are examined. The sensitivity of response on the presence of initial wrinkling imperfections is investigated. Finally, the effect of external pressure on the mechanical response is discussed.

The present study aims at establishing the theoretical basis for understanding and solving a significant number of structural instabilities related to confined cylindrical shells, which are encountered often in numerous practical engineering applications.

ΔΟΜΙΚΗ ΣΥΜΠΕΡΙΦΟΡΑ ΚΑΙ ΕΥΣΤΑΘΕΙΑ ΧΑΛΥΒΔΙΝΩΝ ΚΥΛΙΝΔΡΙΚΩΝ ΚΕΛΥΦΩΝ ΥΠΟ ΠΛΕΥΡΙΚΟΥΣ ΠΕΡΙΟΡΙΣΜΟΥΣ

ΔΑΝΙΗΛ ΒΑΣΙΛΙΚΗΣ

Πανεπιστήμιο Θεσσαλίας, Τμήμα Μηχανολόγων Μηχανικών, 2012

Επιβλέπων: Δρ. Σπύρος Α. Καραμάνος, Αναπληρωτής Καθηγητής.

Περίληψη

Η παρούσα διδακτορική διατριβή εξετάζει τη δομική συμπεριφορά και ευστάθεια λεπτότοιχων χαλύβδινων κυλινδρικών κελυφών με πλευρικούς περιορισμούς που υπόκεινται σε δομικές φορτίσεις, και ειδικότερα σε εξωτερική πίεση και διαμήκη κάμψη. Κίνητρο της παρούσας έρευνας είναι η παρουσία των ανωτέρω προβλημάτων σε πρακτικές εφαρμογές μηχανικού, και συγκεκριμένα, στην αντοχή υπόγειων ή/και εγκιβωτισμένων αγωγών υπό εξωτερική πίεση και τη δομική συμπεριφορά εσωτερικώς επενδυμένων αγωγών υδρογονανθράκων (lined pipes) υπό καμπτική ένταση. Ιδιαίτερη έμφαση δίδεται στην δομική ευστάθεια και πιο συγκεκριμένα στην διερεύνηση του κρίσιμου φορτίου (αστοχία με τη μορφή λυγισμού), της μεταλυγισμικής συμπεριφοράς, και της ευαισθησίας σε αρχικές ατέλειες. Η παρούσα διερεύνηση είναι υπολογιστική και χρησιμοποιεί για αυτό το σκοπό δι-διάστατα και τρι-διάστατα μοντέλα προσομοίωσης. Το εξεταζόμενο κυλινδρικό κέλυφος καθώς επίσης και το αντίστοιχο μέσο εγκιβωτισμού προσομοιώνονται με πεπερασμένα στοιχεία τα οποία λαμβάνουν υπόψη μη-γραμμική συμπεριφορά υλικού και γεωμετρίας. Χρησιμοποιείται ένα γενικό πρόγραμμα πεπερασμένων στοιχείων για την προσομοίωση του κελύφους και της αλληλεπίδρασης με το μέσο εγκιβωτισμού.

Αρχικά διεξάγεται μια εκτενής βιβλιογραφική ανασκόπηση των εξεταζόμενων προβλημάτων, όπου γίνεται αξιολόγηση και ταξινόμηση των διαθέσιμων αναλυτικών λύσεων και πειραματικών δεδομένων. Στη συνέχεια αναπτύσσεται και πιστοποιείται η αριθμητική μεθοδολογία προσομοίωσης. Εξετάζεται η αντοχή κελυφών από ιδεατό ελαστικό υλικό έναντι λυγισμού, προσφέροντας έτσι τη δυνατότητα σύγκρισης των υπολογιστικών αποτελεσμάτων με διαθέσιμες αναλυτικές προβλέψεις κλειστού τύπου.

Ακολούθως, διερευνάται η απόκριση των χαλύβδινων κελυφών και τα υπολογιστικά αποτελέσματα συγκρίνονται με διαθέσιμα πειραματικά αποτελέσματα.

Στην περίπτωση των εγκιβωτισμένων κελυφών υπό εξωτερική πίεση, τα υπολογιστικά αποτελέσματα της εργασίας παρουσιάζονται στη μορφή δρόμων ισορροπίας πίεσης-μετατόπισης και δείχνουν μια ασταθή μεταλυγισμική συμπεριφορά μετά το σημείο της μέγιστης πίεσης. Αυτή η συμπεριφορά υποδεικνύει μια σημαντική ευαισθησία του κρίσιμης πίεσης σε αρχικές ατέλειες. Μελετάται η επίδραση του λόγου διαμέτρου-προς-πάχος, του ορίου διαρροής του υλικού, της τριβής, και της παραμορφωσιμότητας του περιβάλλοντος μέσου στην απόκριση του κελύφους. Σημειώνεται ότι, ακόμα και στην περίπτωση ενός άκαμπτου περιβάλλοντος μέσου, η μέγιστη πίεση είναι σημαντικά μικρότερη της πίεσης που προκαλεί πλήρη πλαστικοποίηση του κελύφους. Τέλος, με βάση τα υπολογιστικά αποτελέσματα, αναπτύσσεται μια απλοποιητική μεθοδολογία σχεδιασμού, η οποία είναι συμβατή με τις πρόσφατες γενικές διατάξεις των ευρωπαϊκών κανονισμών σχεδιασμού για την αστοχία κελυφών. Η μεθοδολογία αυτή μπορεί να χρησιμοποιηθεί για σχεδιαστικούς σκοπούς.

Στην περίπτωση των εγκιβωτισμένων κελυφών υπό διαμήκη κάμψη, η ανάλυση αναφέρεται στην περίπτωση των επενδυμένων αγωγών, εστιάζοντας στη συμπεριφορά του λεπτότοιχου εσωτερικού αγωγού. Χρησιμοποιώντας την αριθμητική προσομοίωση, παρακολουθούνται οι τάσεις και οι παραμορφώσεις στην κρίσιμη περιοχή της θλίψης, δίνοντας έμφαση σε πιθανή αποκόλληση του κελύφους από το μέσο εγκιβωτισμού, και κυρίως στο σχηματισμό των κυματοειδών πτυχώσεων (τοπικός λυγισμός). Διερευνώνται η παράμετρος οβαλοποίησης, η καμπτική ροπή, η τοπική περιμετρική καμπυλότητα, οι αξονικές τάσεις και οι περιμετρικές τάσεις. Εξετάζεται η επίδραση στην κρίσιμη καμπυλότητα και στο μήκος κύματος του πάχους του κελύφους, της τριβής, της προέντασης του κελύφους, και της ακαμψίας του μέσου εγκιβωτισμού. Επίσης διερευνάται η ευαισθησία της απόκρισης στην παρουσία αρχικών ατελειών. Τέλος, εξετάζεται η επίδραση της εξωτερικής πίεσης στην μηχανική συμπεριφορά του συστήματος.

Το Κεφάλαιο 2 αφορά τη μελέτη της δομικής συμπεριφοράς και ευστάθειας εγκιβωτισμένων αγωγών που υπόκεινται σε εξωτερική πίεση. Κίνητρο για την μελέτη του υπόψιν προβλήματος αποτέλεσε η δομική συμπεριφορά των υπόγειων αγωγών ύδατος ή υδρογονανθράκων που περιβάλλονται από έδαφος ή είναι εγκιβωτισμένοι σε σκυρόδεμα. Στην περίπτωση των υπόγειων αγωγών (buried pipelines), όταν ο υδροφόρος ορίζοντας βρίσκεται πάνω από το επίπεδο του αγωγού, το νερό φτάνει στον αγωγό διαμέσου του διαπερατού περιβάλλοντος του εδάφους ή του σκυροδέματος. Αυτό έχει ως συνέπεια την

ανάπτυξη κατάστασης υδροστατικής πίεσης γύρω από τον αγωγό, η οποία μπορεί να οδηγήσει σε αστοχία λυγισμού (buckling) του τοιχώματος του χαλύβδινου αγωγού. Η αστοχία των εγκιβωτισμένων αγωγών υπό υδροστατική πίεση είναι σημαντικά διαφορετική από την αστοχία λόγω θερμικών φορτίων, η οποία συχνά αναφέρεται ως "λυγισμός συρρίκνωσης" (shrink buckling). Στην περίπτωση της αστοχίας λόγω συρρίκνωσης, η θλιπτική δύναμη κατά την περιφέρεια απελευθερώνεται αμέσως μετά την αστοχία, ενώ αντίθετα στην περίπτωση της αστοχίας λόγω υδροστατικής πίεσης, το φορτίο της πίεσης εξακολουθεί να ασκείται και στο μεταλυγισμικό στάδιο.

Στο Κεφάλαιο 3 εξετάζεται το δεύτερο θέμα της παρούσας διδακτορικής διατριβής, το οποίο αναφέρεται στη διερεύνηση της μηχανικής συμπεριφοράς και ευστάθειας των λεγόμενων επενδυμένων αγωγών (lined pipes) υπό κάμψη και εξωτερική πίεση. Ο επενδυμένος σωλήνας είναι ένας σωλήνας διπλού τοιχώματος που αποτελείται από δύο σωλήνες που βρίσκονται σε επαφή. Αποτελείται από έναν παχύ εξωτερικό σωλήνα από κοινό ανθρακούχο χάλυβα και έναν λεπτότοιχο εσωτερικό σωλήνα από ανοξείδωτο χάλυβα, ο οποίος αναφέρεται και ως "σωλήνας επένδυσης" (liner). Ο επενδυμένος αγωγός είναι μια σχετικά πρόσφατη τεχνολογική λύση που έχει προταθεί με επιτυχία για υποθαλάσσιους χαλύβδινους αγωγούς μεταφοράς υδρογονανθράκων (πετρέλαιο, αέριο κτλ), διότι εξασφαλίζει αντίσταση έναντι της εσωτερικής διάβρωσης του αγωγού και παράλληλα αντοχή στη συνδυασμένη καταπόνηση εξωτερικής πίεσης και διαμήκους κάμψης οι οποίες αναπτύσσονται κυρίως κατά την πόντιση του αγωγού. Ο επενδυμένος σωλήνας παράγεται με την εισαγωγή του εσωτερικού σωλήνα στον εξωτερικό, μέσω μιας κατάλληλης θερμο-υδραυλικής διαδικασίας κατασκευής. Στην κατεργασία αυτή, η διασύνδεση μεταξύ των δύο σωλήνων είναι καθαρά μηχανικής φύσεως, με την έννοια ότι το υλικό του εσωτερικού σωλήνα και αυτό του εξωτερικού σωλήνα παραμένουν δυο ξεχωριστά υλικά, σε αντίθεση με ότι συμβαίνει στη μεταλλουργική κατεργασία όπου τα δύο υλικά ενώνονται και συμπεριφέρονται ως ένα. Στην περίπτωση των επενδυμένων αγωγών, όταν εφαρμόζεται διαμήκης κάμψη, ο αγωγός οβαλοποιείται και σε ένα συγκεκριμένο στάδιο της παραμόρφωσης ο εσωτερικός αγωγός παρουσιάζει δομική αστάθεια στη μορφή ομοιόμορφων μικρών κυμάτων πτύχωσης (uniform wave wrinkles). Στη συνέχεια, και σε ένα προχωρημένο στάδιο της καμπτικής παραμόρφωσης, παρατηρείται η μετάβαση της μορφής της κυματοειδούς πτύχωσης σε μία δευτερεύουσα μορφή πτύχωσης με διπλάσιο μήκος κύματος και με πολύ εντονότερο μέγεθος. Η δημιουργία πτυχώσεων σημαντικού μεγέθους είναι μη επιθυμητή, ως εκτούτου, η ακριβής

πρόβλεψη της αστοχίας του εσωτερικού αγωγού σε λυγισμό είναι βαρύνουσας σημασίας για τον ασφαλή δομικό σχεδιασμό των υπόψη αγωγών.

Μεταξύ των δύο υπό εξέταση προβλημάτων υπάρχουν σημαντικές ομοιότητες. Και τα δύο προβλήματα αναφέρονται στη δομική συμπεριφορά και ευστάθεια ενός λεπτότοιχου μεταλλικού κελύφους το οποίο είναι εγκιβωτισμένο. Ο εγκιβωτισμός αυτός επηρεάζει σημαντικά και αλλάζει την συμπεριφορά του κελύφους και αυτό έχει ως συνέπεια η γνωστή θεωρία και οι υπάρχουσες επιλύσεις των προβλημάτων για τα μη εγκιβωτισμένα κελύφη να μη μπορούν να εφαρμοστούν άμεσα στις παρούσες περιπτώσεις. Στο πρώτο πρόβλημα των εγκιβωτισμένων αγωγών υπό εξωτερική πίεση, ο λεπτότοιχος μεταλλικός αγωγός περιορίζεται από το περιβάλλον μέσο, με αποτέλεσμα ο αγωγός να μη μπορεί να οβαλοποιηθεί ελεύθερα όταν αναπτύσσεται εξωτερική πίεση. Αντίστοιχα, στο δεύτερο πρόβλημα των επενδυμένων αγωγών υπό διαμήκη κάμψη, ο λεπτότοιχος εσωτερικός σωλήνας περιορίζεται από τον παχύ εξωτερικό σωλήνα, με αποτέλεσμα ο εσωτερικός σωλήνας να μην είναι ελεύθερος να οβαλοποιηθεί από την επιβολή της κάμψης και να μην αστοχεί με τρόπο παρόμοιο με αυτόν των μη εγκιβωτισμένων αγωγών. Επιπλέον, και στις 2 περιπτώσεις, η αποκόλληση του λεπτότοιχου κελύφους από το περιβάλλον μέσο είναι το κρίσιμο φαινόμενο που οδηγεί στην αστοχία με τη μορφή λυγισμού (δομική αστάθεια).

Η παρούσα έρευνα αποσκοπεί στην δημιουργία θεωρητικού υπόβαθρου για την κατανόηση και την επίλυση ενός σημαντικού αριθμού προβλημάτων εγκιβωτισμένων κυλινδρικών κελυφών, τα οποία αναφέρονται σε πολλές πρακτικές εφαρμογές.

Table of contents

1. Introduction

The present dissertation offers an in-depth investigation of the structural behavior and stability of thin-walled cylindrical shells under various loading conditions in the presence of lateral confinement. The work is motivated by practical engineering problems where the confinement can be a surrounding medium or another shell. Two principal structural loading conditions are mainly examined; the structural behavior of confined cylinders (a) under external pressure, and (b) under longitudinal bending. The first issue is motivated by the structural behavior of buried water or hydrocarbon pipelines surrounded by saturated soil medium or concrete encasement. In particular, when the groundwater table is above the pipeline level, the water reaches the pipe through the permeable surrounding soil or concrete, and hydrostatic pressure conditions develop around the pipeline, which may cause buckling of the steel pipeline wall. Buckling of confined cylinders under hydrostatic pressure is quite different than buckling under thermal effects, sometimes referred to as "shrink buckling". In "shrink buckling", hoop compressive force is relieved immediately after buckling occurs, whereas in hydrostatic buckling, pressure load is always present in the post-buckling stage.

The second issue examined in the present dissertation refers to the mechanical behavior and wrinkling of confined cylindrical shells under longitudinal bending. The work focuses on the mechanical behavior of lined pipes. The lined pipe is a double-wall pipe, composed by two pipes that are in contact; a thick-walled carbon steel "outer pipe" and a thin-walled corrosion-resistant inner pipe, referred to as "liner" pipe. Lined pipe is a relatively recent alternative solution and a promising technological application of offshore hydrocarbon (oil, gas etc.) steel pipelines for ensuring internal corrosion resistance and withstanding normal transportation pressure as well as structural loads. A lined pipe is produced by inserting the liner pipe into the external carbon steel pipe, through an appropriate manufacturing process, so that the bond between the two pipes is purely mechanical, in the sense that the outer pipe material and the liner pipe material remain two distinct materials. When longitudinal bending curvature is applied, the lined pipe ovalizes and, at a certain stage of deformation, the liner buckles in the form of short-wave wrinkles (uniform wrinkling). Such an event is undesired, and therefore, prediction of liner buckling is of significant importance for the safe design of these pipes.

There exist several similarities between the two above problems; they both refer to the structural behavior and stability of thin-walled steel shells embedded in a confinement

medium. This confinement affects and alters substantially the behavior of the shell, so that existing solutions and test data for the corresponding unconfined shells cannot be applied in the present case. In the first problem of externally-pressurized confined pipes, the thin-walled steel pipe is constrained by the surrounding medium, so that the pipe cannot buckle in an oval form when external pressure is developed. In the second problem of confined cylinders under longitudinal bending, the thin-walled cylindrical "liner" is constrained by the thick-walled outer pipe, so that the liner is not free to ovalize under bending and may not buckle in a way similar to the one observed in the unconfined cylinders. This common characteristic of confinement connects the two subjects, justifies the parallel investigation, and allows the derivation of general conclusions.

In the following section 1.1, a brief description of the structural behavior and stability of unconfined cylinders under external pressure and longitudinal bending is presented in order to introduce the reader to the original problem of cylindrical shell stability under external pressure and longitudinal bending, before continuing to the investigation of the corresponding problems in confined cylinders.

1.1 Structural behavior and stability of unconfined cylinders

1.1.1 Unconfined cylinders under external pressure

When uniform external pressure is applied to a cylinder, during the initial stages of loading, the cross-section is uniformly shrinking, maintaining its circular shape up to a critical pressure. Nevertheless, at a certain stage, the cylinder collapses and deformation of the cross-section occurs abruptly in the form of ovalization [1]. Any such collapse failure normally will develop into a propagating collapse failure, since the critical collapse pressure of a circular cylinder is several times larger than the propagation pressure [2].

Research on cylindrical tube buckling under external pressure dates back to the middle of the nineteenth century. In an early study, Bresse [3], using small deflection theory, studied the stability of a thin circular elastic ring under external hydrostatic pressure. In particular, the constitutional law is taken into account assuming isotropic elastic behavior, as well as the basic kinematics formulae are used in which the total deformation is formed as the sum of the membrane and bending strain. The equilibrium equations are determined in terms of the radial and tangential mid-surface displacements. The primary equilibrium path is defined, assuming uniform shrinkage of the ring cross-section, i.e. the radial displacement is proportionate to the value of the external pressure, whereas the tangential

displacement is equal to zero. Considering the above assumptions, the following expression is derived:

$$p_e = \frac{3EI}{R^3}, \tag{1}$$

where p_e is the critical buckling pressure, E is the modulus of elasticity, I is the moment of inertia of the ring's cross-section, and R is the mean radius of the ring. Bryan [4] used the minimum potential energy criterion of stability to formulate an expression similar to Eq. (1) for the case of an infinitely long elastic pipe under external hydrostatic pressure. Using small deflection theory, the normalized equations of stability are formed. Periodic (trigonometric) functions for the radial and tangential displacements are assumed, and appropriate boundary conditions for the prevention of the rigid body motion are applied. In order to account for the plane strain conditions associated with the case of an infinitely long cylinder (pipe), the term E in Eq. (1) has been replaced by the term $E/(1-\nu^2)$. Considering this modification and substituting for $I = t^3/12$, where a unit width is considered in the longitudinal direction of the cylinder, the resulting equation is:

$$p_e = \frac{2E}{1-\nu^2}\left(\frac{t}{D}\right)^3, \tag{2}$$

where D is the mean diameter of the pipe, t is the wall thickness, and ν is the Poisson's ratio. Equations (1) and (2) are frequently credited to Timoshenko because of the summary of ring stability presented in his classical text [5]. For a more detailed presentation of this buckling problem, the reader is referred to the classic book of Brush & Almroth [6]. The corresponding shape of the buckled cylinder is described by the following functions for the radial w and the hoop u displacements of the cross-section:

$$w = A\cos(2\theta), \tag{3}$$

$$u = -\frac{A}{2}\sin(2\theta), \tag{4}$$

where A is an arbitrary factor. A schematic representation of the radial and the hoop displacements is depicted in Figure 1. Assuming small values for the above displacements, the membrane hoop strain is also small, so that the failure mode is referred to as "first-order" inextensional or simply inextensional. More specifically the membrane strain ε_m is:

$$\varepsilon_m = \frac{u' + w}{R} + \frac{1}{2}\left(\frac{u - w'}{R}\right)^2. \tag{5}$$

Inserting (3),(4) and keeping only linear terms with respect to A, one readily obtains $\varepsilon_m = 0$, which implies that the circumferential length of the cylinder does not change at the initial post-buckling stage.

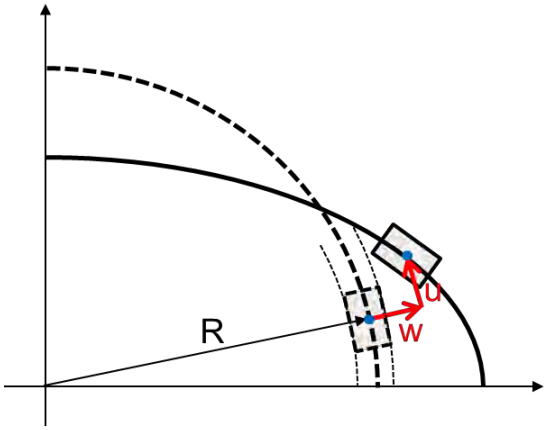

***Figure 1**: Schematic representation of radial (w) and tangential or hoop (u) mid-surface displacements.*

In general, external pressure applied in cylindrical shells causes compressive hoop stresses in the cylinder wall, so that the stability of the cylinder cross-section depends on both the circumferential (hoop) stiffness of the cylinder against ovalization and the yield strength. However, for thin-walled cylinders, the hoop stiffness is small, and therefore, elastic collapse instability occurs at an average hoop stress well below the proportional or yield limit. In other words, thin-walled cylinders, when subjected to uniform external hydrostatic pressure, buckle in the elastic range in the form of an oval shape (Figure 2).

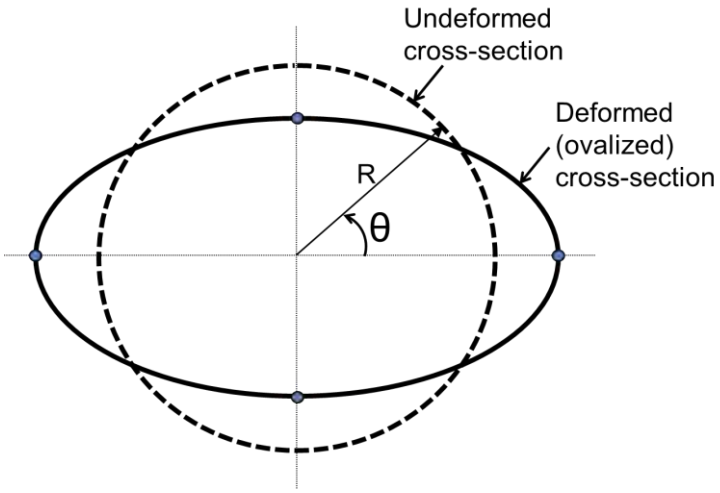

***Figure 2**: Schematic representation of ovalization of the cylinder cross-section.*

The above elastic critical pressure in equation (2) is valid for steel cylinders with rather high values of the diameter-to-thickness ratio. In such a case, the value of p_e is significantly below the yield pressure p_y, i.e. the pressure that causes full plastification of the cylinder. From thin-walled vessel theory, and considering a von Mises yield criterion, this plastic pressure p_y is readily calculated equal to [6]:

$$p_y = 2\frac{\sigma_y}{\sqrt{1-\nu+\nu^2}}\left(\frac{t}{D}\right), \tag{6}$$

where σ_y is the yield stress of the material under uniaxial stress conditions, and factor $1/\sqrt{1-\nu+\nu^2}$ accounts for increase of yield stress in the hoop direction due to plane strain conditions. Assuming $\nu = 0.30$ for metals, this factor is equal to 1.13. Dividing the two pressures is equations (2) and (6), one obtains:

$$\frac{p_e}{p_y} = 0.98\frac{E}{\sigma_y}\left(\frac{t}{D}\right)^2. \tag{7}$$

The formulae (2) and (6) are directly applicable for the external pressure design of offshore pipes and tubulars. Various versions of the elastic buckling pressure formula (2) have been widely used in several design specifications [7],[8],[9], that employ appropriate safety factors accounting for initial imperfections and residual stresses.

Upon buckling, considerable high stresses are developed at the four points of the ovalized cylinder cross-section, shown by dots in Figure 2, that lead to plastic strains, and as a consequence to the formation of a plastic hinge collapse mechanism [10].

Buckling of cylindrical shells under external pressure is characterized by significant sensitivity with respect to initial imperfections, as it was found in the numerical work of Kyriakides and Babcock [11]. In addition, the experimental and numerical work of Yeh and Kyriakides [12] demonstrated that the collapse pressure of inelastic thick-walled tubes is sensitive to the parameters of initial ovality, thickness variation, residual stresses, inelastic anisotropy, material parameter, and length of the ovalized section. Assuming a quasi 2D numerical model, similar to the one used in Chapter 2 of the present study, with 4-node reduced-integration shell elements for the cylinder, and considering a small imperfection in the form of an oval shape, the imperfection sensitivity of a steel cylinder with $D/t = 200$, is examined. In Figure 3, the equilibrium paths pressure-ovalization for different imperfection amplitudes are depicted, whereas in Figure 4, the normalized maximum pressure is shown in terms of the imperfection amplitude. The external pressure is normalized by the plastic

pressure p_y, whereas the ovalization parameter ζ is defined as $\zeta = (D_{\max} - D_{\min})/2D$. The initial imperfection is considered a vertical residual displacement at the top of the cylinder, which follows the application of a radial load, and is normalized by the radius R of the cylinder. The theoretical value of p_e is 0.057 MPa, whereas the one of p_y is 3.537 MPa. Curve (a) corresponds to the response of a quasi-perfect cylinder. The maximum pressure occurs at point A, somewhat higher than the value of p_e, whereas the descending branch of the path corresponds to the formation of plastic hinge mechanism. Note that all curves, independent of the value of initial imperfection, merge, because of the plastic-hinge mechanism formation.

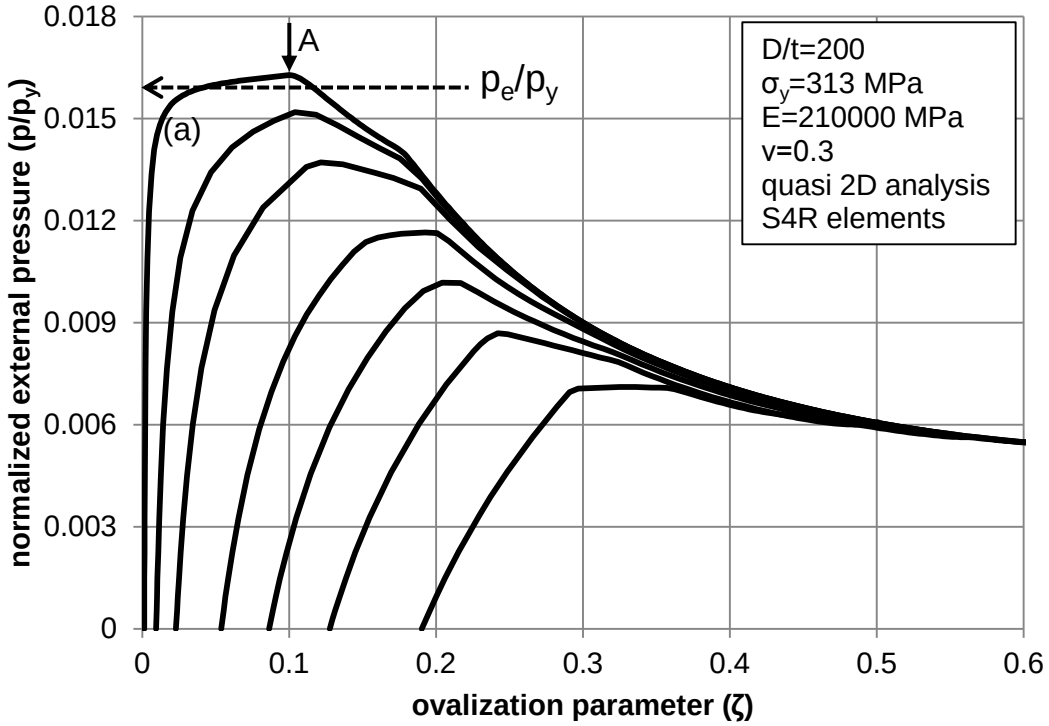

***Figure 3**: Equilibrium paths pressure-displacement of a steel cylinder under external pressure for different values of initial imperfection.*

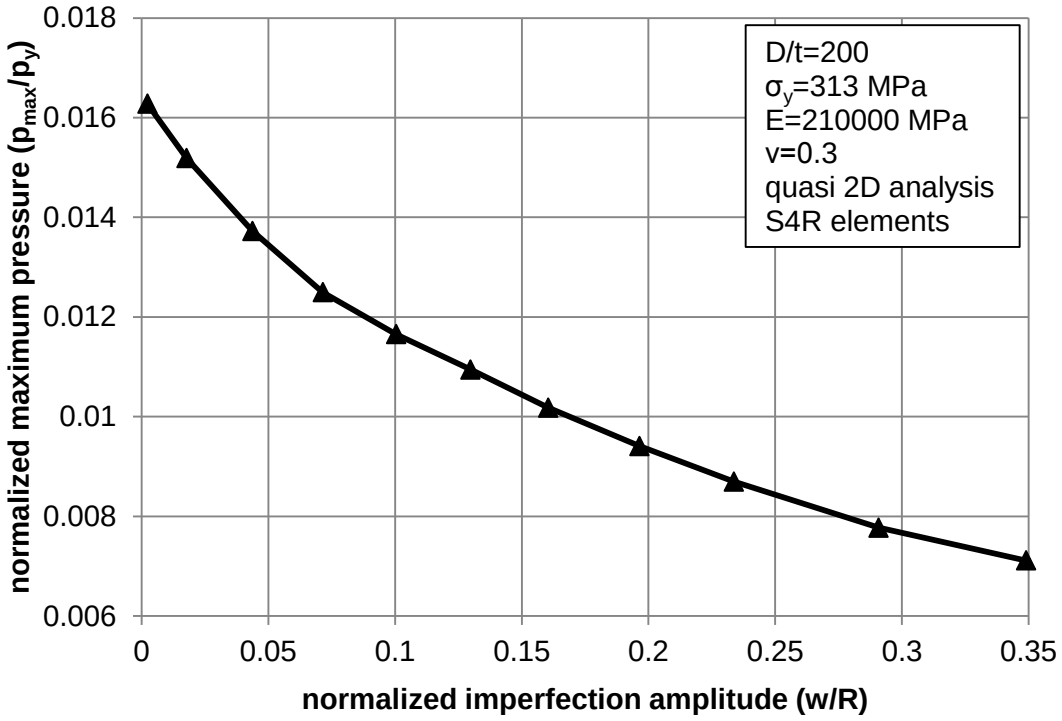

***Figure 4**: Effect of initial imperfections on the maximum external pressure sustained by a steel cylinder.*

The problem of steel cylindrical shells under external pressure has direct implications in offshore pipelaying operations because of the so-called "Propagating Buckle", where a local collapse in a long pipe under external pressure propagates flattening the entire pipe, often at high velocity. The lowest pressure at which a buckle will propagate is known as the propagation pressure [13],[14]. For typical offshore pipelines, the propagation pressure is only a small fraction of the collapse pressure.

1.1.2 Unconfined cylinders under longitudinal bending

The response of elongated steel cylinders under longitudinal bending is a problem encountered in numerous engineering applications. The accurate prediction of buckling deformation is a crucial issue towards safeguarding the structural integrity of the steel cylinder. When a long thin-walled cylinder subjected to longitudinal bending curvature, its cross-section ovalizes (Figure 2) resulting in loss of bending stiffness in the form of limit point instability. This phenomenon is referred to as "ovalization instability" or "Brazier effect". In fact, Brazier [15] has been the first to detect and quantify this phenomenon. Assuming elastic behavior and an inextensional deformation shape for ovalization, similar

to the previous case of cylinder under external pressure, he calculated the ultimate bending moment and the corresponding curvature according to the following formulae:

$$M_{BR} = 0.987 \frac{Et^2 R}{\sqrt{1-\nu^2}}, \tag{8}$$

$$k_{BR} = 0.471 \frac{t}{R^2 \sqrt{1-\nu^2}}, \tag{9}$$

where E is the Young's modulus, t is the wall thickness, R is the cylinder radius, and ν is the Poisson's ratio. Reissner [16] has been the first to investigate ovalization instability for both initially straight and curved tubes, taking under consideration the effects of pressure. This buckling response of elastic tubes has also investigated more thoroughly in later publications [17],[18]. This phenomenon is more pronounced in long cylinders, free of boundary conditions. However, experimental results in [19] have shown that the increased axial stress at the compression side due to ovalization may cause, at a certain stage of deformation, bifurcation instability (buckling) in a form of longitudinal short wave-type "wrinkles" (Figure 5) usually before reaching a limit moment. This buckling of cylinders occurs within a relatively narrow area around the maximum compression side ($\theta=\pi/2$ in Figure 2), which is often called "buckling zone". Ovalization induces hoop stresses and strains, resulting in a multi-axial stress/strain state at the buckling zone. A typical moment-curvature equilibrium path of a thin-walled elastic cylinder under longitudinal bending loading is shown in Figure 6. Considering a cross-sectional ovalization analysis, referred to as "2D", the buckling phenomena are excluded, thus the response appears a maximum moment due to ovalization. On the other hand, considering 3D analysis, bifurcation from the ovalization equilibrium path is observed in the form of wave wrinkles. This bifurcation occurs before the maximum moment is reached, and a secondary equilibrium path is followed.

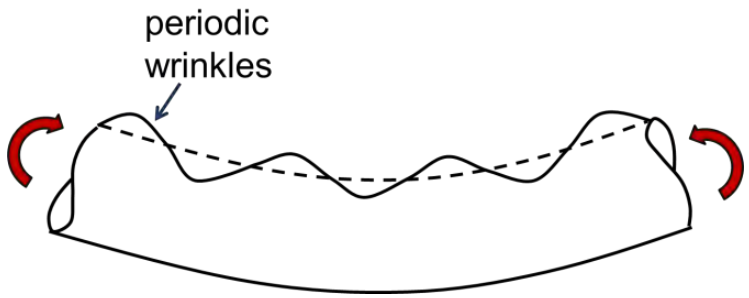

***Figure 5**: Schematic representation of periodic wrinkles at the compression side of a bent cylindrical member.*

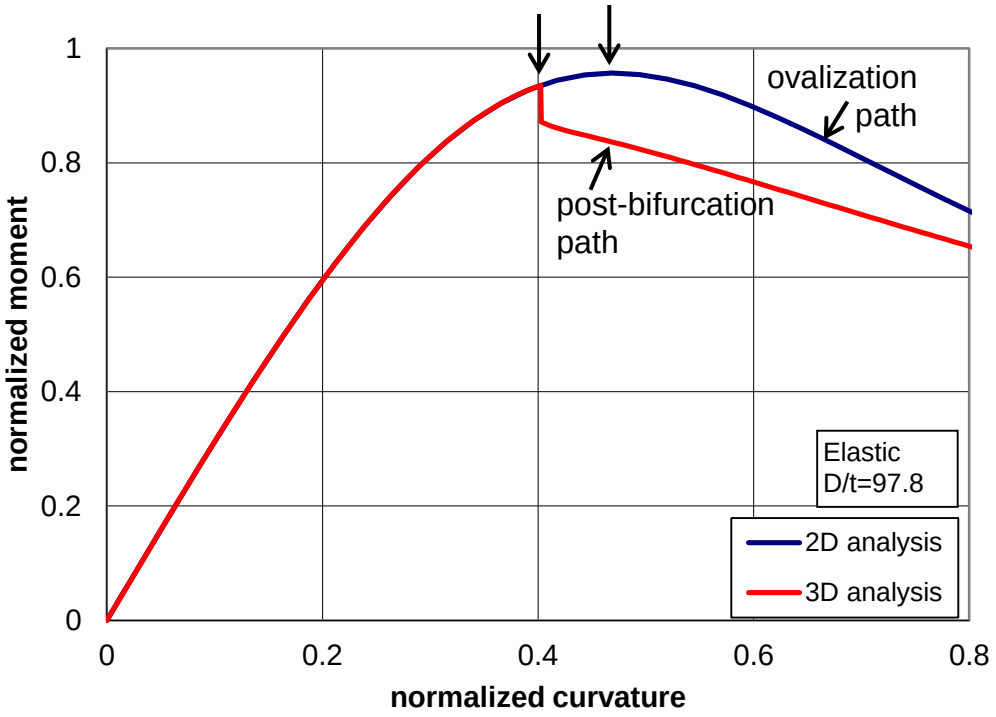

***Figure 6**: Moment-curvature response of a thin-walled elastic cylinder under longitudinal bending; numerical results for 2D and 3D analysis.*

Bifurcation instability of ovalized tubes subjected to bending was recognized in early publications [15]. An attempt to predict the bending buckling of elastic tubes was reported in [20], postulating that the buckling moment of a cylinder under bending corresponds to a nominal stress quite similar to the buckling stress of a cylinder with the same radius under uniform compression. This argument has been employed to develop a simplified bifurcation formulation proposed in [21] for predicting shell buckling. More specifically, it is assumed that buckling is fully determined by the stress and deformation inside the zone of the initial buckle. This assumption has also been referred to as "local buckling hypothesis". According to the above hypothesis, in the case of a long cylindrical shell under longitudinal bending, buckling will occur at the critical location when the axial compressive stress σ_{x0} and the hoop curvature $1/r_{\theta 0}$ satisfy the following equation:

$$\sigma_{x0} = \frac{E}{\sqrt{3\left(1-\nu^2\right)}} \frac{t}{r_{\theta 0}}. \qquad (10)$$

The change of hoop curvature $1/r_{\theta 0}$ due to bending is shown schematically in Figure 7. It is interesting to note that Eq. (10) is the classical Donnell's equation for a uniformly compressed elastic circular cylinder with radius $r_{\theta 0}$ in the meridional direction. Subsequent

works [22],[23],[24] demonstrated numerically that bifurcation predictions from this hypothesis for the case of elongated unconfined cylindrical elastic shells subjected to bending are in very good agreement with finite element results.

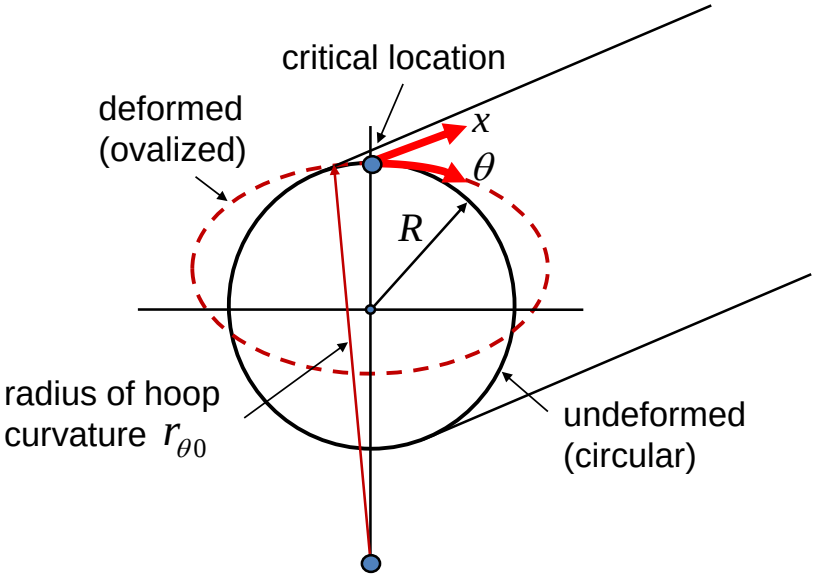

***Figure 7**: Schematic representation of local hoop curvature during ovalization of the cylindrical shell.*

According to the above simplified formulation, the corresponding buckling wavelength can also be estimated. Assuming that the state of stress is constant within the buckling zone, axi-symmetric conditions can be considered so that the value of the buckling half-wavelength L_{hw} can be estimated by the following equation, which stems from axi-symmetric buckling analysis of elastic cylindrical shells under uniform meridional compression [5]:

$$L_{hw} = \left[\frac{\pi^4}{12\left(1-\nu^2\right)}\right]^{1/4} \sqrt{r_{\theta 0} t}\,. \qquad (11)$$

The above refer to cylinders made of elastic material for the range of D/t values of interest. A particularity of the bending behavior of steel tubes is that buckling occurs in the plastic range. First yielding may not offer a reliable measure of bending strength and deformation capacity. Experimental evidence [19] has demonstrated that rather thick-walled cylinders, with D/t ratio values below 40, exhibit significant inelastic deformation before buckling occurs in the form of localized wrinkles at the compression side of the cylinder. In several engineering applications, it is important to determine the curvature at which bifurcation (buckling) would occur, and this bifurcation curvature depends on the

value of D/t ratio. For thicker cylinders [22], uniform wrinkling may not be catastrophic, allowing significant inelastic deformations and, eventually, limit-moment instability. Beyond the limit point, stiffness is reduced and at a certain point, the cylinder would fail because of localized deformation. On the other hand, thinner cylinders exhibit a secondary bifurcation and buckling localization, before a limit moment is reached.

Several analytical attempts have been reported to develop a simplified formulation for predicting buckling of steel cylinders similar to the one proposed previously for elastic cylinders. Those attempts have employed both the elastic-plastic material moduli for J_2-flow or J_2-deformation theory of plasticity. Despite the superiority of J_2-deformation theory, those attempts have not been successful.

Buckling of shells under axial compression and bending is generally characterized by significant sensitivity with respect to initial imperfections. This was investigated in the early work of Koiter [25], and concluded that imperfection sensitivity of a structure is directly related to its initial post-buckling behavior. Numerical results from thin-walled cylindrical shells subjected to bending [22],[26] have showed that the ultimate bending load and the corresponding critical curvature are reduced with increasing imperfection amplitude.

1.2 Scope of the present work

The mechanical behavior presented in the previous section refers exclusively to cylinders without confinement. However, in many technological applications, steel cylinders are confined within a surrounding medium or another shell. Because of this interaction, existing numerical solutions and analytical predictions for the buckling resistance of unconfined thin-walled cylinders are inadequate to predict the stage at which the cylinder buckles. The following two subsections offer a short description for two problems investigated in the present dissertation, outlining the purpose of the present study.

1.2.1 Confined cylinders under external pressure

In several engineering applications, steel cylinders subjected to external pressure are confined within a surrounding medium. Under those conditions, the cylinders may buckle because of excessive hoop compression. Typical examples of externally-pressurized cylinders which may fail under confined conditions are (a) buried steel pipelines [27], (b) thin-walled liners used to rehabilitate damaged pipelines [28], (c) tunnels and ducts that

transport gases or liquids in power plants are often lined with cylindrical steel shells [29], and (d) steel tubes as casing in oil and gas production wells [30].

Chapter 2 of the present dissertation investigates the mechanical response of thin-walled cylinders surrounded by a rigid or deformable medium, subjected to uniform external pressure, applied directly on the outer cylinder surface. Emphasis is given on structural stability in terms of buckling, post-buckling, imperfection sensitivity, and medium deformability. The present investigation is computational and employs a quasi two-dimensional model, assuming no variation of load and deformation along the cylinder axis. The cylinder and the surrounding medium are simulated with nonlinear finite elements that account for both geometric and material nonlinearities.

The behavior of cylinders made of elastic material embedded in a rigid cavity is examined first, and a successful comparison of the numerical results is conducted with available closed-form analytical solutions and experimental data for rigidly-confined elastic cylinders [31],[32]. Subsequently, the external pressure response of confined thin-walled steel cylinders is examined in terms of their sensitivity on the presence of the initial out-of-roundness of the cylinder and the initial gap between the cylinder and the surrounding medium. The numerical results are presented in the form of pressure-deformation equilibrium paths and show an unstable post-buckling response (rapid drop of pressure) beyond the maximum pressure level, indicating severe imperfection sensitivity on the value of the maximum pressure. A plastic-hinge mechanism is also developed that results in a closed-form expression and illustrates the post-buckling response of the cylinder in an approximate yet very representative manner. Furthermore, the effects of the deformability of the surrounding medium are examined. In particular, soil embedment conditions are examined, with direct reference to the case of buried thin-walled steel pipelines. The distribution of plastic deformation within the steel cylinder, as well as the variation of cylinder-medium contact pressure around the cylinder cross-section are also depicted and discussed.

The numerical results are employed to develop an efficient design methodology, which is compatible with the recent general provisions of European design rules and recommendations for shell buckling [33],[34], and could be used for design purposes. The numerical results show good comparison with available experimental results [35],[36], the proposed design methodology and with a simplified closed-form expression [35], which could also be used for design purposes. Furthermore, a relevant chapter for the design of confined steel cylinders, within the framework of the European Design Recommendations

[34], is developed and presented in Appendix A, for possible inclusion of the present work in future editions of the EDR.

Finally, based on the numerical results, a comparison is attempted between the present buckling problem and the problem of "shrink buckling". The differences between those two problems of confined cylinder buckling are pin-pointed, emphasizing the significantly different response of the two problems with respect to the presence of initial imperfections.

1.2.2 Confined cylinders under longitudinal bending

In several engineering applications, cylindrical members subjected to longitudinal bending are confined within a surrounding medium or another shell. Some representative examples of these applications are (a) the bending response of a lined pipe (sometimes referred to as mechanically-clad pipe) [37],[38], where a corrosion-resistant thin-walled liner is fitted inside a carbon–steel outer pipe, (b) the nano-composite tubes [39],[40], where an inner carbon nanotube is confined in a polymer matrix, and (c) the buried steel pipelines under strike-slip tectonic fault displacements [41], where permanent ground deformation is applied on the pipeline.

The study in Chapter 3, without loss of generality, focuses on the application of lined pipes and investigates extensively the wrinkling of such pipes under bending loading with or without the presence of external pressure. The lined pipe is a double-wall pipe, composed by two pipes that are in contact; a thick-walled "outer pipe" and a thin-walled inner pipe, referred to as "liner" pipe. The motivation of this study stems mainly from the use of such pipes in energy pipeline applications (oil, gas etc.). Lined pipes are produced through an appropriate manufacturing procedure, consisting of heating the outer pipe, inserting the liner and pressurizing it until both pipes come to contact, and finally cooling the outer pipe [37],[38]. Considering the liner pipe as a thin-walled cylindrical shell prone to buckling, the lateral confinement due to the deformable outer pipe constitutes a paramount parameter for its mechanical behavior. It is noted that single-wall pipes under bending ovalize and buckle before reaching a limit moment [19]. On the other hand, in double-wall pipes, the liner is not free to ovalize, and because of this confinement, existing numerical solutions [23],[24] or analytical predictions [21] for the bending buckling resistance of unconfined thin-walled tubes are inadequate to predict the buckling resistance of the bent liner. Therefore, to predict the response and the buckling strength of the thin-walled liner, it is necessary to account for its contact with the confining thick-walled outer pipe.

In the present investigation, the problem is solved numerically, using nonlinear finite elements to simulate the lined pipe and the interaction between the liner and the outer pipe. Nonlinear geometry with large strains is taken into account, and the material of both pipes is elastic-plastic. First, an ovalization bending analysis of the lined pipe is conducted, where a slice of the pipe between two adjacent cross-sections is considered, excluding the possibility of buckling. Stresses and strains in the compression zone are monitored throughout the deformation stage, detecting possible detachment of the liner from the outer pipe and the formation of wrinkles. Subsequently, a three-dimensional analysis is conducted to examine the wrinkling behaviour of elastic and steel lined pipes under bending with or without the presence of external pressure. The possibility of bifurcation in a wrinkling pattern, including the possibility for a secondary bifurcation, is examined. The values of corresponding buckling curvature are determined and comparison with available experimental results is conducted in terms of wrinkle height development and the corresponding buckling wavelength. The results of the present research can be used for safer design of lined pipes in pipeline applications.

1.3 References

[1] Murphy, C.E., Langner, C.G. (1985). "Ultimate Pipe Strength Under Bending, Collapse and Fatigue", *Proceedings of the 4th International Conference on Offshore Mechanics and Arctic Engineering (OMAE)*, Dallas, USA.

[2] Kyriakides, S., Corona, E. (2007). *Mechanics of Offshore Pipelines. Vol. 1: Buckling and Collapse.* Elsevier, Oxford, UK.

[3] Bresse, J.A.C. (1866). *Cours de Mécanique Appliquée*, 2nd Ed., Paris, France.

[4] Bryan, G.H. (1888). "Application of the energy test to the collapse of a long thin pipe under external pressure". *Cambridge Philosophical Society Proceedings*, Vol. 6, pp. 287-292, Cambridge, U.K.

[5] Timoshenko, S., Gere, J.M. (1961). *Theory of Elastic Stability*, 2nd Ed., McGraw Hill, New York, NY.

[6] Brush, D.O., Almroth, B.O. (1975). *Buckling of Bars, Plates, and Shells*, McGraw-Hill, New York, NY.

[7] American Petroleum Institute (1999). *Design, Construction, Operation and Maintenance of Offshore Hydrocarbon Pipelines (Limit State Design),* API RP 1111, 3rd edition, Washington, DC.

[8] Det Norske Veritas (2000). *Design Rules for Submarine Pipelines*, DNV-OS-F101, Oslo, Norway.

[9] American Petroleum Institute (1993). *Recommended Practice for Planning, Designing and Constructing Fixed Offshore Platforms*, API RP2A-LRFD, 1st edition, Washington, DC.

[10] Kyriakides, S., Babcock, C.D. (1982). "On the initiation of a propagating buckle in offshore pipelines", *Third International Conference on the Behavior of Offshore Structures*, Boston, MA, Vol. 2, pp. 187-199.

[11] Kyriakides, S., Babcock, C.D. (1981). "Large deflection collapse analysis of an inelastic inextensional ring under external pressure", *International Journal of Solids and Structures*, Vol. 17, No. 10, pp. 981-993.

[12] Yeh, M.K., Kyriakides, S. (1986). "On the Collapse of Inelastic Thick-Walled Tubes under External Pressure", *Journal of Energy Resources Technology*, Vol. 108 pp. 35-47.

[13] Kyriakides, S., Babcock, C.D., Elyada, D. (1984). "Initiation of Propagating Buckles From Local Pipeline Damages", *Journal of Energy Resource Technology*, Vol. 106, No. 1, pp. 79-87.

[14] Nogueira, A.C., Tassoulas, J.L. (1994). "Buckle Propagation: Steady-State Finite Element Analysis" *Journal of Engineering Mechanics*, ASCE, Vol. 120, No. 9, pp. 1931-1944.

[15] Brazier, L.G. (1927). "On the flexure of thin cylindrical shells and other "thin" sections", *Proceedings of the Royal Society of London*, Series A, Vol. 116, No. 773, pp. 104-114.

[16] Reissner, E. (1959). "On finite bending of pressurized tubes". *Journal of Applied Mechanics*, ASME, Vol. 26, pp. 386-392.

[17] Corona, E., Kyriakides, S. (1988). "On the Collapse of Inelastic Tubes under Combined Bending and Pressure". *International Journal of Solids and Structures*, Vol. 24, No. 5, pp. 505-535.

[18] Karamanos, S.A., Tassoulas, J.L. (1991). "Stability of Inelastic Tubes under External Pressure and Bending", *Journal of Engineering Mechanics*, ASCE, Vol. 117, No. 12, pp. 2845-2861.

[19] Kyriakides, S., Ju, G.T. (1992). "Bifurcation and Localization Instabilities in Cylindrical Shells under Bending I: Experiments". *International Journal of Solids and Structures*, Vol. 29, pp. 1117-1142.

[20] Seide, P., Weingarten, V.I. (1961). "On the buckling of circular cylindrical shells under pure bending". *Journal of Applied Mechanics*, ASME, Vol. 28, pp. 112–116.

[21] Axelrad, E.L. (1965). *Refinement of buckling-load analysis for tube flexure by way of considering precritical deformation*. [in Russian]. Izvestiya Akademii Nauk SSSR, Otdelenie Tekhnicheskikh Nauk, Mekhanika i Mashinostroenie, 4, 133-139.

[22] Ju, G.T., Kyriakides, S. (1992). "Bifurcation and Localization Instabilities in Cylindrical Shells under Bending II: Predictions". *International Journal of Solids and Structures*, Vol. 29, pp. 1143-1171.

[23] Karamanos, S.A. (2002). "Bending Instabilities of Elastic Tubes", *International Journal of Solids and Structures,* Vol. 39, No. 8, pp. 2059-2085.

[24] Houliara, S., Karamanos, S.A. (2006). "Buckling and Post-Buckling of Pressurized Thin-Walled Elastic Tubes under In-Plane Bending", *International Journal of Nonlinear Mechanics*, Vol. 41, No. 4, pp. 491-511.

[25] Koiter, W.T. (1963). "The Effect of Axisymmetric Imperfections on the Buckling of Cylindrical Shells under Axial Compression", *Proceedings of Koninklijke Nederlandse Akademie Van Wetenschappen,* Amsterdam, Series B, Vol. 66, pp. 265–279.

[26] Houliara, S., Karamanos, S.A. (2010). "Stability of Long Transversely-Isotropic Elastic Cylinders under Bending", *International Journal of Solids and Structures,* Vol. 47, No. 1, pp. 10-24.

[27] Watkins, R.K. (2004). "Buried Pipe Encased in Concrete", *International Conference on Pipeline Engineering & Construction,* ASCE, San Diego, CA.

[28] Omara, A.M., Guice, L.K., Straughan, W.T., Akl, F.A. (1997). "Buckling Models of Thin Circular Pipes Encased in Rigid Cavity", *Journal of Engineering Mechanics,* ASCE, Vol. 123, No. 12, pp. 1294-1301.

[29] Ullamn, F. (1964). "External Water Pressure Designs for Steel-Lined Pressure Shafts", *Water Power,* Vol. 16, pp. 298-305.

[30] Ahrens, T. (1970). "An In-Depth Analysis of Well Casings and Grouting: Basic Considerations of Well Design – II", *Water Well Journal*, pp. 49-51.

[31] Glock, D. (1977). "Überkritisches Verhalten eines Starr Ummantelten Kreisrohres bei Wasserdrunck von Aussen und Temperaturdehnung" (Post-Critical Behavior of a Rigidly Encased Circular Pipe Subject to External Water Pressure and Thermal Extension), *Der Stahlbau,* Vol. 7, pp. 212-217.

[32] El-Sawy, K., Moore, I.D. (1998). "Stability of Loosely Fitted Liners Used to Rehabilitate Rigid Pipes", *Journal of Structural Engineering,* ASCE, Vol. 124, No. 11, pp. 1350-1357.

[33] Comité Européen de Normalization (2007). Strength and Stability of Shell Structures, EN 1993-1-6, Eurocode 3, part 1-6, Brussels, Belgium.

[34] European Convention for Constructional Steelwork (2008). *Buckling of Steel Shells, European Design Recommendations*, 5th Edition, ECCS Publication No. 125, J.M. Rotter and H. Schmidt Eds., Brussels, Belgium.

[35] Montel, R. (1960). "Formule Semi-Empirique pour la Détermination de la Pression Extérieure Limite d'instabilité des Conduits Métalliques Lisses Noyées Dans du Béton" (A semi-empirical formula for determining the limiting external pressure for the collapse of smooth metal pipes embedded in concrete), *La Houille Blanche,* No. 5, pp. 560-568.

[36] Borot, M. (1957). "Essais des Conduits Métalliques Noyées Dans du Béton", *La Houille Blanche,* No. 6, pp. 881-887.

[37] Focke, E. (2007). *Reeling of Tight Fit Pipe,* Ph.D. Thesis. Delft University of Technology, Delft, The Netherlands.

[38] de Koning, A.C., Nakasugi, H., Ping, L. (2004), "TFP and TFT Back in Town (Tight Fit CRA Lined Pipe and Tubing)", *Stainless Steel World,* p.53-61.

[39] Vodenitcharova, T., Zhang, L.C. (2006). "Bending and Local Buckling of a Nanocomposite Beam Reinforced by a Single-Walled Carbon Nanotube", *International Journal of Solid and Structures,* Vol. 43, pp. 3006-3024.

[40] Lourie, O., Cox, D.M., Wagner, H.D. (1998). "Buckling and Collapse of Embedded Carbon Nanotubes", *The American Physical Society,* Vol. 81, No. 8, pp. 1638-1641.

[41] Vazouras, P., Karamanos, S.A., Dakoulas, P. (2010). "Finite element analysis of buried steel pipelines under strike-slip fault displacements", *Soil Dynamics and Earthquake Engineering*, Vol. 30, No. 11, pp. 1361-1376.

2. Confined cylinders under external pressure

2.1 Introduction

In several engineering applications, steel cylinders subjected to external pressure are confined within a surrounding medium. Under those conditions, the cylinders may buckle because of excessive hoop compression. Buried steel pipelines [1] under such loading conditions can often fail in the form of structural instability; when the groundwater table is above the pipeline level, the water reaches the pipe through the permeable surrounding soil or concrete encasement, and hydrostatic pressure conditions develop around the pipeline, which may cause buckling of steel pipeline wall. In addition, thin-walled liners, made of steel or plastic material, used to rehabilitate damaged pipelines [2], may also fail under similar loading conditions. Furthermore, tunnels and ducts that transport gases or liquids in power plants are often lined with cylindrical steel shells [3], which may buckle because of external pressure under lateral confinement. Finally, steel tubes employed as casing in oil and gas production wells [4] are also typical examples of externally-pressurized cylinders, which may fail under confined conditions.

In all the above applications, significant hoop stresses develop in the cylinder wall due to either thermal effects or hydrostatic pressure conditions because of ground water and the permeability of the surrounding medium. When these hoop stresses exceed a critical level, the steel cylinder loses its structural stability and buckles. In such a case, due to the surrounding medium, the cylinder wall is not free to deform in the outward direction, and buckling occurs in the form of an “inward lobe” at a pressure level significantly higher than the one under unconfined conditions. A schematic representation of the “inward lobe” buckling shape is depicted in Figure 8, whereas the corresponding failure mode by an external pressure experiment [5] is shown in Figure 9.

The study presented in this part of dissertation focuses on buckling and post-buckling of confined cylinders under uniform external pressure, motivated by the structural response of buried pipelines surrounded by saturated soil medium or concrete encasement. When the groundwater table is above the pipeline level, the water reaches the pipe through the permeable surrounding soil or concrete and hydrostatic pressure conditions develop around the pipeline, which may cause buckling of the steel pipeline wall. It should be noted that buckling of confined cylinders under hydrostatic pressure is quite different than buckling under thermal effects, sometimes referred to as “shrink buckling” [6],[7],[8],[9],[10],[11].

In “shrink buckling”, hoop compressive force is relieved immediately after buckling occurs, whereas in hydrostatic buckling, pressure load is always present in the post-buckling stage. For an extensive literature review on the “shrink buckling” problem, the reader is referred to the paper by Omara et al. [2]. In section 2.6 of the present chapter, a direct comparison between the present problem of “hydrostatic buckling” and the problem of “shrink buckling” is offered, based on numerical simulation results.

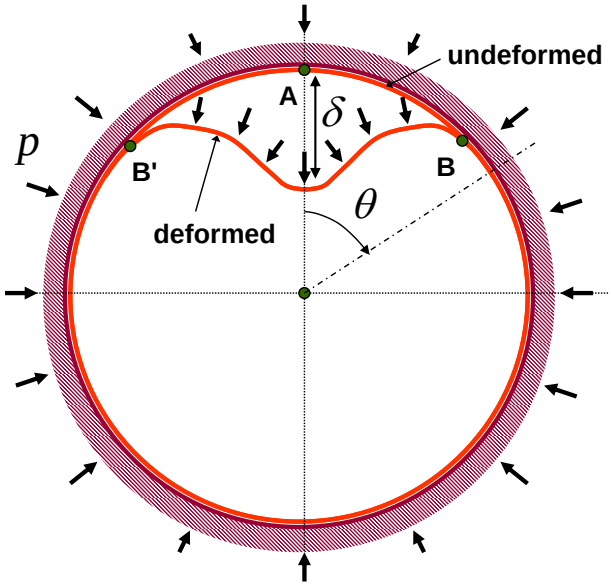

***Figure 8**: Schematic representation of the buckling problem of an externally-pressurized cylinder confined by the surrounding medium.*

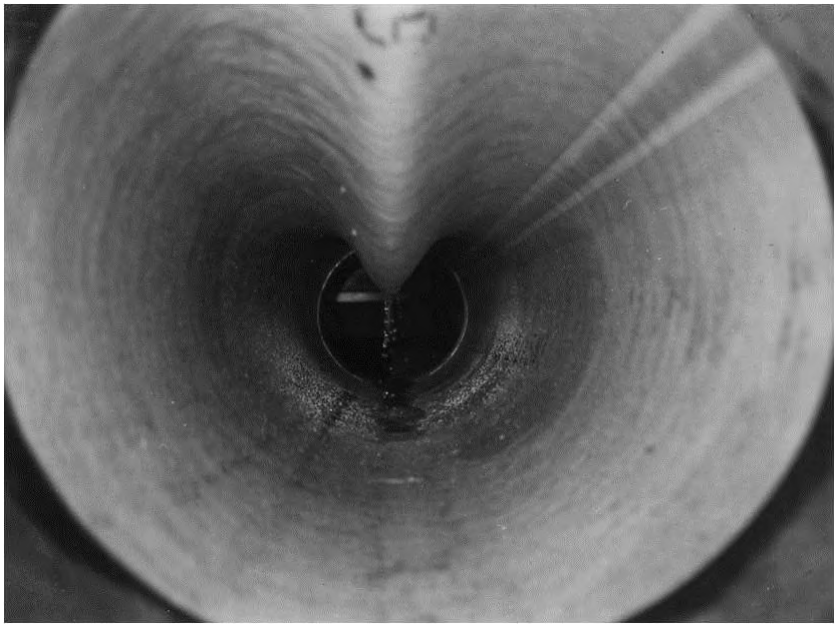

***Figure 9**: External pressure collapse of a confined pipe; buckling mode in the form an “inward lobe”. Experimental testing by Omara et al. [5].*

2.1.1 Literature review

The single-lobe mode buckling of Figure 8 has been observed in experiments (Figure 9, [5]) and in real applications of externally-pressurized cylinders under confined conditions. The first analytical attempt to predict this buckling behavior has been reported in the paper by Glock [12]. Glock presented an energy formulation and solution of the hydrostatic buckling problem of rigidly confined elastic cylinders, assuming no friction between the ring and the stiff (non-deformable) medium, as well as no variation of stress and deformation in the axial direction of the cylinder. Minimization of the potential energy and assuming a constant hoop membrane force around the cylinder cross-section, resulted in the following expression for the buckling pressure:

$$p_{GL} = \frac{E}{1-\nu^2}\left(\frac{t}{D}\right)^{2.2}, \tag{12}$$

where E is the Young's modulus, ν is Poisson's ratio, D is the cylinder diameter and t is the wall thickness. A brief presentation of this analytical solution is offered in the subsection 2.3.2 of the present chapter, whereas for a concise presentation of the Glock's solution, the reader is referred to the paper of Omara et al. [2]. It is interesting to note that for diameter-to-thickness (D/t) values between 100 and 300, which are typical values for buried pipelines and rehabilitation liners, the value of pressure p_{GL} calculated from equation (12) is significantly higher than the buckling (bifurcation) pressure p_e of a long (free of boundary conditions) externally-pressurized perfectly-round elastic cylinder under unconfined conditions, given by the following formula [13]:

$$p_e = \frac{2E}{1-\nu^2}\left(\frac{t}{D}\right)^3. \tag{13}$$

Combination of equations (12) and (13), results in:

$$\frac{p_{GL}}{p_e} = 0.5\left(\frac{D}{t}\right)^{0.8}. \tag{14}$$

It can be readily verified that the ultimate value of pressure p_{GL} calculated from equation (12) is 20 – 48 times higher than the buckling pressure p_e under unconfined conditions.

The validity of Glock's equation (12) in predicting the buckling pressure of tightly-fitted elastic cylinders in a rigid cavity has been verified by the finite element results reported by El-Sawy and Moore [14]. Based on their numerical results and accounting for the presence of initial gap g between the cylinder and the rigid surrounding medium

("loosely-fitted cylinders"), El-Sawy and Moore proposed the following empirical analytical expression for the buckling pressure of elastic cylinders:

$$p_{EM} = \frac{2E}{1-\nu^2}\left(\frac{t}{D}\right)^3\left(\frac{25+700(t/D)+315(g/R)}{0.15+130(t/D)+1400(t/D)^2+145(g/R)}\right). \qquad (15)$$

The last term within the parenthesis in the right-hand side of equation (15) expresses the increase of the classical elastic formula for unconfined conditions [see equation (13)] when rigid confining conditions are imposed on the externally-pressurized cylinder. Assuming a zero value of initial gap ($g=0$), the comparison between equation (15) and Glock's formula (12) shows that the former empirical formula can predict quite accurately the buckling pressure of tightly-fitted elastic cylinders in a rigid cavity. The validity of Glock's formula has also been tested against with experimental data [15],[16],[17].

In a later publication, Boot [18] enhanced Glock's solution [12] to account for the presence of initial gap between the cylinder and the non-deformable surrounding medium, and reported implicit analytical expressions for the buckling pressure. The effects of confinement deformability on the structural behavior of a confined elastic ring have been investigated by Bottega [19], who examined analytically the behavior of two concentric, contacting elastic rings, subjected to two self-equilibrating interfacial point loads. Li and Kyriakides [20] studied the problem of two concentric, contacting elastic rings, subjected to external pressure, and extended those results to investigate buckling propagation in an elastic cylinder in contact with an outer elastic cylindrical shell [21]. Those publications indicated that the stiffness of the outer (confining) elastic ring has a significant effect on the structural behavior and the buckling capacity of the inner elastic ring.

The above works on confined cylinder buckling refer to cylinders with elastic material behavior. Compared with the numerous publications on elastic cylinders, relatively few investigations exist on the corresponding buckling problem of steel cylinders, which is associated with elastic-plastic material behavior. As a first approximation, the ultimate external pressure capacity can be estimated as the pressure that causes first yielding at the outer fiber of the cylinder wall. Adopting this concept, Montel [22] used Timoshenko's solution for thin ring deflection [23] and experimental results [24] to develop a semi-empirical formula for the buckling pressure of cylinders embedded in a rigid (non-deformable) cavity, in terms of the material yield stress σ_y, the cylinder geometry D/t, the initial out-of-roundness with amplitude δ_0, and the initial gap with maximum value g between the cylinder and the rigid cavity:

$$p_M = \frac{14.1\,\sigma_y}{(D/t)^{1.5}\left[1+1.2(\delta_0+2g)/t\right]}. \tag{16}$$

Montel [22] proposed equation (16) for a range of parameters, namely $60 \le D/t \le 340$, $250MPa \le \sigma_y \le 500MPa$, $0.1 \le \delta_0/t \le 0.5$, $g/t \le 0.25$ and $g/R \le 0.0025$. Clearly, the ultimate pressure p_M predicted by equation (16) is a decreasing function of both imperfection types δ_0 and g as well as a decreasing function of the diameter-to-thickness ratio D/t. Furthermore, it can be readily shown that for D/t between 100 and 300, the value of p_M is well below the yield or plastic pressure p_y of the cylinder, i.e. the nominal pressure that causes full plastification of the cylinder wall. From thin-walled vessel theory, and considering a von Mises yield criterion under plane strain conditions for the deforming cylinder cross-section, this plastic pressure p_y is readily calculated equal to:

$$p_y = 2\,\frac{\sigma_y}{\sqrt{1-\nu+\nu^2}}\left(\frac{t}{D}\right), \tag{17}$$

where σ_y is the yield stress of the material under uniaxial stress conditions, and factor $1/\sqrt{1-\nu+\nu^2}$ accounts for increase of yield stress in the hoop direction due to plane strain conditions. Assuming $\nu = 0.30$ for metals, this factor is equal to 1.13. Note that the plastic pressure p_y is a decreasing function of the D/t ratio. Combining equations (16) and (17), and assuming $\nu = 0.30$, one obtains for perfect cylinders ($\delta_0 = g = 0$):

$$\frac{p_M}{p_y} = 6.24\left(\frac{t}{D}\right)^{0.5}. \tag{18}$$

It is interesting to note that, for D/t values ranging between 100 and 300, Montel's equation predicts a pressure capacity p_M ranging from 36% to 62.4% of the plastic pressure p_y.

Failure at first yielding was also assumed by Amstutz [25], who using a two-dimensional model developed a formula for the external pressure collapse of embedded rings, which has been widely used for design purposes. The problem was also investigated by Jacobsen [26]. Assuming failure at first yielding, accounting for the presence of gap between the cylinder and the rigid medium, and considering a cosine function to describe the single-lobe buckling shape, Jacobsen resulted in implicit analytical expressions for the ultimate external pressure. A numerical solution for the ultimate pressure sustained by a

steel cylinder embedded in a rigid cavity was reported by Yamamoto and Matsubara [27], using elastic-plastic ring analysis through beam finite elements and assuming a uniform gap between the steel ring and the confining medium. The importance of material nonlinearity on the cylinder response was noted, and an empirical formula, valid for low-strength steel $\left(\sigma_y = 235MPa\right)$ that fits well with the finite element results, was developed through a curve fitting procedure.

A more rigorous investigation of buckling and post-buckling behavior of confined cylinders under external pressure, was conducted by Kyriakides and Youn [28] using a semi-analytical formulation, based on nonlinear ring theory. The ring was assumed inextensional, and elastic-plastic behavior was modeled through a bilinear material curve. The results of Kyriakides and Youn [28] have been used to study buckle propagation in confined long metal pipes [29]. Motivated by the structural design of rehabilitation metal liners, El-Sawy, extending the work in [14], examined numerically the buckling response of tightly-fitted [30] and loosely-fitted [31] steel cylinders, surrounded by a rigid boundary and subjected to external pressure. Parametric studies in terms of yield stress σ_y, and diameter-to-thickness ratio D/t have been conducted, accounting for the initial gap between the cylinder and the surrounding stiff boundary, and the numerical results were compared with the analytical results of Jacobsen [26]. An empirical equation showing the border between elastic and plastic buckling has also been developed.

2.1.2 Scope of the present research

The present work, motivated by the structural behavior of buried pipelines, focuses on the structural stability of steel cylinders under uniform external pressure confined by a deformable medium. Furthermore, the study considers the development of a simple and efficient methodology for the structural stability design of confined steel cylinders, within the framework of the new European shell stability design rules [32] and recommendations [33]. The cylinders are thin-walled with diameter-to-thickness ratio (D/t) that ranges between 100 and 300, which is typical for water pipelines or rehabilitation liners, and may fail under external pressure (vacuum) conditions in a “single-lobe” shape. Assuming constant pressure around the pipe, and no variation of stress and deformation in the axial direction of the cylinder, a quasi two-dimensional idealized problem under plane strain conditions is considered. Both the cylinder and the medium are modeled using finite elements, which account for inelastic effects and large deformations. The analysis is aimed

primarily at tracing the pressure-displacement equilibrium path, and determining the maximum pressure sustained by the cylinder, for different values of D/t ratio and yield stress σ_y of steel material. The sensitivity of ultimate pressure with respect to initial out-of-roundness of the ring geometry and the presence of a small gap between the ring and the medium are investigated.

The response of imperfect elastic cylinders with different values of the D/t ratio is examined first for rigid confinement, and the value of the elastic imperfection reduction ("knock-down") factor is determined. Subsequently, buckling of perfect and imperfect steel cylinders that buckle in the inelastic regime is examined considering a rigid confinement and different values of the yield stress σ_y of steel material, presenting the results in terms of a "slenderness shell parameter". A simple plastic-hinge model is also developed to illustrate cylinder response beyond the ultimate pressure. Furthermore, the effects of elastic medium deformability, expressed by the medium modulus E', on the cylinder buckling pressure are examined. The influence of preloading on the top of the medium are also investigated. The distribution of plastic deformation and the variation of cylinder-medium contact pressure around the cylinder cross-section are also depicted. Next, a methodology for the design of confined steel cylinders, within the framework of the new European shell stability design rules [32] and recommendations [33], is developed, which accounts for rigid and deformable medium. The present finite element results are compared with experimental results [22],[24], the proposed design methodology and available analytical results [12],[14],[22], towards better understanding of confined cylinder behavior. Furthermore, a relevant chapter for the design of confined steel cylinders, within the framework of the European Design Recommendations [33], is developed and presented in Appendix A, for possible inclusion of the present work in future editions of the EDR. Finally, the problem of "shrink buckling" is modeled and the results are compared with available experimental data, as well as results from the corresponding hydrostatic buckling problem.

2.2 Finite element simulation

The structural behavior of confined cylinders under uniform external pressure is examined numerically using nonlinear finite element tools. The general-purpose finite element program ABAQUS [34] is employed to simulate the buckling response of pressurized confined cylinders. The analysis considers nonlinear geometry through a large-strain description of the deformable medium, as well as inelastic material behavior.

Assuming no variation of loading and deformation in the longitudinal direction of the cylinder, the finite element model is quasi two-dimensional with one element in the longitudinal direction of the cylinder, considering a strip of the cylinder under plane-strain conditions, i.e. restraining displacements in the longitudinal direction. Because of the symmetry of the single-lobe post-buckling shape of the cylinder, half of the cylinder cross-section is analyzed, applying appropriate symmetry conditions at the $\theta = 0$ plane. Four-node reduced-integration shell elements (S4R) are employed for the modeling of the thin-walled cylinder, whereas eight-node reduced-integration solid elements (C3D8R) are used to simulate the surrounding medium. A typical finite element mesh for the elastic medium used in the present analyses is shown in Figure 10. In this model, L and H are equal to 1.5 and 3 cylinder diameters respectively. Following a short parametric study, it has been concluded that consideration of a larger medium domain, and the use of a finer finite element mesh have a negligible effect on the numerical results. Furthermore, a total of 150 shell elements around the cylinder half circumference have been found to be adequate to achieve convergence of solution and accuracy of the numerical results.

A J_2 flow (von Mises) plasticity model, with isotropic hardening is employed in the analysis to simulate inelastic behavior of the steel material of the cylinder. Following a short parametric study, the use of a kinematic hardening rule was shown to have no influence on the numerical results. The soil material is considered elastic in the majority of cases examined in this paper. In a few cases, soil material is also described through an elastic-perfectly plastic Mohr-Coulomb constitutive model, characterized by cohesion c, friction angle ϕ, elastic (Young's) modulus E', and Poisson's ratio ν. A contact algorithm is considered to simulate the interface between the cylinder and the medium. Unless otherwise specified, frictionless contact is assumed in the results. A few analyses have been performed to examine the effects of friction, which is considered through the friction coefficient μ, where $\mu = \tan\varphi$, and φ is the friction angle of the interface between the cylinder and the medium. Uniform external pressure is applied around the

cylinder, and the nonlinear pressure-deflection ($p-\delta$) equilibrium path is traced using a Riks continuation algorithm.

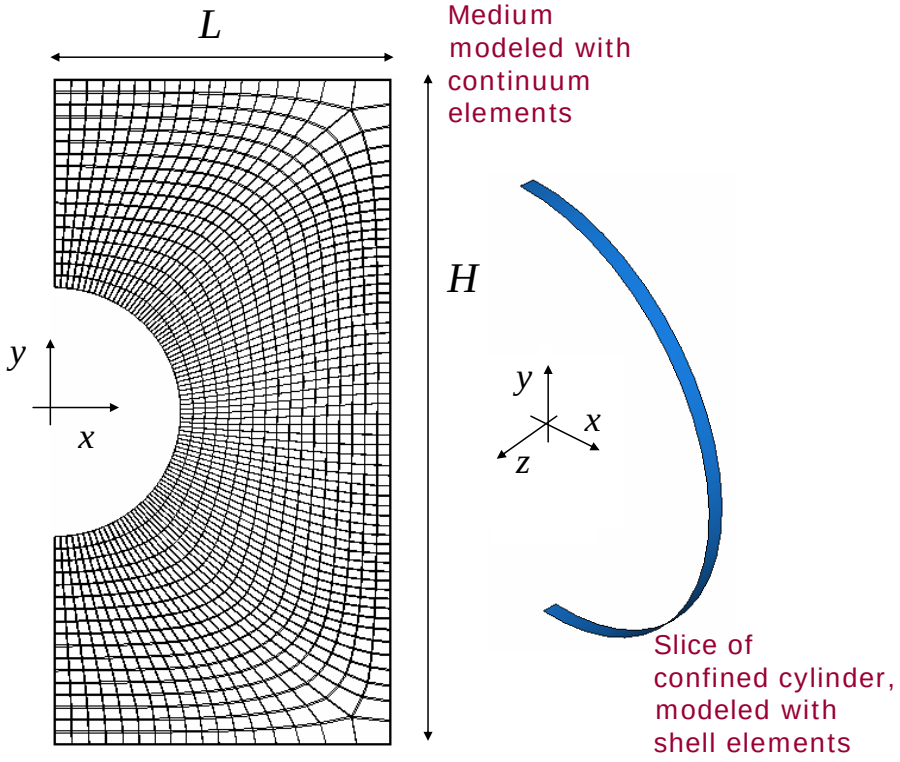

Figure 10: *Finite element model of cylinder-medium system.*

The sensitivity of cylindrical response and strength on the presence of initial imperfections is of particular importance in the present study. Two types of initial imperfections are considered. The first type of imperfection is an initial gap between the confining medium and the cylinder. The gap is introduced in the model, assuming that the circular cavity of the medium has a radius slightly larger than the circular cylinder radius, and that the cylinder and the cavity are initially in contact at $\theta=\pi$ (Figure 11a), so that the maximum gap between the cylinder and the medium occurs at $\theta=0$, and it is denoted as g.

The second type of imperfection is a small initial "out-of-roundness" imperfection on the steel cylinder in the form of a small localized displacement pattern at the vicinity of the $\theta=0$ location. It is an imperfection of the shape of the buckling mode of the confined cylinder ("single-lobe" mode). One way to impose this initial out-of-roundness in steel cylinders is through the consideration of a small downward vertical load applied at the $\theta=0$ location. After the load is removed, and despite the elastic rebound of the steel

cylinder wall, the cylinder at this location contains a small residual displacement δ_0, which is considered as the initial out-of-roundness amplitude, as shown in Figure 11b. Clearly, this type of method may not be suitable for elastic cylinders, due to the complete recovery of shape during the unloading step. Alternatively, this out-of-roundness imperfection can be imposed considering an initial stress-free displacement pattern, in the form of a "single-lobe" at the vicinity of the $\theta = 0$ location, chosen in the form of the consecutive shapes of the perfect confined elastic cylinder under external pressure. This method of imposing initial out-of-roundness is suitable for both elastic and elastic-plastic (steel) cylinders.

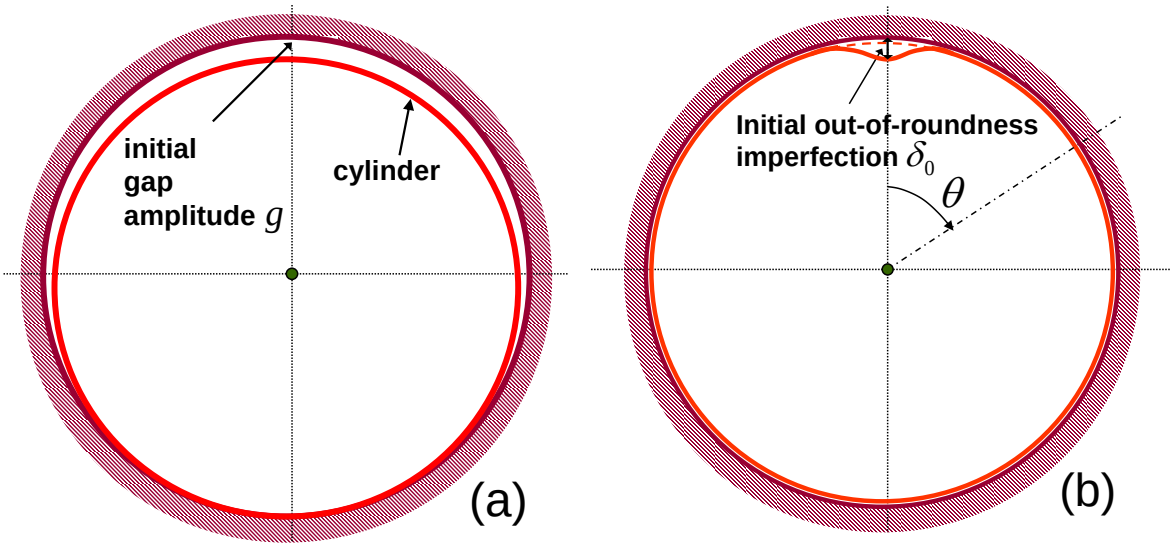

***Figure 11**: Schematic representation of a confined ring with (a) gap-type initial imperfection and (b) "out-of-roundness" initial imperfection.*

2.3 Buckling of confined elastic cylinders

Using the finite element simulation described in the previous section, the response of thin-walled rigidly-confined elastic cylinders with D/t values between 100 and 300 is examined in this section. The cylinder capacity is compared with analytical expressions and numerical results reported by Glock [12] and El-Sawy & Moore [14], as well as with available experimental data [15],[16],[17]. The material of the cylinder is considered elastic with a modulus E equal to 210,000 MPa and Poisson's ratio ν equal to 0.3. A frictionless interface is considered between the elastic cylinder and the confining medium. The modulus of the surrounding medium E' has a value equal to 21,000 MPa, which is the one-tenth of the modulus E of the steel material. Considering this value of E', the confining medium is practically non-deformable and may be considered as rigid. Numerical results with a value of E' higher than $0.1E$ have shown no influence on the cylinder response. The value of Poisson's ratio ν for the surrounding medium is considered equal to 0.3.

2.3.1 Perfect elastic cylinders

The pressure-displacement curves depicted in Figure 12 show the equilibrium path of pressure p versus the vertical displacement δ of point A at $\theta = 0$ (see Figure 8), normalized by the cylinder radius R (δ/R), for "perfect cylinders", i.e. zero gap between the cylinder and the medium ($g/R = 0$), and a negligible geometric initial out-of-roundness ($\delta_0/R = 0$). All equilibrium paths are characterized by a point of maximum (limit) pressure $p_{\max}$, beyond which, the cylinder exhibits a significant drop of pressure, indicating an unstable behavior. In all cases examined, the computed values of $p_{\max}$, shown in Figure 13 with symbol ▲, are in excellent agreement with analytical predictions p_{GL} obtained by equation (12) and p_{EM} expressed through the closed-form expression (15). Note that the value of maximum pressure $p_{\max}$ is more than 20 times larger than the value of the corresponding elastic buckling pressure p_e under unconfined conditions, expressed by equation (13). The large values of the $p_{\max}/p_e$ ratio express quantitatively the very significant effect of confinement on the buckling resistance. Furthermore, the results offer a very good verification of the validity of Glock's analytical solution for confined elastic cylinders in a stiff (non-deformable) medium, with no imperfections. It is interesting to

note that Glock's predictions and, therefore, the present finite element results are in close agreement with the experimental data reported in [15],[16],[17].

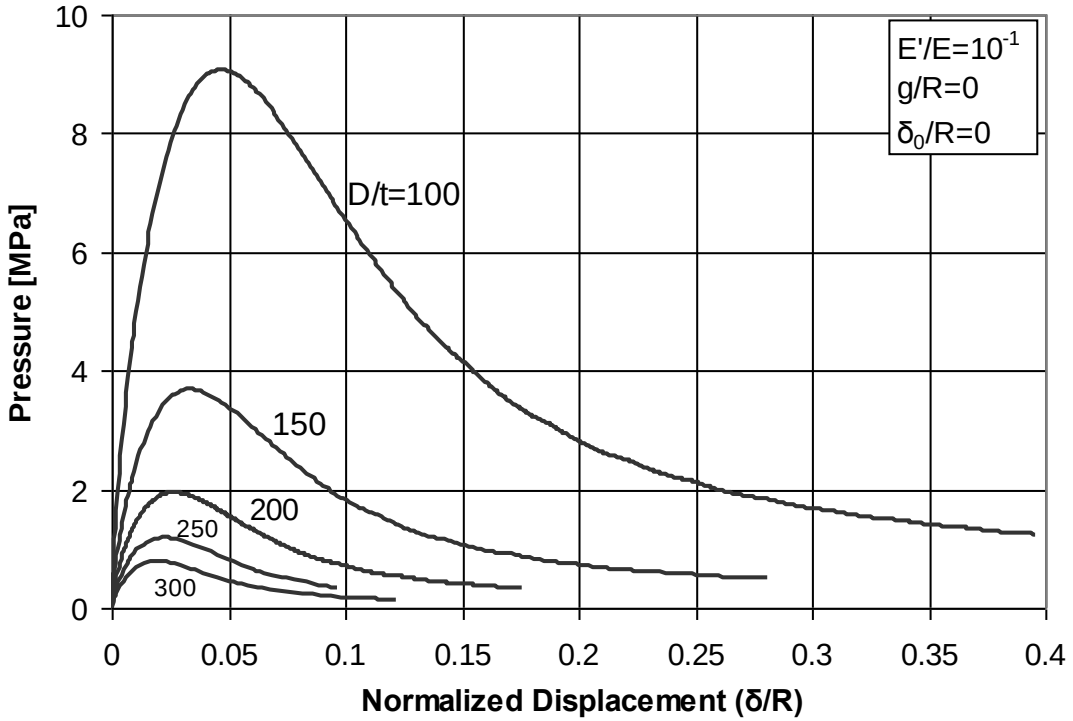

Figure 12: *Response of "perfect" elastic cylinders under external pressure embedded in a rigid confinement medium.*

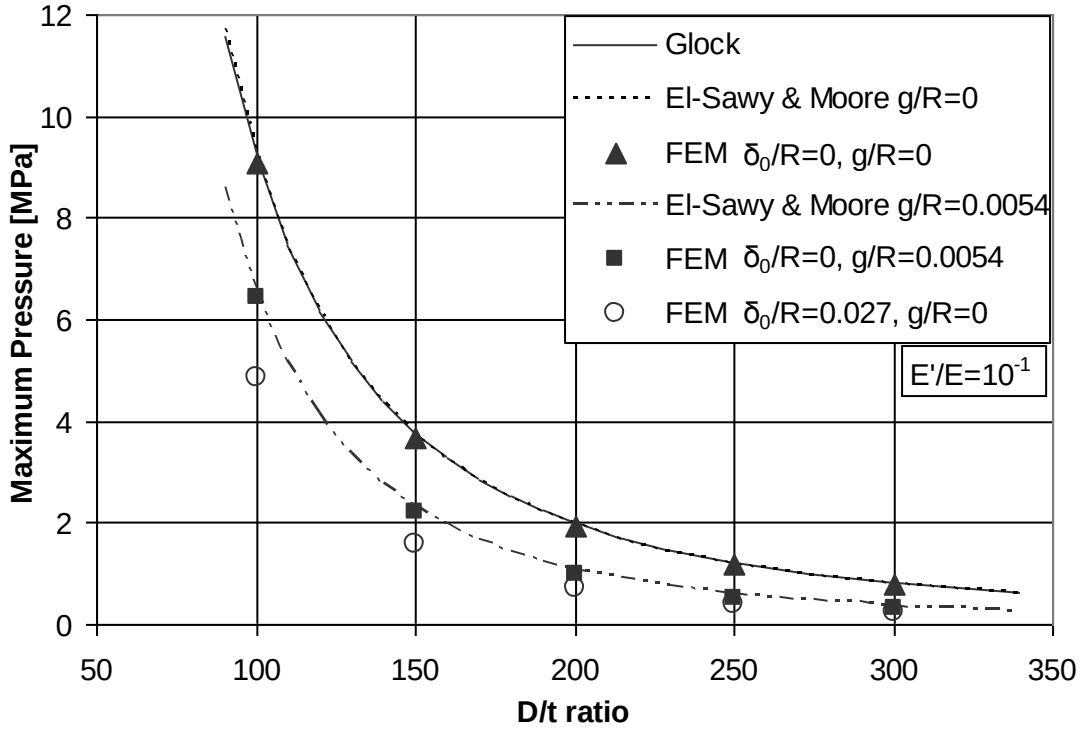

Figure 13: *Comparison between numerical results and analytical predictions from Glock's equation (12) and El-Sawy & Moore equation (15) for the buckling pressure of rigidly-confined elastic cylinders.*

2.3.2 Glock's analytical solution

A brief presentation of Glock's analytical solution [12] for external pressure buckling of elastic rings confined within a rigid medium is presented below. The kinematics was based on the Donnell approximations of thin-ring equations [13]. More specifically, the total hoop axial strain is given by the following equation as a sum of membrane and bending strain:

$$\varepsilon_\theta = \varepsilon_m + kz\,, \tag{19}$$

where the membrane and bending strain are given in terms of the radial w and tangential u displacements of the ring reference line at mid-thickness as follows:

$$\varepsilon_m = \frac{1}{R}\left(u' - w\right) + \frac{1}{R^2}w'^2\,, \tag{20}$$

$$k = \frac{w''}{R^2}\,. \tag{21}$$

Ring deformation consists of two parts, the "buckled" region and the "unbuckled" region as shown in Figure 14.

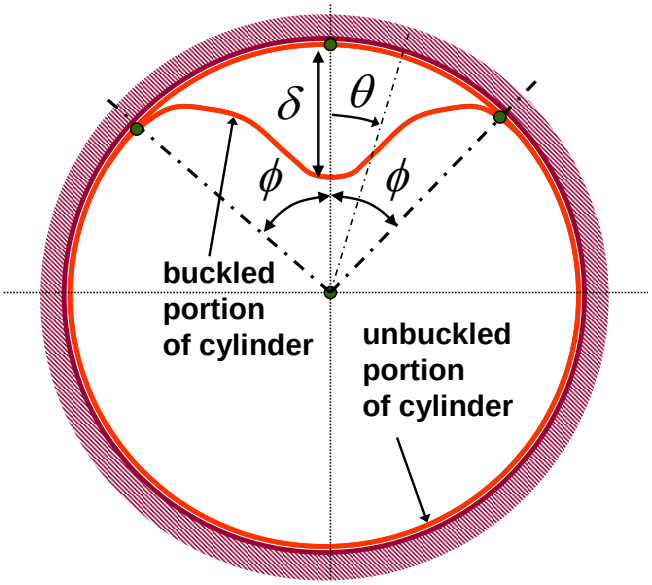

Figure 14*: Schematic representation of Glock's model [12]; the cylinder is divided in two parts, a buckled portion and an unbuckled portion.*

An assumed shape function $w(\theta)$ for the buckled region is considered in the following form:

$$w(\theta) = \delta \cos^2\left(\frac{\pi\theta}{2\phi}\right), \tag{22}$$

where ϕ is the angle that defines the border between the "buckled" and the "unbuckled" ring portions, so that $-\phi \le \theta \le \phi$. Forming the total potential energy Π of the ring, assuming a constant hoop axial force N_{ave} around the ring, and requiring minimization of Π with respect to both δ and ϕ, closed-form expressions for the pressure p, the amplitude of buckled shape δ, and the axial force N are obtained in terms of angle ϕ:

$$\frac{\delta}{R} = -\frac{6pR^3}{EI}\left(\frac{\phi}{\pi}\right)^4 + 10\left(\frac{\phi}{\pi}\right)^2, \tag{23}$$

$$\frac{pR^3}{EI} = \left(\frac{\pi}{\phi}\right)^2\left[1 \pm \frac{1}{6}\sqrt{16 - \frac{80}{3}\left(\frac{EI}{EAR^2}\right)\left(\frac{\pi}{\phi}\right)^5}\right], \tag{24}$$

$$N = \frac{5}{3}\frac{EI}{R^2}\left(\frac{\pi}{\phi}\right)^2. \tag{25}$$

Subsequently, minimization of pressure in terms of angle ϕ, results in final closed-form expressions for the critical pressure p_{GL}, the corresponding angle ϕ_{cr}, and the corresponding amplitude of the buckling shape:

$$\frac{p_{GL}R^3}{EI} = 0.969\left(\frac{EAR^2}{EI}\right)^{2/5}, \tag{26}$$

$$\left(\frac{\pi}{\phi}\right)_{cr} = 0.856\left(\frac{EAR^2}{EI}\right)^{1/5}, \tag{27}$$

$$\left(\frac{\delta}{R}\right)_{cr} = 2.819\left(\frac{EI}{EAR^2}\right)^{2/5}. \tag{28}$$

Thus, for the case of a ring under plane-strain conditions, equation (26) can be written in the form of equation (1).

Consecutive deformation configurations of an imperfection-free elastic cylinder with D/t equal to 200 under external pressure are shown in Figure 15a and the corresponding points on the pressure–deflection path are depicted in Figure 15b. The numerical results indicate that the maximum pressure $p_{\max}$ is equal to 1.948 MPa and occurs at the stage where the local curvature at $\theta = 0$ becomes zero (i.e. when "flattening" of the cylinder wall occurs). These outcomes are in agreement with the analytical solution of Glock [12]. From equation (12), Glock's prediction is equal to 1.999 MPa, very close to the numerical value. Furthermore, using equations (21) and (22) of Glock's solution, and conducting the appropriate differentiation of the radial displacement function $w(\theta)$, the local change of hoop curvature k_0 at the buckle location $\theta = 0$ is calculated as follows:

$$k_0 = \frac{w''(0)}{R^2} = -\frac{\delta}{2R^2}\left(\frac{\pi}{\phi}\right)^2. \tag{29}$$

Therefore, at the stage of maximum (critical) pressure, the change of hoop curvature $k_{0,cr}$ can be obtained analytically substituting equations (27) and (28) into equation (29) to get:

$$k_{0,cr} = -1.033\frac{1}{R} \simeq -\frac{1}{R}. \tag{30}$$

Adding the value of equation (30) to the initial hoop curvature (equal to $1/R$), the instantaneous total hoop curvature of the deformed configuration at the stage of buckling is readily computed equal to zero. This result from Glock's solution implies that the maximum pressure occurs at the stage where the local curvature at the $\theta = 0$ location becomes zero, i.e. the cylinder becomes locally flat and immediately after inversion of the cylinder wall occurs. The above analytical prediction shows a very good correlation with and is verified by the numerical results shown in Figure 15.

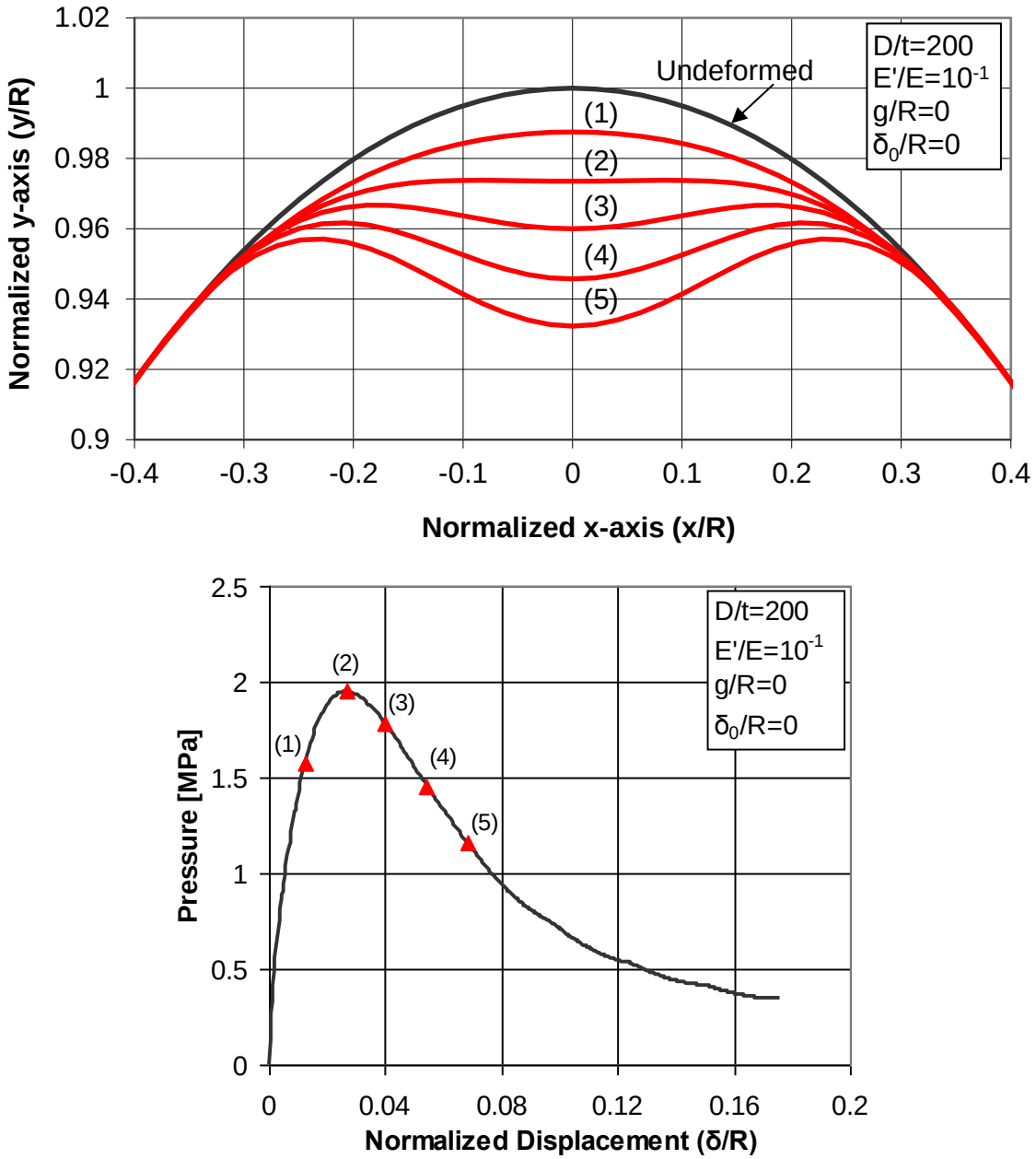

Figure 15: *(a) Consecutive deformation shapes of a tightly-fitted elastic cylinder; (b) Configuration (2) corresponds to the ultimate pressure stage.*

Table 1 depicts the values of maximum pressure, as well as hoop stress, inward radial displacement at the critical location $\theta = 0$, and the size of the detachment zone at buckling stage, obtained by both numerical analysis and Glock's analytical solution. The value of the nominal hoop stress σ_{nom}, corresponding to the following formula:

$$\sigma_{nom} = \frac{pD}{2t} \tag{31}$$

from elementary mechanics of materials, is of particular interest. Furthermore, stresses, σ_a and σ_b refer to the membrane and bending stress respectively and are given by the following formulae [12]:

$$\sigma_a = \frac{N}{A} = \frac{5}{9} E \left(\frac{t}{D} \right)^2 \left(\frac{\pi}{\varphi} \right)^2, \tag{32}$$

$$\sigma_b = \frac{M}{I} \frac{t}{2} = \frac{E}{1-\nu^2} \frac{t}{D}. \tag{33}$$

In Table 1, stresses σ_a and σ_b are both normalized by the value of σ_{nom} at buckling, i.e. considering $p = p_{\max}$ in equation (31). In general, a fairly good comparison has been obtained between the numerical results and the analytical solution for elastic cylinders provided in [12].

	D/t=100		D/t=200		D/t=300	
	Analytical [12]	FEM (present)	Analytical [12]	FEM (present)	Analytical [12]	FEM (present)
p_{max} [MPa]	9.187	9.066	1.999	1.948	0.819	0.788
δ_{cr}/R	0.04563	0.04598	0.0262	0.0255	0.0189	0.0211
φ_{cr} [rad]	0.4669	0.4674	0.3539	0.3591	0.3009	0.2952
k_{cr}	1.033	1.127	1.033	1.087	1.033	1.144
σ_{nom} [MPa]	453.3	-	194.8	-	118.2	-
σ_a/σ_{nom}	1.17	1.20	1.18	1.22	1.20	1.28
σ_b/σ_{nom}	5.09	5.78	5.93	6.47	6.51	8.44

Table 1: *Comparison between analytical results [12] and numerical results for rigidly-confined elastic cylinders.*

An important observation refers to the magnitude of the hoop stresses. The above results demonstrate that equation (31) may not be a reliable formula for computing the hoop stress on the pressurized cylinder at the prebuckling stage. In addition, although the value of membrane stress σ_a is comparable with the value of σ_{nom}, the value of σ_b is significantly higher, implying a substantial bending deformation before buckling. It is also noted that the above results assume elastic behavior of the cylinder material. Therefore, it is

expected that steel cylinders will have a reduced strength due to early yielding caused by the development of significant bending stress σ_b.

The numerical results of Figure 16 show that at low levels of external pressure loading, membrane hoop stress is developed at the critical location $\theta = 0$ of the cylinder as also predicted by the equation (31) of the nominal hoop stress. At this stage, bending stresses are not significant. However, beyond a level of about half the maximum pressure, the bending stress is considerably increased, reaching a value of 5.3 times the membrane stress, just before buckling. Furthermore, the membrane stress is increased and deviates from the value of nominal hoop stress predicted by the equation (31) before buckling.

An attempt to predict the increase of hoop stresses due to local deformation of the pressurized cylinder at the critical region is offered by the following AISI formula [35]:

$$\sigma = \frac{pD}{2t}\left(1+\frac{\delta}{2R}\right). \tag{34}$$

In this equation, the nominal hoop stress of equation (31) is multiplied by an amplification factor that depends on the radial displacement δ. However, as shown in Figure 16, the proposed AISI formula does not improve the predictions of equation (31), and does not account for the development of significant bending stresses.

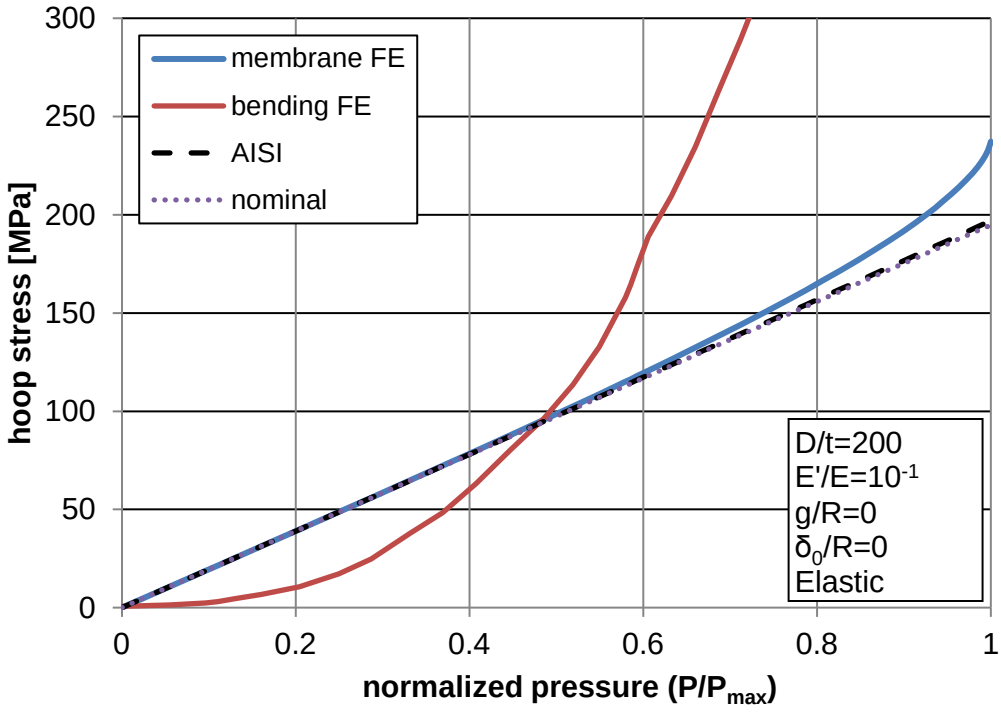

Figure 16: *Membrane and bending stresses at the critical location compared with the analytical formula of AISI recommendation [35] for hoop stress.*

2.3.3 Verification by experimental data

In the previous paragraphs, the excellent comparison of Glock's equation with the present numerical results has been established. Limited published experimental data are available for evaluating the theoretical models and numerical results of confined cylinders under external pressure. These experimental works refer to confined cylinders made of elastic material, but the tests have not been published in public domain. A brief description of three sets of data is offered in the paper by Omara [2]; the corresponding tests have been performed by Aggarwal and Cooper [15], Lo et al. [16], and Guice et al. [17]. A short overview is presented below for the sake of completeness.

Aggarwal and Cooper [15] conducted external pressure tests of 49 confined cylinders at Coventry Polytechnic, U.K. in 1984 with a range of D/t from approximately 30 to 90 and a variety of material properties (modulus of elasticity from 895.7 MPa to 2521.74 MPa). In these tests, the cylinders were inserted first in steel pipes. Subsequently, the pressure was applied and increased between the cylinder and casing in increments of approximately 10% of the expected failure pressure, until failure. Internal observation was carried out to determine when buckling occurred. As expected, the experimental failure pressure was found to be much larger than the theoretical buckling pressure obtained by equation (13) for elastic unconfined cylinders under external pressure. In other words, buckling resistance of the cylinders appeared to be significantly enhanced by the constraining effects of the surrounding pipe. Comparison of test results with predictions offered by the equation (12) of Glock [12] for confined cylinders, indicated a very good agreement.

Lo et al. [16] conducted an experimental program at Utah State University in 1993 sponsored by Shell Development Company to evaluate the buckling resistance of confined cylinders made with various epoxy resins. The specimens of the tests had a constant outside diameter and different thicknesses. The results of these tests were also found to compare very well with the predictions from Glock's equation.

Finally, Guice et al. [17] conducted tests on the long-term effects of hydrostatic pressures on confined cylinders under the Corps of Engineers Construction Productivity Advancement Research (CPAR) program in 1994 at Louisiana Tech University. Seven different products from five companies were evaluated. Several short-term tests for each product were also conducted. Test specimens were 12 inches in diameter and D/t ratio

ranged from 30 to 60. The comparison of those tests with Glock's equation is also very good.

The comparison of the above confined cylinder tests with both the confined (Glock) theory equation (12) and unconfined theory equation (13) is summarized in Table 2, taken from ref. [2], in terms of the average test values. The values in Table 2 indicate (a) good comparison with Glock's equation and (b) the paramount effect of confinement on the maximum pressure capacity sustained by the cylinder.

Data	**P_{TEST} / $P_{PREDICTION}$**	
	Confined theory, Eq. (12)	Unconfined theory, Eq. (13)
Aggarwal and Cooper [15]	1.20	11.89
Shell Development Company [16]	1.10	13.38
Louisiana Tech University [17]	0.90	9.81

Table 2: *Comparison of experimental data with analytical predictions* [2].

2.3.4 Imperfection sensitivity

The numerical results obtained for perfect elastic cylinders in Figure 12 indicate a substantial drop of pressure in the equilibrium path beyond the critical pressure point, which is a severe indication of imperfection sensitivity. Furthermore, in Figure 13, numerical results for the maximum pressure of imperfect elastic cylinders are presented, which also demonstrate that the behavior of the confined elastic cylinders is sensitive to the presence of initial imperfections. In the present study, two types of initial imperfections are considered, namely initial gap between the cavity and the outer surface of the cylinder, and initial out-of-roundness in the form of a localized inward deformation at $\theta = 0$.

The structural behavior of the externally-pressurized cylinder and the effects of confinement can be better understood, if one follows the pressure-displacement curve of the deforming cylinder, assuming a small gap between the cylinder and the rigid confining medium, in the form depicted in Figure 11a. The corresponding numerical results are shown in Figure 17 and offer a first indication of imperfection sensitivity in the presence of an initial gap between the pressurized cylinder and the confining medium, a situation referred to as "loosely-fitted" cylinder. The results refer to elastic cylinders with D/t ratio

equal to 200, whereas the gap size g is less or equal to 2.7×10^{-3} times the cylinder radius R, i.e. less than 27% of the cylinder thickness. These numerical results indicate a significant effect of the gap on the maximum pressure carried out by the elastic cylinder. In particular, a gap size equal to only 6.7% of the cylinder thickness is responsible for a 10.9% reduction of maximum pressure with respect to the maximum pressure that an imperfection-free cylinder can sustain.

Furthermore, the behavior under very low levels of external pressure is considered, as shown in Figure 17b. Initially, the cylinder exhibits uniform contraction, until the pressure corresponding to p_e is reached, i.e. the elastic buckling pressure under unconfined conditions, calculated from equation (13). At that pressure level, the cylinder buckles in an oval shape [13] but, very quickly, it accommodates itself within the confinement boundary, and this is represented by the change of slope in the pressure-displacement diagram, also shown in Figure 17b. Therefore, the cylinder is able to sustain significant further increase of external pressure, as represented by the increase of pressure beyond the critical pressure level for unconfined conditions (p_e).

Under those confined conditions, the top part of the cylinder, i.e. the part corresponding to the maximum gap location, behaves similar to an arch subjected to uniform external pressure and supported at the two “touchdown” points. This leads to buckling in the form of an inward single-lobe buckling mode, sometimes referred to as “inversion buckling”, characterized by a limit point on the pressure-deformation equilibrium path and unstable response beyond the limit point represented by a rapid drop of pressure, as shown in Figure 17a. The value of pressure at the limit point is referred to as maximum pressure $p_{\max}$. For the particular case of imperfection-free cylinders it is also referred to as critical pressure, denoted as p_{cr}.

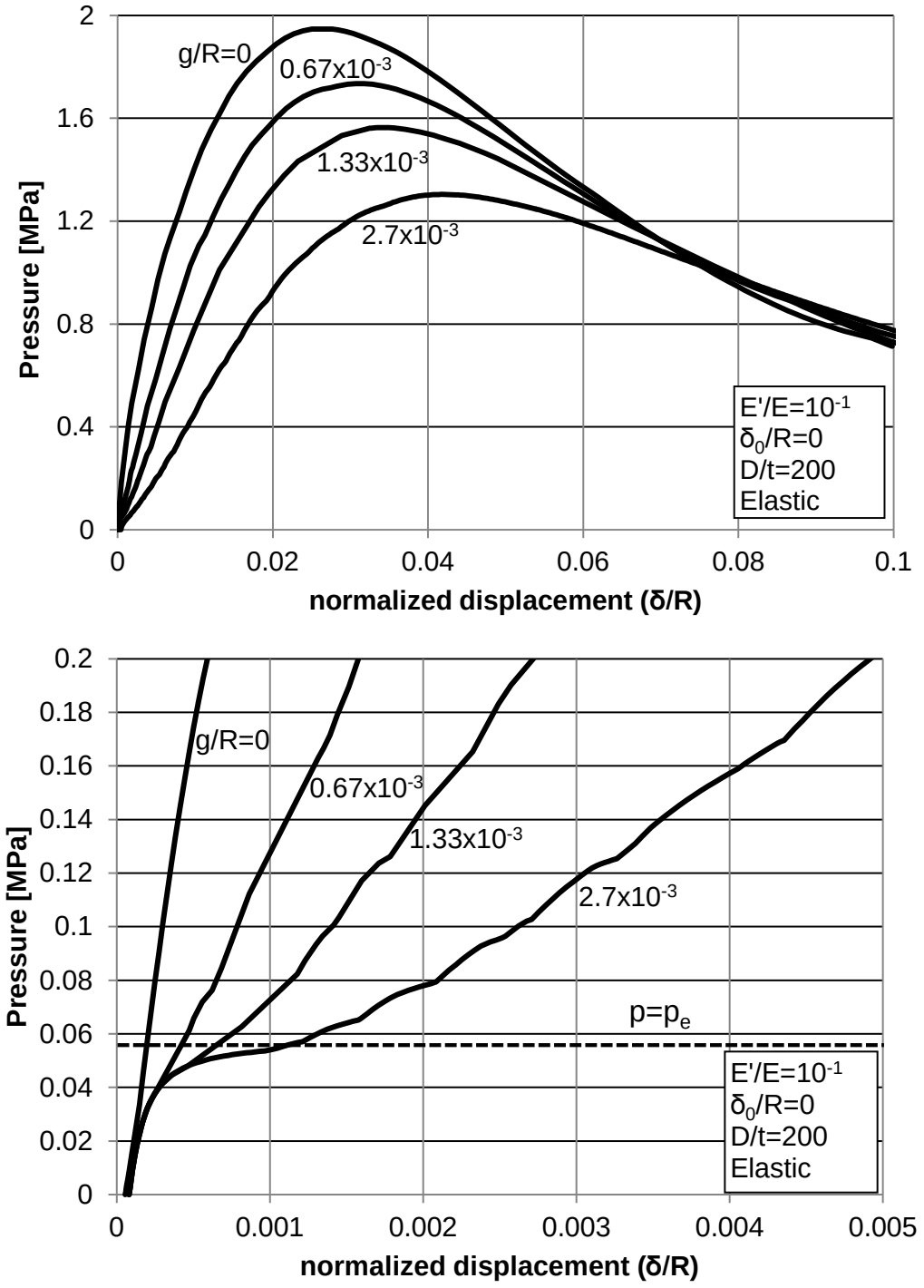

Figure 17*: Structural response of rigidly-confined elastic cylinders in the presence of small gaps; (a) general response and (b) initial response for very low-pressure values.*

The initial out-of-roundness imperfection, in case of elastic cylinders, is imposed assuming a stress-free initial configuration that follows the buckled shapes of the perfect elastic cylinder, as depicted in Figure 15a. Particularly in Figure 13, the initial out-of-roundness imperfection of amplitude $\delta_0/R = 0.027$ follows the shape of the perfect elastic cylinder at the point of maximum pressure, as depicted in the configuration (2) of Figure 15a. It is noted also that the numerical results for $g/R = 5.4\times10^{-3}$ (symbol ■) in Figure 13 are in very good agreement with the empirical equation (15) proposed by El-Sawy and Moore [14]. Furthermore, Figure 18 depicts the pressure-displacement curves of an elastic cylinder with D/t ratio equal to 200, and demonstrates the imperfection sensitivity of the cylinder response. The values of initial out-of-roundness amplitude (δ_0/R) correspond to the initial values of the pressure-displacement curves on the horizontal axis of the graph. Figure 19 and Figure 20 show the sensitivity of maximum pressure value on the amplitude of initial out-of-roundness and initial gap imperfection respectively.

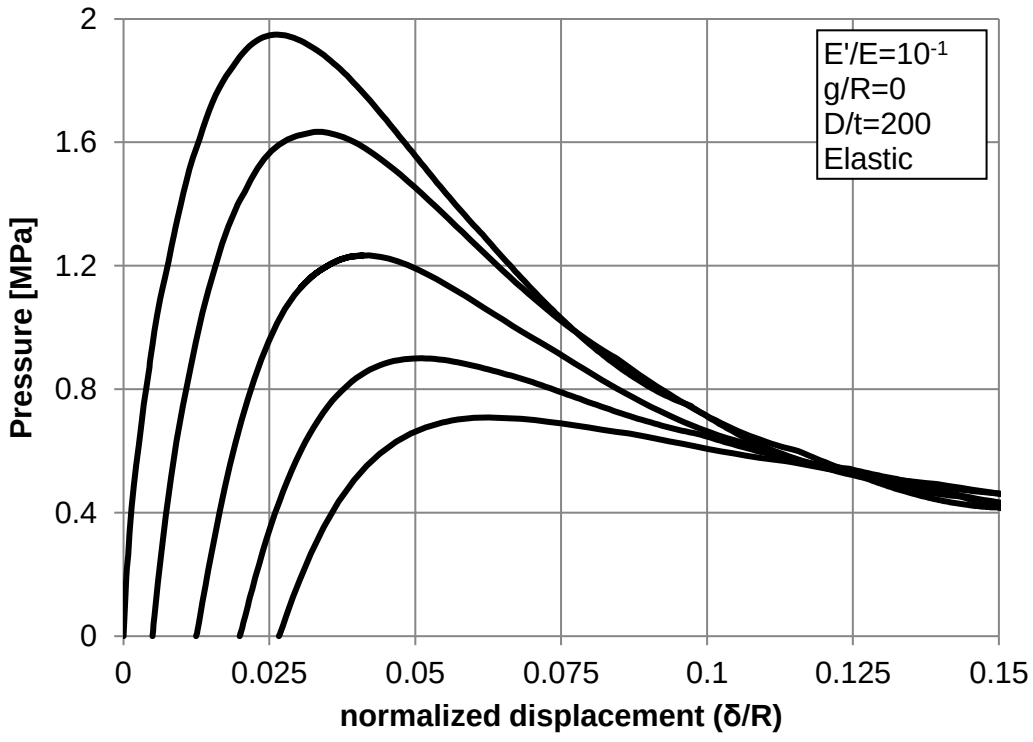

***Figure 18**: Structural response of rigidly-confined elastic cylinders in the presence of small initial out-of-roundness imperfection amplitudes.*

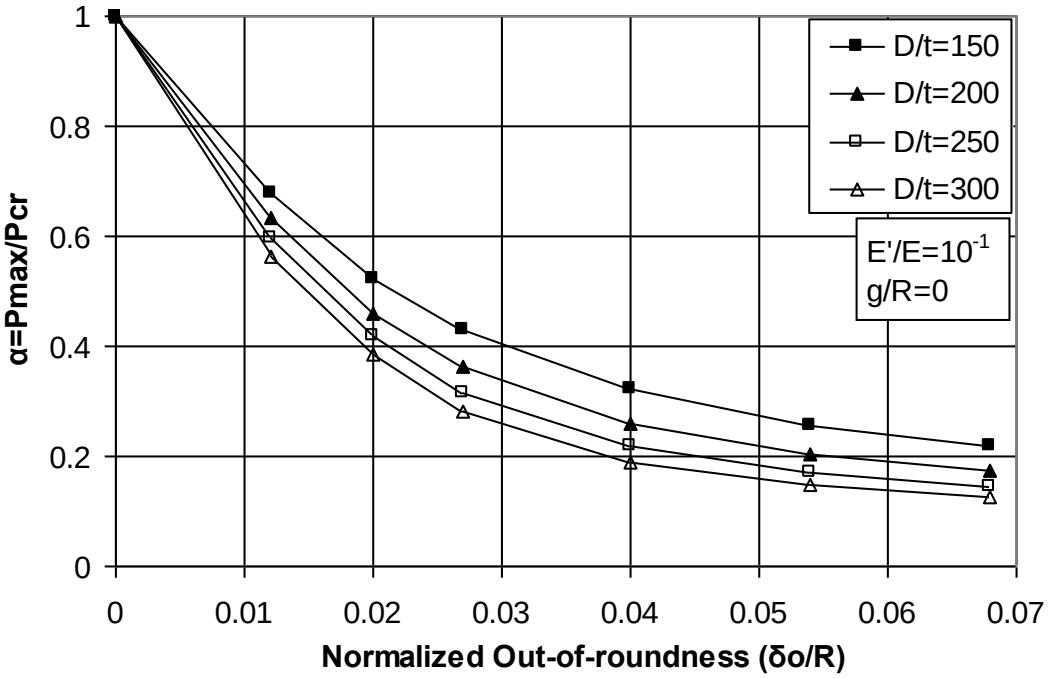

***Figure 19**: Buckling pressure of imperfect elastic cylinders over the buckling pressure of the corresponding perfect elastic cylinders in terms of initial out-of-roundness.*

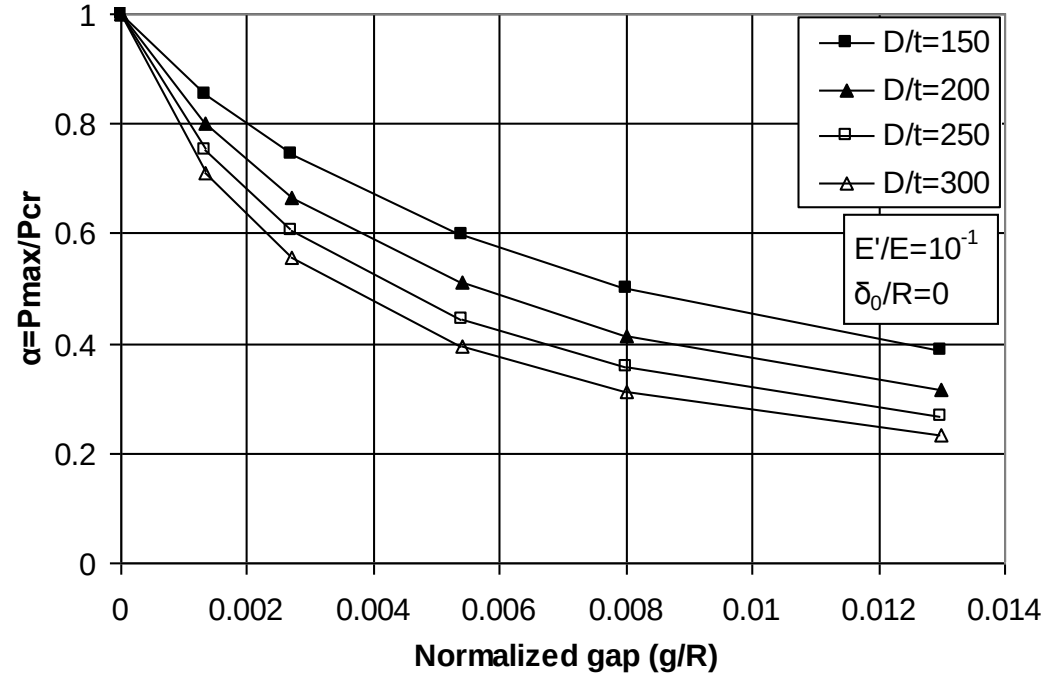

***Figure 20**: Buckling pressure of imperfect elastic cylinders over the buckling pressure of the corresponding perfect elastic cylinders in terms of initial gap.*

The above sensitivity on initial imperfections can be expressed in terms of the so-called "imperfection reduction factor" α, sometimes referred to as "knock-down" factor, also adopted in [32],[33] for the buckling load of imperfect elastic shells, so that:

$$p_{\max} = \alpha p_{cr} . \tag{35}$$

For the purposes of the present study, the reduction factor α, is assumed in the following form:

$$\alpha = \frac{C}{\Delta^m}, \tag{36}$$

where Δ is an imperfection parameter that represents the size of the initial imperfection, considering both out-of-roundness and gap, and C, m are constant coefficients to be determined from the numerical results. The results in Figure 19 and Figure 20 indicate a dependency of the imperfection sensitivity on the D/t value. Based on those results, this imperfection parameter is considered in the following form:

$$\Delta = \left(\frac{\delta_0 + Kg}{R} \right) \sqrt{\left(\frac{D}{t} \right)} . \tag{37}$$

In the above expression, coefficient K expresses the relative influence of the two forms of imperfections (gap and out-of-roundness) on the ultimate pressure $p_{\max}$. From the numerical results of Figure 20, a value equal to 3 is obtained for this coefficient ($K = 3$). Upon determining the value of K, a standard curve fitting technique is employed, the values of C and m are calculated equal to 0.15 and 0.7 respectively, so that the elastic reduction factor becomes:

$$\alpha = \frac{0.15}{\Delta^{0.7}} = \frac{0.15}{\left[\left(\frac{\delta_0 + 3g}{R} \right) \sqrt{\left(\frac{D}{t} \right)} \right]^{0.7}} . \tag{38}$$

The imperfection reduction factor predicted through equation (38) is plotted against finite element results in Figure 21. The comparison indicates that equation (38) can provide good predictions for the ultimate pressure of externally-pressurized elastic cylinders in the presence of initial imperfections.

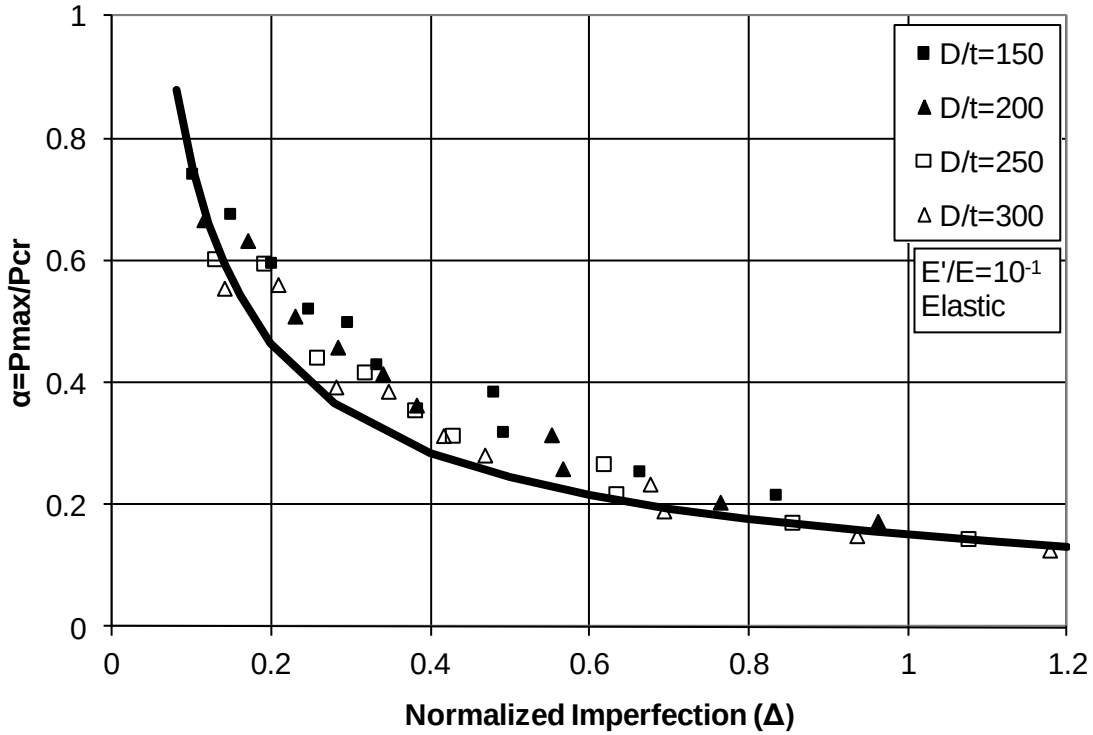

Figure 21*: Imperfection sensitivity of rigidly confined elastic cylinders under external pressure; finite element results and predictions of equation (38).*

Alternatively, the reduction of maximum pressure due to the presence of initial out-of-roundness imperfections in externally-pressurized elastic cylinders confined within a rigid cavity can be also expressed with respect to the imperfection amplitude by the following expression:

$$\frac{p_{\max}}{p_{cr}} = 1 - C\left(\frac{\delta_0}{t}\right)^n, \tag{39}$$

where p_{cr} is the buckling pressure of the corresponding ‘‘perfect” cylinder (referred to as “critical pressure”), C is a positive constant that depends on the D/t ratio, and exponent n expresses the rate of decay. This equation is considered in the same form as the sensitivity imperfection formula from general post-buckling theory of elastic systems [36],[37]. Figure 22 presents an attempt to fit the above formula (39) with the finite element results. It is interesting to note that for the range of small values of imperfection amplitude, the value of 2/3 on the exponent n results in good predictions of the maximum pressure of imperfect cylinders.

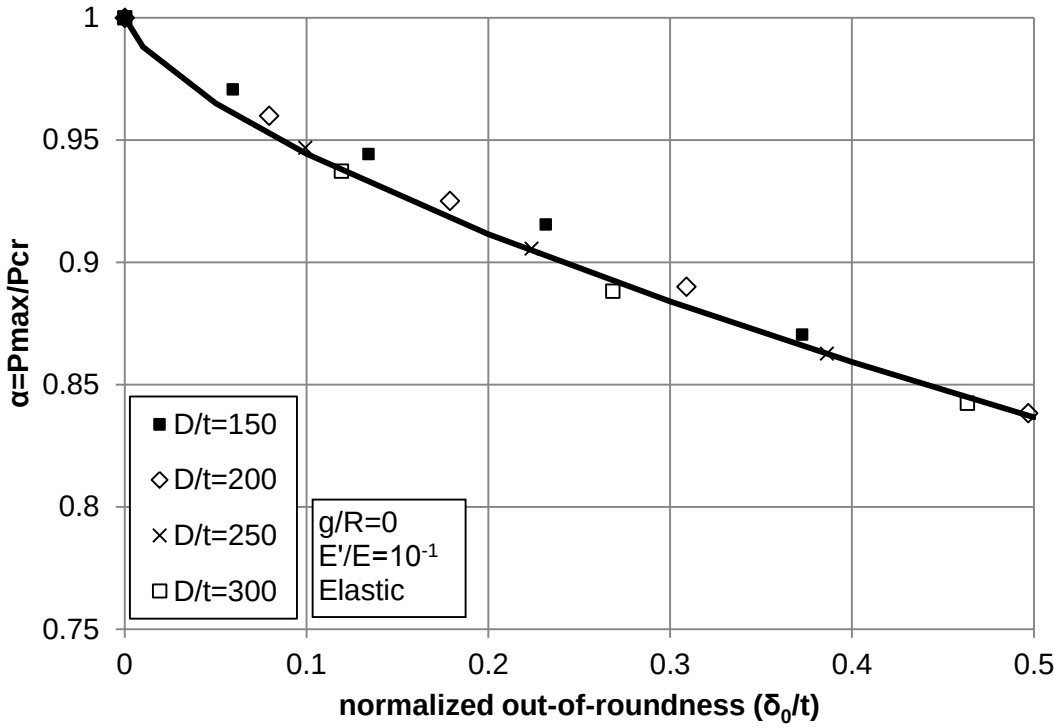

***Figure 22**: Effects of small initial out-of-roundness imperfection amplitudes on the buckling pressure of imperfect elastic cylinders; FEM results and predictions from the imperfection sensitivity formula of equation (39).*

2.4 Buckling of confined steel cylinders

The results presented in the previous section refer exclusively to cylinders with elastic material response. They also apply to very thin-walled steel cylinders that buckle in the elastic range. However, in the majority of practical applications, buckling of steel cylinders occurs beyond yielding of the steel material. Using the numerical models described in the previous sections, the structural stability of externally-pressurized confined steel cylinders is examined in the present section, assuming an elastic confining medium and a frictionless interface between the cylinder and the medium. The values of pressure p are normalized by the yield pressure $p_y = (2\times 1.13)\sigma_y t/D$ [see equation (17)], whereas the displacement δ of point A at $\theta = 0$ (see Figure 8) is normalized by the cylinder radius R.

The material of the cylinder is steel, with yield stress σ_y and ultimate stress σ_u equal to 313 MPa and 492 MPa respectively, whereas post-yield hardening is zero up to engineering strain equal to 1.5%. The nominal stress – engineering strain (s-e) curve is depicted in Figure 23. The s-e values of Figure 23 are converted to true stress – plastic strain values according to the following equations to be inserted in ABAQUS:

$$\sigma_{true} = \sigma_{nom}(1+e), \tag{40}$$

$$\varepsilon_{\ln}^{p} = \ln(1+e) - \frac{\sigma_{true}}{E}. \tag{41}$$

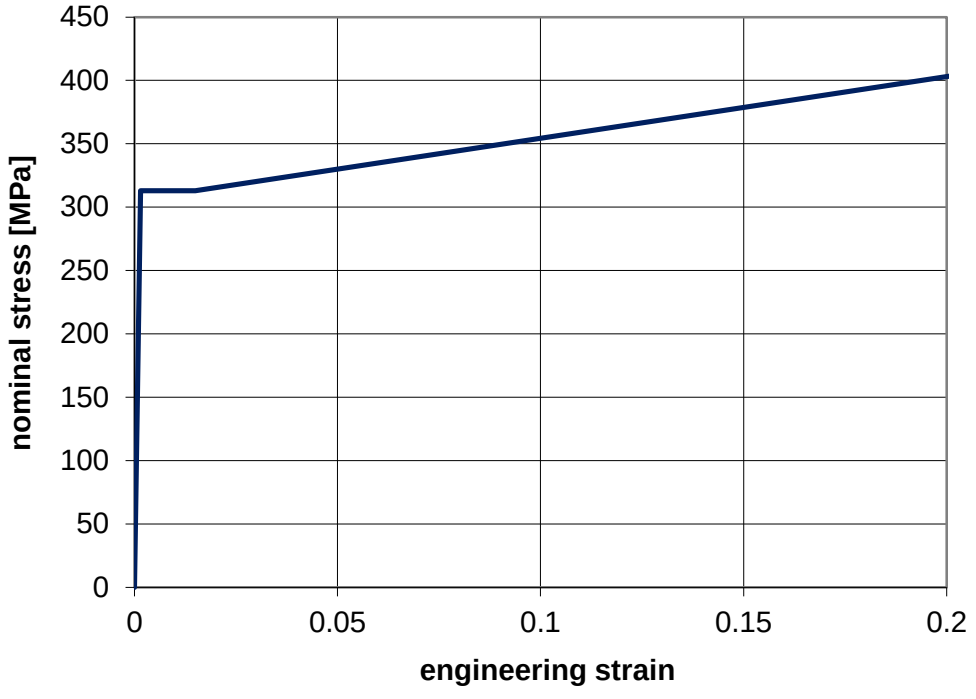

***Figure 23**: Stress-strain curve of the cylinder material.*

2.4.1 Rigid confinement

2.4.1.1 General response

The response of a thin-walled steel cylinder with $D/t = 200$ is shown in Figure 24 for different values of initial out-of-roundness. The values of initial out-of-roundness amplitude (δ_0/R) correspond to the initial values of the pressure-displacement curves on the horizontal axis of the graph. A zero gap between the cylinder and the medium, and a confinement medium modulus E' equal to 10% of E are assumed (E'=21,000 MPa). The value of E' corresponds to practically rigid confinement (e.g. concrete encasement). Numerical results with higher values of E' indicated no further influence on the response. The equilibrium curves in Figure 24 represent the nonlinear relationship between the applied pressure and the downward displacement of the cylinder point at $\theta = 0$. The results demonstrate that the value of the ultimate pressure $p_{\max}$ is substantially smaller than the yield pressure p_y, even for negligible initial imperfection.

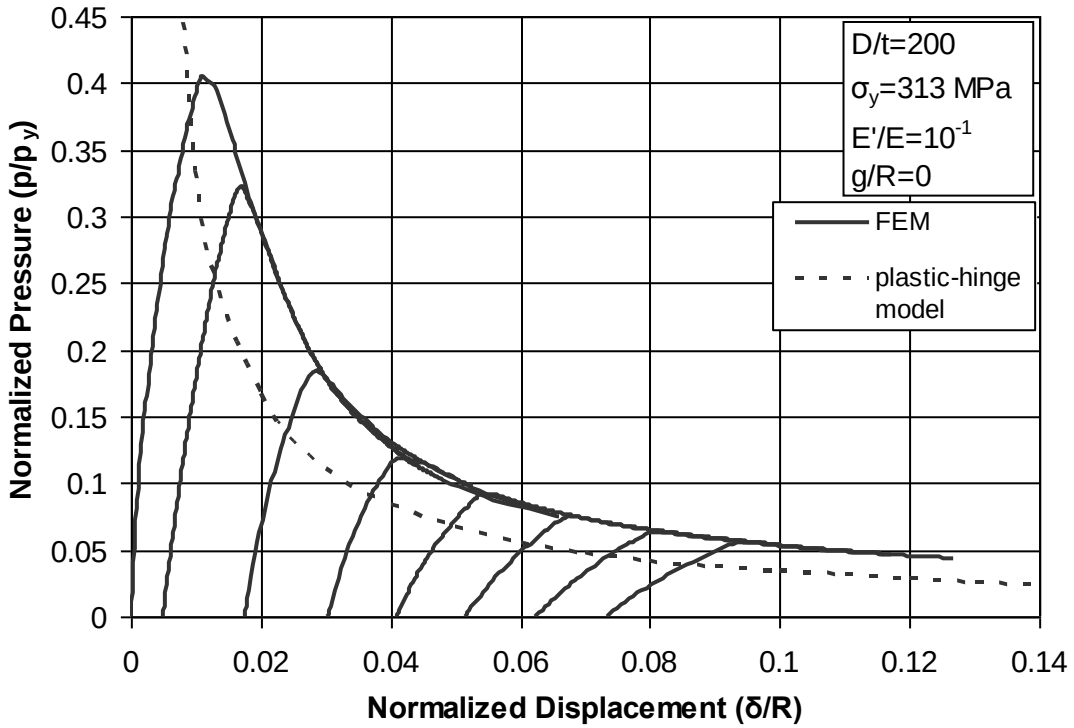

***Figure 24**: Response of tightly-fitted steel cylinders ($g/R = 0$), embedded in a rigid confinement medium; numerical results for different values of initial out-of-roundness and plastic-hinge collapse mechanism equation (49).*

Comparison between the numerical results from the elastic case (Figure 12) and those shown in Figure 24 for steel cylinders shows that, in steel cylinders, the ultimate pressure capacity $p_{\max}$ occurs at a lower level of pressure, because of the significant effect of inelastic material behavior on the pressure capacity of the cylinder. Furthermore, the finite element results indicate that the maximum pressure of elastic-plastic (steel) cylinders occurs very soon after first yielding, and corresponds to a deformation stage before "flattening" of the cylinder wall occurs at $\theta = 0$ location. Figure 25a depicts the successive deformed configurations of the steel cylinder, whereas the corresponding points on the pressure–deflection path are depicted in Figure 25b. A comparison between deformed shapes from elastic and inelastic cylinder behavior, which both correspond to the same deflection of point A ($\delta/R = 0.932$), is shown in Figure 26. This comparison indicates that the "post-buckling" shape of inelastic cylinders is characterized by more abrupt changes of local curvature at the symmetry point A and the "touchdown" point B, which is attributed to the concentration of plastic deformation at those points.

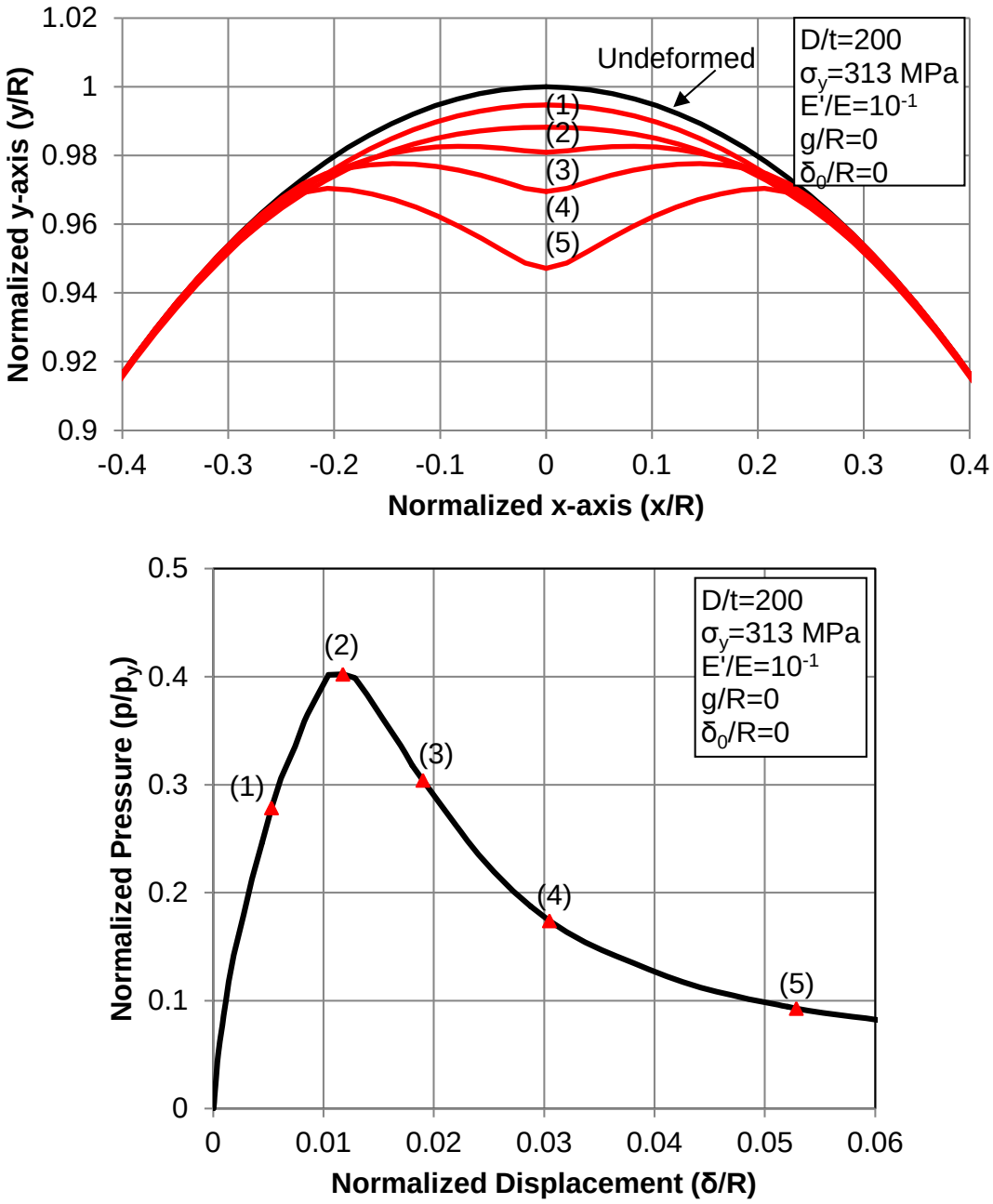

***Figure 25**: (a) Consecutive deformation shapes of an initially "perfect" steel cylinder, (b) corresponding points on the pressure-deflection path; configuration (2) corresponds to the ultimate pressure stage.*

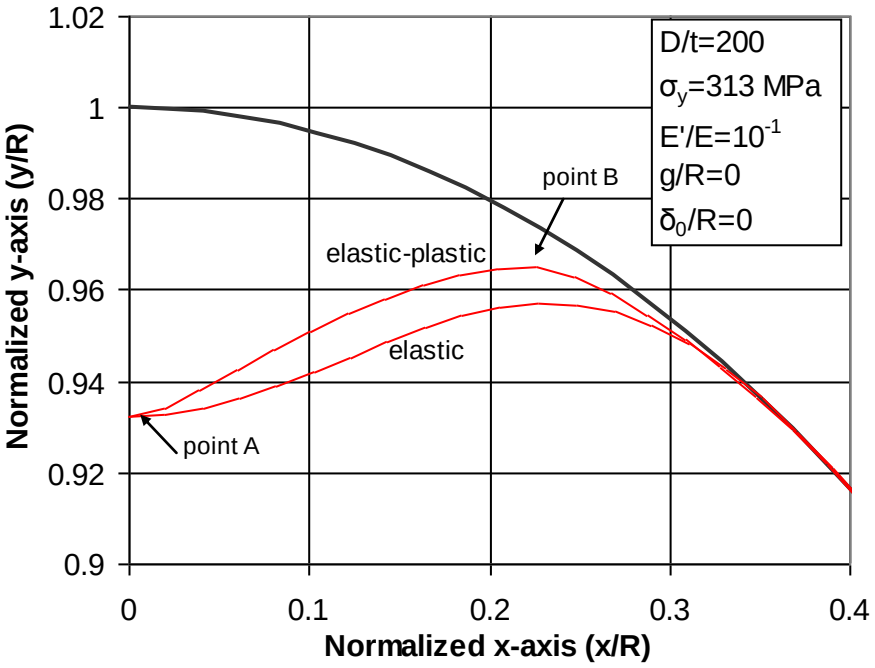

Figure 26: *Comparison between deformed shapes from elastic and inelastic cylinder behavior, which both correspond to the same deflection of point A ($\delta/R = 0.932$).*

Upon reaching the maximum pressure p_{max}, the cylinder behavior becomes unstable, with significant drop of pressure capacity, and this is responsible for a severe sensitivity of the p_{max} value to the presence of initial imperfections. Particularly, the numerical results in Figure 24, for the cylinder under consideration, show that initial out-of-roundness of amplitude less than 1% of the cylinder radius results in a 40% reduction of the ultimate pressure p_{max} with respect to the maximum pressure of the imperfection-free cylinder. The unstable "post-buckling" behavior is due to the development of a plastic collapse mechanism with one stationary plastic hinge at symmetry point A, and two moving hinges at the two "touchdown" points B and B' (see Figure 8). Using a simple kinematic model, described in the next paragraph, it is possible to approximate this mechanism, and obtain a closed-form expression, which can estimate the buckling pressure of an externally-pressurized rigidly confined steel cylinder. The formation of plastic hinges at points A and B is readily observed in Figure 27, in which the distribution of plastic deformation along the cylinder perimeter is depicted in terms of the equivalent plastic strain.

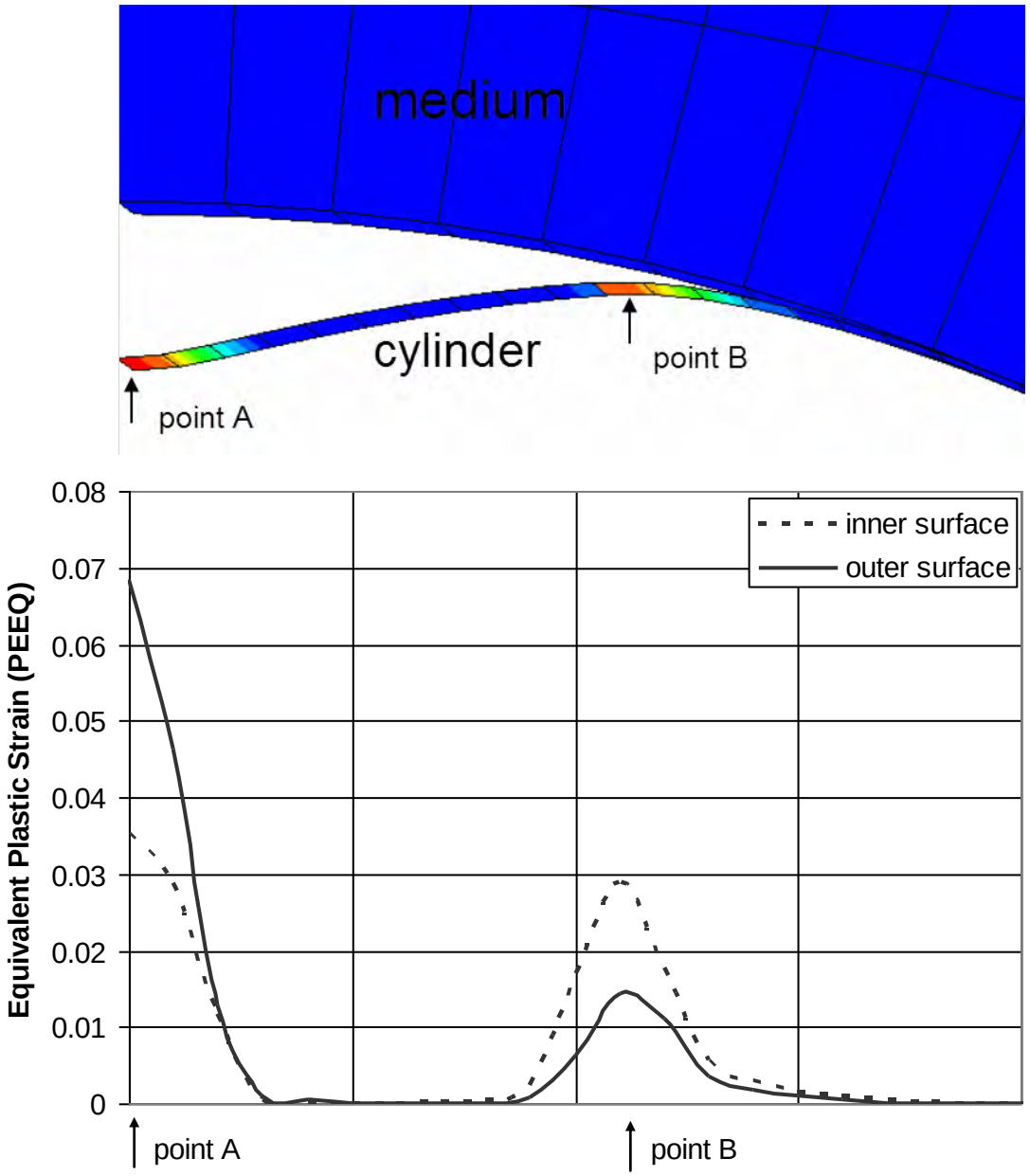

***Figure 27**: Distribution of plastic deformation in terms of equivalent plastic strain, along the pipe section in the buckled area ($E'/E = 10^{-1}$, $D/t = 200$).*

2.4.1.2 Plastic-hinge collapse mechanism

Motivated by the numerical results, an approximation of the plastic-hinge mechanism is developed to illustrate the post-buckling collapse behavior of a confined cylinder, subjected to external pressure, based on a simple kinematic model as shown in Figure 28. The model is symmetric with respect to the $\theta = 0$ axis, with two moving plastic hinges at B and B', and one stationary plastic hinge, initially located at A (i.e. at $\theta = 0$).

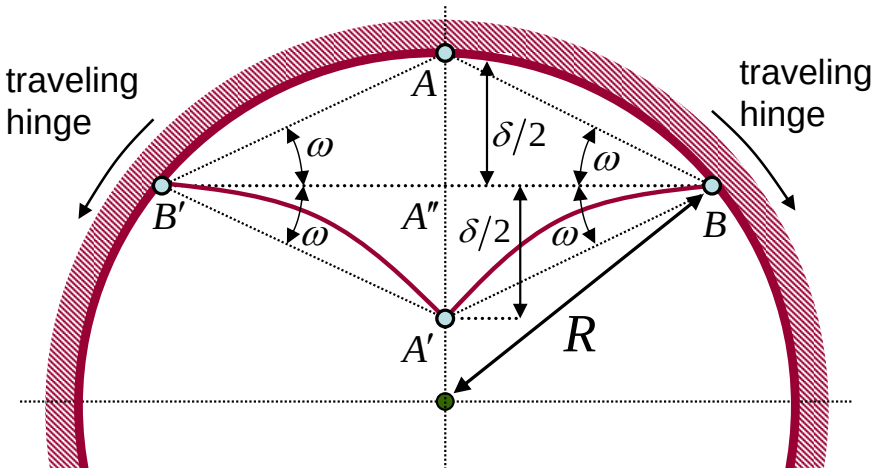

***Figure 28**: Definition of three-hinge model, describing plastic collapse mechanism.*

It is assumed that the material is rigid-plastic and that deformation occurs only in the plastic hinges. Assuming inextentionality of the deformed ring, the length of $A'B$ is equal to the length of AB. Equilibrium is enforced equating the internal plastic work rate $\dot{W}_{int}$, dissipated at the plastic hinges, with the external work rate $\dot{W}_{ext}$ of the external pressure:

$$\dot{W}_{int} = \dot{W}_{ext}. \tag{42}$$

Internal work rate is considered equal to the product of the full-plastic moment M_p of the cylinder wall times the rate of relative rotations at all three plastic hinges $\sum \dot{\omega}$, neglecting the work required for the translation of the moving hinges at B and B'. For a cylinder segment of unit length and thickness t, with negligible effects of hoop compression on the plastic moment, $M_p = \sigma_y t^2/4$. External work rate $\dot{W}_{ext}$ per unit length is equal to the product of pressure p times the rate of change of the area enclosed by the cylinder cross-section ΔA. Therefore, equation (42) can be written approximately as follows:

$$M_p\left(\sum \dot{\omega}\right) = p\left(\Delta A\right)^{\cdot}. \tag{43}$$

From the geometry of the deformed ring (Figure 28), one readily obtains:

$$\Delta A = \left(A''B\right)\delta, \tag{44}$$

$$\tan\omega = \frac{\delta}{2\left(A''B\right)}, \tag{45}$$

$$\left(A''B\right) = \sqrt{R\delta - \frac{\delta^2}{4}}, \tag{46}$$

$$\sum \omega = 8\omega. \tag{47}$$

Inserting equations (44)-(47) into equation (43), and conducting the appropriate differentiations, one obtains the following equilibrium equation for arbitrary rate $\dot{\omega}$:

$$p = \frac{4M_p}{3R\delta - \delta^2}\,. \tag{48}$$

The above closed-form expression can also be written in the following dimensionless form:

$$\frac{p}{p_y} = \left(\frac{t}{D}\right)\frac{2}{3\left(\frac{\delta}{R}\right) - \left(\frac{\delta}{R}\right)^2}\,. \tag{49}$$

In Figure 24, equation (49) is plotted together with the numerical results, verifying that the pressure beyond its maximum value is a rapidly decreasing function of cylinder deformation. Furthermore, the comparison shows that equation (49) underestimates the pressure by about 30-35%. This difference is attributed to the non-consideration of the additional internal work required for hinges B and B' to travel along the cylinder perimeter. The development of a more sophisticated plastic collapse mechanism, which accounts for this additional internal work, is out of the scope of the present work.

2.4.1.3 Imperfection sensitivity

The presence of a small gap between the cylinder and the surrounding medium may also have significant effect on the maximum pressure, as shown in Figures 29. The gap size, denoted as g, is the maximum distance between the cylinder and the cavity inner surface at $\theta = 0$, and it is normalized by the cylinder radius R. The numerical results in Figures 29, compared with the corresponding results of Figure 24, indicate that the presence of a rather small gap results in a significant reduction of the ultimate pressure capacity $p_{\max}$ of the cylinder. For zero initial out-of-roundness ($\delta_0/R = 0$), the ultimate pressure capacity is reduced by 40% for an initial gap size equal to 0.27% of the cylinder radius R (or equivalently equal to 27% of the cylinder thickness t) and by 64% for a gap size equal to 0.8% of the cylinder radius R (or equal to 80% of t). In both cases depicted in Figures 29, the maximum pressure is further decreased in the presence of initial out-of-roundness imperfections (δ_0/R).

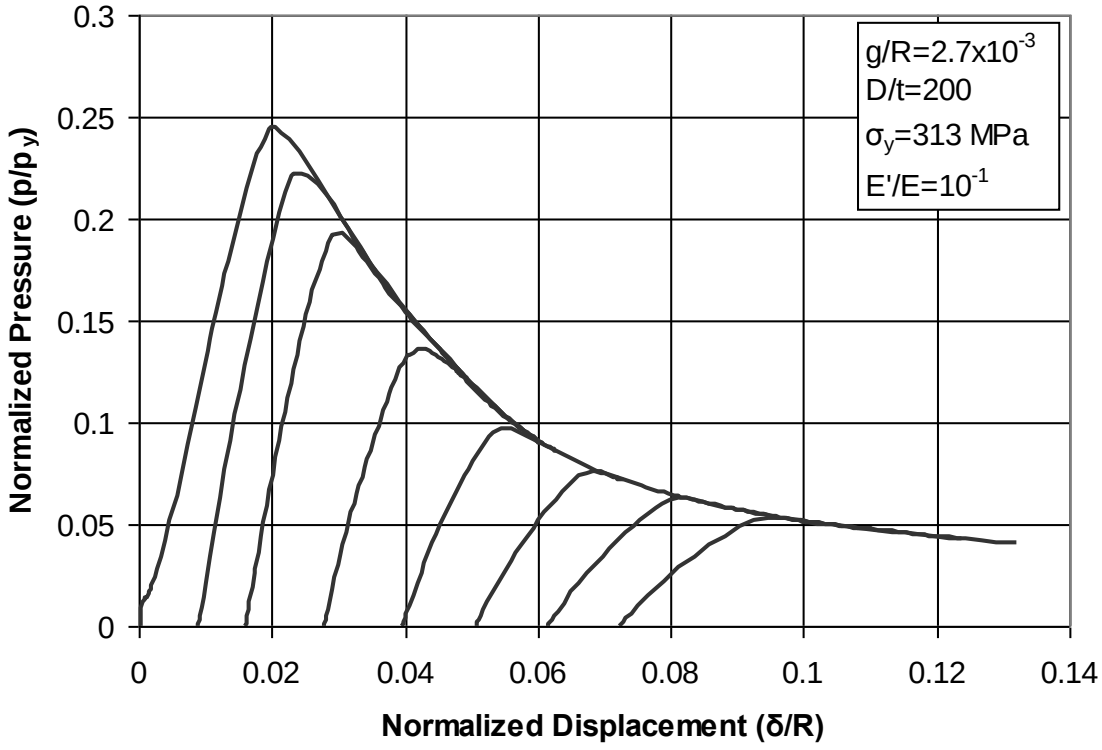

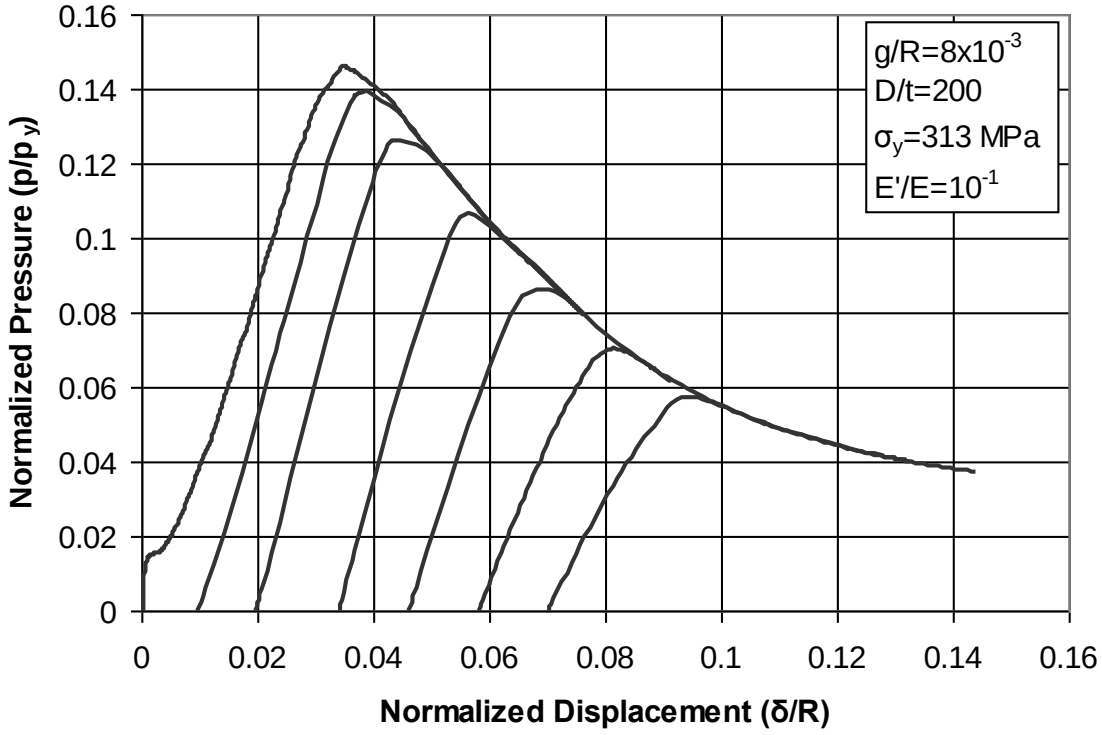

***Figures 29**: Effects of initial out-of-roundness and initial gap on the external pressure response of a loosely-fitted steel cylinder embedded in a rigid confinement medium.*

The effects of initial gap (g/R) and out-of-roundness (δ_0/R) imperfections on the maximum pressure ($p_{\max}/p_y$) are summarized in Figure 30 for a cylinder with $D/t=200$ and $\sigma_y=313$ MPa. The finite element results indicate that for values of initial out-of-roundness δ_0 greater than 3.5% of the cylinder radius R, the value of maximum pressure $p_{\max}$ is independent of the value of initial gap g.

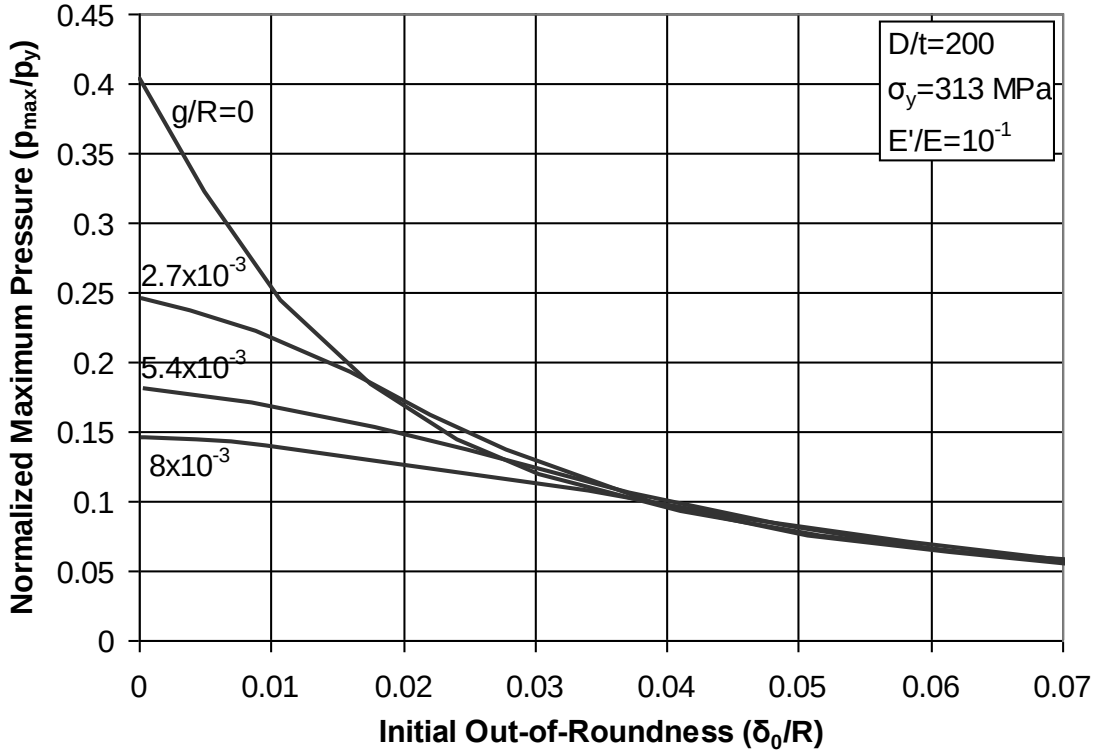

***Figure 30**: Effects of initial out-of-roundness and initial gap on the maximum pressure sustained by a confined steel cylinder embedded in a rigid confinement medium.*

One should note that the overall behavior of the pressurized loosely-fitted steel cylinder is similar to the one described in the previous section for elastic cylinders, shown in Figure 17. In Figure 31, the initial cylinder response, i.e. under low levels of external pressure ($p/p_y \le 0.05$), is depicted for three different values of initial gap size ($g/R=0$, $g/R=2.7\times10^{-3}$, $g/R=8\times10^{-3}$). The pressure-displacement path for the two cases with nonzero initial gap is characterized by an abrupt change of slope at pressure level near $p/p_y=0.016$. The cylinder is initially contracted due to external pressure and "buckles" in an oval form (e.g. [13]) at the pressure level of $p/p_y=0.016$, which corresponds to the

critical buckling pressure p_e for elastic unconfined cylinders, calculated from Eq. (13). Nevertheless, upon buckling, the cylinder very quickly accommodates itself within the rigid cavity, allowing for significant further increase of external pressure. This is represented by the increase of pressure beyond the critical pressure level ($p/p_y = 0.016$). The smaller the gap size, the sooner the pressure increases. Under those conditions, the top part of the cylinder behaves similar to an arch subjected to uniform external pressure, supported at the two "touchdown" points. This leads to the so-called "inversion buckling", characterized by a limit-point on the pressure-deformation equilibrium path and unstable response beyond the limit point.

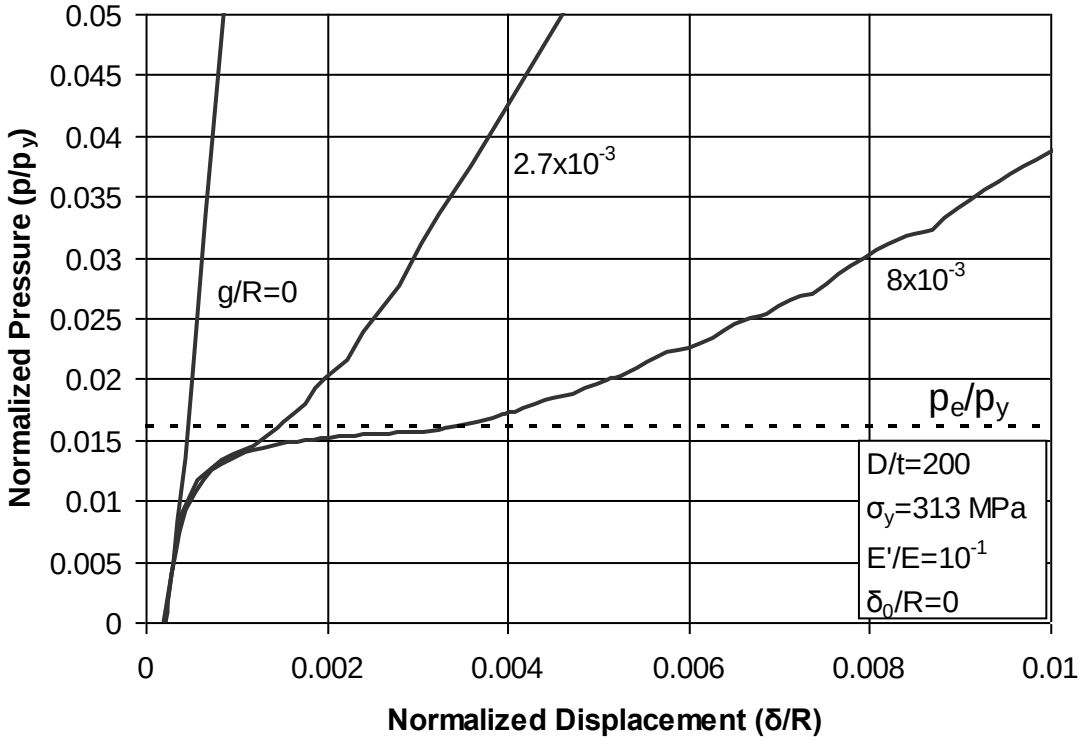

***Figure 31**: External pressure response of confined steel cylinders with $\delta_0/R = 0$ for different values of initial gap (g/R), embedded in a rigid confinement medium $\left(E'/E = 10^{-1}\right)$; low pressure levels.*

A graphical summary of the above described structural behavior of confined elastic or steel cylinders with initial gap between the cylinder and the surrounding medium is depicted in Figure 32.

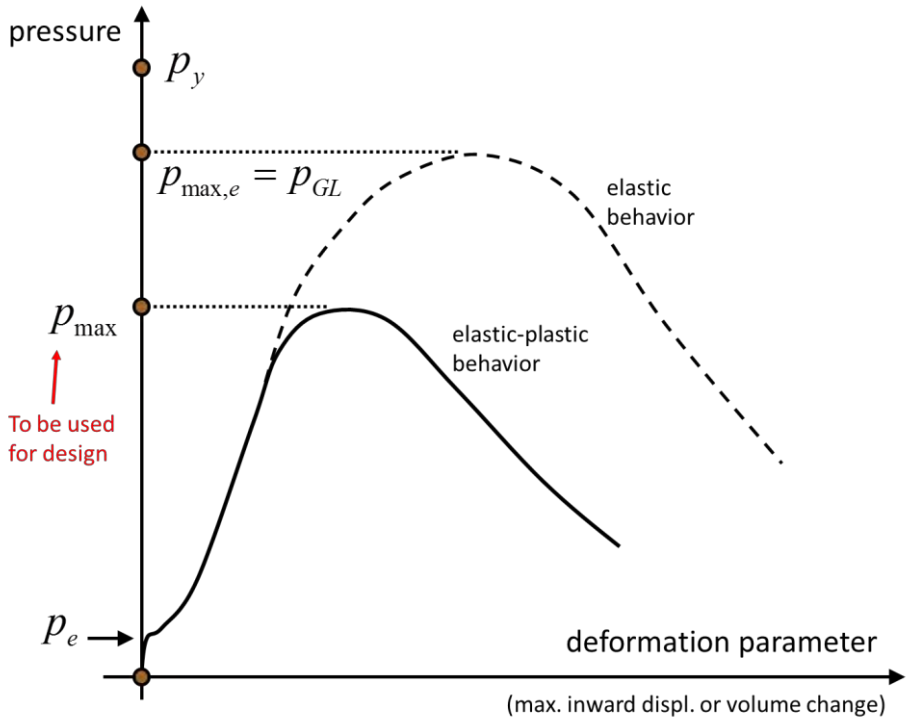

***Figure 32**: Graphical summary of the structural behavior of confined cylinders with initial gap between the cylinder and the surrounding medium*

2.4.1.4 Effect of D/t ratio

The value of maximum external pressure that the cylinder can sustain depends on the value of the D/t ratio. Figure 33 shows the response of a thicker steel cylinder ($D/t = 100$) under external pressure, confined within a stiff boundary. The response is similar to the one presented in Figure 24 for the thin-walled cylinder with $D/t = 200$. However, the ultimate pressure $p_{\max}$ for the thicker cylinder ($D/t = 100$) is higher than the ultimate pressure of the thin-walled cylinder ($D/t = 200$), and closer to the plastic pressure p_y. On the other hand, one should notice that $p_{\max}$ is still lower than the plastic pressure of the cylinder p_y, even in the absence of initial imperfections. The simplified model equation (49) is also included in Figure 33 and it is compared with the finite element results. The comparison indicates that this equation offers an approximation of the post-buckling behavior, verifying

the rapid decrease of pressure upon reaching p_{max}, similar to the case of the thin-walled cylinder ($D/t = 200$), discussed in a previous paragraph.

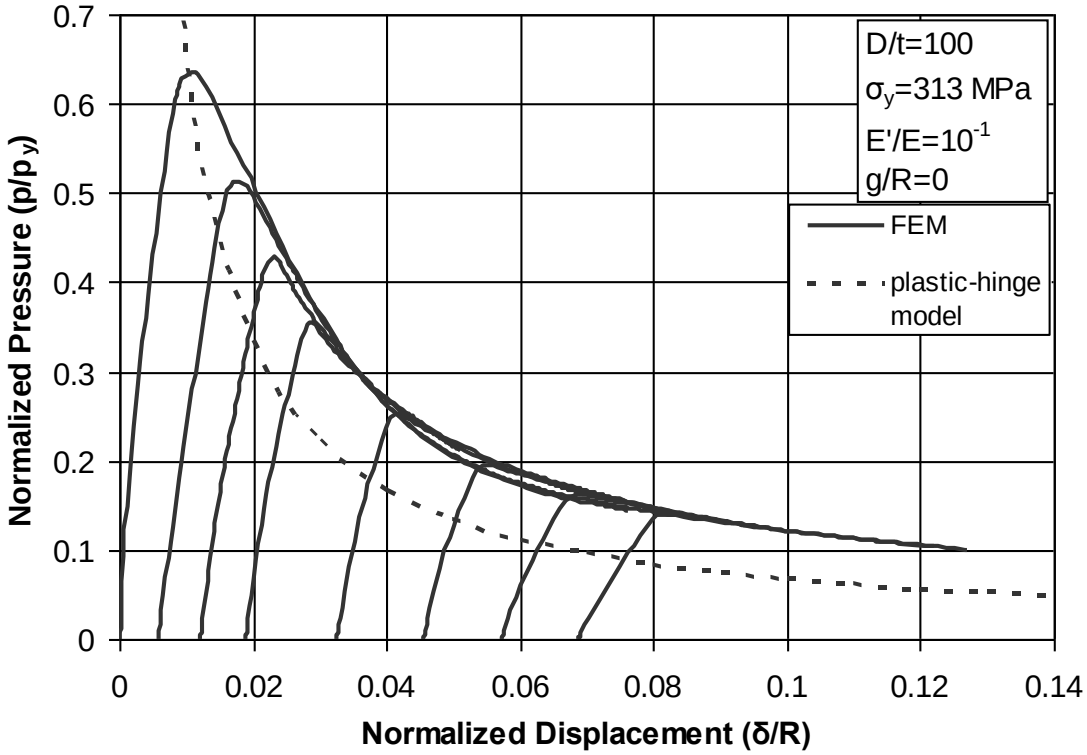

***Figure 33**: Response of tightly-fitted steel cylinders ($g/R = 0$) with $D/t = 100$, embedded in a rigid confinement medium ($E'/E = 10^{-1}$); numerical results for different values of initial out-of-roundness and plastic-hinge collapse mechanism equation (49).*

The variation of ultimate pressure p_{max} with respect to initial out-of-roundness is shown in Figure 34 for three values of D/t ratio (D/t =100, 150, 200) and for zero gap between the cylinder and the medium ($g/R = 0$). The imperfection sensitivity is similar for all three cases, as indicated by the three curves of Figure 34.

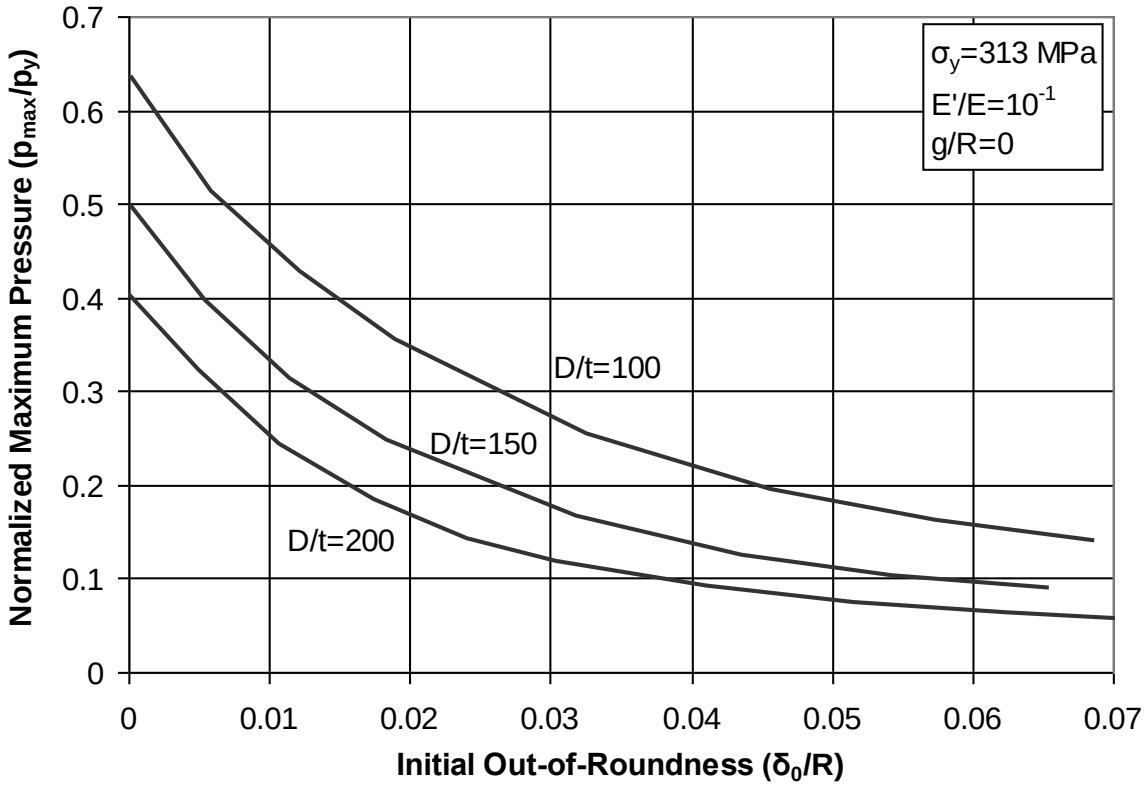

Figure 34*: Effects of initial out-of-roundness and D/t ratio on the maximum pressure sustained by a confined steel cylinder embedded in a rigid confinement medium.*

2.4.1.5 Effect of yield stress

The response of cylinders with different steel material properties embedded in a rigid surrounding medium is shown in Figure 35. In particular, three different values of yield stress σ_y ($235\,MPa$, $313\,MPa$ and $566\,MPa$) are considered and the results are compared with the case of elastic cylinder. The numerical results demonstrate that a higher yield strength σ_y results in an increase of the ultimate pressure $p_{\max}$. The results of Figure 35 are also depicted in Figure 36 in a dimensionless form demonstrating that the value of the ultimate pressure $p_{\max}$ is substantially smaller than the yield pressure p_y.

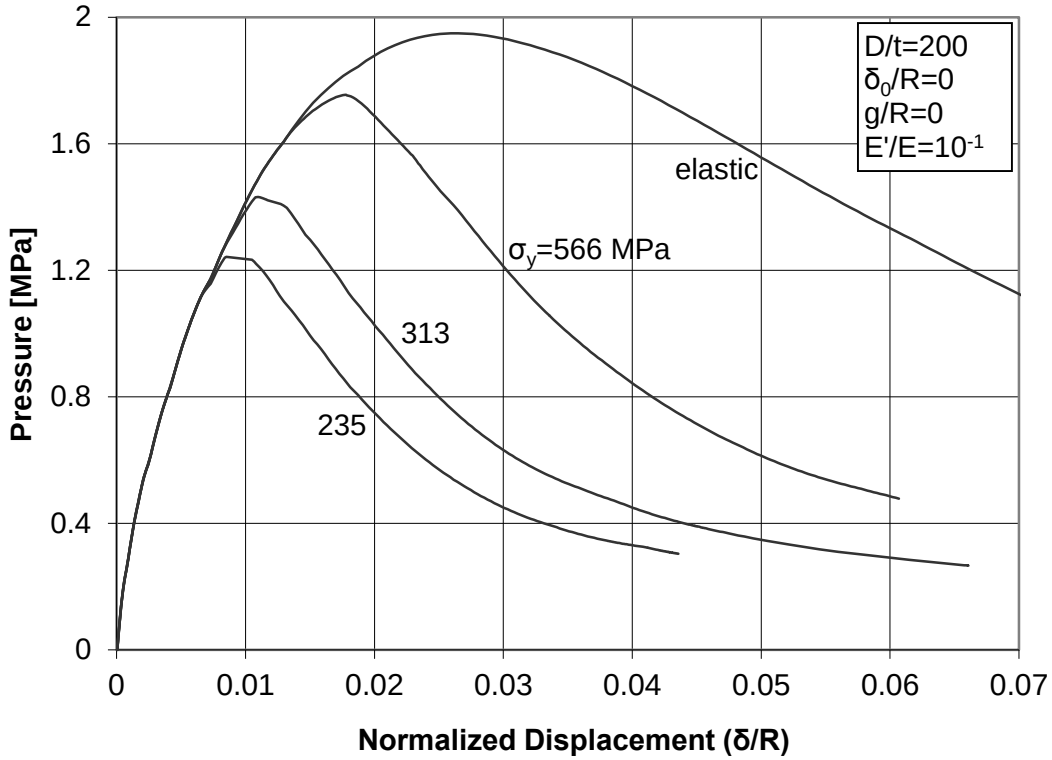

***Figure 35**: Response of steel cylinders with different values of σ_y, embedded in a rigid confinement medium ($E'/E = 10^{-1}$); pressure in [MPa] versus normalized displacement.*

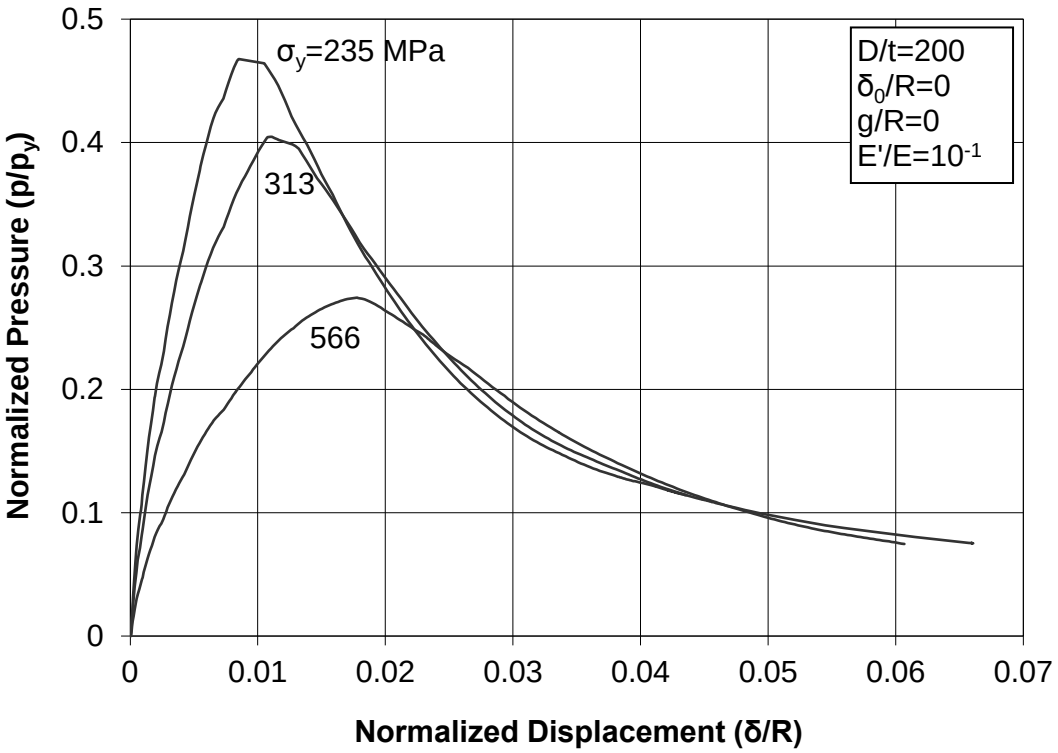

***Figure 36**: Normalized response of steel cylinders with different values of σ_y, embedded in a rigid confinement medium ($E'/E = 10^{-1}$).*

2.4.2 Deformable confinement

The results presented in the previous sections refer exclusively to the case of cylinders enclosed within a non-deformable (rigid) cavity, considering an elastic confinement medium with high values of modulus E'. However, quite often in buried pipeline applications, the steel cylinder is embedded in a soft medium, which should be modelled as a deformable cavity. In the present section, using the finite element tools, the influence of embedment flexibility on the mechanical response of externally-pressurized cylinders is examined. Motivated by the buckling problem of externally-pressurized buried pipelines, the top boundary of the finite element model is free, whereas the nodes on the three other boundaries are fixed.

2.4.2.1 General response

The influence of medium deformability on the buckling response of a steel cylinder ($\sigma_y = 313$ MPa, $D/t = 200$) with no imperfections ($\delta_0 = g = 0$) for different values of the confining medium modulus E' is shown in Figure 37 in terms of the pressure-deformation curves. In this analysis, the gravity load of the surrounding medium is not considered. The results indicate that there is a substantial reduction of the $p_{\max}$ value with decreasing values of E', due to the elastic deformation of the medium. This reduction is attributed to the more pronounced deformations of the confined steel cylinder within the soft medium, under moderate pressure levels. Furthermore, with decreasing values of E', the response becomes smoother, and it characterized by a “plateau” on the equilibrium path about the maximum pressure. Figure 38, Figure 39, and Figure 40 depict the pressure versus deformation equilibrium paths of steel cylinders for different values of initial out-of-roundness, for three values of E'/E ratio, equal to 10^{-3}, 10^{-4} and 3.3×10^{-5} respectively. The last value of medium stiffness E' corresponds to loose sand [38].

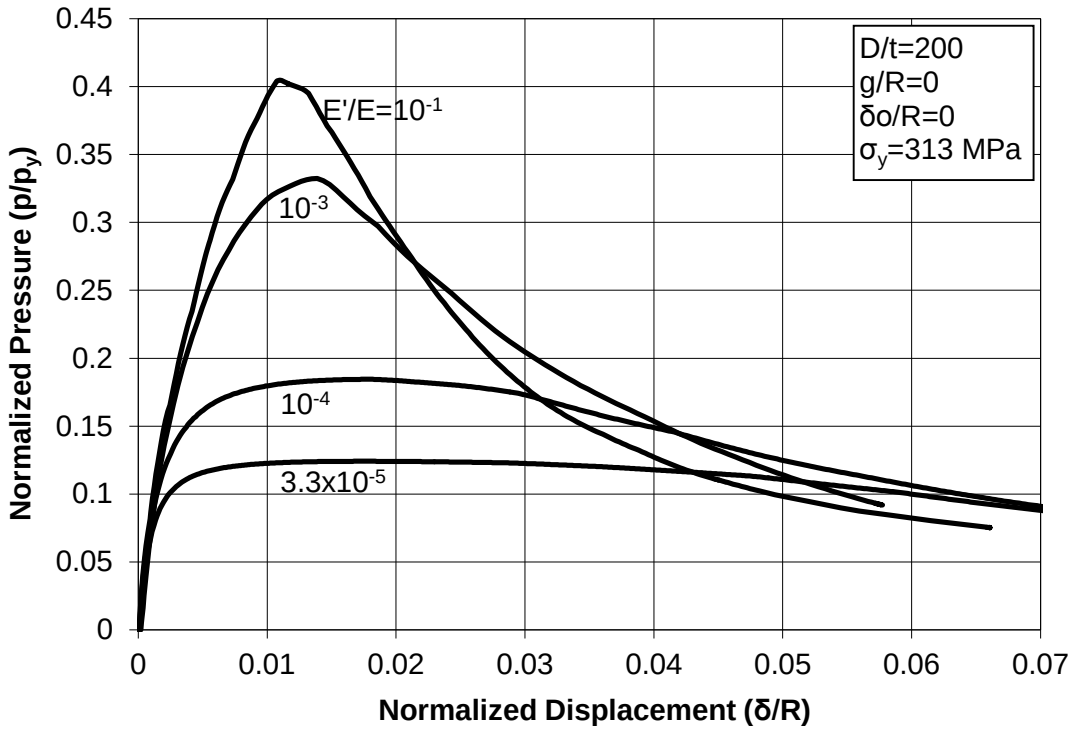

***Figure 37**: Pressure versus deformation equilibrium paths of perfect steel cylinders ($g/R=0$, $\delta_0/R=0$) for different values of confinement medium modulus (E'/E).*

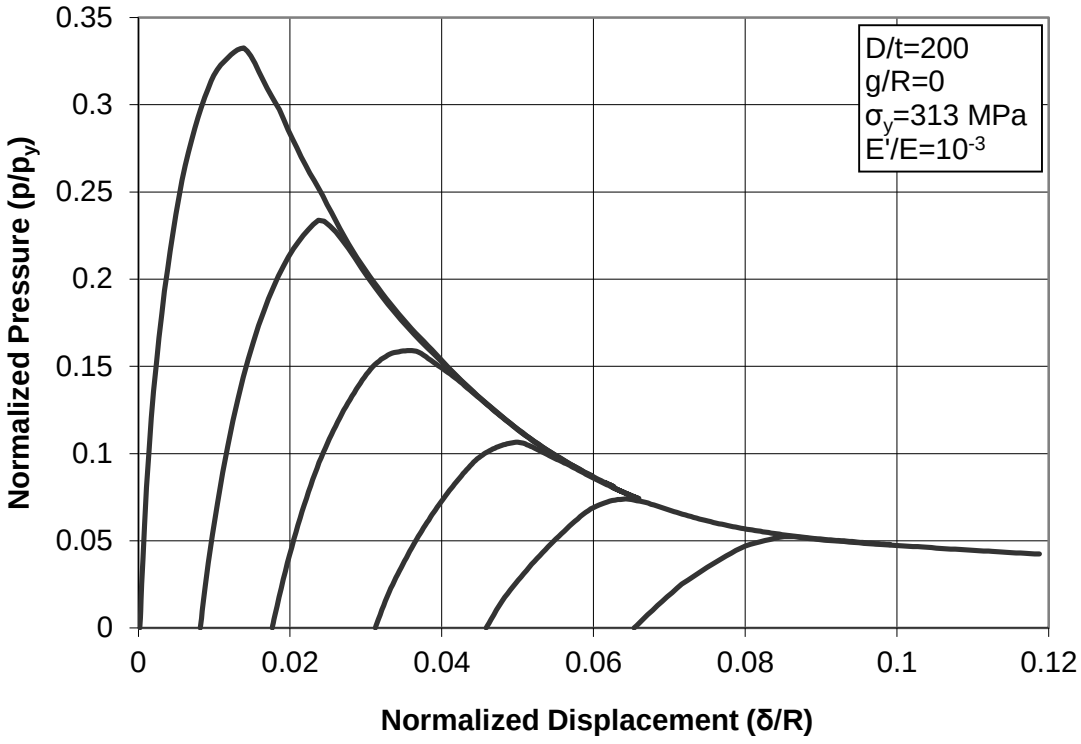

***Figure 38**: Response of tightly-fitted steel cylinders ($g/R=0$), embedded in a confinement medium with $E'/E=10^{-3}$, for different values of initial out-of-roundness.*

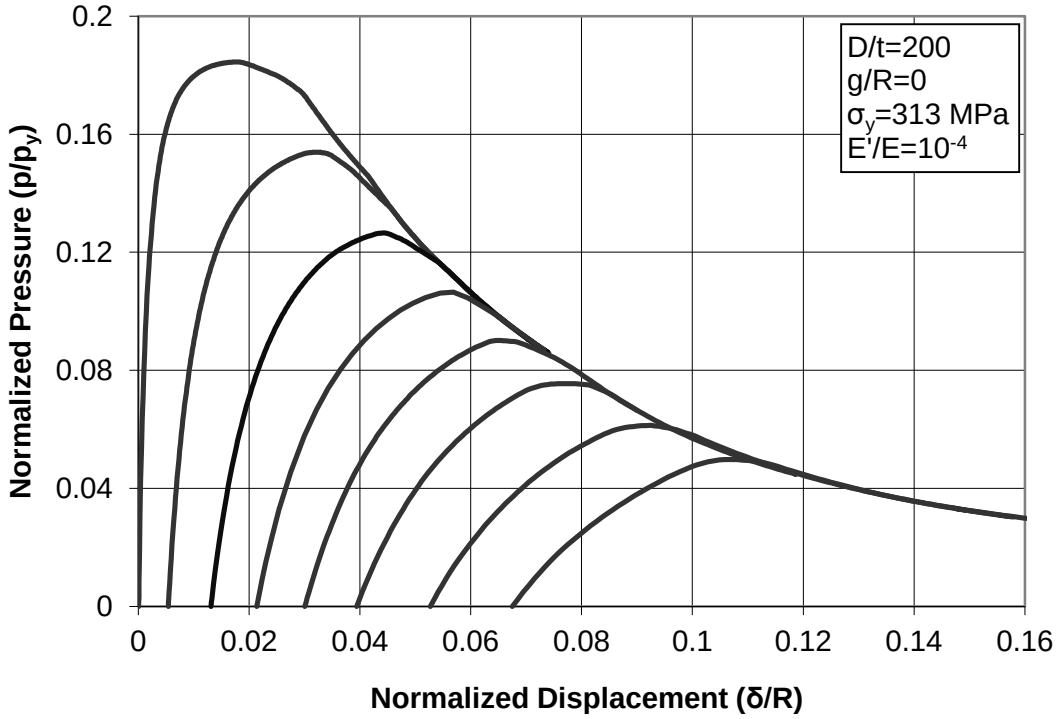

***Figure 39**: Response of tightly-fitted steel cylinders ($g/R=0$), embedded in a confinement medium with $E'/E=10^{-4}$, for different values of initial out-of-roundness.*

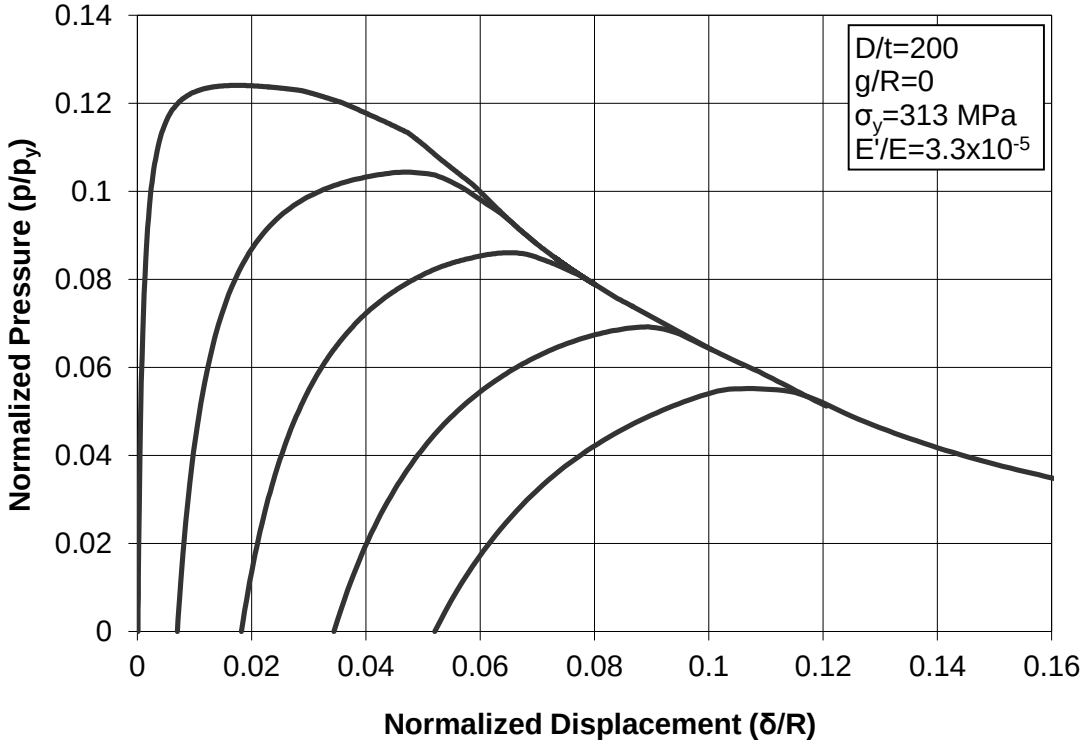

***Figure 40**: Response of tightly-fitted steel cylinders ($g/R=0$), embedded in a confinement medium with $E'/E=3.3\times10^{-5}$, for different values of initial out-of-roundness.*

For the better understanding of the effect of confinement on the buckling response of confined cylinders, the ultimate pressure capacity p_{max}, is depicted with respect to a modulus ratio parameter, defined as $x=-\log(E'/E)$. Figure 41 shows the drop of the p_{max} value with decreasing values of E' for an elastic and a steel "perfect" cylinder $(\delta_0/R=g/R=0)$ with $D/t=200$. It is interesting to note that for $E'/E\le 3\times10^{-4}$, the two curves coincide, indicating that buckling of steel cylinders with $D/t=200$ in a highly deformable medium occurs in the elastic range. In other words, the effects of confinement are significantly reduced.

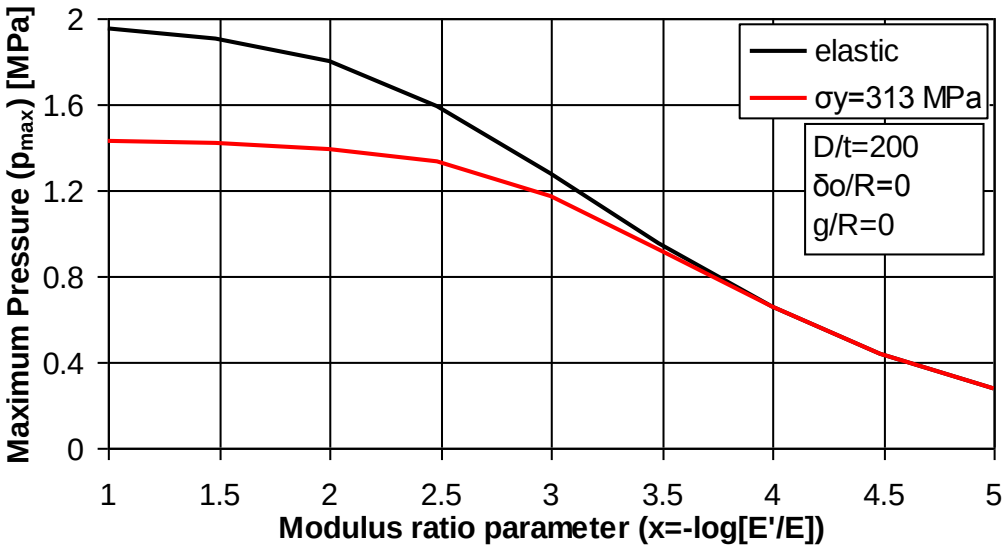

***Figure 41**: Comparison between elastic and steel perfect cylinders ($\delta_0/R=g/R=0$) with respect to the E'/E value.*

2.4.2.2 Imperfection sensitivity

The variation of maximum pressure with respect to initial out-of-roundness for four different values of the confinement medium modulus E' is plotted in Figure 42 and in Figure 43 for zero $(g/R=0)$ and non-zero gap $\left(g/R=5.4\times10^{-3}\right)$ respectively. The results indicate that there is a significant imperfection sensitivity, which is more pronounced for stiff confinement than for deformable confinement. Comparison between the results from Figure 42 and Figure 43 indicate that the presence of gap affects the value of maximum pressure but this effect becomes less important increasing the flexibility of the surrounding medium.

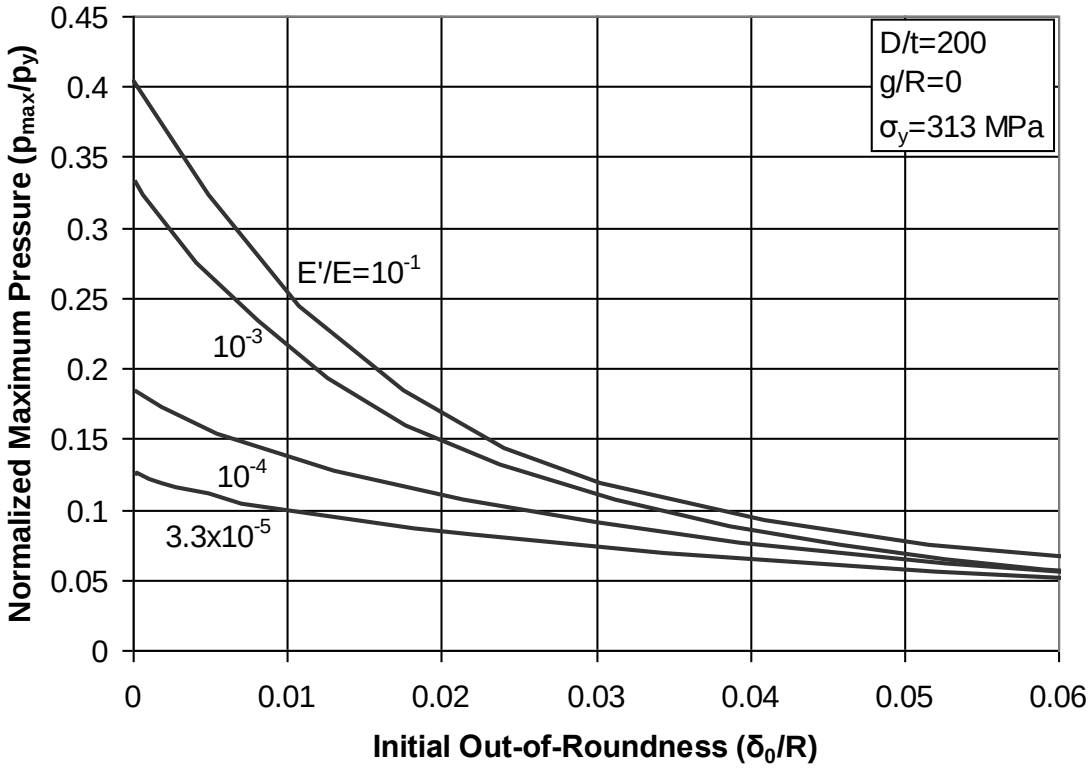

***Figure 42**: Effects of initial out-of-roundness and stiffness of confinement medium (E'/E) on the maximum pressure sustained by a confined steel cylinder ($g/R = 0$).*

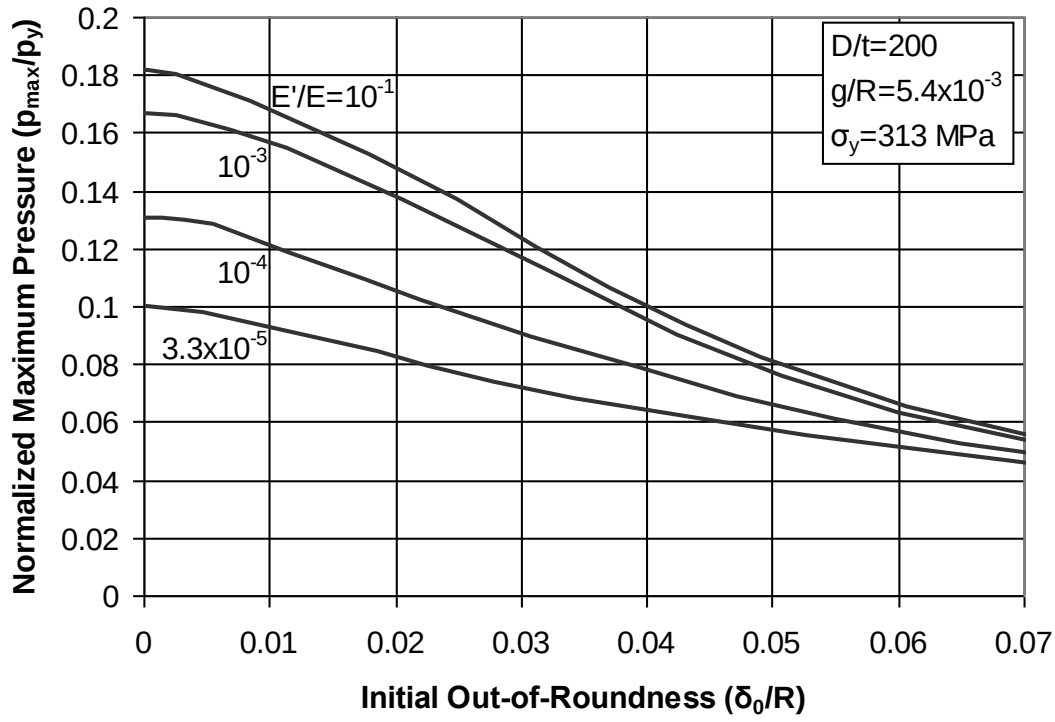

***Figure 43**: Effects of initial out-of-roundness and stiffness of confinement medium (E'/E) on the maximum pressure sustained by a confined steel cylinder ($g/R = 5.4\times10^{-3}$).*

Figures 44 show the drop of the $p_{\max}$ value with decreasing values of E' for elastic and steel imperfect cylinders with $D/t = 200$; particularly for (a) $\delta_0/R = 0.012,\ g/R = 0$, and (b) $\delta_0/R = 0,\ g/R = 0.0027$. These figures indicated that buckling of steel cylinders in a highly deformable medium (high values of the modulus ratio parameter) occurs in the elastic range.

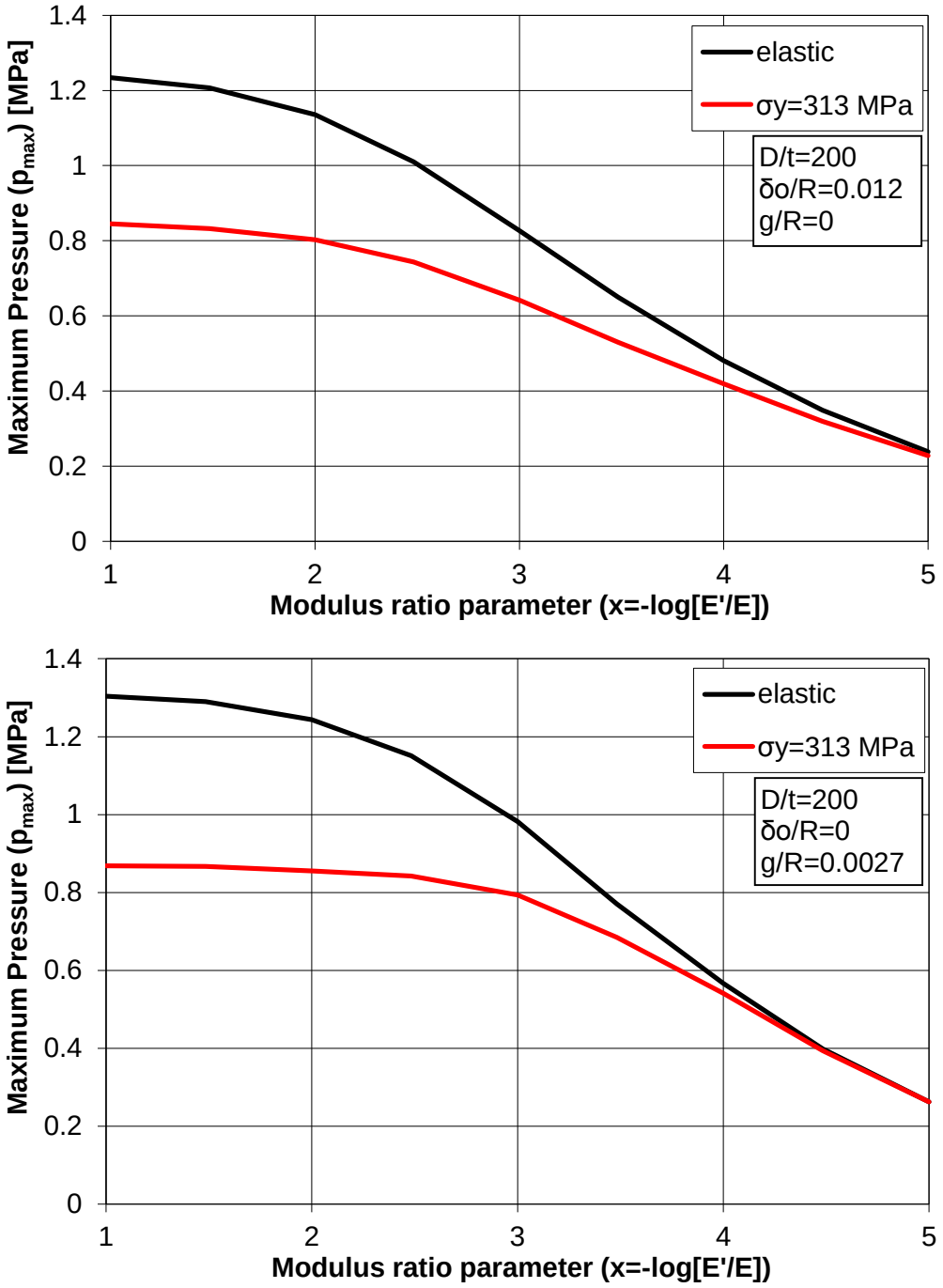

***Figures 44**: Comparison between elastic and steel cylinders with respect to the E'/E value for (a) $\delta_0/R = 0.012,\ g/R = 0$, and (b) $\delta_0/R = 0,\ g/R = 0.0027$.*

2.4.2.3 Effect of D/t ratio

The influence of D/t ratio on the $p_{\max}/p_{\max,\infty}$ versus E' relationship, where $p_{\max,\infty}$ is the ultimate pressure of the cylinder in a rigid confinement ($E' \to \infty$), can be neglected as shown in Figure 45.

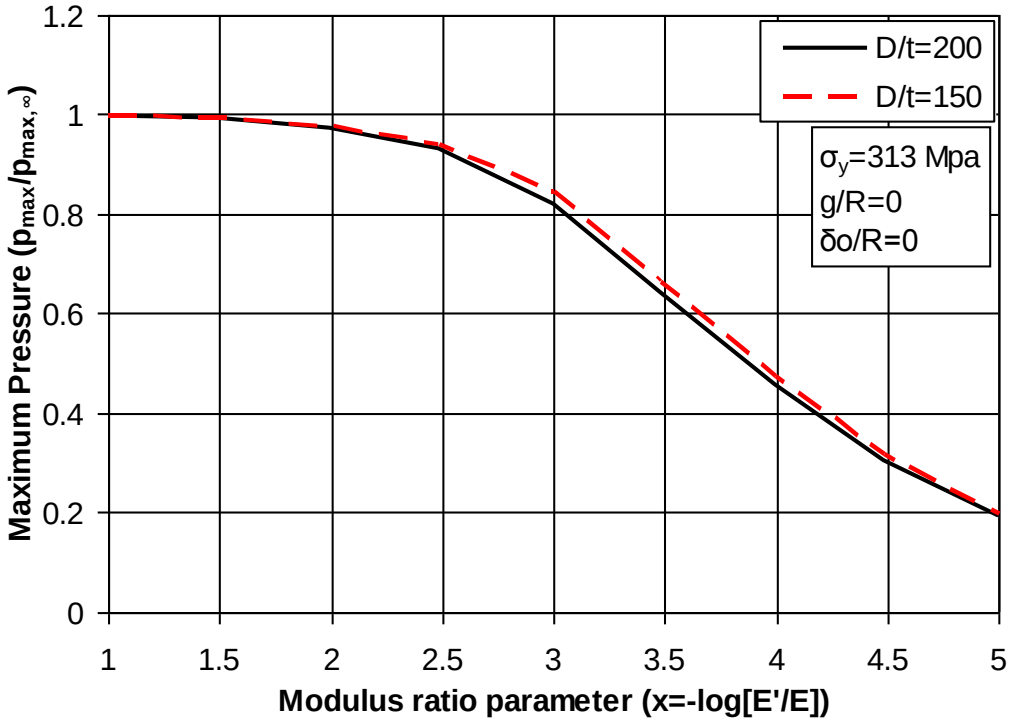

***Figure 45**: Variation of maximum pressure with respect to the E'/E value for perfect steel cylinders ($\delta_0/R = g/R = 0$) and different values of D/t ratio.*

2.4.2.4 Effect of yield stress

The response of cylinders with different steel material properties embedded in a soft confinement ($E'/E = 3.3\times10^{-5}$) are shown in Figure 46. Unlike the case where a stiff boundary is considered (Figure 35) in which a higher yield strength σ_y results in an increase of the ultimate pressure $p_{\max}$, in the case of a soft confinement medium (Figure 46), the ultimate pressure $p_{\max}$ seems to be rather insensitive to the value of yield stress σ_y. In such a case, the value of $p_{\max}$ is quite small, due to the small contribution of the surrounding medium. In all three cases ($235\,MPa$, $313\,MPa$ and $566\,MPa$) of Figure 46, buckling occurs in the elastic range and, therefore, yielding of steel material occurs after a maximum pressure occurs. The results of Figure 46 are also depicted in Figure 47 in a dimensionless form.

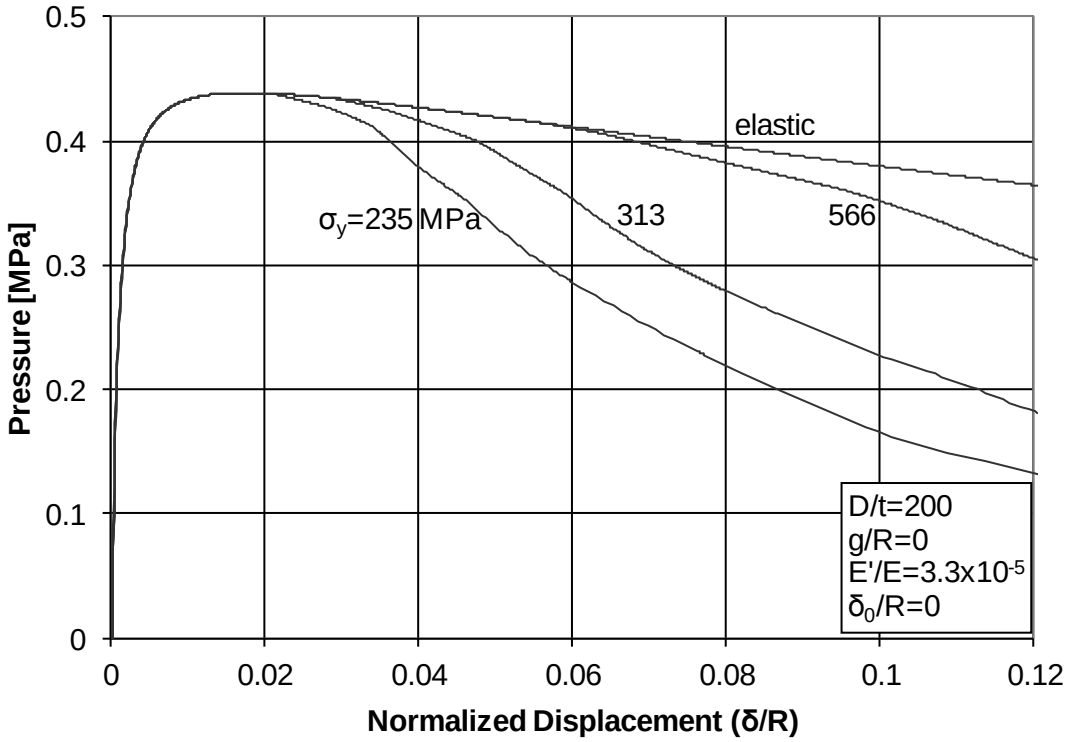

***Figure 46**: Response of steel cylinders with different values of σ_y, embedded in a soft medium ($E'/E = 3.3\times10^{-5}$); pressure in [MPa] versus normalized displacement.*

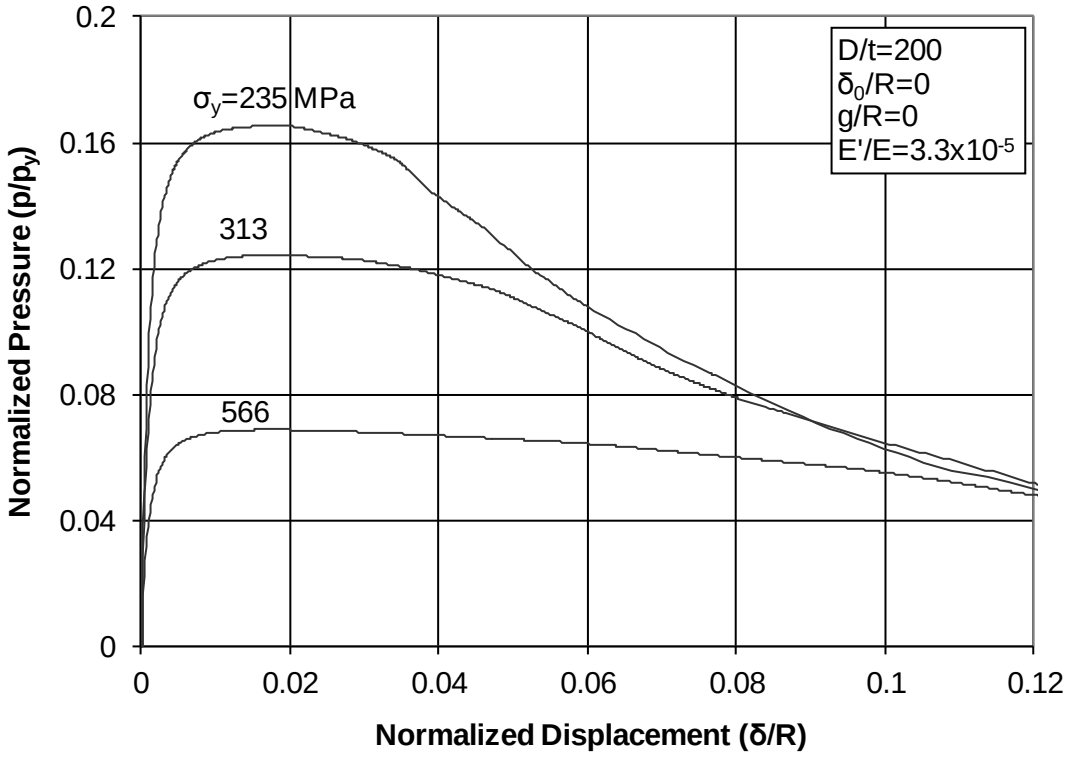

***Figure 47**: Normalized response of steel cylinders with different values of σ_y, embedded in a soft confinement medium ($E'/E = 3.3\times10^{-5}$).*

2.4.2.5 Contact pressure

The contact pressure developed in the interface between the cylinder and the medium is shown in Figure 48 for the case of a soft confinement modulus E' ($E'/E = 3.3\times10^{-5}$). Note that the maximum contact pressure occurs at point A_2, which is located at the "touchdown" area with maximum plastic deformation.

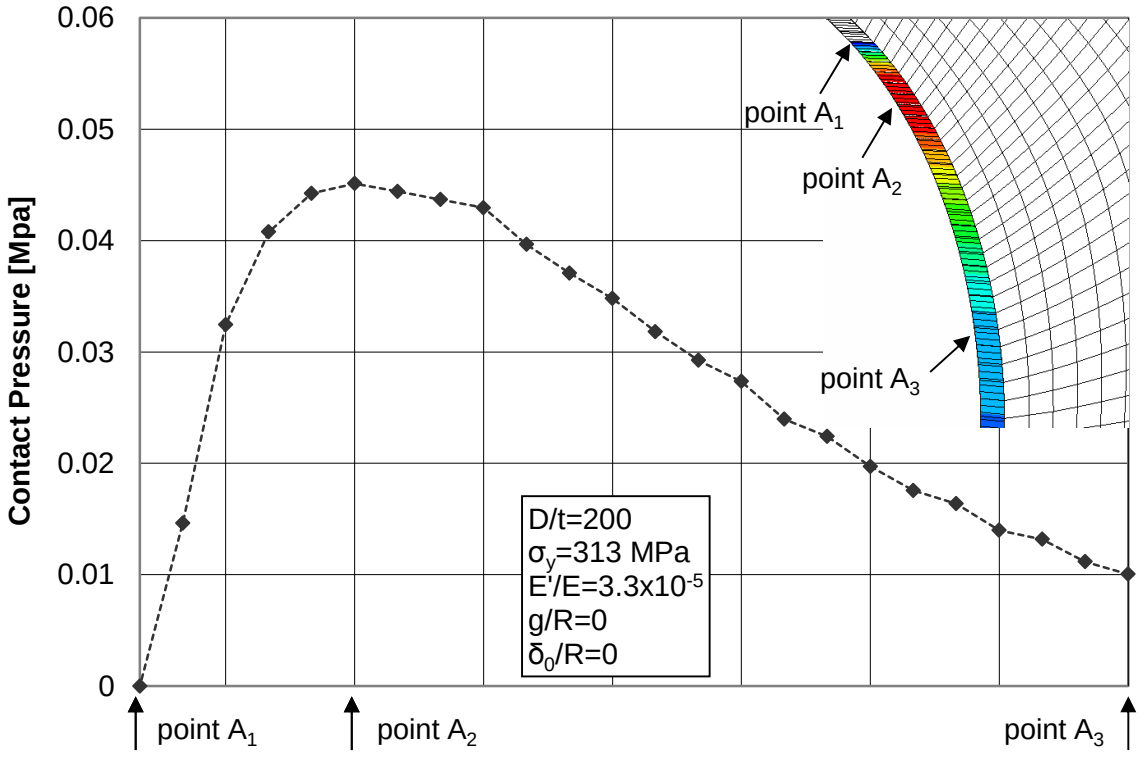

***Figure 48**: Variation of contact pressure between the steel cylinder and the elastic medium.*

2.4.2.6 Effect of friction

Figure 49 and Figure 50 show the effects of friction between the cylinder and the medium for a value of $E'/E = 10^{-3}$ and a small value of $E'/E = 3.3\times10^{-5}$ respectively. Friction is considered through the friction coefficient μ, where $\mu = \tan\varphi$ and φ is the friction angle of the interface. In the present case, assuming a soil material with friction angle φ_S equal to 32°, the value of φ is considered equal to 10° and 16° (i.e. 1/3 and 1/2 of the value of φ_S), corresponding to μ values equal to 0.176 and 0.287 respectively. The numerical results show that the consideration of friction results in a small increase of the ultimate capacity p_{max}. The friction effect is somewhat more pronounced in the case of a very soft confinement medium ($E'/E = 3.3\times10^{-5}$). On the other hand, in the case of rigid confinement, this effect has been found to be negligible.

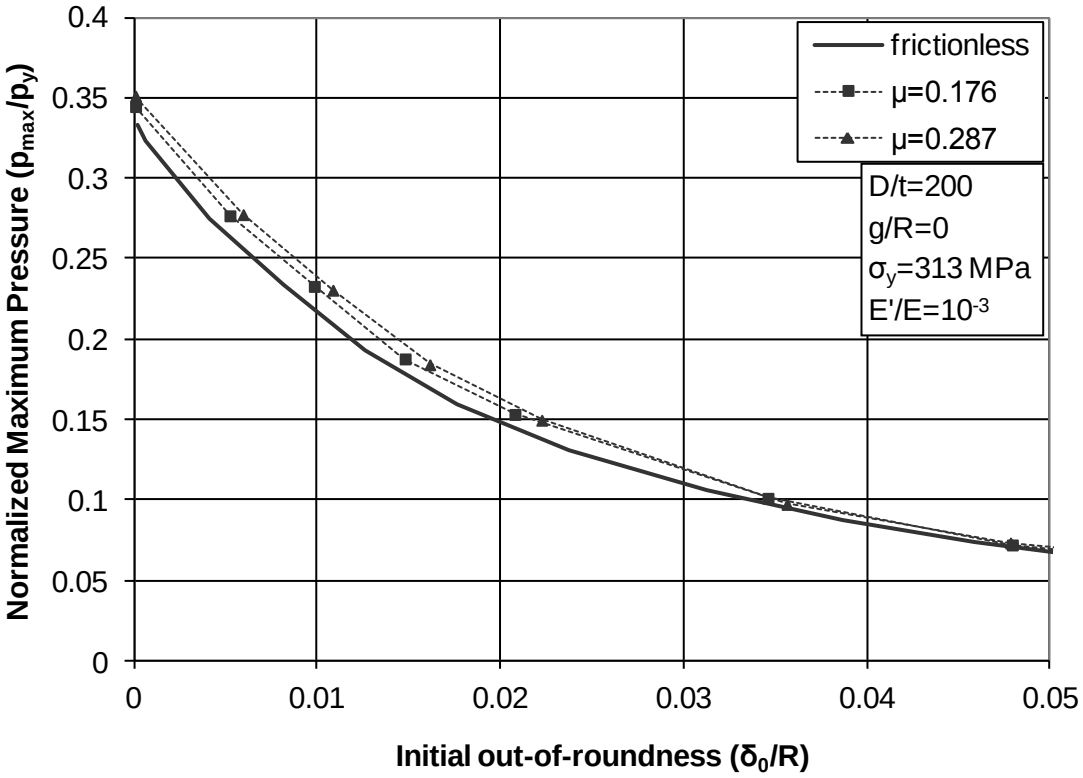

***Figure 49**: Effects of friction between the steel cylinder and the elastic surrounding medium for* $E'/E = 10^{-3}$.

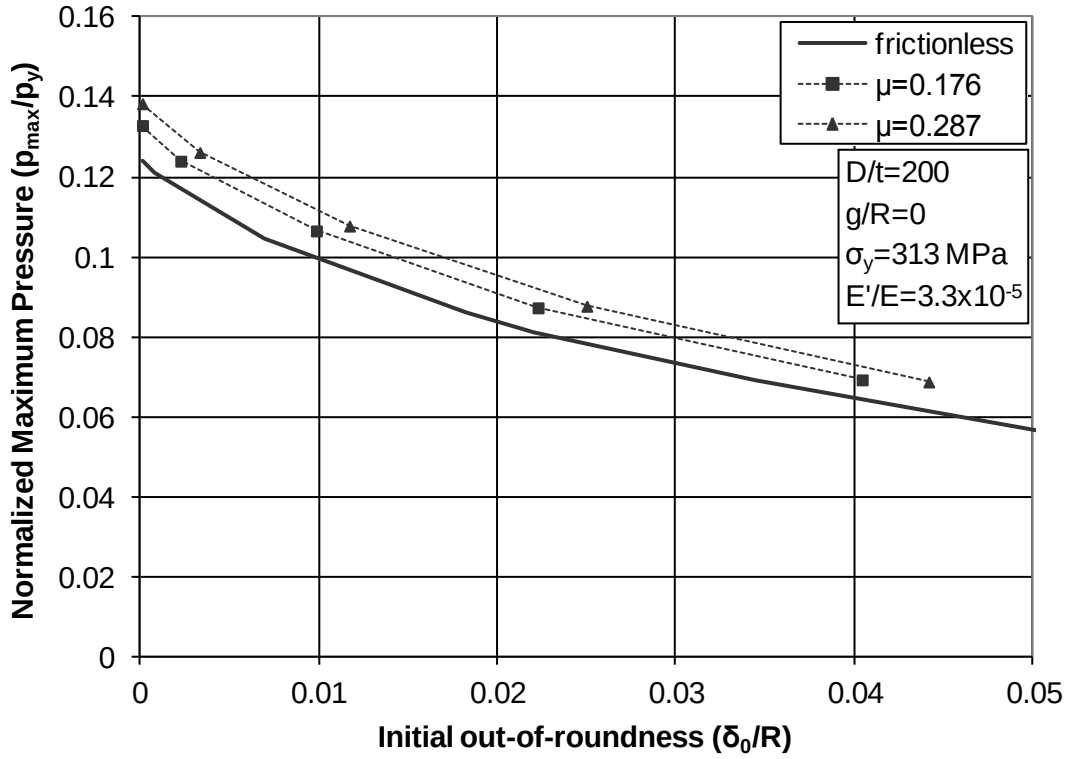

***Figure 50**: Effects of friction between the steel cylinder and the elastic surrounding medium for* $E'/E = 3.3\times10^{-5}$.

2.4.3 Effect of preloading

2.4.3.1 General response

The effect of vertical preloading on the top of the surrounding medium is shown in Figure 51 and Figure 52 for the case of soft surrounding medium ($E'/E = 3.3\times10^{-5}$). Preloading is considered in the form of a vertical pressure q on the top edge of the medium, which is applied first and it is kept constant while the external pressure p is increased. The values of q in Figure 51 represent loading in a buried pipeline from overlying soil of height that ranges between 0 and 15 meters, assuming a unit weight of soil equal to $15 kN/m^3$. The values of vertical pressure q are normalized by the quantity $q_0 = \sigma_y (t/R)^2$ ($q^* = q/q_0$). The numerical results show that, in the case of soft medium, preloading has a beneficial effect on the pressure capacity of the cylinder. On the other hand, negligible effects on the cylinder response have been observed in the case of a stiff medium.

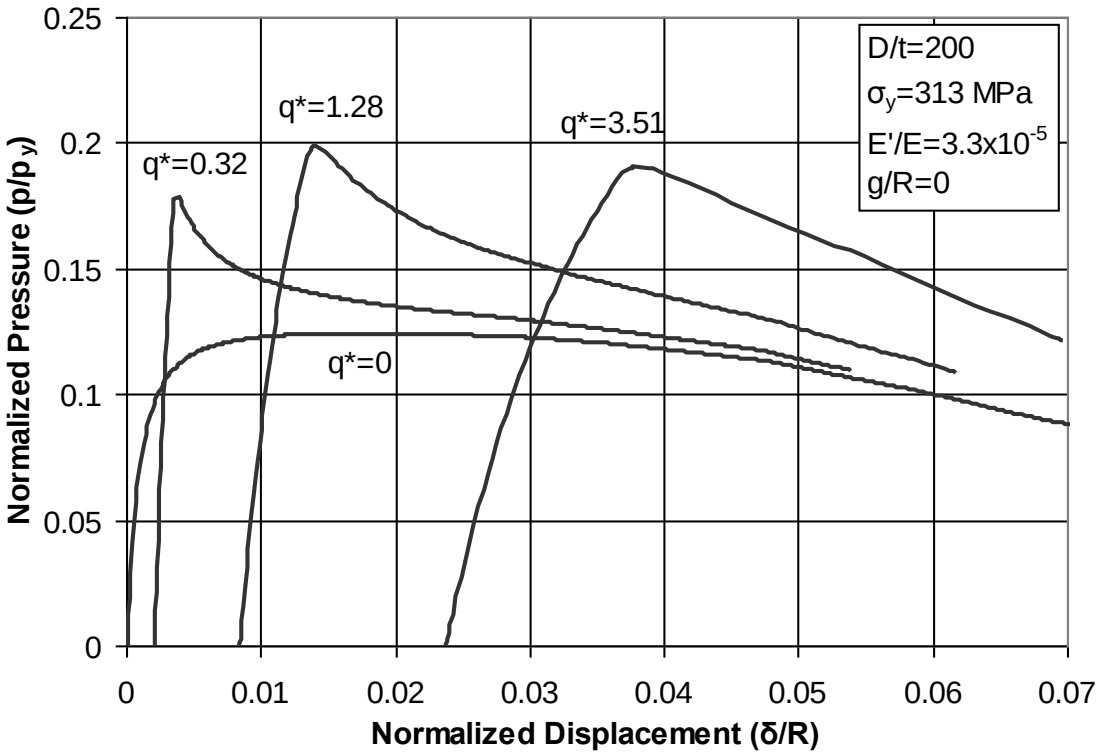

***Figure 51**: Effects of uniform preloading at the top of the surrounding medium, on pressure response of confined steel cylinders.*

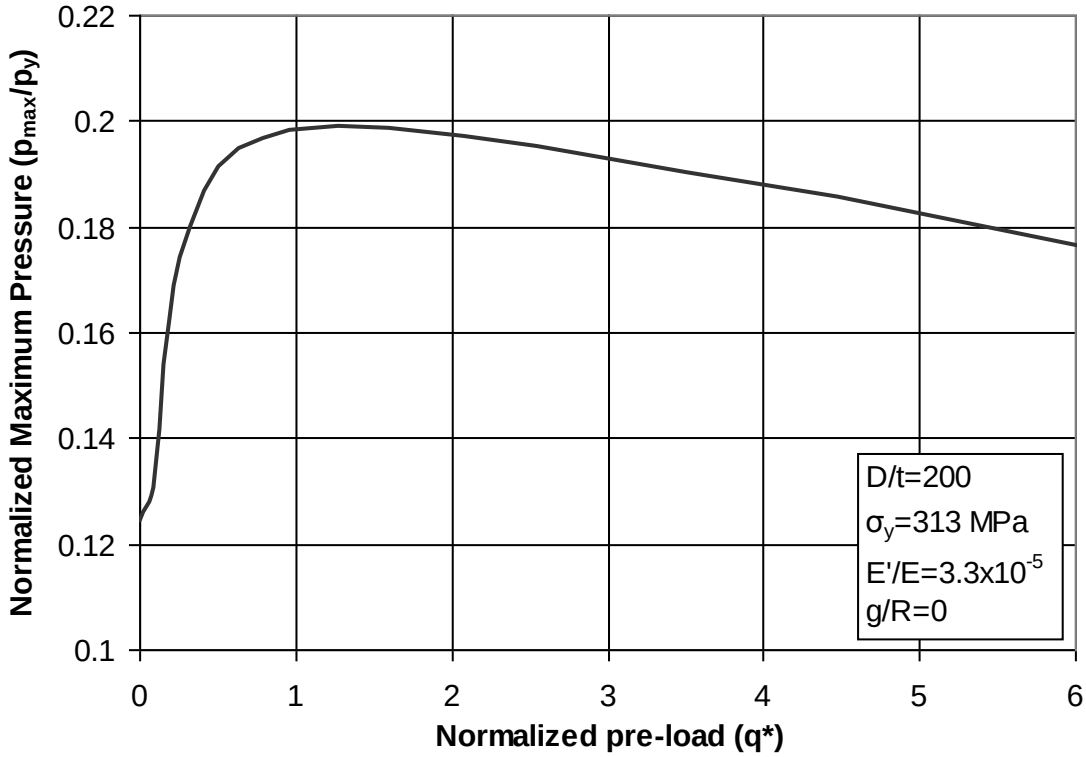

Figure 52: *Variation of maximum pressure* p_{max} *, sustained by the cylinder, in the presence of preloading at the top of the surrounding medium.*

2.4.3.2 Effect of gravity

The previous results have been obtained without considering gravity of the surrounding medium. In the following, the effects of gravity on the structural response of the cylinder are examined. Motivated by the case of buried pipelines, soil conditions are considered for the surrounding medium. Figure 53 and Figure 54 show the pressure-displacement response of a steel cylinder with $D/t=200$, for $\nu=0.3$ and $\nu=0.49$ respectively. The steel cylinder (σ_y=313 MPa) is embedded in an elastic medium of density equal to 20 kN/m^3 and Young's modulus E' ranging from 25 to 100 MPa, which is typical for clays [38]. In this analysis, gravity of the cylinder/soil system is considered as a first step, and subsequently, external pressure has been applied on the outer surface of the cylinder. The results in Figure 53 refer to $\nu=0.3$ and indicate a high value of $p_{\max}$ at small values of E'. This observation is more pronounced in Figure 54 which refers to $\nu=0.49$, a nearly-incompressible medium.

This indication can be explained if the detachment w of the cylinder from the surrounding medium replaces the displacement δ of the cylinder in the horizontal axis. The corresponding graphs are shown in Figure 55 and Figure 56 for low values of E'. Due to gravity loading, the cylinder remains in contact with the medium up to a significant level of pressure and buckling is prevented. Immediately after detachment, buckling occurs quite abruptly, associated with a rapid drop of pressure. This sudden collapse is more pronounced in the case of a nearly-incompressible medium $(\nu=0.49)$, as shown in Figure 56. In the case of a high value of E', detachment occurs at relatively low pressure levels and the behavior has similarities with the one described in the previous sections for rigid boundary.

For the better understanding of the effect of the gravity on the structural behavior of the confined cylinders, the corresponding results without the presence of gravity are reported. In particular, Figure 57 depicts the pressure-displacement response of a perfect steel cylinder (σ_y=313 MPa) with $D/t=200$, and for a nearly-incompressible elastic medium $(\nu=0.49)$ with Young's modulus E' ranging from 25 to 100 MPa. Finally, in Figure 58, the critical pressure values with or without the presence of gravity are compared in terms of the Young's modulus of the elastic medium.

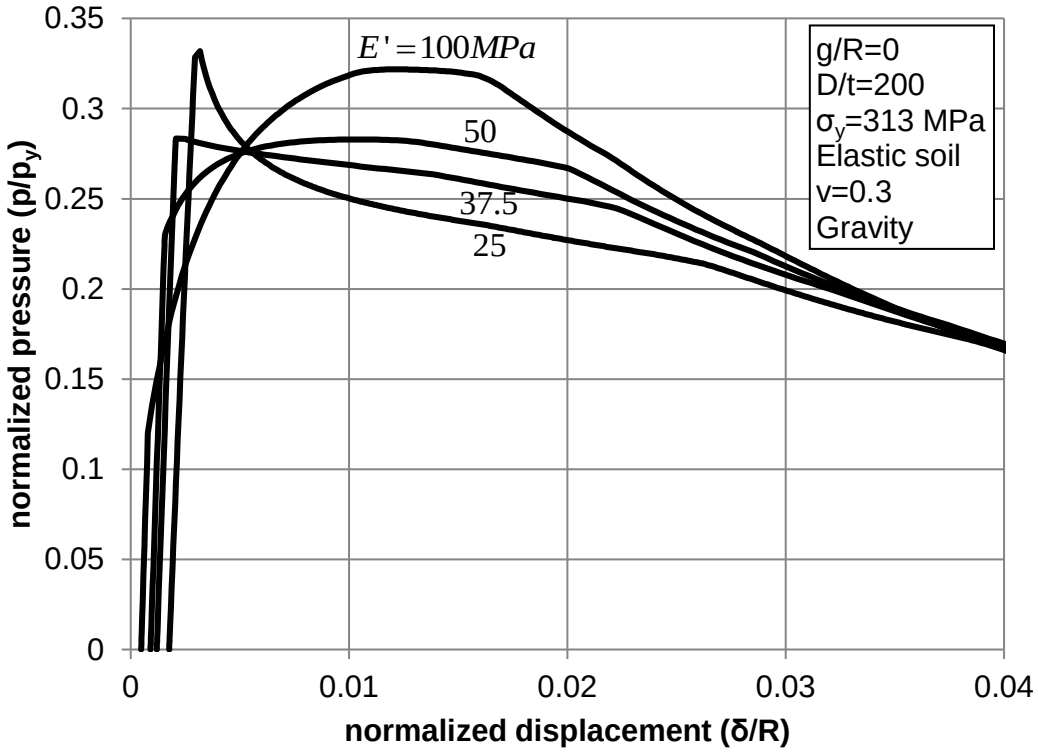

Figure 53: *Structural response of perfect steel cylinders for different values of confinement medium modulus; pressure versus displacement* (δ) *equilibrium paths for* $\nu = 0.3$.

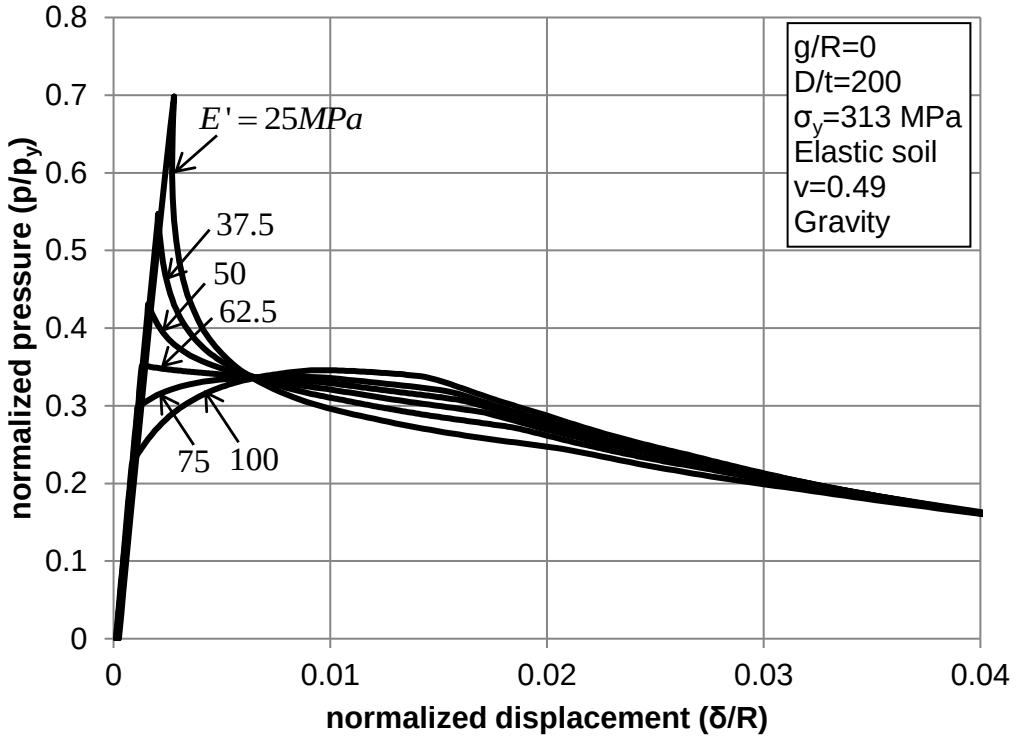

Figure 54: *Structural response of perfect steel cylinders for different values of confinement medium modulus; pressure versus displacement* (δ) *equilibrium paths for* $\nu = 0.49$.

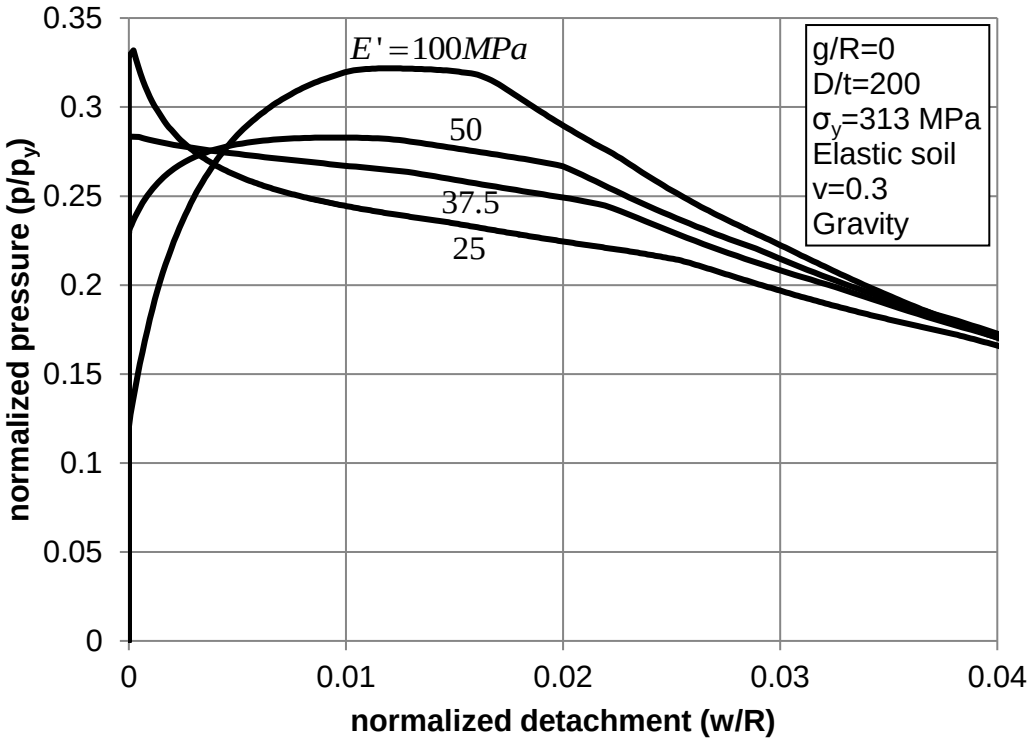

Figure 55: *Structural response of perfect steel cylinders for different values of confinement medium modulus; pressure versus detachment* (w) *equilibrium paths for* $\nu = 0.3$.

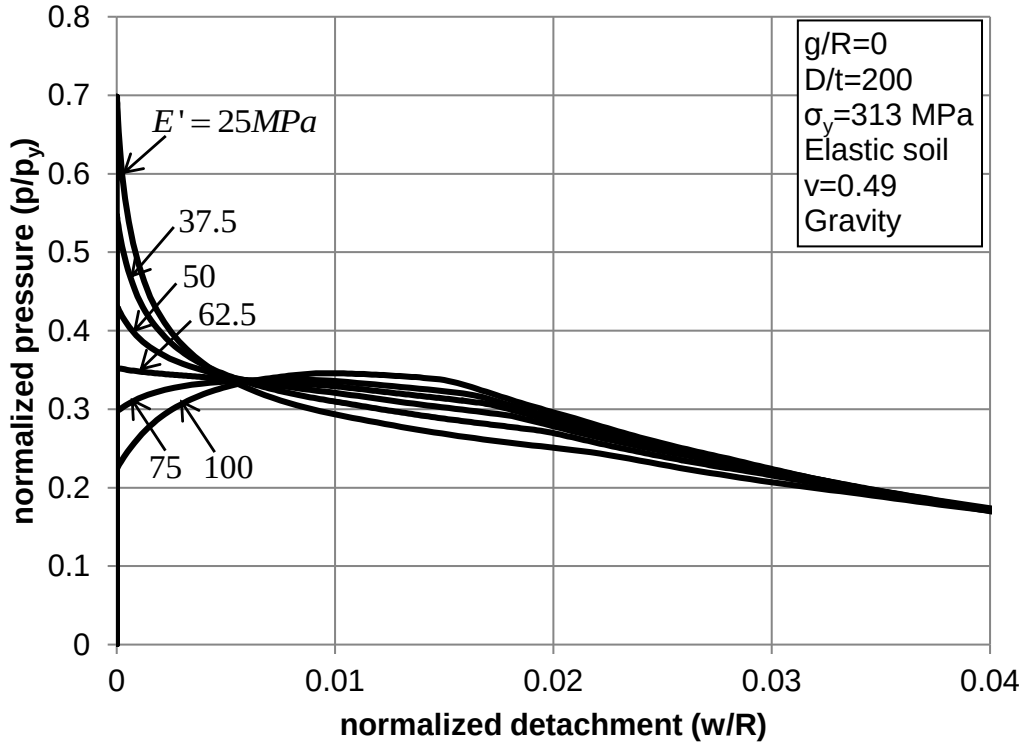

Figure 56: *Structural response of perfect steel cylinders for different values of confinement medium modulus; pressure versus detachment* (w) *equilibrium paths for* $\nu = 0.49$.

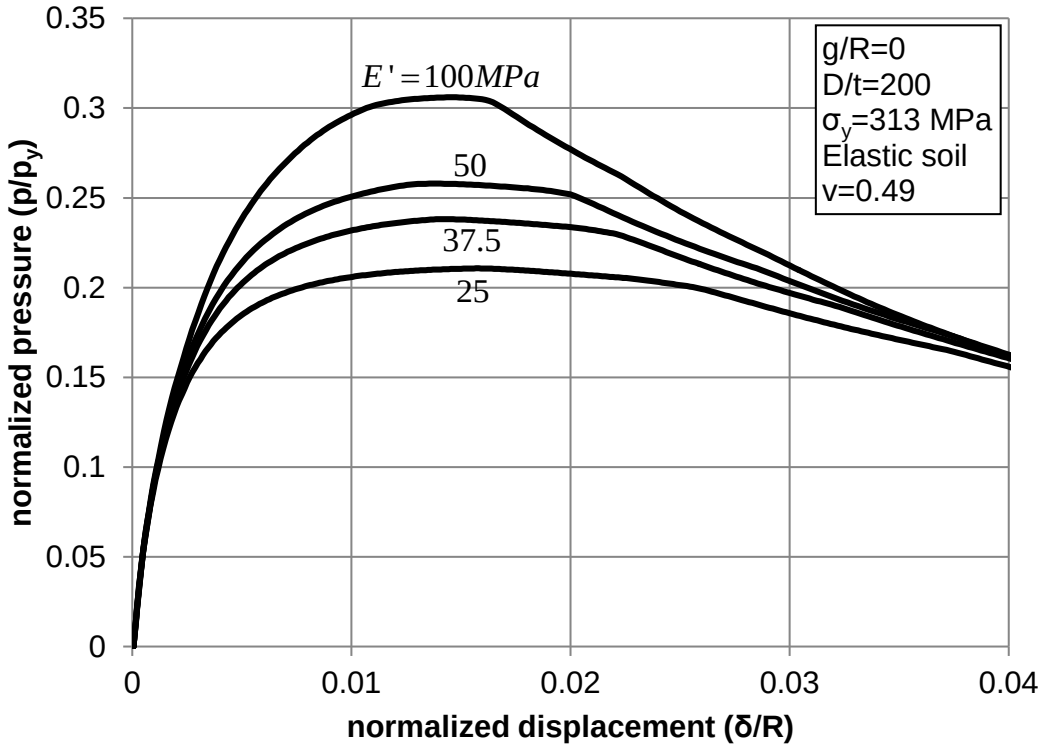

Figure 57: *Pressure versus displacement equilibrium paths of perfect steel cylinders for different values of confinement medium modulus without the presence of gravity.*

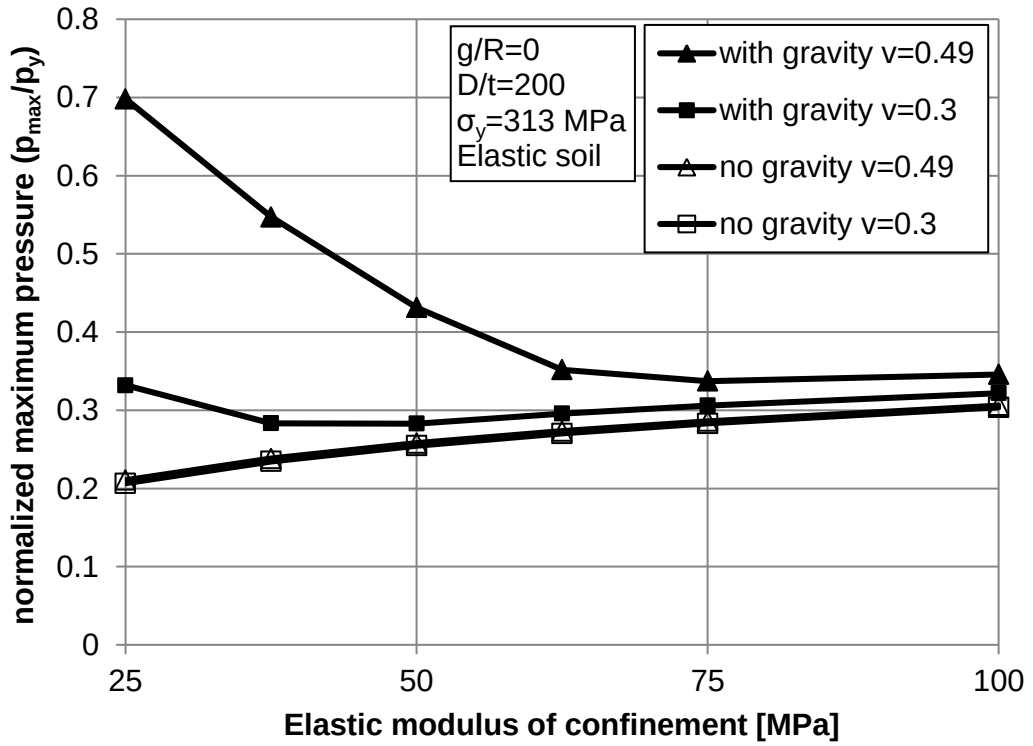

Figure 58: *Effect of gravity on the maximum pressure of perfect steel cylinders for different values of confinement medium modulus.*

2.4.3.3 Elastic-plastic medium

Finally, the behavior of a steel cylinder with $D/t = 200$, embedded in a deformable elastic-plastic medium is examined. The medium is considered a soft-to-firm clay, which is modeled through a Mohr-Coulomb inelastic material model, with cohesion $c = 50$ kPa, friction angle $\varphi = 0^{\circ}$, Young's modulus $E' = 25$ MPa and Poisson's ratio $\nu = 0.49$. The effects of gravity have been taken into account, as an initial loading step. Figure 59 shows the structural response of the steel cylinder in terms of the pressure-displacement curve for the elastic-plastic medium, compared with the corresponding curve assuming elastic medium. The two curves practically coincide. They slightly deviate only after significant deformation, well into the post-buckling range. The coincidence of the two curves is more pronounced when stiffer soil properties are employed. Figure 60 shows the distribution of plastic deformation in the deformable medium at a displacement value of 30 mm $(\delta / R = 0.04)$, well beyond the buckling stage. Plastic deformation occurs at the "touchdown" points B and B' (see Figure 8), where the pressurized cylindrical arch is supported. It is interesting to note that at the stage where buckling occurs, no plastic deformation is detected within the medium.

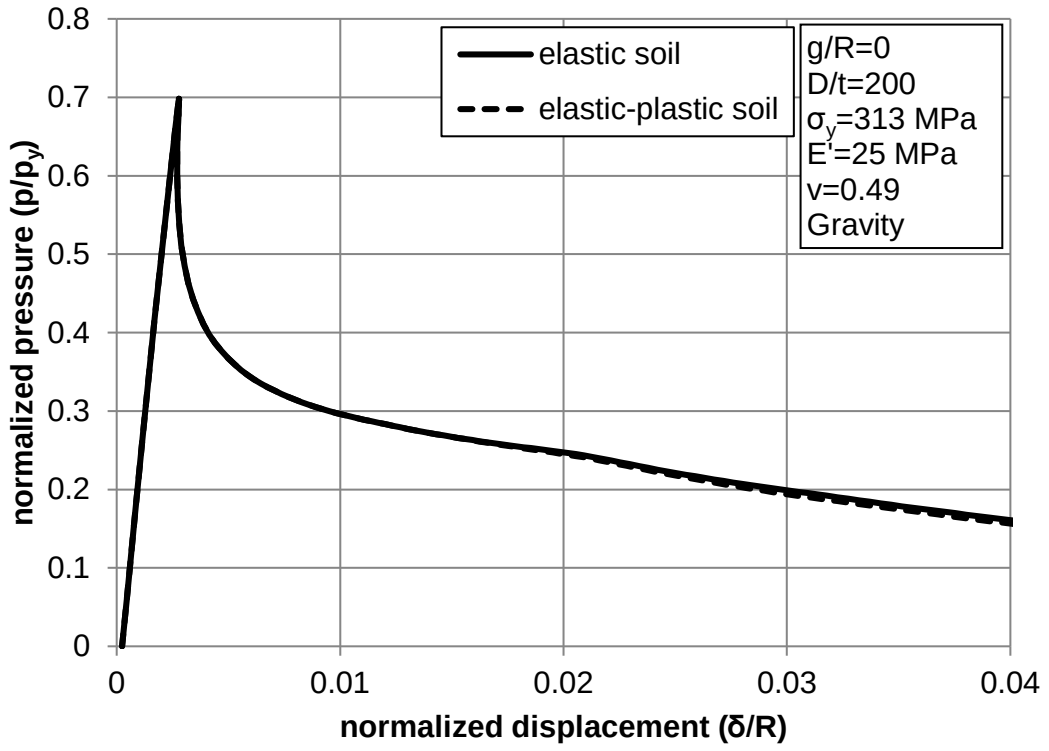

Figure 59: *Effect of elastic-plastic medium on the structural response of confined steel cylinder.*

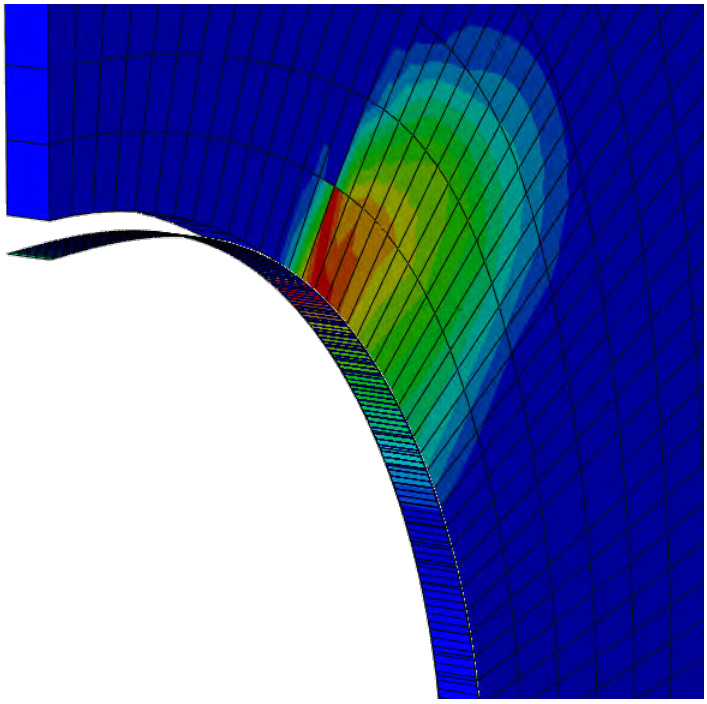

Figure 60: *Distribution of equivalent plastic strain on the medium.*

2.5 Development of design methodology

For the purposes of describing buckling of confined cylinders in the inelastic range in a simple and efficient manner, a general methodology for the design of confined steel cylinders is adopted, within the framework of the new European shell stability design rules [32] and recommendations [33]. The proposed methodology is based on the so-called "shell slenderness" parameter, defined as follows [32],[33]:

$$\lambda = \sqrt{\frac{R_{pl}}{R_{cr}}}, \tag{50}$$

where R_{pl} represents the load that causes full-plastic failure and R_{cr} the load corresponding to the elastic buckling condition of the perfect cylinder. In the present case, the fully-plastic pressure p_y of equation (17) can be used for R_{pl}, whereas Glock's critical pressure p_{GL} in equation (12) offers a very good analytical expression for the critical pressure R_{cr}, so that the slenderness parameter in equation (50) can be written as follows:

$$\lambda = \sqrt{\frac{p_y}{p_{GL}}} = \sqrt{\frac{2.26\,\sigma_y(1-\nu^2)}{E}\left(\frac{D}{t}\right)^{1.2}}. \tag{51}$$

2.5.1 Rigid confinement

In the case of perfect elastic cylinders ($g = \delta_0 = 0$) embedded in a stiff confinement $\left(E'/E = 10^{-1}\right)$, the numerical results in Figure 12 show that the ultimate pressure $p_{\max}$ is equal to the one predicted by equation (12), i.e. equal to p_{GL}. Therefore, combining equations (12) and (51), one can write:

$$\frac{p_{\max}}{p_y} = \frac{1}{\lambda^2}, \tag{52}$$

Neglecting strain hardening effects, the value of p_y cannot be exceeded, i.e. $p_{\max} \le p_y$. Therefore, it would be tempting to argue that for steel cylinders with slenderness values λ less than unity, the maximum pressure $p_{\max}$ would be equal to p_y, whereas equation (52) would express the maximum pressure of steel cylinders with slenderness values λ greater than unity.

The validity of the above argument is examined using the present numerical tools, and the corresponding results are depicted in Figure 61, for imperfection-free cylinders within a

stiff confinement medium and for three values of yield stress σ_y ($235\,MPa$, $313\,MPa$ and $566\,MPa$). Specifically, the variation of ultimate pressure $p_{\max}$ normalized by the fully-plastic pressure p_y is depicted in terms of dimensionless "slenderness" parameter λ. Nevertheless, the numerical results in Figure 61 do not support the above argument. In particular, it is shown that for λ values less than 2.2, the buckling pressure $p_{\max}$ deviate significantly from equation (52). On the other hand, for λ values greater than 2.2, the buckling pressure $p_{\max}$ can be expressed quite accurately by equation (52), which implies that buckling occurs in the elastic range. In other words, the value of 2.2, denoted by λ_p, defines the transition between elastic and inelastic buckling regime.

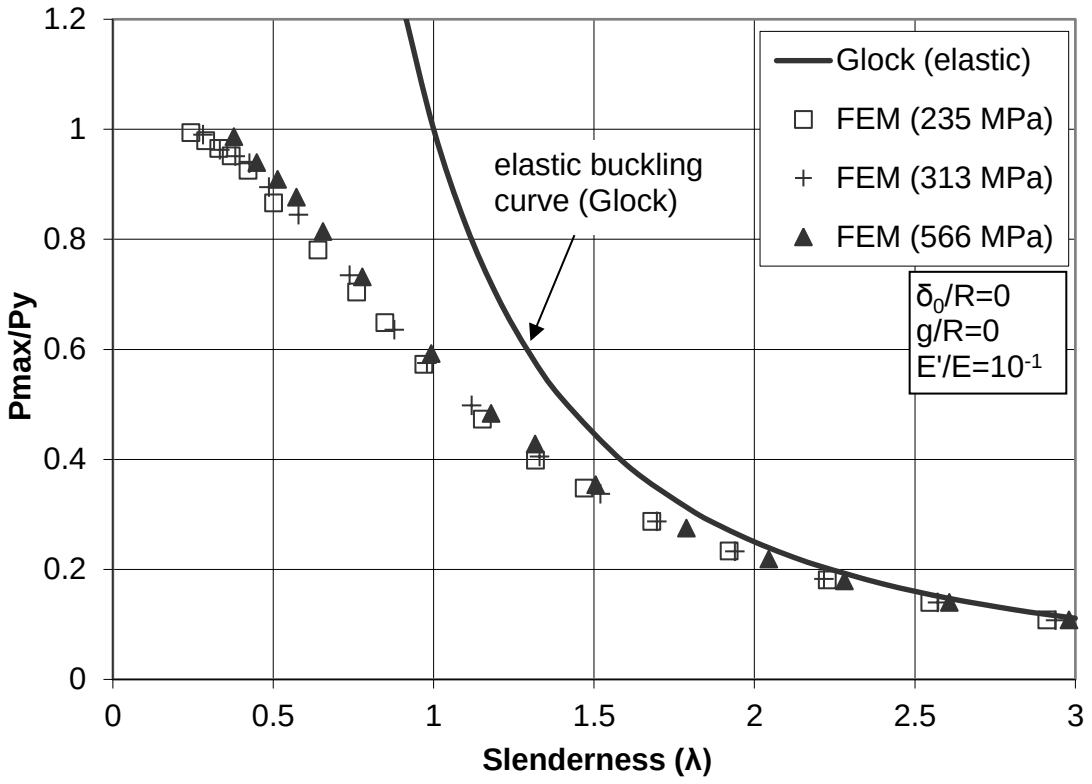

Figure 61: *Variation of maximum pressure $p_{\max}$ of steel cylinders with no imperfections ($g/R=0$, $\delta_0/R=0$), embedded in a rigid confinement medium ($E'/E=10^{-1}$) with respect to the slenderness parameter λ defined in equation (51).*

For slenderness values λ less than λ_p, i.e. for buckling in the inelastic range, the numerical results fall well below equation (52). In particular, the value of $p_{\max}$ approaches

the plastic pressure p_y for rather small values of λ. The numerical results of Figure 61 indicate that a value of λ equal to 0.25 is representative of the cylinder behavior. This is a characteristic slenderness value denoted as λ_0, and referred to as "squash limit relative slenderness".

Based on the above results, it is possible to develop a buckling curve that expresses the maximum pressure $p_{\max}$ in terms of the slenderness value λ of the cylinder. This curve should consider the general case of imperfect cylinders, so that it is used for design purposes. More specifically, taking into account the definition of the imperfection reduction factor α in equation (35), one can write:

$$\frac{p_{\max}}{p_y} = \frac{\alpha}{\lambda^2}, \tag{53}$$

which is valid for the elastic buckling range, i.e. for $\lambda \geq \lambda_p = 2.2$. The value of the imperfection reduction factor α can be computed from equation (38). For values of λ less than the plastic limit slenderness ($\lambda_p = 2.2$), buckling is associated with material behavior in the inelastic range. In such a case, the maximum pressure values $p_{\max}$ deviate from the elastic solution (52). In particular, for very small values of λ, the value of $p_{\max}$ approaches the plastic pressure p_y.

In the absence of a closed-form analytical expression for the buckling pressure in the inelastic regime, similar to elastic buckling equation (12) for elastic buckling, the following expression, introduced in [32],[33], is adopted:

$$\frac{p_{\max}}{p_y} = 1 - \beta\left(\frac{\lambda - \lambda_0}{\lambda_p - \lambda_0}\right)^{\eta}, \tag{54}$$

where β is constant, and η depends on imperfection parameter Δ [equation (37)]. Equation (54) is valid for intermediate values of cylinder slenderness $\lambda_0 \leq \lambda \leq \lambda_p$. Finally, for slenderness values less than λ_0, the cylinder collapses due to the development of excessive plastic deformation, so that neglecting strain hardening, one can write:

$$\frac{p_{\max}}{p_y} = 1. \tag{55}$$

It is important to note that, the value of β in equation (54) is determined equating expressions (53) and (54) for $\lambda = \lambda_p$, and one readily obtains:

$$\beta = 1 - \frac{\alpha}{\lambda_p^2}. \tag{56}$$

Furthermore, the numerical results indicate a dependence of η on the initial imperfection, which can be expressed as follows:

$$\eta = 0.6 - 3\Delta, \quad \eta \geq 0.3, \tag{57}$$

where Δ is the imperfection parameter and is given by equation (37).

Figures 62 show the predictions of the above design methodology for perfect and imperfect $(\delta_0/R = 0.012)$ steel cylinders against the numerical finite element results for three values of yield stress σ_y ($235\,MPa$, $313\,MPa$ and $566\,MPa$ respectively). The comparisons indicate that the proposed methodology offers an efficient approach for predicting the ultimate pressure of confined cylinders in both the elastic and the inelastic range.

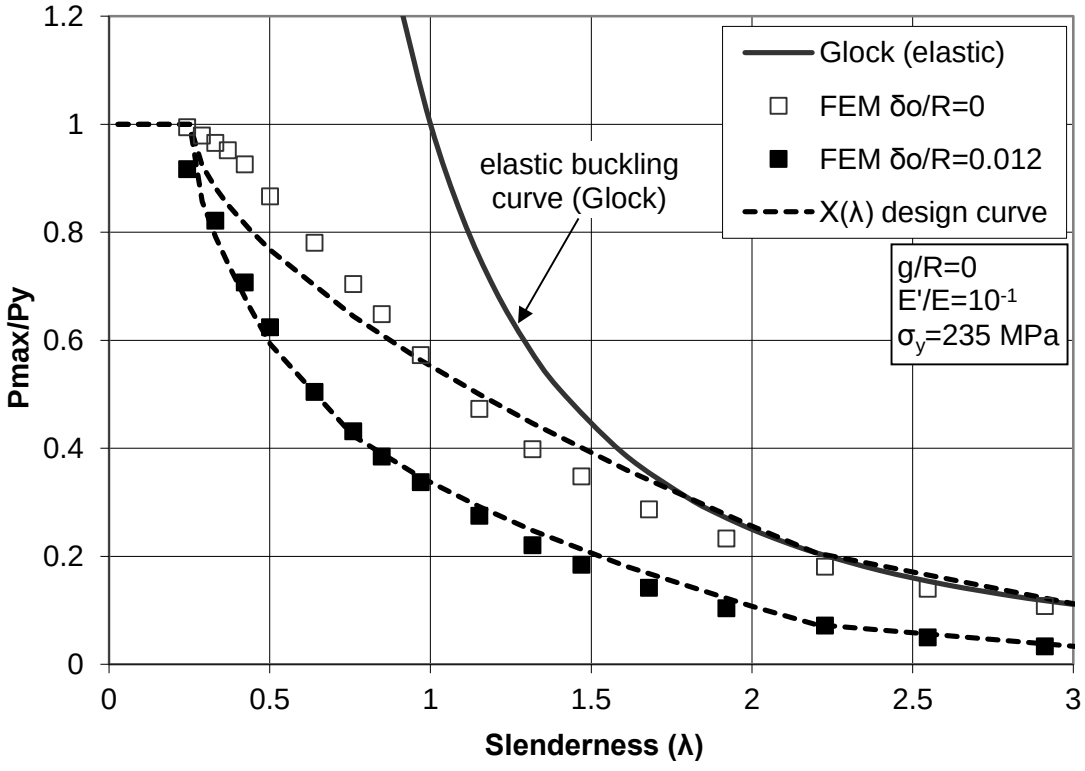

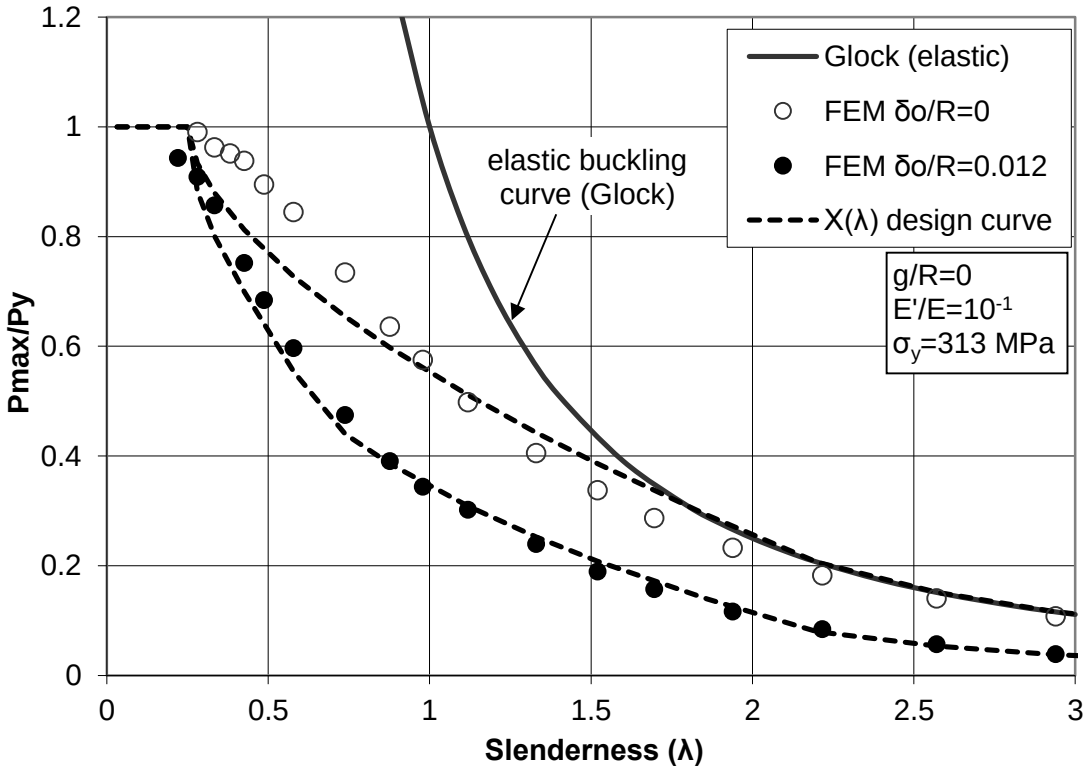

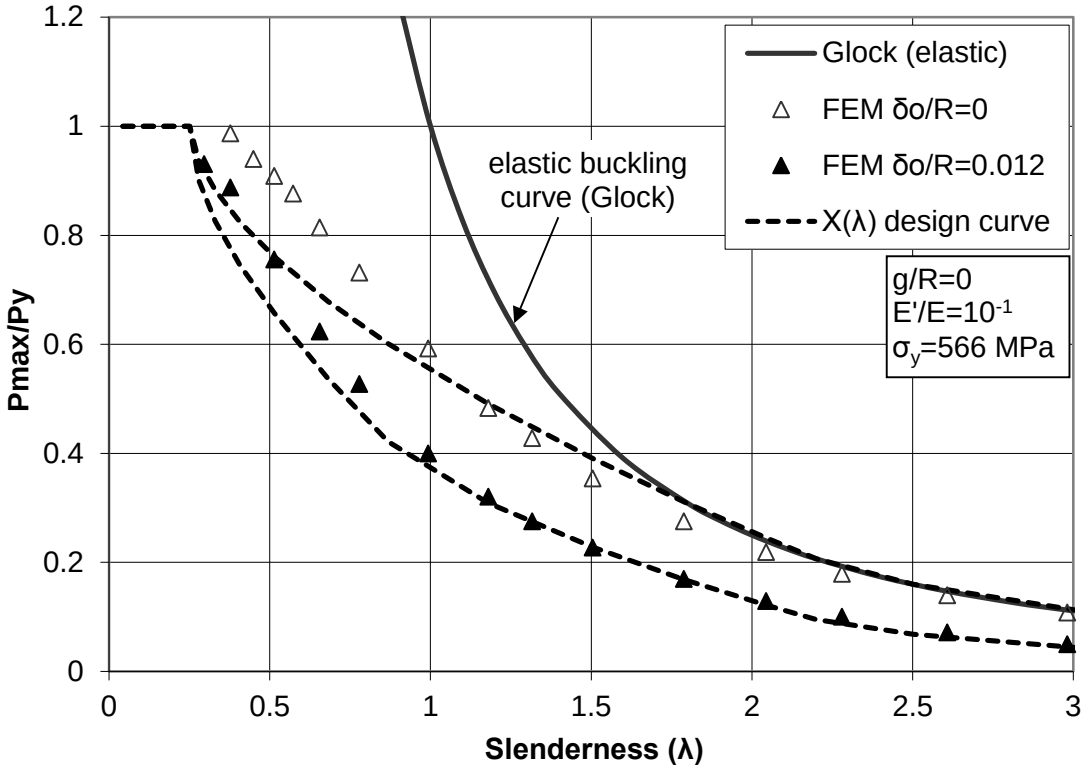

Figures 62*: Variation of maximum pressure* p_{max} *of steel cylinders embedded in a rigid confinement medium with respect to the slenderness parameter* λ *defined in equation (51); finite element results and predictions of equations (53), (54), (55).*

Summarizing the above proposed methodology for the prediction of the buckling pressure $p_{\max}$ of confined steel cylinders in a rigid cavity $\left(E'/E=10^{-1}\right)$, the following equations with the corresponding applicability ranges are concluded:

$$\frac{p_{\max}}{p_y}=1, \qquad \text{for } \lambda\le\lambda_0=0.25. \tag{58}$$

$$\frac{p_{\max}}{p_y}=1-\beta\left(\frac{\lambda-\lambda_0}{\lambda_p-\lambda_0}\right)^{\eta}, \qquad \text{for } \lambda_0\le\lambda\le\lambda_p. \tag{59}$$

$$\frac{p_{\max}}{p_y}=\frac{\alpha}{\lambda^2}, \qquad \text{for } \lambda\ge\lambda_p=2.2. \tag{60}$$

The methodology is fully compatible with the general methodology for shell buckling design [32],[33], and could be used for design purposes.

2.5.2 Deformable confinement

It is also possible to incorporate the effect of E'/E in the present design methodology proposed above, introducing an appropriate reduction factor f, expressing the ratio of $p_{\max}$ in a deformable medium over $p_{\max,\infty}$:

$$f=\frac{p_{\max}}{p_{\max,\infty}}, \tag{61}$$

where $p_{\max,\infty}$ is the ultimate pressure of the cylinder in a rigid confinement $\left(E'\to\infty\right)$. Based on the corresponding numerical results for deformable confinement presented in the subsection 2.4.2, the reduction factor f can be written as follows:

$$f(x)=\begin{cases}-0.05x^2+0.1x+0.95 & \text{if } 1\le x\le 5\\ 1 & \text{if } x\le 1\end{cases}, \tag{62}$$

where x is the modulus ratio parameter,

$$x=-\log\left(\frac{E'}{E}\right), \tag{63}$$

which can be used for an efficient description of the effects of medium deformability on the ultimate pressure.

The comparison between numerical results and the analytical predictions is shown in Figure 63 and demonstrate that equation (62) can be used for an efficient description of the effects of medium deformability on the ultimate pressure.

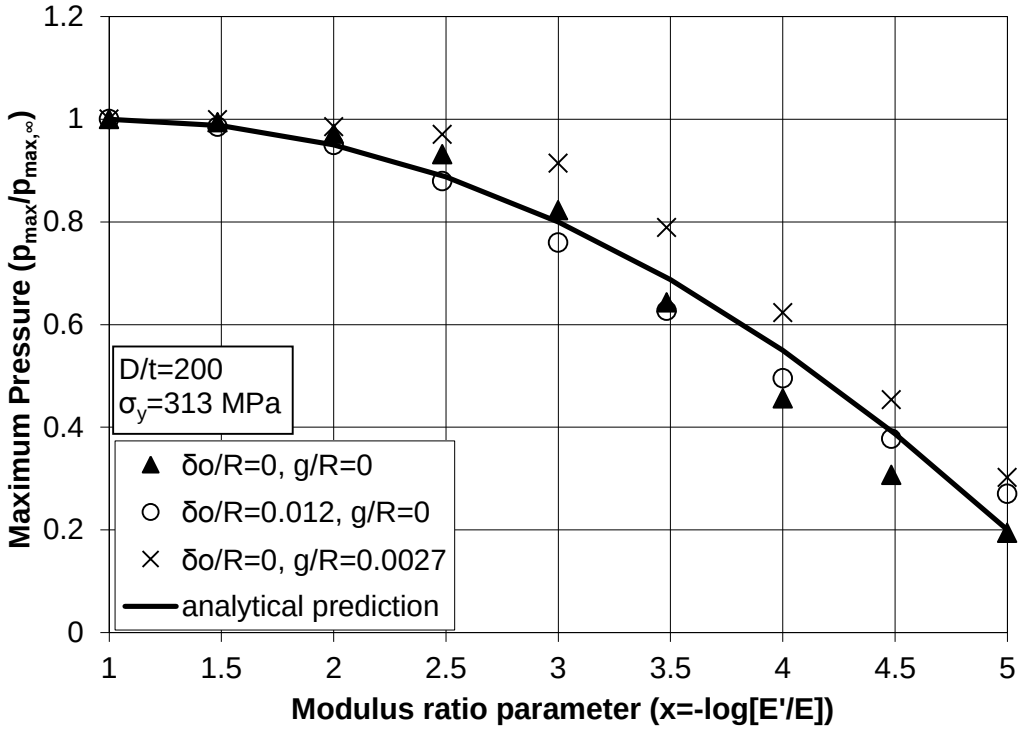

Figure 63*: Comparison between numerical results and analytical prediction from equation (62) for the maximum pressure with respect to the* E'/E *value.*

The design methodology developed in the present section is summarized in the following steps:

- Step 1: Calculate p_y and p_{GL} from equations (17) and (12) respectively, as well as the slenderness parameter of the cylinder λ from equation (51).
- Step 2: Compute the elastic imperfection sensitivity parameter α from equation (38). Subsequently, compute coefficient β from equation (56), and exponent η from equation (57).
- Step 3: Depending on the value of λ, calculate the ultimate pressure capacity $p_{\max}$ from equations (53), (54) or (55). This is the ultimate pressure for rigid confinement.
- Step 4: In the case of a deformable medium, multiply the value of $p_{\max}$ with the value of f from equation (62).

The above proposed methodology is compatible with the design provisions for shell buckling in [32],[33]. Furthermore, a relevant chapter for the design of confined steel cylinders, within the framework of the European Design Recommendations [33], is proposed in Appendix A.

2.5.3 Montel's equation

As an alternative to the design methodology proposed above, equation (16) proposed by Montel [22] can be used to estimate the buckling pressure of imperfect steel cylinders under external pressure confined within a rigid (non-deformable) cavity. The Montel's simplified equation and the corresponding applicability ranges were briefly presented in the literature review of the present chapter (subsection 2.1.1). However, for convenience, the simplified formula is reminded below:

$$p_M = \frac{14.1\,\sigma_y}{\left(D/t\right)^{1.5}\left[1+1.2\left(\delta_0+2g\right)/t\right]}. \tag{64}$$

The predictions of Montel's equation are compared with the present finite element results in Figures 64. The comparison shows that, despite its simplicity, the empirical formula (64) can provide reliable, yet somewhat conservative, estimates of the maximum pressure sustained by a cylinder encased in a stiff boundary, within a good level of accuracy, even beyond the applicability ranges specified in the publication of Montel [22]. Therefore, the formula can be used for the design of buried pipelines encased in concrete or other cylinders confined within a stiff medium.

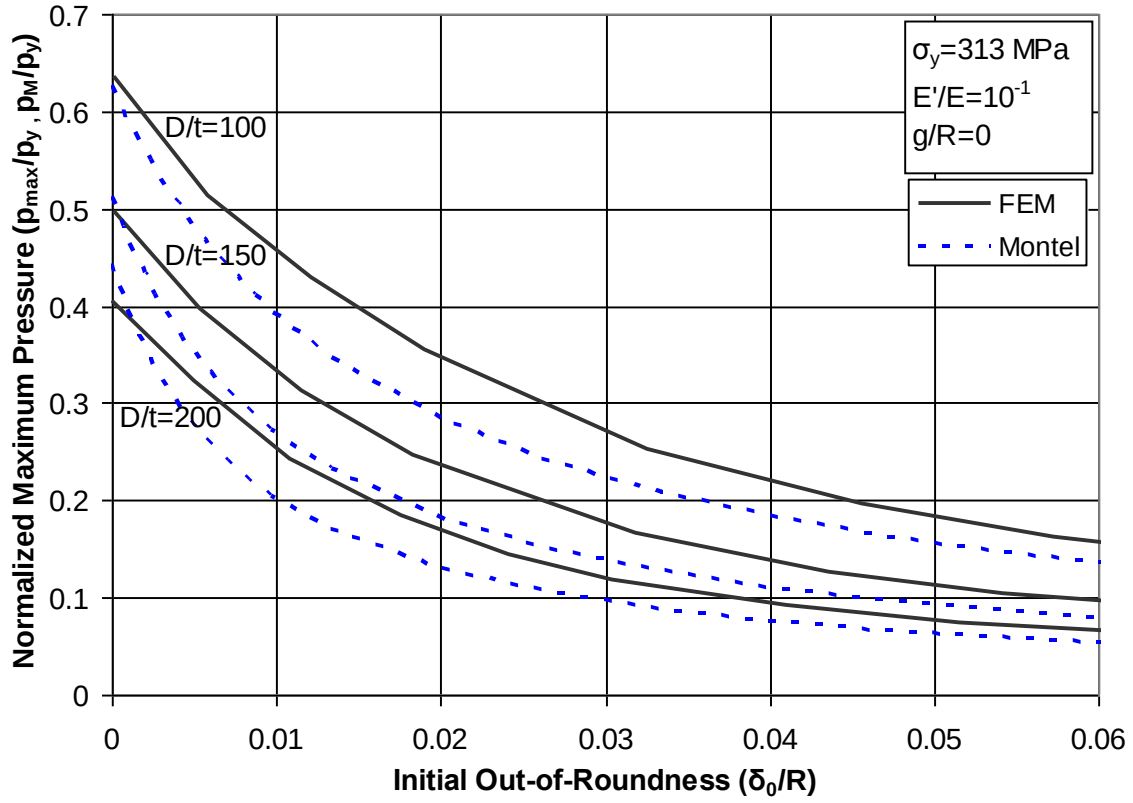

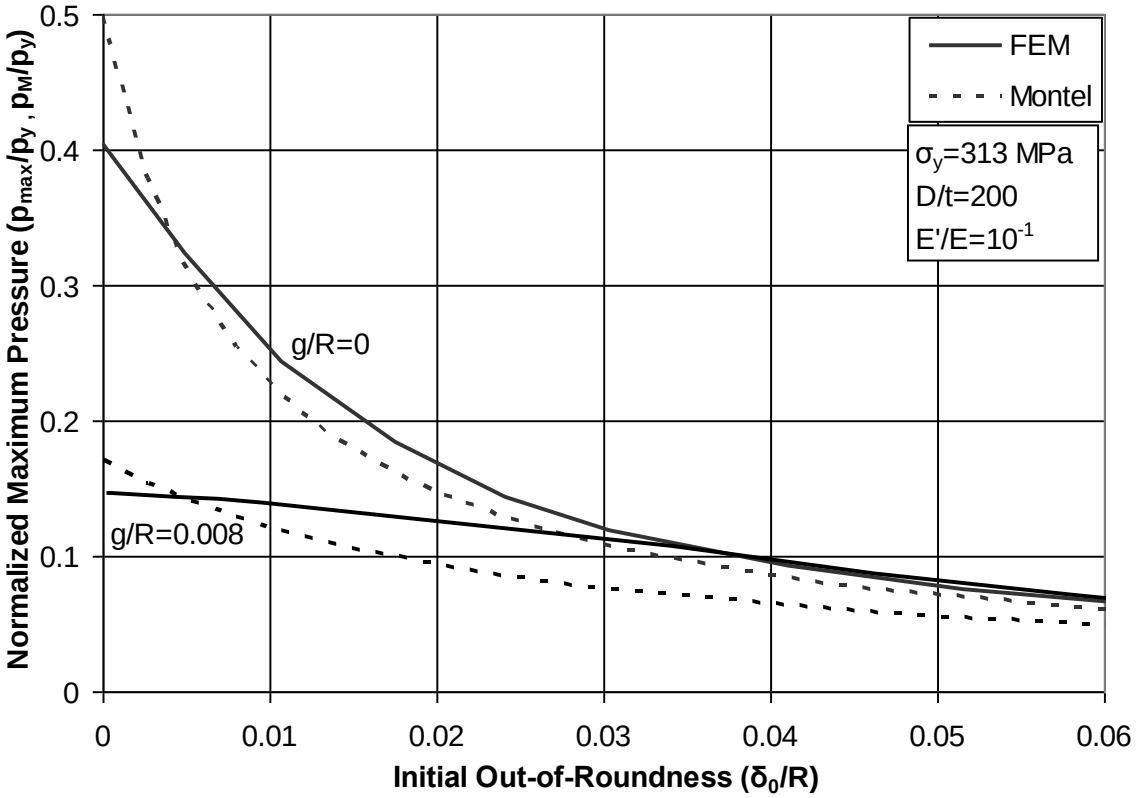

***Figures 64**: Comparison between numerical results and analytical predictions from Montel's equation (16) of steel cylinders embedded in a rigid confinement medium with respect to the out-of-roundness imperfection (a) for different values of D/t ratio and (b) for different values of gap imperfection amplitude* g/R.

2.5.4 Comparison with experimental data

Montel [22] documents a series of tests on small- and large-scale specimens of steel pipes confined in concrete [24]. Equation (64) was developed by evaluating these test results and attempting to fit the most significant parameters governing the problem into a single equation. Most tests were carried out with steel grades with σ_y equal to $350\,MPa$. Tests with these steel qualities were conducted for a range of D/t ratios corresponding to the validity range provided by Montel $\left(60 \le D/t \le 340\right)$. In this range, equation (64) yields quite accurate results for the critical buckling pressure. However, fewer tests were conducted with higher-strength steel qualities and all of these had D/t ratio of about 140. The limitation of the computational value of yield strength that can be used in equation (64) was derived from these tests.

In the present study, four of those tests are compared with the numerical results and the proposed design methodology. The main geometric and material properties for each test specimen are reported in Table 3, whereas the values of critical pressure are summarized and compared in Table 4. Test #1 and Test #2 obtained from two identical small-scale specimens with D/t ratio equal to 66.7, yield strength σ_y equal to $304\,MPa$, initial out-of roundness $\delta_0/R = 0.009$ and initial gap $g/R = 0.0002$. The corresponding pressure displacement curve obtained numerically is compared in Figure 65 with the experimental results. Test #3 has $D/t = 133.33$, yield strength $\sigma_y = 451\,MPa$ and initial out-of roundness $\delta_0/R = 0.005$, while Test #4 has $D/t = 142.8$, $\sigma_y = 746\,MPa$, and $\delta_0/R = 0.007$. Since no initial gap between pipe and medium was measured for these tests, a typical value of g/R equal to 0.00067 was chosen for these two tests. For the test (Test #4) with steel yield strength of $746\,MPa$, the value of σ_y in equation (64) was assumed equal to $500\,MPa$ as proposed by Montel, because it exceeds the applicability limit of the equation. The pressure-displacement equilibrium paths obtained numerically for the Test #3 and Test #4 are depicted in Figure 66 and Figure 67 respectively and compared with the experimental critical pressure value. In general, it is shown a good comparison between the experimental and numerical results.

	Test #1	Test #2	Test #3	Test #4
D/t ratio	66.7	66.7	133.3	142.8
Out-of-roundness (δ_0/R)	0.009	0.009	0.005	0.007
Initial gap (g/R)	0.0002	0.0002	0.00067	0.00067
Yield strength (σ_y) [*MPa*]	304	304	451	746

Table 3: *Geometric and material characteristics of test specimens.*

	Maximum Pressure			
	Test #1	Test #2	Test #3	Test #4
Experimental	6.1 MPa	6.7 MPa	2.9 MPa	2.6 MPa
Numerical (FEM)	6.14 MPa	6.14 MPa	2.84 MPa	2.88 MPa
Design Methodology	5.47 MPa	5.47 MPa	2.70 MPa	2.57 MPa
Montel Equation (64)	5.74 MPa	5.74 MPa	2.75 MPa	2.42 MPa

Table 4: *Comparison of critical pressure between experimental, numerical and analytical results.*

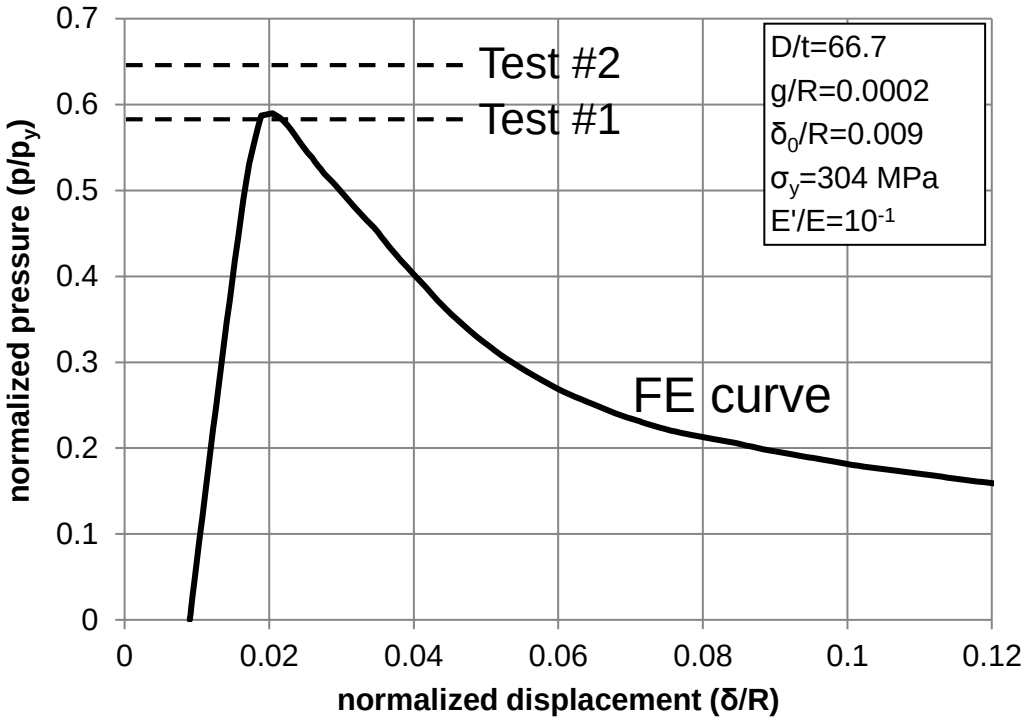

Figure 65*: Pressure-displacement equilibrium path for two identical tests (Test #1 and Test #2) and comparison with experimental results.*

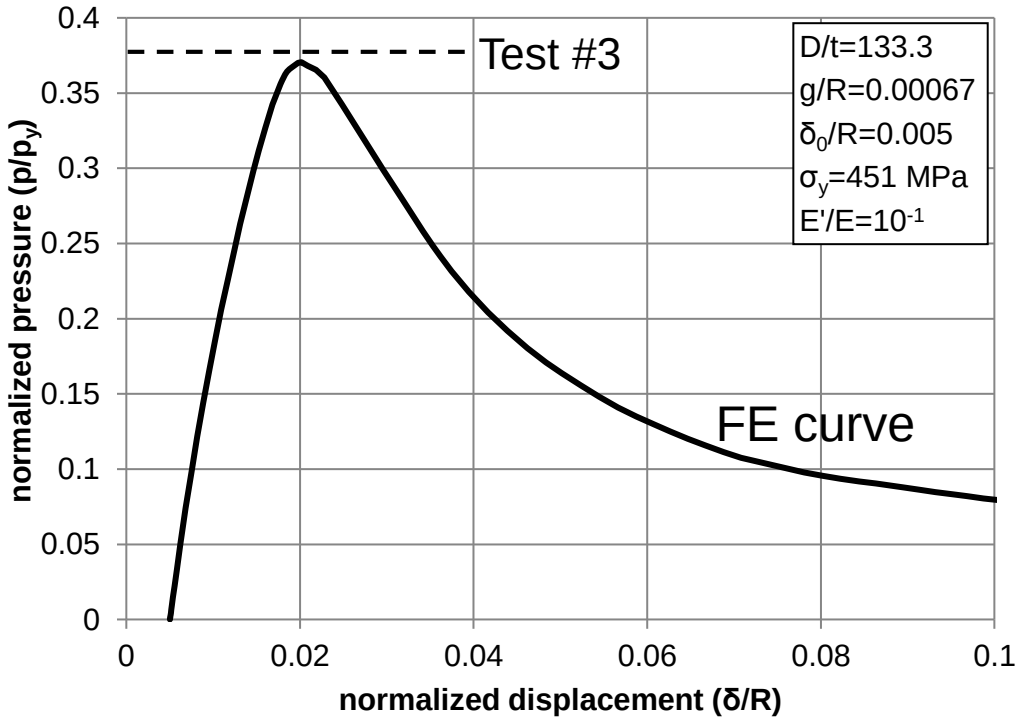

***Figure 66**: Pressure-displacement equilibrium path for the Test #3 and comparison with the experimental critical pressure.*

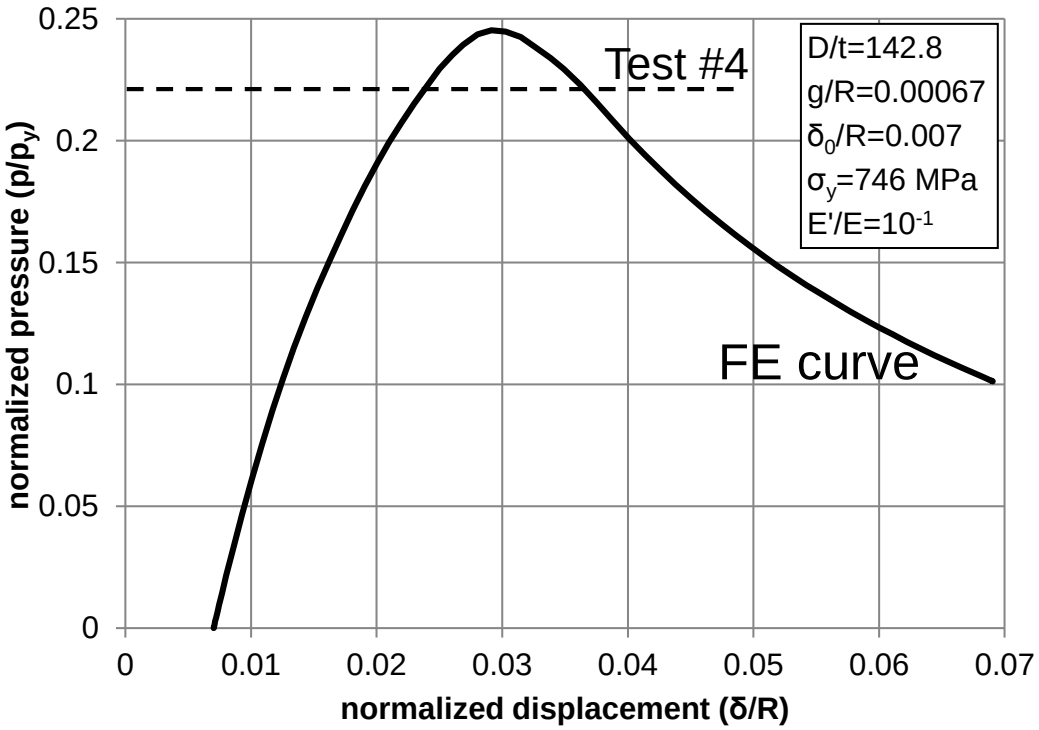

***Figure 67**: Pressure-displacement equilibrium path for the Test #4 and comparison with the experimental critical pressure.*

2.6 Shrink buckling of confined cylinders

2.6.1 Introduction

The single-lobe buckling mode of a thin-walled cylinder or ring in a cavity, shown in Figure 8, can be obtained with two types of loading. The first type of loading is external pressure on the cylinder outer surface, sometimes referred to as "hydrostatic pressure" problem, investigated extensively in the previous sections (particularly in sections 2.3, 2.4 and 2.5). Alternatively, this buckling mode may be obtained under thermal loading, where the cavity prevents the extension of the encased cylinder. Similar to thermal loading, shrink buckling may also occur when the outer cavity contracts (shrinks), moving inwards and applying external pressure to the encased cylinder, forcing it to buckle. In several practical applications, sleeving the inside of cylinders can lead to shrink buckling as well. In all those cases, the resultant buckling is often referred to as "shrink buckling", as opposed to "hydrostatic buckling" presented in the previous sections.

Early works on this subject have been conducted by [7] and [11], pin-pointing the importance of initial imperfections on the maximum compression. Notable analytical contributions on the problem of "shrink buckling" have been reported in [39]-[42], whereas Sun et al. in [43] presented a thorough experimental investigation of the problem, using a simple set-up of compressed hemi-circular very thin-walled rings ($D/t \geq 400$) within a rigid cavity, focusing on the effects of initial imperfections.

The shrink buckling problem has several similarities but it is not the same as the hydrostatic buckling problem. The main difference is that in shrink buckling under thermal loading or sleeving, the buckled part of the cylinder is laterally free, whereas in hydrostatic buckling, pressure load is always present, applied on the buckled portion of the cylinder in the post-buckling stage. To understand the consequences of this difference on the mechanical behavior and strength of the loaded cylinder, a series of numerical simulations are conducted in the course of the present study, simulating the experimental set-up of Sun et al. [43], shown in Figure 68. It consists of a thin-walled cylindrical specimen encased within a rigid hemi-circular cavity, compressed symmetrically at points B and B'. A small imperfection is imposed in the central point A, assuming an initial stress-free displacement pattern, in the form of an inward localized displacement.

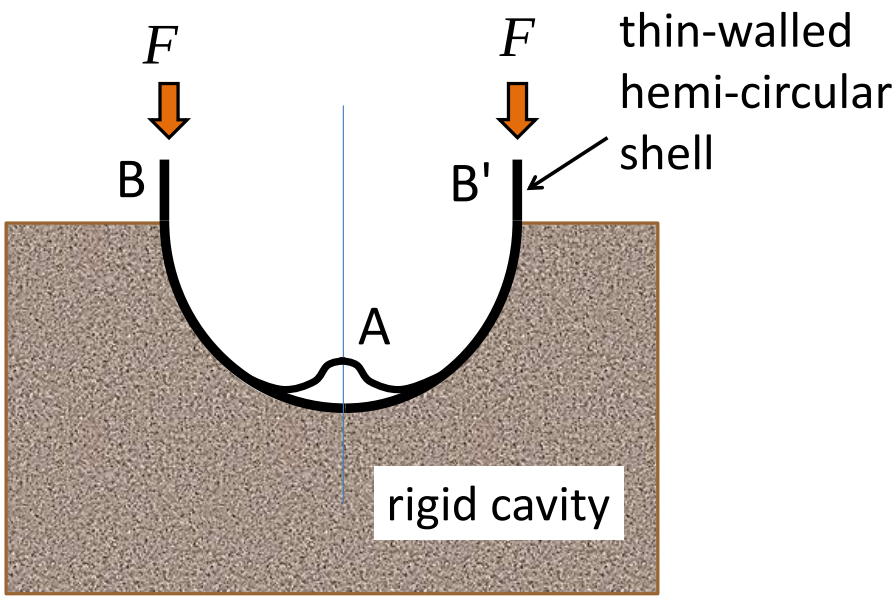

***Figure 68**: Schematic representation of test set-up [43].*

2.6.2 Finite element modeling

The numerical model employed for simulating this experiment is shown in Figure 69 and it is very similar to the one described in section 2.2; shell elements and solid elements are used to model the cylinder and the rigid cavity respectively. The material of the cavity is considered isotropic elastic with Young's modulus $E' = 21{,}000$ MPa and Poisson's ratio $\nu = 0.30$, corresponding to rigid confinement conditions. Numerical results are obtained for the case of an elastic and a steel cylinder. Both cylinders have a D/t ratio equal to 200, whereas the material of the steel cylinder has a yield stress equal to 313 MPa, similar to the material used extensively in section 2.4.

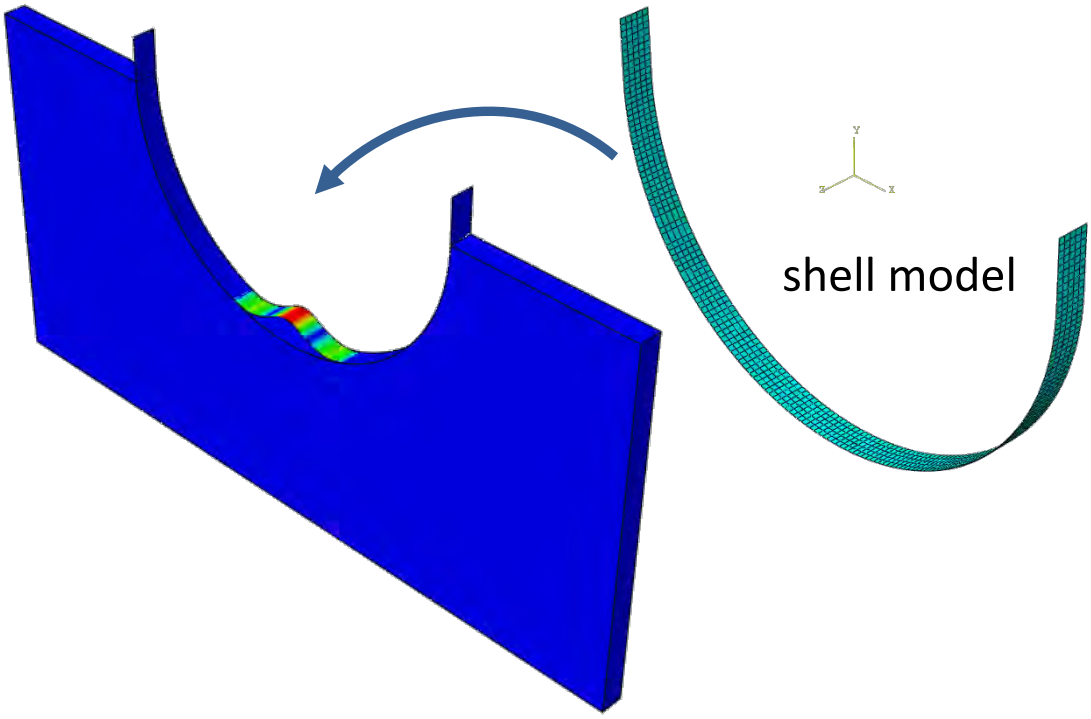

Figure 69: *Finite element model of cylinder-medium system.*

2.6.3 Numerical results

The numerical results are presented in Figure 70, showing the maximum (buckling) acting stress at points B and B' in terms of the size of initial imperfection. Both curves are decreasing functions of the imperfection amplitude. The acting stress σ is equal to the force F applied at points B and B' divided by the cross-sectional area of the ring model. For value of initial imperfection approaching zero, the curve for the elastic cylinder goes asymptotically to infinity. This implies the absence of buckling for a geometrically perfect system, a conclusion also reported in early analytical works [41], as well as in the tests of Sun et al. [43]. The steel cylinder has a similar behavior, but the buckling stress is significantly reduced with respect to the corresponding stress of the elastic cylinder. In addition, for small values of imperfection amplitude ($\delta_0/t \le 0.4$), the steel ring fails due to yielding at a stress level equal to the yield stress of the material σ_y^* under plane strain conditions.

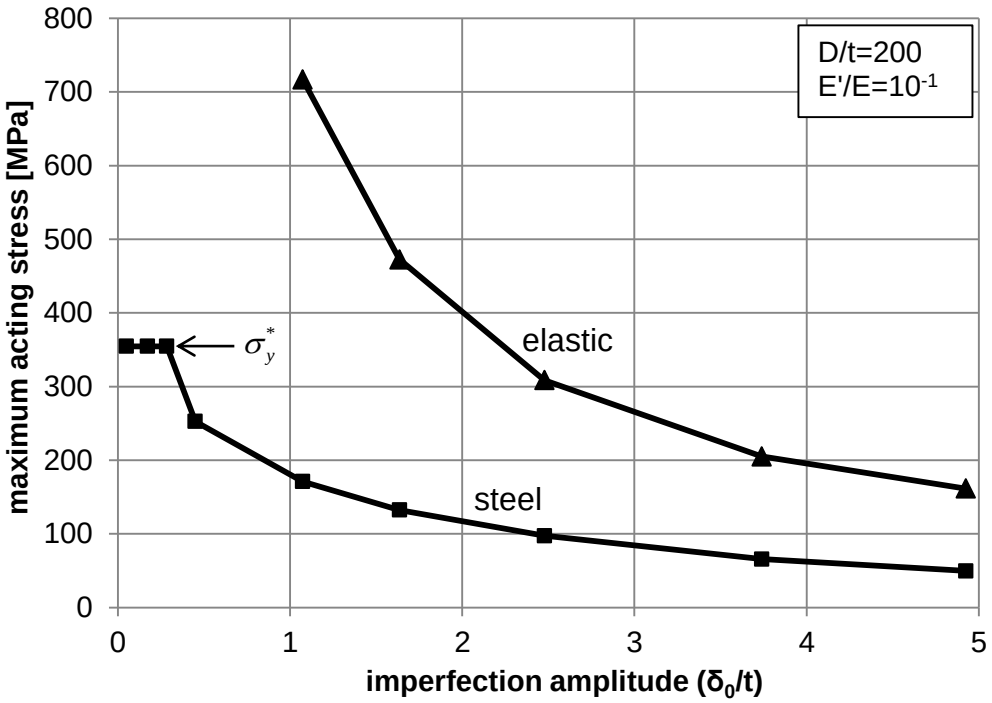

Figure 70: *Maximum acting stress for rigidly confined elastic and steel cylinders.*

The absence of buckling in an imperfection-free cylinder constitutes the main difference between the shrink buckling and the hydrostatic buckling problem. As noted, this is attributed to the fact that hydrostatic pressure is always applied on the post-buckled portion of the cylinder, whereas external loading is released from the buckled portion in the case of shrink buckling.

2.7 Conclusions

The mechanical behavior of thin-walled elastic and steel cylinders, surrounded by a deformable elastic medium, has been examined in terms of their structural stability under uniform external pressure. The study is motivated by the structural response of buried water or hydrocarbon pipelines surrounded by saturated soil medium or concrete encasement. The examination is computational using a nonlinear quasi two-dimensional model through the employment of the general-purpose finite element program ABAQUS.

Numerical results for the ultimate pressure of cylinders of elastic material are found to be in very close agreement with available closed-form analytical predictions [12],[14] and are also supported by available experimental data [15],[16],[17]. Furthermore, the numerical results show a significant sensitivity of the ultimate pressure in terms of initial imperfections, in the form of both initial out-of-roundness of the cylinder cross-section and the presence of initial gap between the cylinder and the surrounding medium. It is also demonstrated that reduction of the medium modulus results in a substantial reduction of the pressure capacity of the cylinder. The pressure-deflection equilibrium paths indicate a rapid drop of pressure capacity after reaching the maximum pressure level. A three-hinge plastic collapse mechanism with one stationary and two moving plastic hinges is developed that results in a closed-form expression and illustrates the post-buckling response of the cylinder in an approximate yet very representative manner. The maximum plastic deformation within the steel cylinder as well as the maximum contact pressure between the cylinder and the medium occurs at the vicinity of the moving hinges. Furthermore, the vertical preloading of the medium results in a pronounced increase of the ultimate pressure sustained by the cylinder.

Based on the numerical results, and to predict the ultimate pressure in the inelastic range in a simple and efficient manner, a systematic methodology is developed, which is based on a “shell slenderness” parameter. The methodology is compatible with the general provisions of recent European shell stability design rules [32] and recommendations [33] for shell buckling, and could be used for design purposes. Furthermore, the simplified formula proposed in [22] is found to be quite close to and on the conservative side of the present numerical results and could also be used for the prediction of buckling pressure of buried pipelines and other rigidly encased steel cylinders. Moreover, experimental results [22],[24] compare very well with the numerical results, as well as with the predictions of the proposed design methodology.

The corresponding problem of "shrink buckling" has also been examined, through a rigorous simulation of experiments reported in [43], and the main differences with the hydrostatic buckling problem have been pin-pointed, emphasizing the significantly different response of the two problems with respect to the presence of initial imperfections.

Finally, it should be noticed that according to several design recommendations, the external pressure capacity of steel pipelines encased in a rigid cavity (e.g. concrete encasement), was taken equal to the nominal pressure that causes yielding of the cylinder, assuming that the rigid confinement prevents instability in the elastic range [1],[35]. The results of the present study demonstrated that this argument may be valid only for the case of shrink buckling. On the other hand, consideration of an ultimate pressure equal to p_y, calculated by equation (17), leads to unsafe design of hydrostatically-loaded cylinders. For the range of D/t ratio of interest, hydrostatically-loaded steel cylinders encased in a rigid cavity are able to sustain only a portion of the yield pressure p_y, even in the absence of initial imperfections.

2.8 References

[1] Watkins, R.K. (2004). "Buried Pipe Encased in Concrete", *International Conference on Pipeline Engineering & Construction,* ASCE, San Diego, CA.

[2] Omara, A.M., Guice, L.K., Straughan, W.T., Akl, F.A. (1997). "Buckling Models of Thin Circular Pipes Encased in Rigid Cavity", *Journal of Engineering Mechanics,* ASCE, Vol. 123, No. 12, pp. 1294-1301.

[3] Ullamn, F. (1964). "External Water Pressure Designs for Steel-Lined Pressure Shafts", *Water Power*, Vol. 16, pp. 298-305.

[4] Ahrens, T. (1970). "An In-Depth Analysis of Well Casings and Grouting: Basic Considerations of Well Design – II", *Water Well Journal*, pp. 49-51.

[5] Omara, A.M., Guice, L.K., Straughan, W.T., Akl, F. (2000). "Instability of Thin Pipes Encased in Oval Rigid Cavity", *Journal of Engineering Mechanics*, ASCE, Vol. 126, No. 4, pp. 381-388.

[6] Hsu, P.T., Elkon, J., Pian, T.H.H. (1964). "Note on the Instability of Circular Rings Confined to a Rigid Boundary", *Journal of Applied Mechanics,* ASME, Vol. 31, No. 3, pp. 559-562.

[7] Chicurel, R. (1968). "Shrink Buckling of Thin Circular Rings", *Journal of Applied Mechanics,* ASME, Vol. 35, No. 3, pp. 608-610.

[8] Bucciarelli Jr., L.L., Pian, T.H.H. (1967). "Effect of Initial Imperfections on the Instability of a Ring Confined in an Imperfect Rigid Boundary", *Journal of Applied Mechanics,* ASME, Vol. 34, No. 4, pp. 979-984.

[9] El-Bayoumy, L. (1972). "Buckling of a Circular Elastic Ring Confined to a Uniformly Contracting Circular Boundary", *Journal of Applied Mechanics,* ASME,, Vol. 39, No. 3, pp. 758-766.

[10] Soong, T.C., Choi, I. (1985). "Bucking of an Elastic Elliptical Ring Inside a Rigid Boundary", *Journal of Applied Mechanics,* ASME, Vol. 52, No. 3, pp. 523-528.

[11] Bottega, W.J. (1989). "On the Behavior of an Elastic Ring within a Contracting Cavity", *International Journal of Mechanical Sciences,* Vol. 31, No. 5, pp. 349-357.

[12] Glock, D. (1977). "Überkritisches Verhalten eines Starr Ummantelten Kreisrohres bei Wasserdrunck von Aussen und Temperaturdehnung" (Post-Critical Behavior of a Rigidly Encased Circular Pipe Subject to External Water Pressure and Thermal Extension), *Der Stahlbau,* Vol. 7, pp. 212-217.

[13] Brush, D.O., Almroth, B.O. (1975). *Buckling of Bars, Plates, and Shells,* McGraw-Hill, New York, NY.

[14] El-Sawy, K., Moore, I.D. (1998). "Stability of Loosely Fitted Liners Used to Rehabilitate Rigid Pipes", *Journal of Structural Engineering,* ASCE, Vol. 124, No. 11, pp. 1350-1357.

[15] Aggarwal, S.C., Cooper, M.J. (1984). "External Pressure Testing of Insituform Lining", *Internal Report,* Coventry (Lanchester) Polytechnic, Coventry, U.K.

[16] Lo, K.H., Chang, B.T.A., Zhang, Q., Wright, W.J. (1993). "Collapse Resistance of Cured-In-Place Pipes", Proceedings of the North American Society for Trenchless Technology, No-Dig '93., San Jose, CA., E2:1-13.

[17] Guice, L.K., Straughan, W.T., Norris, C.R., Bennett, R.D. (1994). "Long-Term Structural Behavior of Pipeline Rehabilitation Systems", Technical Report No. 302, Trenchless Technology Center, Louisiana Tech University, Ruston, La.

[18] Boot, J.C. (1998). "Elastic buckling of cylindrical pipe linings with small imperfections subject to external pressure", *Trenchless Technology Research,* Vol. 12, No. 1-2, pp. 3-15.

[19] Bottega, W.J. (1993). "On the Separation of Concentric Elastic Rings", *International Journal of Mechanical Sciences,* Vol. 31, No. 5, pp. 349-357.

[20] Li, F.S., Kyriakides, S. (1991). "On the Response and Stability of two Concentric, Contracting Rings under External Pressure", *International Journal of Solids and Structures,* Vol. 27, No. 1, pp. 1-14.

[21] Li, F.S., Kyriakides, S. (1990). "On the Propagation Pressure of Buckles in Cylindrical Confined Shells", *Journal of Applied Mechanics,* ASME, Vol. 57, pp. 1091-1094.

[22] Montel, R. (1960). "Formule Semi-Empirique pour la Détermination de la Pression Extérieure Limite d'instabilité des Conduits Métalliques Lisses Noyées Dans du Béton" (A semi-empirical formula for determining the limiting external pressure for the collapse of smooth metal pipes embedded in concrete), *La Houille Blanche,* No. 5, pp. 560-568.

[23] Timoshenko, S., Gere, J.M. (1961). *Theory of Elastic Stability,* 2nd Ed., McGraw Hill, New York, NY.

[24] Borot, M. (1957). "Essais des Conduits Métalliques Noyées Dans du Béton", *La Houille Blanche,* No. 6, pp. 881-887.

[25] Amstutz, E. (1969). "Das Einbeulen von Schacht – und Stollenpanzerungen", *Schweizerische Bauzeitung,* Vol. 87, pp. 541-549. (U.S. Dept. of the Interior, Translation No. 826).

[26] Jacobsen, S. (1974). "Buckling of Circular Rings and Cylindrical Tubes under External Pressure", *Water Power,* Vol. 26, pp. 400-407.

[27] Yamamoto, Y., Matsubara, N. (1982). "Buckling of a Cylindrical Shell Under External Pressure Restrained by an Outer Rigid Wall", *Proceedings, Symposium on Collapse and Buckling, Structures; Theory and Practice,* Cambridge University Press, London, U.K., pp. 493-504.

[28] Kyriakides, S., Youn, S.K. (1984). "On the Collapse of Circular Confined Rings under External Pressure", *International Journal of Solids and Structures,* Vol. 20, No. 7, pp. 699-713.

[29] Kyriakides, S. (1986). "Propagating Buckles in Long Confined Cylindrical Shells", *International Journal of Solids and Structures,* Vol. 22, No. 12, pp. 1579-1597.

[30] El-Sawy, K. (2001). "Inelastic Stability of Tightly Fitted Cylindrical Liners Subjected to External Uniform Pressure", *Thin-Walled Structures,* Vol. 39, No. 9, pp. 731-744.

[31] El-Sawy, K. (2002). "Inelastic Stability of Loosely Fitted Cylindrical Liners", *Journal of Structural Engineering,* ASCE, Vol. 128, No. 7, pp. 934-941.

[32] Comité Européen de Normalization (2007). Strength and Stability of Shell Structures, EN 1993-1-6, Eurocode 3, part 1-6, Brussels, Belgium.

[33] European Convention for Constructional Steelwork (2008). *Buckling of Steel Shells, European Design Recommendations*, 5th Edition, ECCS Publication No. 125, J.M. Rotter and H. Schmidt Eds., Brussels, Belgium.

[34] Hibbit, H.D., Karlsson, B.I., Sorensen, P. (2007). *Theory Manual*, ABAQUS, version 6.7, Providence, RI, USA.

[35] AISI (1996). "Welded Steel Pipe", *Steel Plate Engineering Data*, Vol.3, American Iron and Steel Institute, Washington, D.C.

[36] Koiter, W.T. (1963). *Elastic stability and post-buckling behaviour*, Proceeding of the Symposium in Nonlinear Problems, pp. 257-275, University of Wisconsin Press, Madison.

[37] Budiansky, B. (1965). *Dynamic buckling of elastic structures: criteria and estimates*, Proceedings of the International Conference in Dynamic Stability of Structures, pp. 83-106.

[38] Jeyapalan, J.K., Watkins, R.K. (2004). "Modulus of Soil Reaction (E') Values for Pipeline Design", *Journal of Transportation Engineering*, ASCE, Vol. 130, No. 1, pp. 43-48.

[39] Hsu, P.T., Elkon, J., Pian, T.H.H. (1964). "Note on the Instability of Circular Rings Confined to a Rigid Boundary", *Journal of Applied Mechanics*, ASME, Vol. 31, No. 3, pp. 559-562.

[40] Bucciarelli Jr., L.L., Pian, T.H.H. (1967). "Effect of Initial Imperfections on the Instability of a Ring Confined in an Imperfect Rigid Boundary", *Journal of Applied Mechanics*, ASME, Vol. 34, No. 4, pp. 979-984.

[41] El-Bayoumy, L. (1972). "Buckling of a Circular Elastic Ring Confined to a Uniformly Contracting Circular Boundary", *Journal of Applied Mechanics*, ASME, Vol. 39, No. 3, pp. 758-766.

[42] Soong, T.C., Choi, I. (1985). "Bucking of an Elastic Elliptical Ring Inside a Rigid Boundary", *Journal of Applied Mechanics*, ASME, Vol. 52, pp. 523-528.

[43] Sun, C., Shaw, W.J.D., Vinogradov, A.M. (1995). "Instability of Confined Rings: An experimental Approach", *Experimental Mechanics*, Vol. 35, No. 2, pp. 97-103.

3. Confined cylinders under longitudinal bending

3.1 Introduction

In several engineering applications, cylindrical members subjected to longitudinal bending are confined within a surrounding medium or another shell. Some representative examples of these applications are (a) the bending response of the lined pipe (sometimes referred to as mechanically-clad pipe), where a corrosion-resistant thin-walled liner is fitted inside a carbon–steel outer pipe, (b) the nano-composite tubes, where an inner carbon nanotube is confined in a polymer matrix, and (c) the buried steel pipelines under strike-slip tectonic fault displacements, where permanent ground deformation is applied on the pipeline. In the present chapter the bending response of the lined pipes is extensively investigated.

Safeguarding the structural integrity of oil and gas steel pipelines requires erosion damage protection from oil or gas pollutants, which include hydrogen sulfide, chlorides, and water. One possibility to ensure internal corrosion resistance of hydrocarbon pipelines would be the use of a corrosion-resistant material for the line pipe, such as a stainless steel or a nickel alloy. However, the cost of producing line pipes thick enough to withstand normal transportation pressure as well as structural loads is prohibitive, considering that most of these materials lack the strength of carbon steels. An alternative solution, which makes the best use of corrosion-resistant alloys and carbon steels, is the use of a “lined pipe”, also referred to as “mechanically clad pipe”. This is a double-wall pipe, consisting of a load-bearing high-strength, carbon steel outer pipe, lined with a thin-walled sleeve made from a corrosion-resistant material (Figures 71). In particular, the so-called “mechanically clad or lined pipe” is a promising application of this concept. It is produced by inserting the liner pipe into the external carbon steel pipe, through an appropriate manufacturing process, so that the bond between the two pipes is purely mechanical, in the sense that the outer pipe material and the liner pipe material remain two distinct materials.

The lateral confinement of the liner pipe due to the deformable outer pipe constitutes the main characteristic of the double-wall pipes with respect to single-wall pipes. Single-wall pipes under bending ovalize (Brazier effect) and buckle before reaching a limit moment. On the other hand, in double-wall pipes, the liner is not free to ovalize and, therefore, the mechanical behaviour of the liner requires consideration of its interaction with the outer pipe.

The study presented in this part of dissertation focuses on the mechanical behavior and wrinkling of lined pipes under the combined action of bending loading and external pressure, motivated by the use of such pipes in offshore pipeline applications (oil, gas etc.) with emphasis on their underwater installation process, where a corrosion-resistant thin-walled liner is fitted inside a carbon steel outer pipe. When longitudinal bending curvature is applied, the lined pipe ovalizes and, at a certain stage of deformation, the liner buckles in the form of short-wave wrinkles.

3.1.1 Literature review

Previous research works on single-wall pipes [1],[2],[3] have demonstrated that the installation of offshore pipelines in deep-water constitutes a crucial stage in underwater pipeline design procedure. At that stage, the pipeline is subjected to significant bending deformation in the presence of external pressure so that, significant stresses develop in the pipeline wall, associated with excessive cross-sectional ovalization and possible local buckling, which may result in pipeline collapse, especially if "buckle propagation" is triggered [4],[5]. Over the last two decades, a substantial amount of research has been dedicated to the bending response of pipes, and design tools for the safe design of deepwater pipelines have been developed and incorporated in relevant design specifications [6],[7]. For a detailed presentation of offshore pipeline mechanics, the reader is referred to the recent book by Kyriakides and Corona [8].

The above research works and design specifications refer exclusively to single-wall pipes. In the case of installing underwater lined pipes, the existing design tools could be used to ensure the structural stability of the load-bearing thick-walled outer pipe. However, under the combined loading conditions of bending deformation and external pressure, the thin-walled liner pipe is not free to ovalize and exhibits significant deformation, which may cause wrinkling of its wall, while the outer pipe remains stable. Therefore, the mechanical behaviour of the liner requires consideration of its interaction with the outer pipe. Because of this interaction, existing numerical solutions and analytical predictions for the bending buckling resistance of unconfined thin-walled tubes [9] are inadequate to predict the curvature at which the liner buckles. In order to predict the curvature at which buckling of the thin-walled liner occurs, it is necessary to account for its contact with the confining thick-walled outer pipe and to examine possible liner detachment from the outer pipe which may lead to wrinkling of the liner. A wrinkle on the liner wall may not be acceptable, because it does not allow proper pipeline pigging, it is obstacle to hydrocarbon flow and is

associated with stress raisers at the buckled area, which would lead to fatigue cracking of the liner wall under repeated loading during operational conditions [10].

The present work investigates the mechanical behavior of lined pipes subjected primarily to bending deformation, focusing on the structural stability (wrinkling) of the thin-walled liner. Previous experimental work on this subject has been conducted at Delft University of Technology and has been reported by Focke [11], motivated by the use of lined pipes in offshore applications, installed with the pipe reeling method. In the above series of experiments, lined pipes (Figures 71) were tested under bending over a variable curvature boundary (Figure 72), simulating the mechanical behavior of an offshore pipe during laying on a stinger (Figure 73). The experiments concerned X65 pipes with nominal diameter equal to 12 inches, lined with 3-mm-thick 316L stainless steel pipes. The experimental results aimed at determining the initiation and the size of liner pipe wrinkling, as well as the degree of ovalization occurring during the spooling-on phase of the pipe reeling process.

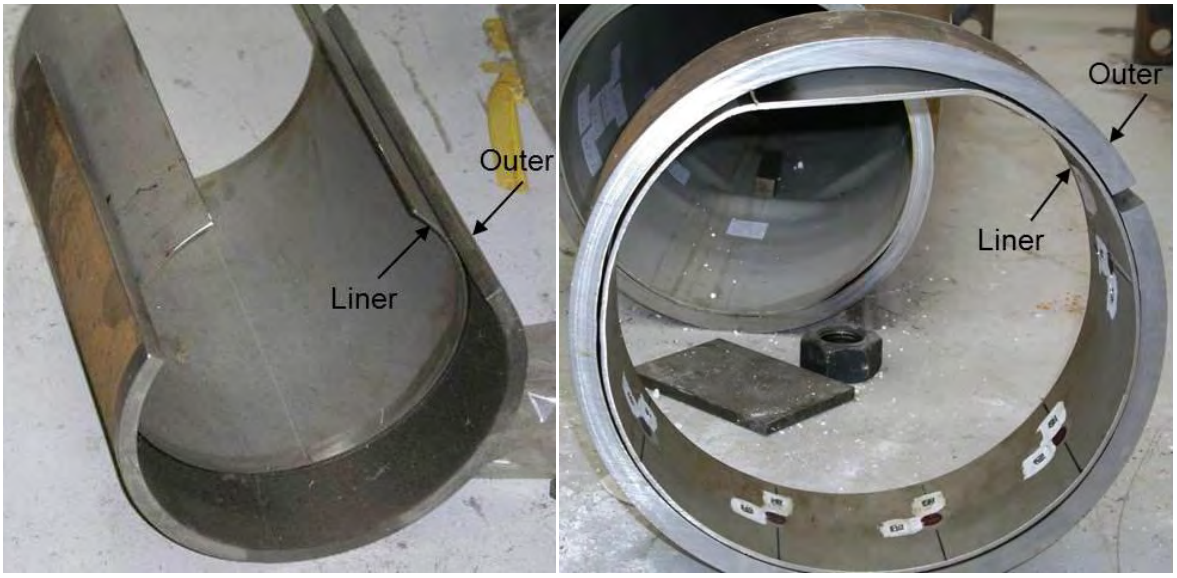

Figures 71*: Typical photos of lined pipes after experimental testing [11].*

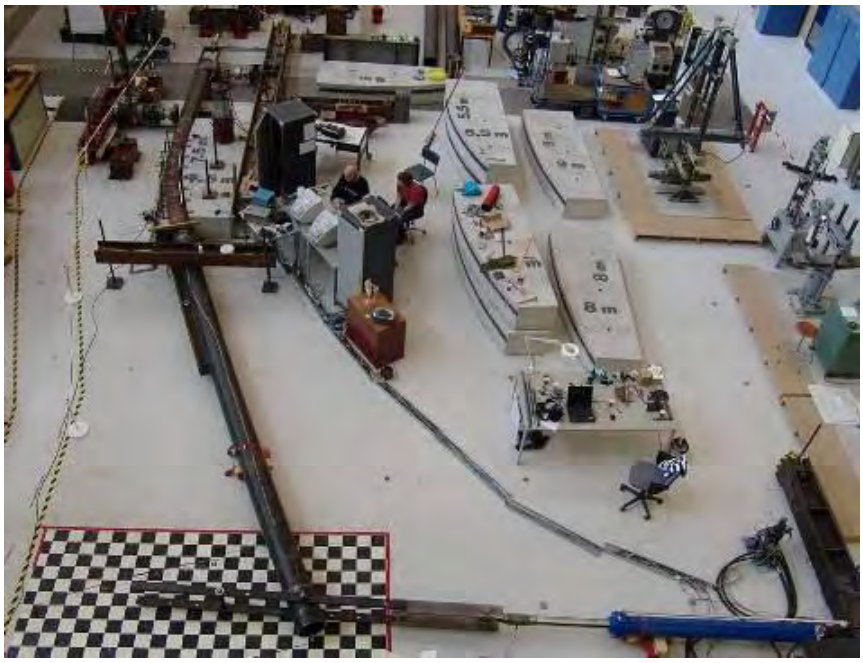

***Figure 72**: Bending rig of experimental testing of lined pipes [11].*

***Figure 73**: Pipe installation by reeling method.*

In the lined pipes tested in [11], the liner was fitted inside the carbon steel outer pipe through a thermo-hydraulic manufacturing process, resulting in a tightly-bonded lined pipe, where the outer pipe "compresses" the liner pipe, introducing a significant hoop compressive stress in the liner, which is often called "residual stress" or "prestressing" and the two pipes are mechanically bonded together. In this process, the outer pipe is heated first. Subsequently, the liner pipe is inserted inside the outer pipe and pressurized internally

so that it is expands and it is in good contact with the outer pipe. Finally, the outer pipe is cooled and the internal pressure of the liner pipe is removed, so that the two pipes are mechanically bonded together. The manufacturing process of those lined pipes, referred to as Tight-Fit Pipes (TFP), is described in detail in [12], while the numerical simulation of this procedure is discussed in Appendix B.

Experimental tests and numerical investigations on liner wrinkling behavior of lined pipes under bending loading have been also conducted at TU Delft and have been reported by Hilberink [13]. In this series of experiments, four-point bending tests of 12 inch lined pipes were conducted (Figure 74) and buckling shapes of the liner pipe were detected and measured (Figure 75). The influence of friction and mechanical bonding (prestressing) on the behavior of the lined pipe during bending is also reported, and the numerical results are compared with experimental data.

***Figure 74**: Four-point bending test of lined pipes [13].*

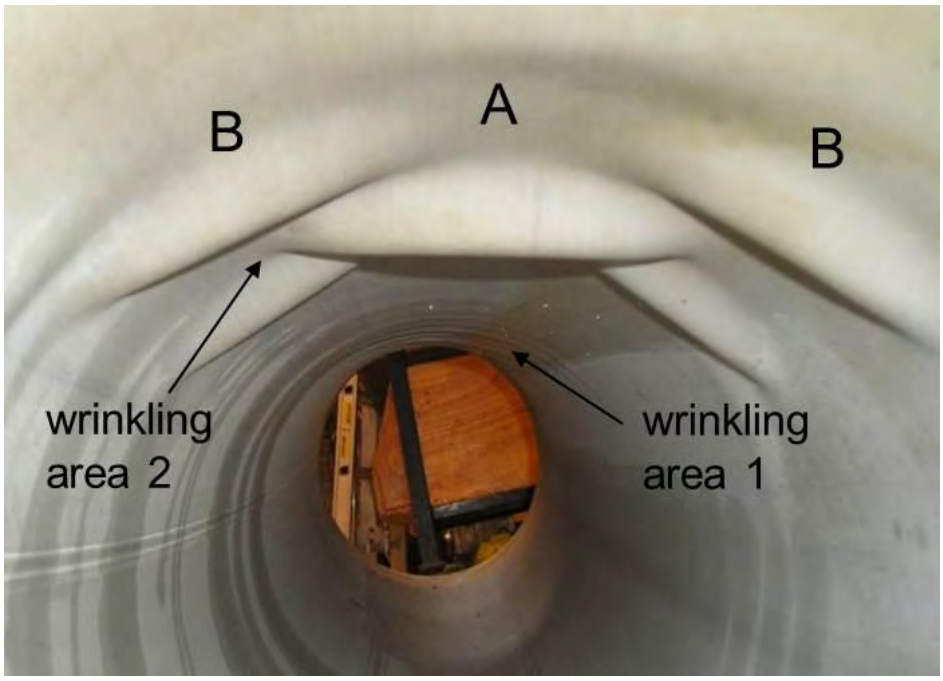

***Figure 75**: Photo of wrinkled liner pipe after experimental testing [13].*

Tkaczyk et al. [14] presented a combined experimental and numerical research program on 6'' and 12'' mechanically lined pipes, candidates for reeling application (Figure 76). Emphasis was given on liner wrinkling development under cyclic loading, to account for installation and in-service conditions. Special tests on wrinkling formation were also conducted and simulated with finite elements.

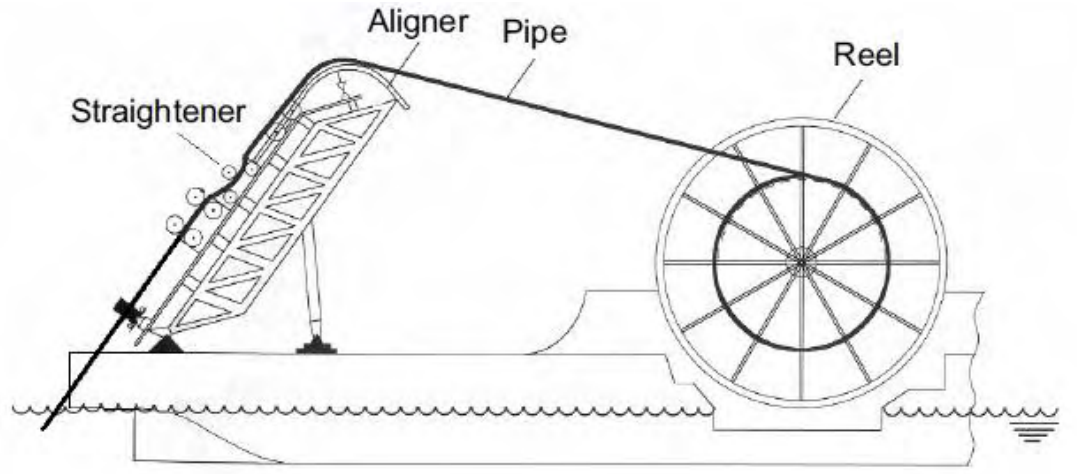

***Figure 76**: Schematic representation of reeling installation procedure [14].*

Recently, Peek and Hilberink [15] presented an analytical bifurcation solution for axisymmetric wrinkling on a lined pipe under axial compression without internal pressure. Their solution indicates that the incipient wrinkling strain for the snug-fit pipe without any imperfections is the same as for a single pipe with 5/3 times the wall thickness of the liner and the same midsurface diameter.

Finally, another engineering application of double-wall pipes under lateral confinement is related to the bending buckling behaviour and stability of a nano-composite tube reinforced by an inner single-walled carbon nanotube. Nowadays, nano-composite tubes are related to significant applications, whereas their investigation considers a shell of an equivalent thickness [16]. The usage of carbon nanotube as reinforcement constituent in composite materials of polymer base, where it is confined in a polymer matrix, is of particular interest. In this application, the nanotube bends together with the polymer confinement and because of its thin wall, it may buckle if compressive stress exceeds a critical value. This problem was investigated in [17], using an analytical approach, based on Brazier's ovalization analysis, enhanced to account for the effects of the confining medium. However, the definition of the critical load is an open issue for discussion and solving [18].

3.1.2 Scope of the present research

The research reported in the present chapter is numerical, based on advanced finite element simulation tools, and is aimed at understanding the mechanical response of the thin-walled liner pipe subjected to bending with or without the presence of external pressure, as well as determining the deformation of the lined pipe at which the liner wrinkles, through a rigorous simulation of the wrinkling process. The lined pipe is modeled using nonlinear finite elements capable at simulating the interaction between the liner and the outer pipe. Inelastic effects of the material properties and nonlinear geometry with large strains are taken into account. The hoop residual stresses due to manufacturing process are inserted to the model as initial conditions (prestressing) and then, bending curvature is applied. First, an ovalization bending analysis of the lined pipe is conducted, where a slice of the pipe between two adjacent cross-sections is considered, excluding the possibility of buckling. In this analysis, the stress and deformation of the liner in the compression zone is monitored, with emphasis on possible detachment (Δ) of the liner from the outer pipe. Furthermore, the liner ovalization (ζ), bending moment (m), local hoop curvature $(1/r_{\theta 0})$, axial stress (σ_{x0}), and hoop (circumferential) stress $(\sigma_{\theta 0})$ are investigated. Using a simple

buckling hypothesis, it is possible to estimate the curvature at which liner wrinkling occurs. Subsequently, a three-dimensional analysis is conducted to examine buckling of the liner in the form of a uniform wrinkling pattern. The curvature κ_{cr} at which buckling occurs and the corresponding buckling wavelength L_{hw} are determined. The transition from a uniform wrinkling configuration to a localized buckling pattern is also investigated. In addition, the sensitivity of response on the presence of initial wrinkling imperfections is investigated.

At first, lined elastic pipes where the elastic liner is stress-free and initially in contact with the elastic outer pipe are examined focusing on the buckling modes of first and second bifurcation. Specifically, lined pipes with nominal diameter equal to 12.75 inch and thickness of the outer pipe ranging between 4 and 60 mm are considered in the analysis. Next, the mechanical behavior of three lined steel pipes (carbon steel pipes, lined with stainless steel pipes) of different dimensions are investigated, taking into account the effects of prestressing. Furthermore, a comparison with available experimental results in terms of the buckling shape, the buckling wavelength, and the wrinkling height is conducted. Finally, the mechanical behavior of lined steel pipes under bending in the presence of external pressure is examined.

3.2 Finite element modeling

The response of lined pipes under uniform bending is examined numerically using nonlinear finite element tools. The general-purpose finite element program ABAQUS [19] is employed to simulate the mechanical response of lined pipes. The analysis considers nonlinear geometry through a large-strain description of the outer and the liner pipe, whereas the material of liner pipe and outer pipe is considered both elastic and elastic-plastic (steel material). In the latter case, the steel materials of the outer and the liner pipe are described through J_2 (von Mises) flow plasticity models with isotropic hardening, calibrated through stress-strain curves from uniaxial tension coupon tests.

The finite element models are three-dimensional, considering a segment of the lined pipe under appropriate boundary conditions. Particularly, in the $z=0$ plane (see Figure 77), $z-$symmetry is assumed, i.e. only in-plane motion of the corresponding nodes on the $x-y$ plane is allowed. In the $z=L$ plane (where L is the length of the strip in $z-$ direction), uniform bending is applied considering a reference point coupled with the nodes of that plane, so that motion of the corresponding nodes is allowed on the rotated plane. Based on experimental observations, symmetry of deformation with respect to the plane of

bending is assumed so that half of the pipe cross-section is analyzed, applying appropriate symmetry conditions on the $\theta = 0$ plane.

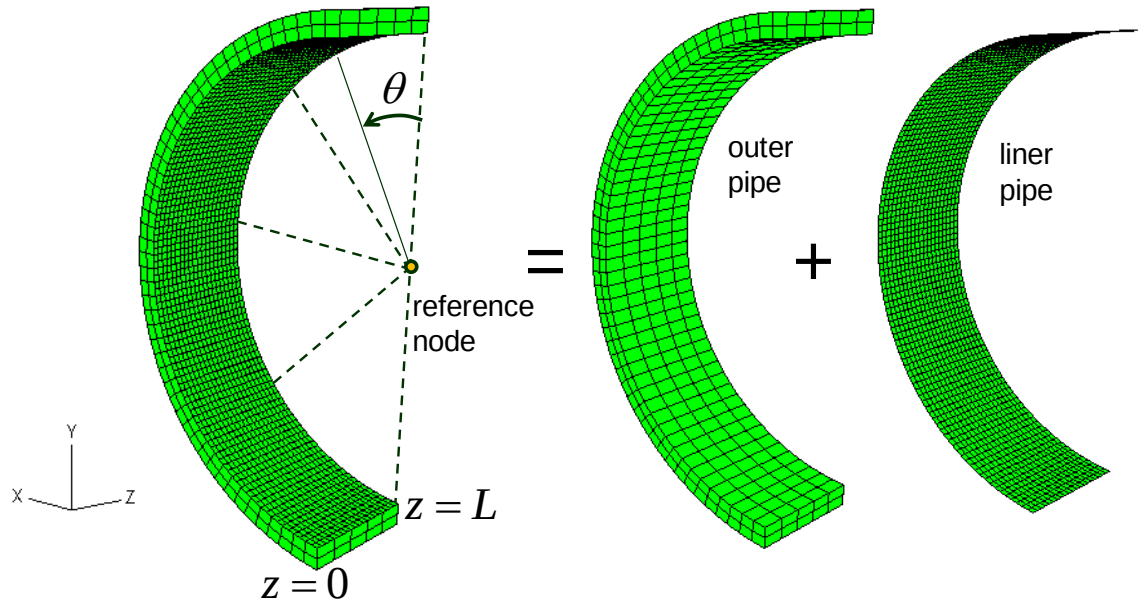

***Figure 77**: Lined pipe model; outer pipe is modelled with solid elements and liner pipe is modelled with shell elements.*

Four-node reduced-integration shell elements (S4R) are employed for the modeling of the thin-walled liner pipe, whereas 20-node brick elements (C3D20R) are used to simulate the thick-walled outer pipe. A typical finite element mesh for the outer and liner pipe used in the present analyses is shown in Figure 77. Following a short parametric study, it has been concluded that consideration of a finer finite element mesh have a negligible effect on the numerical results. Furthermore, a total of 100 shell elements around the half circumference of the cylinder have been found to be adequate to achieve good accuracy of the numerical results.

For conducting an ovalization analysis of the lined pipe, a pipe segment with a small value of L is assumed with no variation of loading and deformation in the longitudinal direction of the pipe, as shown in Figure 77. This is practically a two-dimensional finite element model, with periodic boundary conditions at $z = 0$ and $z = L$. In this model, pipe wall wrinkling phenomena are excluded. To model wrinkling of the liner pipe, this quasi two-dimensional analysis is not adequate; beyond buckling, cross-sectional deformation is no longer constant along the pipe (due to the development of wavy wrinkles), and therefore, a three-dimensional analysis is necessary. In a wavy-type post-buckling configuration (formation of wrinkles) of an infinitely long pipe, shown schematically in Figure 78, cross-

sections $\alpha-\alpha$ and $\beta-\beta$ do not exhibit warping deformation for symmetry reasons. Therefore, for the purposes of the three-dimensional analysis, it is sufficient to analyze only a pipe segment of half-wavelength with appropriate "periodic" boundary conditions at the end-sections $\alpha-\alpha$ and $\beta-\beta$.

The buckling wavelength is not known a priori and, therefore, a sequence of analyses should be conducted for several assumed wavelength values. The actual wavelength is the one that corresponds to the "earliest" bifurcation point on the primary path. Karamanos & Houliara [20],[21] used a similar methodology to analyze single-wall pipes under bending. Regarding the number of elements in the longitudinal direction, 20 elements per half-wavelength are employed in the liner pipe. A contact algorithm is considered to simulate the interface between the liner and the outer pipe. Unless otherwise specified, frictionless contact is assumed in the results. A few analyses have been performed to examine the effects of friction, which is considered through an appropriate the friction coefficient μ.

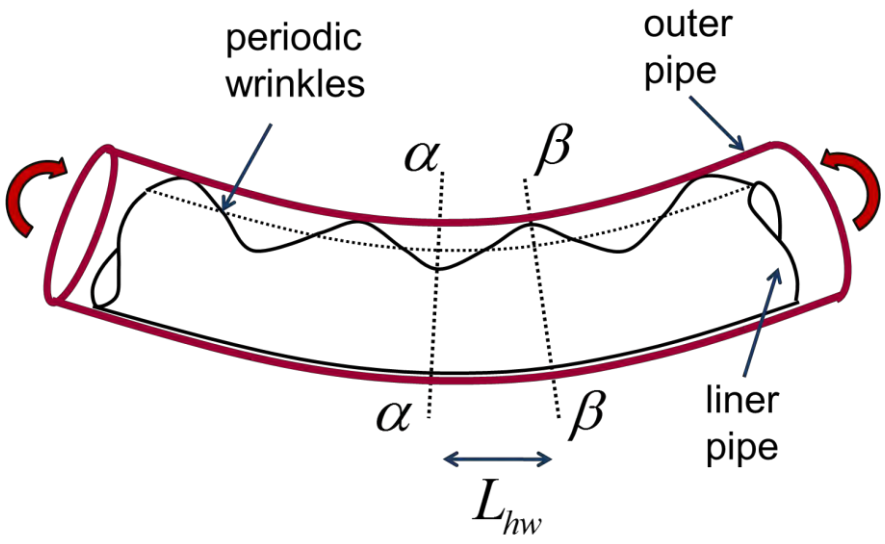

***Figure 78**: Schematic representation of uniformly wrinkled pipe and the corresponding half-wavelength between cross-sections α-α and β-β.*

3.3 Buckling of lined elastic pipes

In the present section, the response of lined elastic pipes under bending loading is examined. The two pipes (liner and outer pipe) are initially in contact and stress-free. Using the numerical tools described in the previous section, an ovalization analysis is conducted first, followed by an investigation of liner pipe wrinkling. A simplified bifurcation solution is also developed, which provides fairly good predictions for the buckling curvature and the corresponding wavelength. Lined pipes with nominal diameter equal to 12.75 inch are considered, following the dimensions of pipes tested in [11] and [13]. The outside diameter of the liner pipe D_l is 296.4 mm, the mean diameter d_l and the thickness t_l of the liner pipe are equal to 293.4 mm and 3 mm respectively, corresponding to a diameter-to-thickness ratio for the liner pipe $\left(d_l/t_l\right)$ equal to 97.8, whereas the thickness of the outer pipe ranges between 4 and 60 mm. For normalization purposes, the dimensionless thickness parameter τ is introduced $\left(\tau = t_o/t_l\right)$, where t_o is the thickness of the outer pipe. The elastic materials of the two pipes have Young's moduli equal to $E_l = 193$ GPa for the liner pipe and $E_o = 210$ GPa for the outer pipe, and Poisson's ratio ν equal to 0.3 for both pipes.

In this section, the values of bending moment M and curvature k are normalized using the expressions $M_e = \dfrac{E_l r_l t_l^{\,2}}{\sqrt{1-\nu^2}}$ and $k_N = \dfrac{t_l}{r_l^{\,2}\sqrt{1-\nu^2}}$ respectively, and will be referred to as "normalized elastic moment" and "normalized elastic curvature" respectively, so that $m_e = M/M_e$ and $\kappa_e = k/k_N$, where r_l is the mean radius of the liner pipe. Ovalization is expressed through the dimensional parameter $\zeta = \left(d_{h,l} - d_{v,l}\right)/2d_l$, where $d_{h,l}$ is the current (deformed) mean diameter in the horizontal direction of the liner, $d_{v,l}$ is the current mean diameter in the vertical direction, and d_l is the initial mean diameter of the liner. Finally, the values of stress are normalized by the stress-like parameter $\sigma_e = \dfrac{E_l t_l}{r_l\sqrt{3\left(1-\nu^2\right)}}$.

3.3.1 Ovalization analysis

The ovalization response of lined pipes made of elastic material is examined first, considering a small length of the pipe (3% of the diameter), so that buckling phenomena associated with pipe wall wrinkling are excluded. Furthermore, unless otherwise specified, the interface between the liner and the outer pipe is considered frictionless. The moment–curvature curve is shown in normalized (non-dimensional) form in Figure 79 (m_e versus κ_e) for different thicknesses of the outer pipe. Furthermore, Figure 80 depicts the normalized ovalization–curvature diagram (ζ versus κ_e) for the liner pipe. It is concluded that the increase of the outer pipe thickness increases the moment capacity of the lined pipes, whereas conversely decreases the development of the ovalization parameter. Consideration of friction in the interface between the liner and the outer pipe has no influence in both moment and ovalization response.

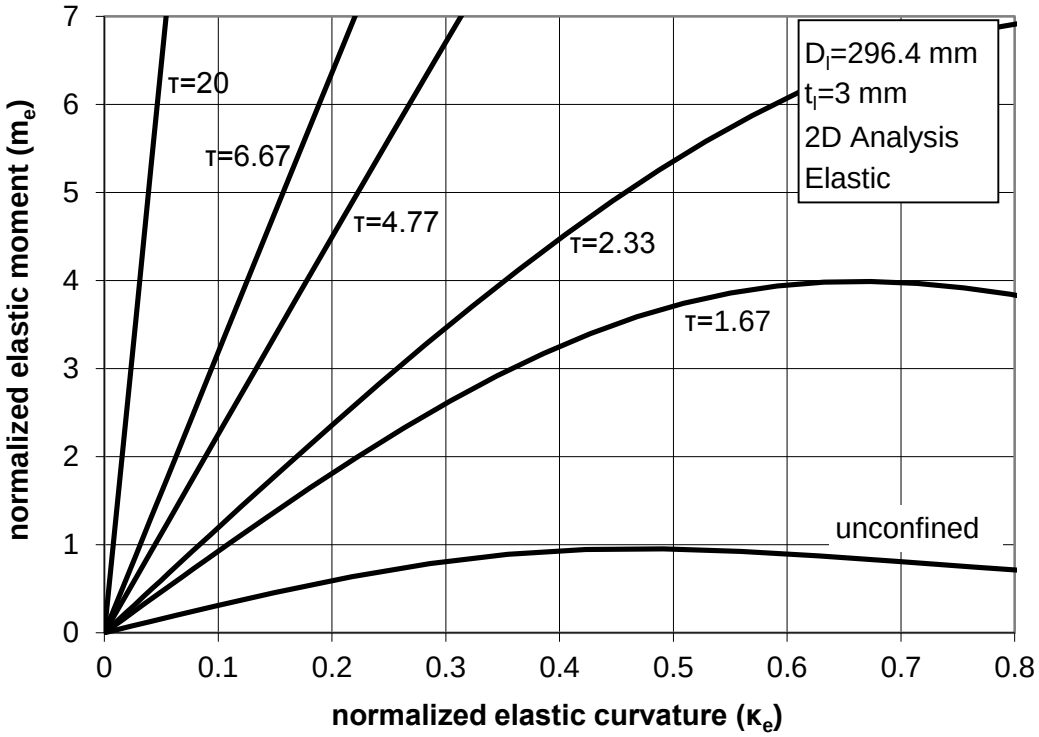

***Figure 79**: Normalized moment of lined elastic pipe for different thicknesses of the outer pipe, obtained from ovalization (2D) analysis.*

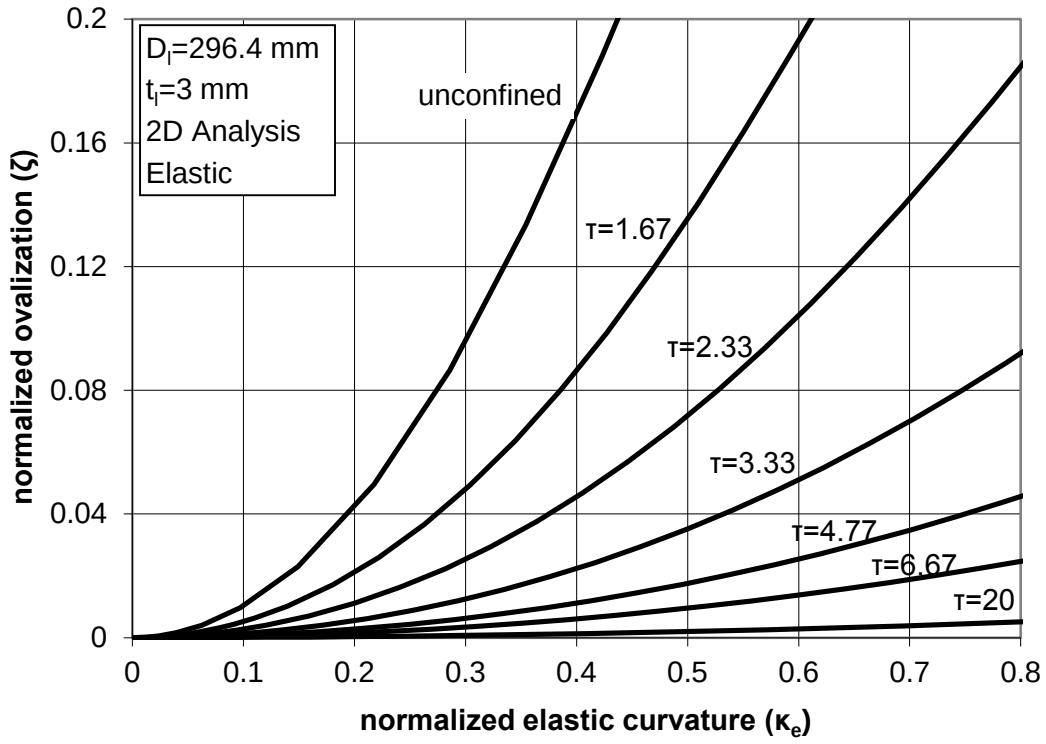

***Figure 80**: Normalized ovalization of lined elastic pipe for different thicknesses of the outer pipe, obtained from ovalization (2D) analysis.*

An important observation from this analysis is that, from the early stages of bending, the liner separates from the outer pipe. The relative distance between liner and outer pipe is expressed as the difference between the corresponding radial displacements of the liner u_l and the outer pipe u_o, at the $\theta = 0$ plane, referred to as "detachment". In Figure 81, the value of detachment is plotted in a normalized form $\left(\Delta = \left(u_l - u_o\right)/t_l\right)$ in terms of bending curvature for different thicknesses of the outer pipe. The numerical results indicate that the value of Δ is an increasing function of bending curvature. In addition, it is concluded that the increase of the outer pipe thickness results in a decrease of the detachment magnitude. Also, it should be stated that for lined pipes with values of relative thickness τ less than 1.67, no detachment occurs between the liner and outer pipe during bending.

The effect of friction on the detachment of the liner from the outer pipe has considered through the friction coefficient μ and is shown in Figure 82 for a τ value equal to 4.77. It is concluded that the friction in the interface between the liner and the outer pipe has a relatively small effect on the response of elastic lined pipes.

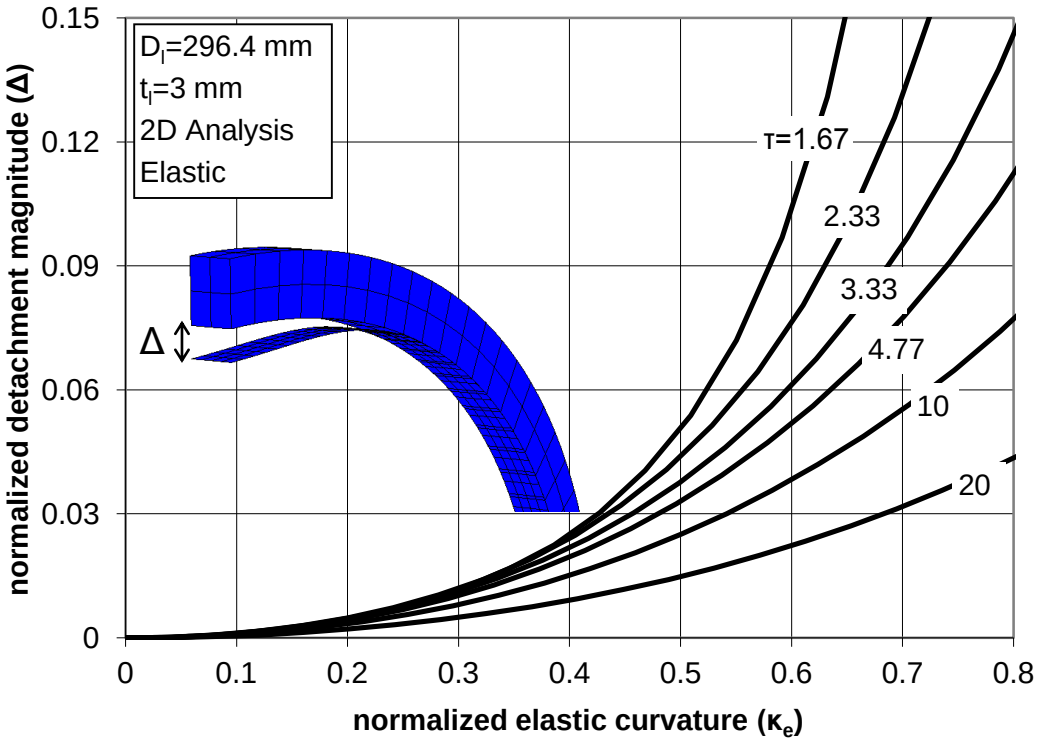

***Figure 81**: Detachment of liner from outer pipe for different thicknesses of the outer pipe.*

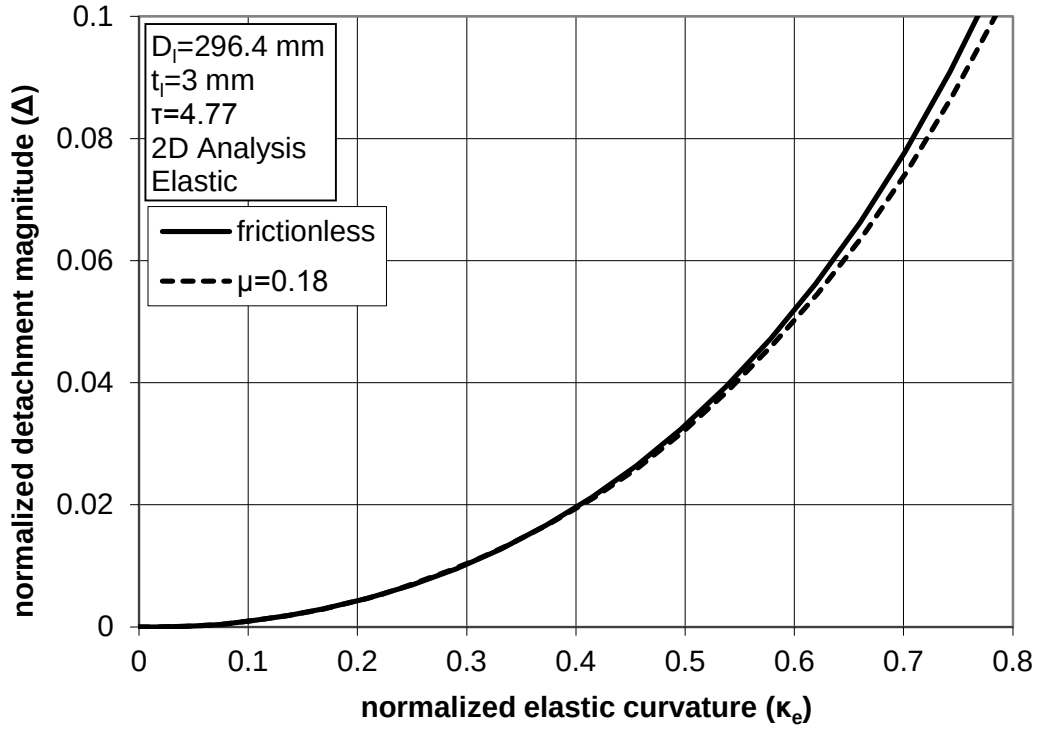

***Figure 82**: Effect of friction on the detachment of liner from outer pipe.*

The local hoop curvature at the $\theta = 0$ plane of the liner pipe, denoted as $1/r_{\theta 0}$, is of particular interest for predicting liner wrinkling in elastic pipes. The change of hoop curvature due to bending at this location is shown schematically in Figure 83. In Figure 84, the value of $1/r_{\theta 0}$, normalized by the initial curvature of the circular pipe in the hoop direction $1/r_l$, is plotted for different values of τ. The decrease of local curvature at this location with increasing bending curvature indicates liner flattening at the compression zone due to cross-sectional ovalization. At this location $(\theta = 0)$, significant axial compressive stress σ_{x0} is developed as a result of bending, as shown in Figure 85 in non-dimensional form. The numerical results indicate a quasi-linear increase of σ_{x0} in terms of bending curvature, for values of τ larger than 4, due to very small cross-sectional ovalization. An important observation of this figure is that the increase of the outer pipe thickness leads to increase of the axial compressive stresses at $\theta = 0$ location. The presence of friction in the interface between the liner and the outer pipe does not affect the aforementioned results of local curvature and axial stress.

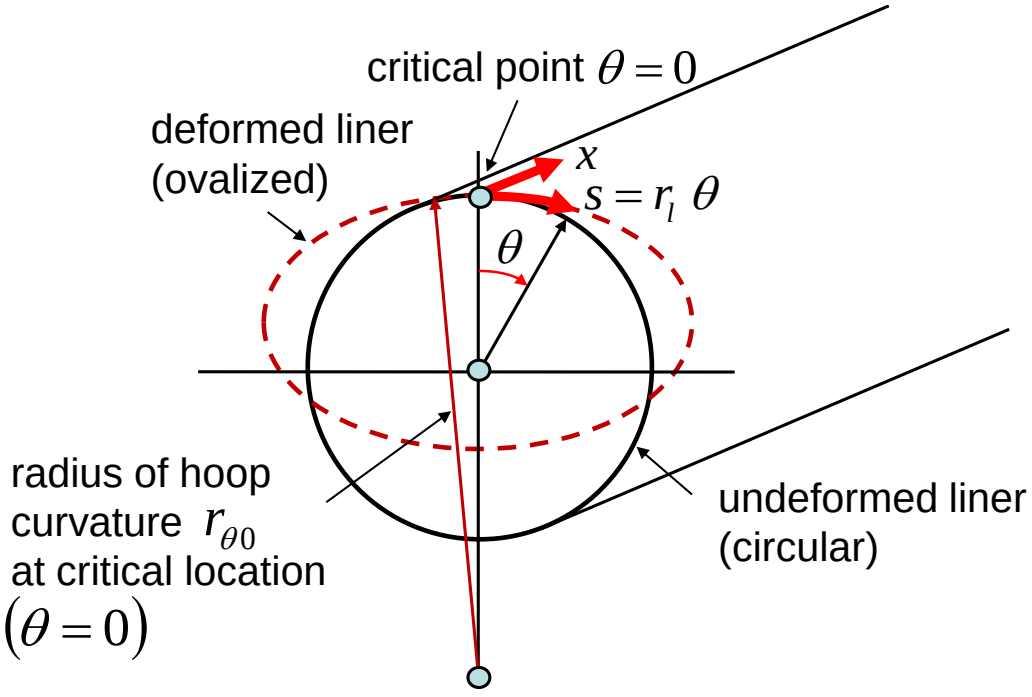

***Figure 83**: Schematic representation of local hoop curvature during ovalization of the liner pipe.*

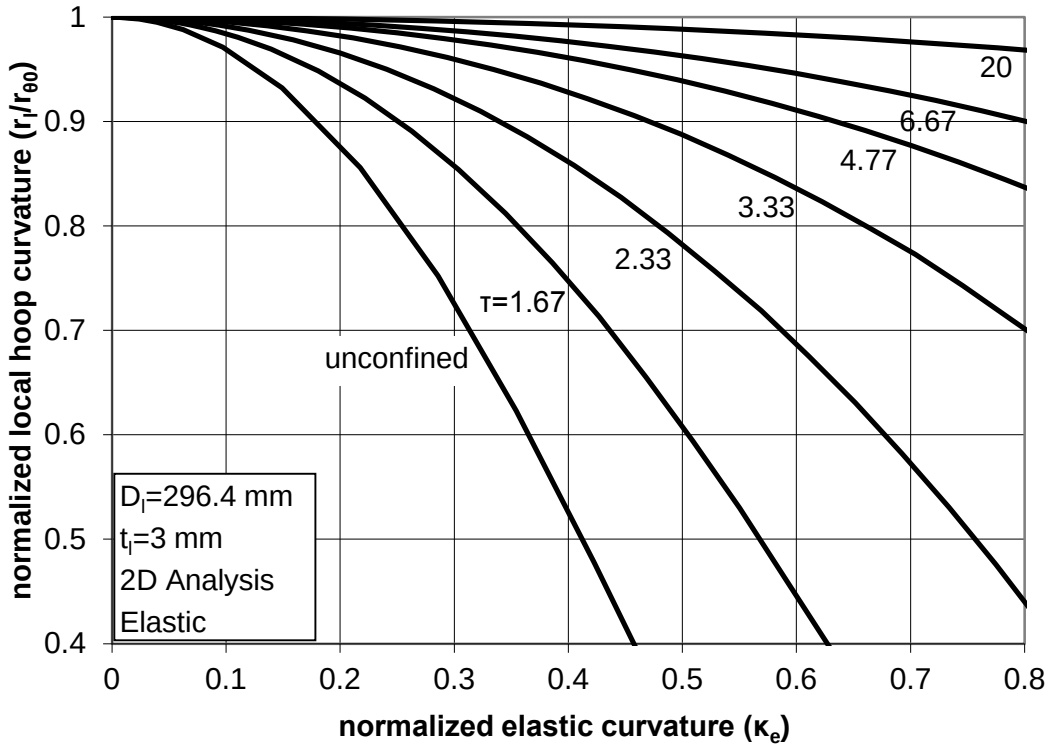

***Figure 84**: Normalized local hoop curvature at the critical location of compressive side of the liner $(\theta = 0)$ for different values of thickness of the outer pipe.*

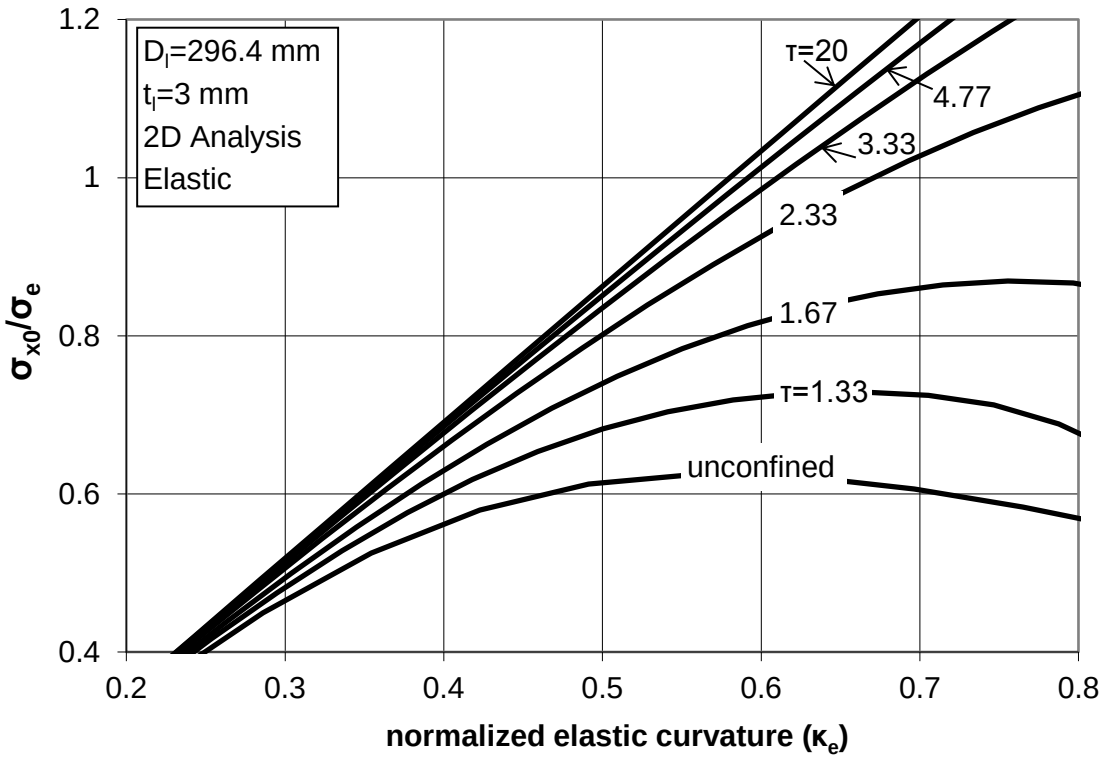

***Figure 85**: Normalized value of stress in the longitudinal direction at the critical location of compressive side of the liner $(\theta = 0)$ for different thicknesses of the outer pipe.*

3.3.2 Simplified analytical bifurcation solution

Based on the previous results of ovalization analysis, it is possible to develop a simplified formulation for predicting wrinkling of the liner pipe. This simplified bifurcation formulation has been proposed elsewhere for predicting shell buckling [22], based on the assumption that buckling is fully determined by the stress and deformation inside the zone of the initial buckle. This assumption has also been referred to as "local buckling hypothesis". According to the above hypothesis, in the case of a long cylindrical shell under longitudinal bending, buckling will occur at the critical location $(\theta = 0)$ when the stress σ_{x0} and deformation $1/r_{\theta 0}$ satisfy the following equation:

$$\sigma_{x0} = \frac{E_l}{\sqrt{3\left(1-\nu^2\right)}} \frac{t_l}{r_{\theta 0}}, \tag{65}$$

also written in terms of the stress-like parameter σ_e as follows:

$$\frac{\sigma_{x0}}{\sigma_e} = \frac{r_l}{r_{\theta 0}}. \tag{66}$$

Equation (65) is the classical Donnell's equation for a uniformly compressed elastic circular cylinder with radius $r_{\theta 0}$ in the meridional direction. Recently, Houliara & Karamanos [20] demonstrated numerically that bifurcation predictions from this hypothesis for the case of elongated unconfined cylindrical elastic shells subjected to bending are in very good agreement with finite element results.

In the case of lined pipes, the ovalization analysis presented in the previous subsection has demonstrated that during bending, the liner pipe detaches from the outer pipe at the vicinity of $\theta = 0$, so that the liner pipe around this location behaves as a cylindrical panel under axial compression (see the sketch in Figure 86). Therefore, it would be reasonable to apply equation (65) based on the results for the axial stress σ_{x0} and the local curvature $1/r_{\theta 0}$, both obtained from the ovalization analysis (Figure 84 and Figure 85). The buckling curvature predicted from equation (65) is shown in Figure 87 with the solid line, for different values of outer pipe thickness.

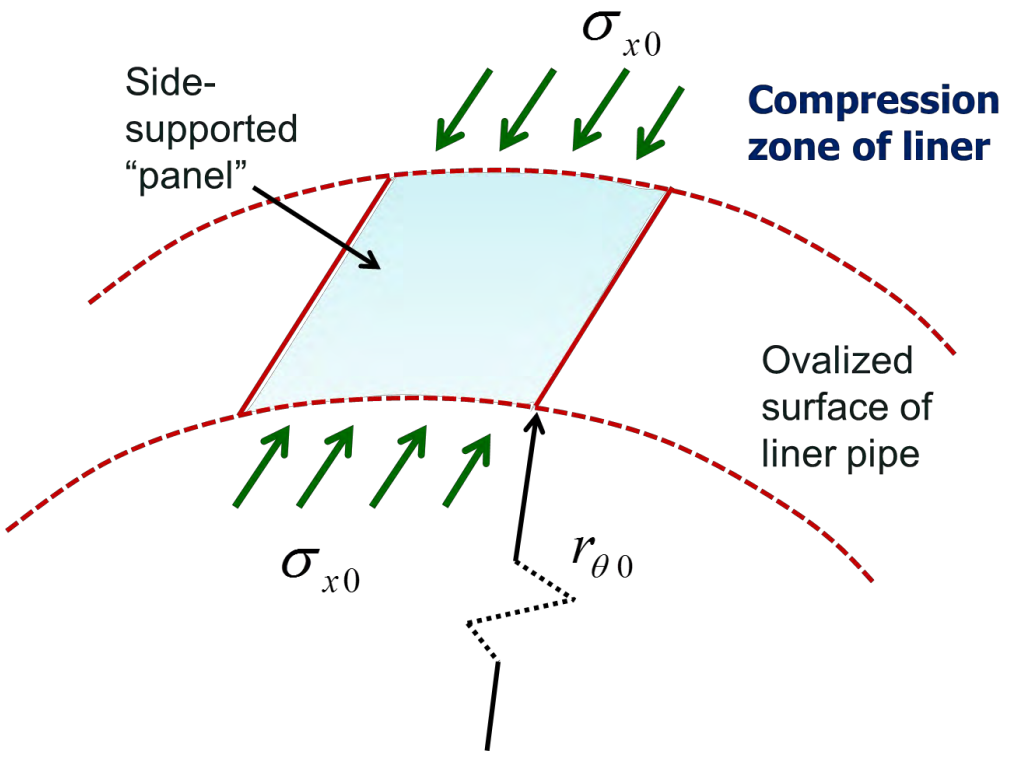

***Figure 86**: Schematic representation of the compression zone of the liner, similar to a laterally-supported "cylindrical shell panel".*

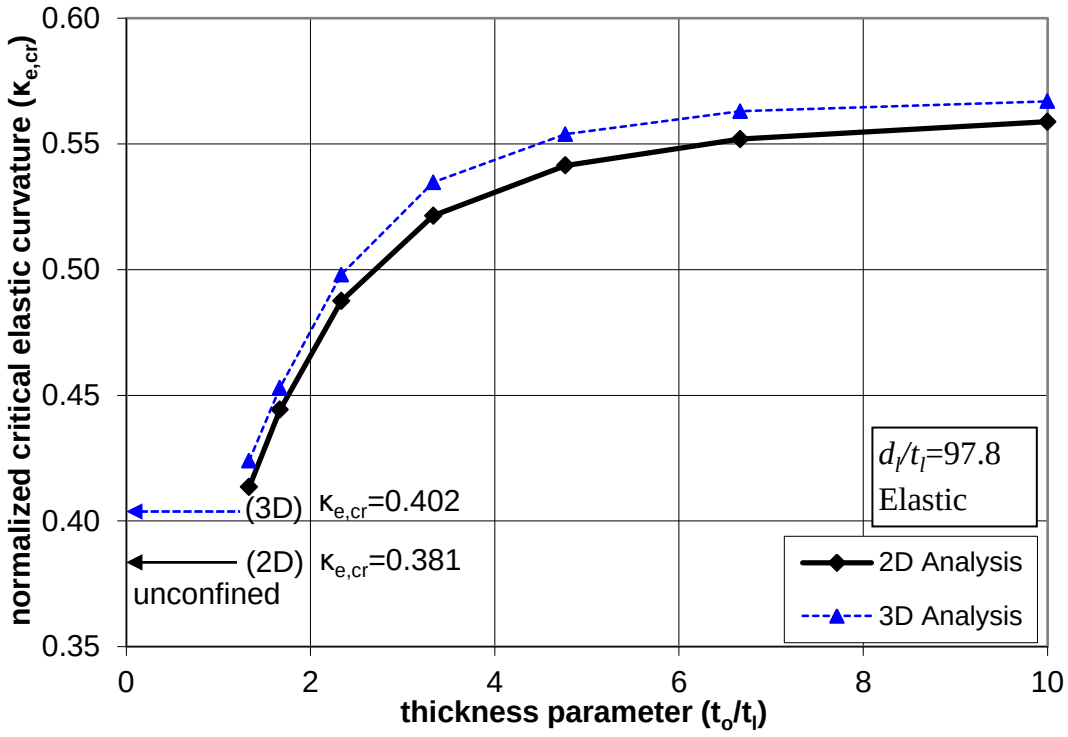

***Figure 87**: Variation of the normalized critical curvature for different thicknesses of the outer pipe.*

According to this simplified formulation, the corresponding buckling wavelength can also be estimated. Assuming that the state of stress is constant within the buckling zone, axi-symmetric conditions can be considered so that the value of the buckling half-wavelength L_{hw} can be estimated by the following equation, which stems from axi-symmetric buckling analysis of elastic cylindrical shells under uniform meridional compression [23]:

$$L_{hw} = \left[\frac{\pi^4}{12\left(1-\nu^2\right)} \right]^{1/4} \sqrt{r_{\theta 0} t_l} \ . \tag{67}$$

For convenience, the normalized half-wavelength l_{hw} is introduced using the following normalization:

$$l_{hw} = L_{hw} \big/ \sqrt{d_l t_l} \ . \tag{68}$$

Combining equations (67) and (68), and assuming a value of Poisson's ratio equal to 0.3, the value of l_{hw} obtained from this simplified solution methodology can be written $l_{hw} = 1.22\sqrt{r_{\theta 0}/r_l}$. The variation of l_{hw} in terms of outer pipe thickness is presented in Figure 88 with the solid line. The results in Figure 88 indicate that the value of l_{hw} is a decreasing function of the value of τ. Finally, the detachment magnitude Δ and the size of the detachment zone L_C/r_l around the buckling location ($\theta = 0$) at the stage of bifurcation predicted above, are shown in Figure 89 and Figure 90, with respect to the relative thickness parameter τ.

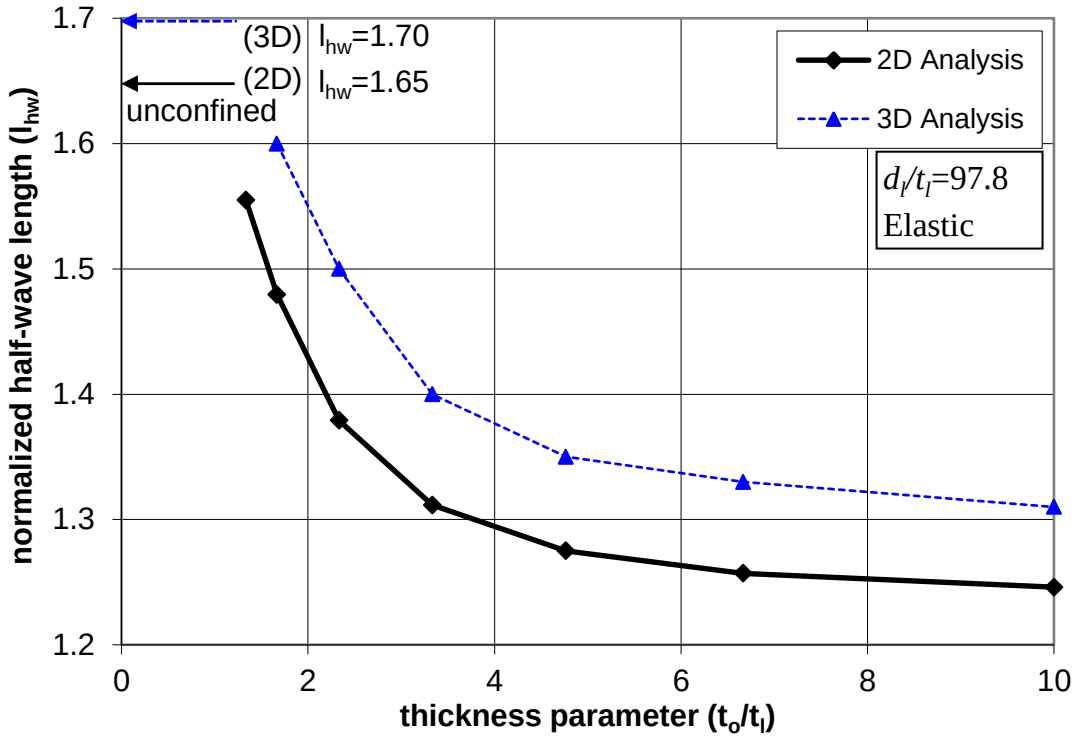

***Figure 88**: Variation of the normalized half-wavelength for different thicknesses of the outer pipe.*

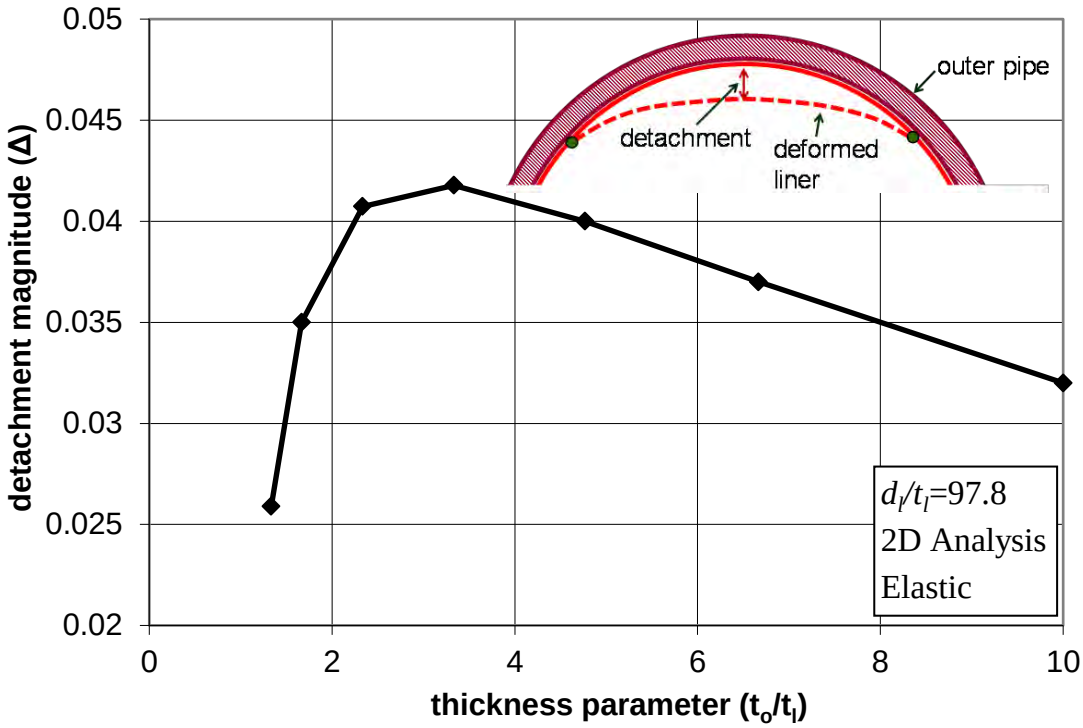

***Figure 89**: Normalized detachment magnitude at buckling for different thicknesses of the outer pipe.*

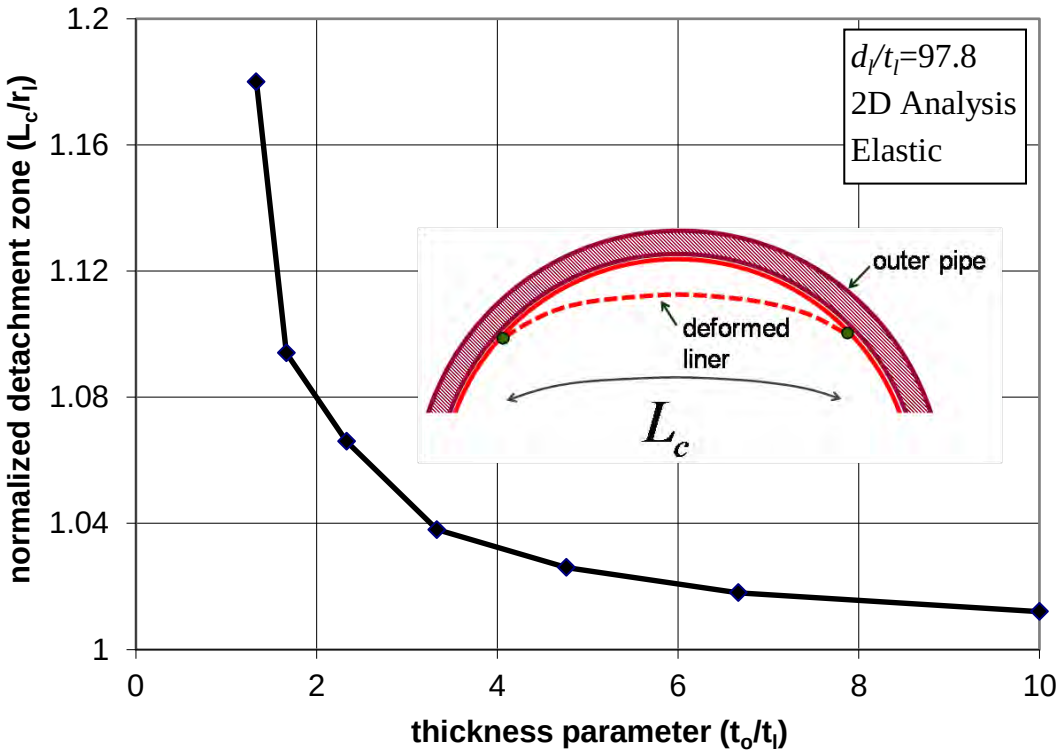

***Figure 90**: Variation of normalized detachment zone at buckling.*

3.3.3 Uniform wrinkling

In this subsection, wrinkling of lined elastic pipes under bending is simulated in a rigorous manner. Bifurcation of liner pipe from a uniform ovalization stage to a uniform (periodic) wrinkling pattern is examined first, using the finite element tools presented in section 3.2. Three values are considered for the thickness of the outer pipe, 10 mm, 14.3 mm and 20 mm, corresponding to values of thickness parameter τ equal to 3.33, 4.77 and 6.67 respectively. To simulate this bifurcation, a three-dimensional analysis is conducted, considering a pipe segment equal to one half-wavelength $\left(L = L_{hw}\right)$. The value of L_{hw} is not known a priori and therefore, for each value of τ, a series of analyses is necessary to obtain the critical half-wavelength, as described in section 3.2. The numerical results for pipes without initial imperfections (perfect pipes) are summarized in Figure 91; the value of critical half-wavelength for $\tau = 3.33$, 4.77 and 6.67 is computed equal to 1.4, 1.35 and 1.33 respectively.

The results shown in Figure 91 indicate that for a certain value of τ, the value of the critical curvature $\kappa_{e,cr}$ is not very sensitive to variations in the assumed value of l_{hw}; the numerical results show that variation of the l_{hw} value between 1.2 and 1.5 results in a variation of only 3% for the $\kappa_{e,cr}$ value. The values of critical curvature $\kappa_{e,cr}$ obtained from three-dimensional numerical analysis for the three values of outer pipe thickness are also shown in Figure 91 with an arrow (↓). Those results for the critical curvature and the corresponding half-wavelength are depicted in Figure 87 and Figure 88, which indicate that predictions from the simplified methodology, based on the results of ovalization analysis, are quite close to and consistent with the finite element results. The main conclusion from the above analysis is that the thickness of the outer pipe has a beneficial effect on the critical curvature of the liner pipe; the bigger the outer pipe thickness, the higher the critical curvature. This conclusion is associated with Figure 80 and Figure 81 which demonstrate that with increasing the thickness of the outer pipe, the smaller is the ovalization and the detachment of the liner pipe. In other words, the above conclusion means that the thickness of the outer pipe plays the role of the confinement of the liner pipe and, as a consequence, the increase of the outer pipe thickness increases the stiffness of the confinement.

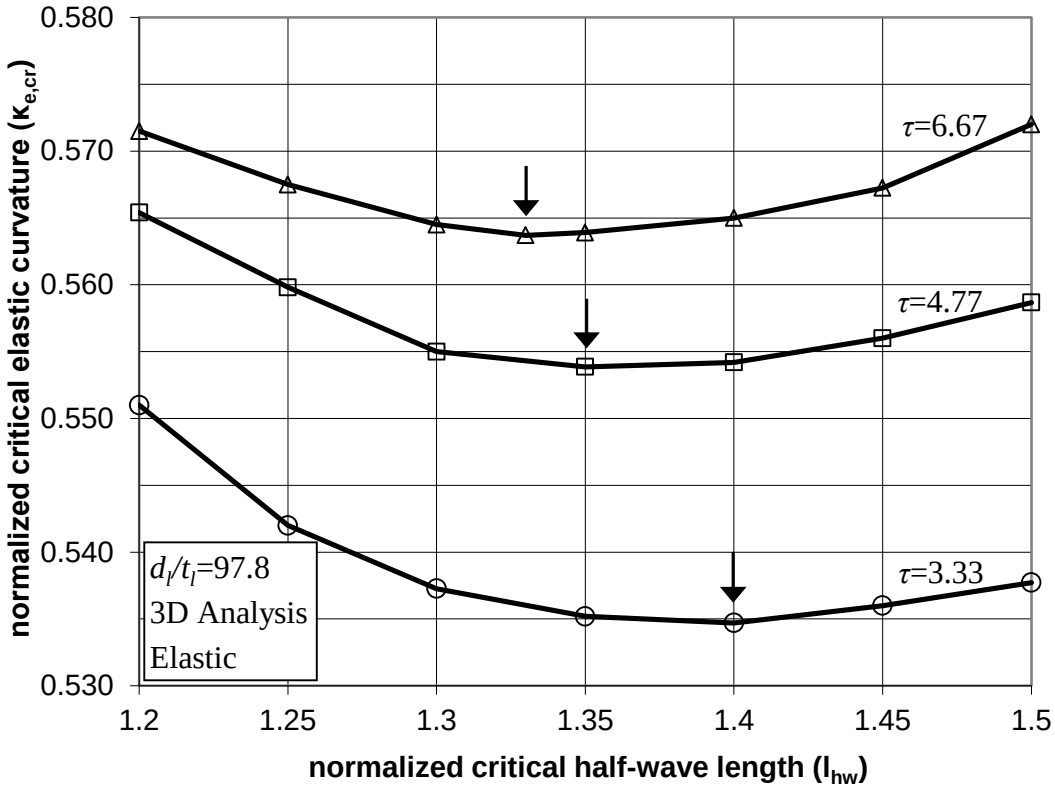

Figure 91*: Variation of the normalized critical elastic curvature ($\kappa_{e,cr}$) of the liner pipe for three different thicknesses of the outer pipe.*

Prior to bifurcation, the pipe exhibits uniform deformation along its length in the form of cross-sectional ovalization. At buckling, a wavy pattern shape suddenly occurs in the form of uniform wrinkling at the compression side of the liner pipe, as shown in Figures 92. In Figures 92d, several wavelengths of the wavy pattern have been reproduced for visualization purposes. Figure 93 shows the development of liner pipe detachment for a perfect lined elastic pipe (no initial imperfections) with thickness ratio τ equal to 4.77. In this case, bifurcation occurs at a value of normalized curvature $\kappa_{e,cr} = 0.554$. At that stage, the wavy pattern of Figures 92d is formed; the displacement of liner point (1) increases abruptly, whereas the corresponding displacement of liner point (2) decreases and reaches the outer pipe. After the formation of the wavy pattern, further increase of bending curvature results in a rapid development of wrinkling, with increasing detachment of liner point (1) from the outer pipe. For perfect lined elastic pipes with thickness ratio τ equal to 3.33 and 6.67, the corresponding values of $\kappa_{e,cr}$ have been calculated equal to 0.535 and 0.564 respectively. It is computationally challenging to simulate the abrupt transition from pre-buckling to post-buckling in imperfection-free elastic lined pipes. One may depend on

numerical noise, but this can be associated with convergence problems. Despite those convergence problems, the results in Figure 91 have been obtained employing an adequately small analysis step, without imposing any imperfection on the liner pipe. Those numerical problems are alleviated using a small-amplitude imperfection in the form of the buckled shape of Figures 92, but this has a certain effect on the response due to imperfection sensitivity as described in the next paragraphs.

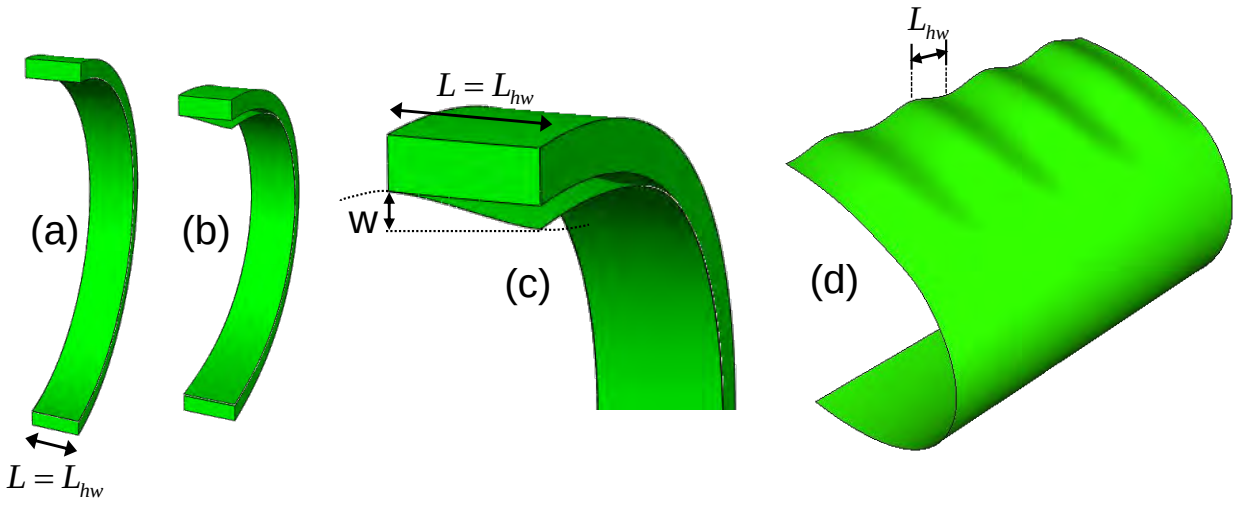

***Figures 92**: Lined pipe configurations; (a) undeformed configuration; (b), (c) and (d) ovalized and buckled liner.*

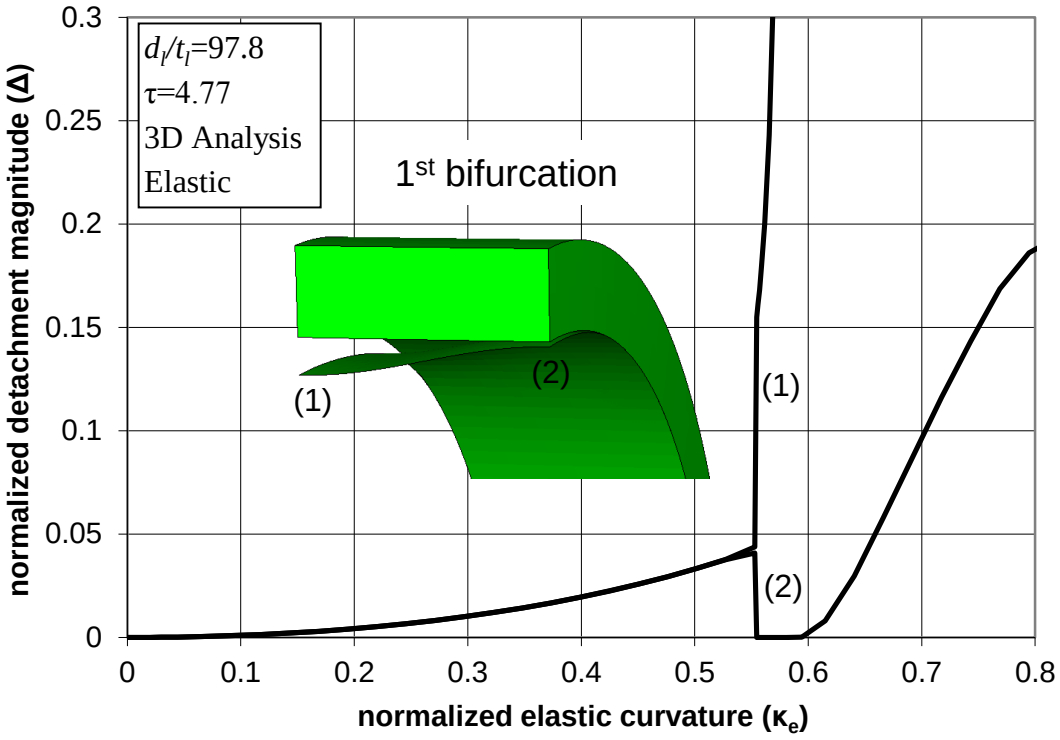

***Figure 93**: Development of liner pipe detachment for a perfect lined elastic pipe.*

Non-perfect pipes are considered next, where the initial imperfection is assumed in the form of the buckling shape obtained from the analysis of the perfect pipe shown in Figures 92. The numerical results for imperfect pipes with very small imperfection amplitudes w_0/t_l (w_0 is the initial value of w in Figures 92c), and with thickness ratio τ equal to 4.77, are shown in Figure 94. The results indicate a smooth transition to the wavy pattern without numerical convergence problems, whereas detachment displacements of points (1) and (2) on the symmetry planes grow rapidly when the bending curvature approaches the value of $\kappa_{e,cr}$. Note that the presence of very small imperfection amplitudes (less than 1% of the liner thickness) has a considerable effect on the liner response and indicate severe imperfection sensitivity.

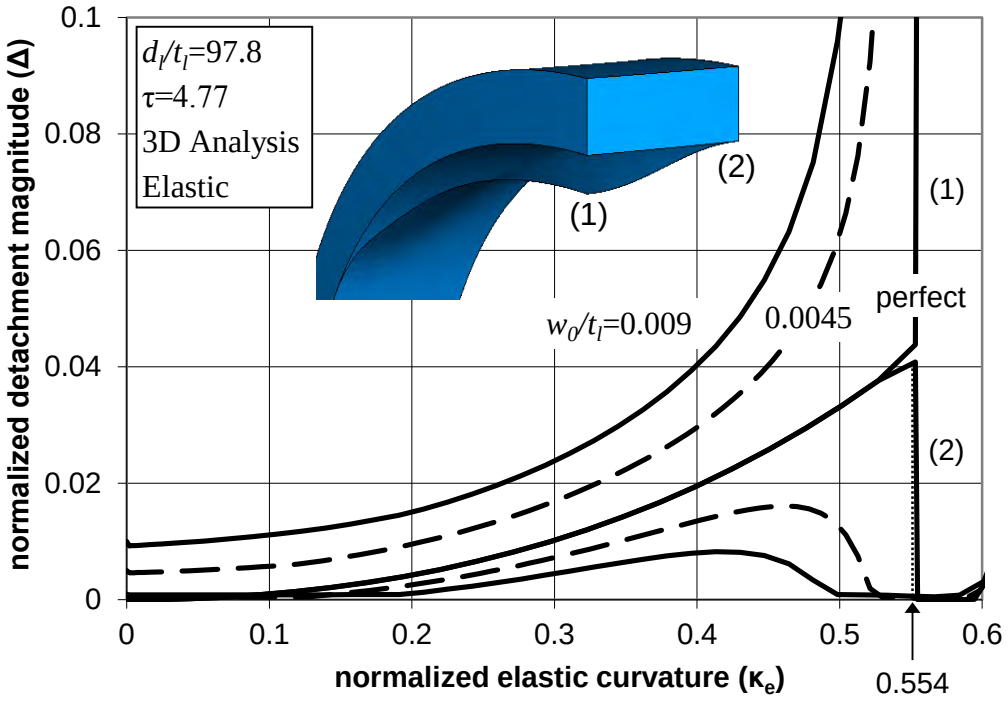

Figure 94: *Variation of the relative distance between liner and outer pipe for different imperfection amplitudes* $\left(w_0/t_l\right)$.

3.3.4 Second bifurcation

Experimental observations [11] have indicated that a long lined pipe, after the occurrence of uniform wrinkling of the liner pipe ("wrinkling area 1" in Figure 75), exhibits a second bifurcation in the form shown in "wrinkling area 2" of Figure 75. More specifically, one of the wrinkles grows rapidly, forming one main buckle, symmetric about the plane of bending (denoted as (A) in Figure 75), and four minor buckles (denoted as (B) in Figure 75) from either side of the main buckle. In such a way, the wavelength of this secondary buckling pattern is equal to twice the wavelength L_{hw} of the first buckling pattern. Based on this experimental observation, a series of three-dimensional analyses have conducted, considering the length of the lined elastic pipe equal to twice the half-wavelength computed in the previous uniform wrinkling analysis (i.e. $L = 2L_{hw}$ as shown in Figures 95). The pipes are imperfect with an imperfection pattern in the shape of the uniform wrinkling mode, as shown in Figures 95a which is actually the shape of Figures 92. The analysis shows that when the applied curvature reaches a certain value $\kappa'_{e,cr}$, liner deformation bifurcates to the shape shown in Figures 95b,c, which is similar to the buckling pattern observed experimentally (Figure 75). A similar methodology for analyzing imperfect cylindrical shells under axial compression has been employed in the early work of Koiter [24]. In Figures 95d, several wavelengths of the wavy pattern have been reproduced for visualization purposes. In Figure 96, the value of secondary bifurcation curvature $\kappa'_{e,cr}$ is plotted with solid line in terms of the imperfection amplitude, for the three values of thickness ratio $\tau = 3.33$, 4.77 and 6.67. Note that the values of $\kappa'_{e,cr}$ for zero (negligible) imperfection amplitude are 0.549, 0.576 and 0.588; these values represent the curvature of perfect lined elastic pipes at which secondary bifurcation occurs and are somewhat larger than the corresponding values of $\kappa_{e,cr}$ corresponding to first bifurcation, equal to 0.535, 0.554 and 0.564 respectively. The sensitivity of response on the presence of initial imperfections assumed in the form of the secondary buckling mode, shown in Figures 95b,c, is also examined. The corresponding numerical results are plotted in Figure 96, with dotted line, and indicate a somewhat more severe sensitivity to this type of imperfection. It is also noted that, numerically, it has not been possible to simulate secondary buckling in elastic lined pipes with imperfection amplitude w_0 less than 0.1% of the liner thickness t_l.

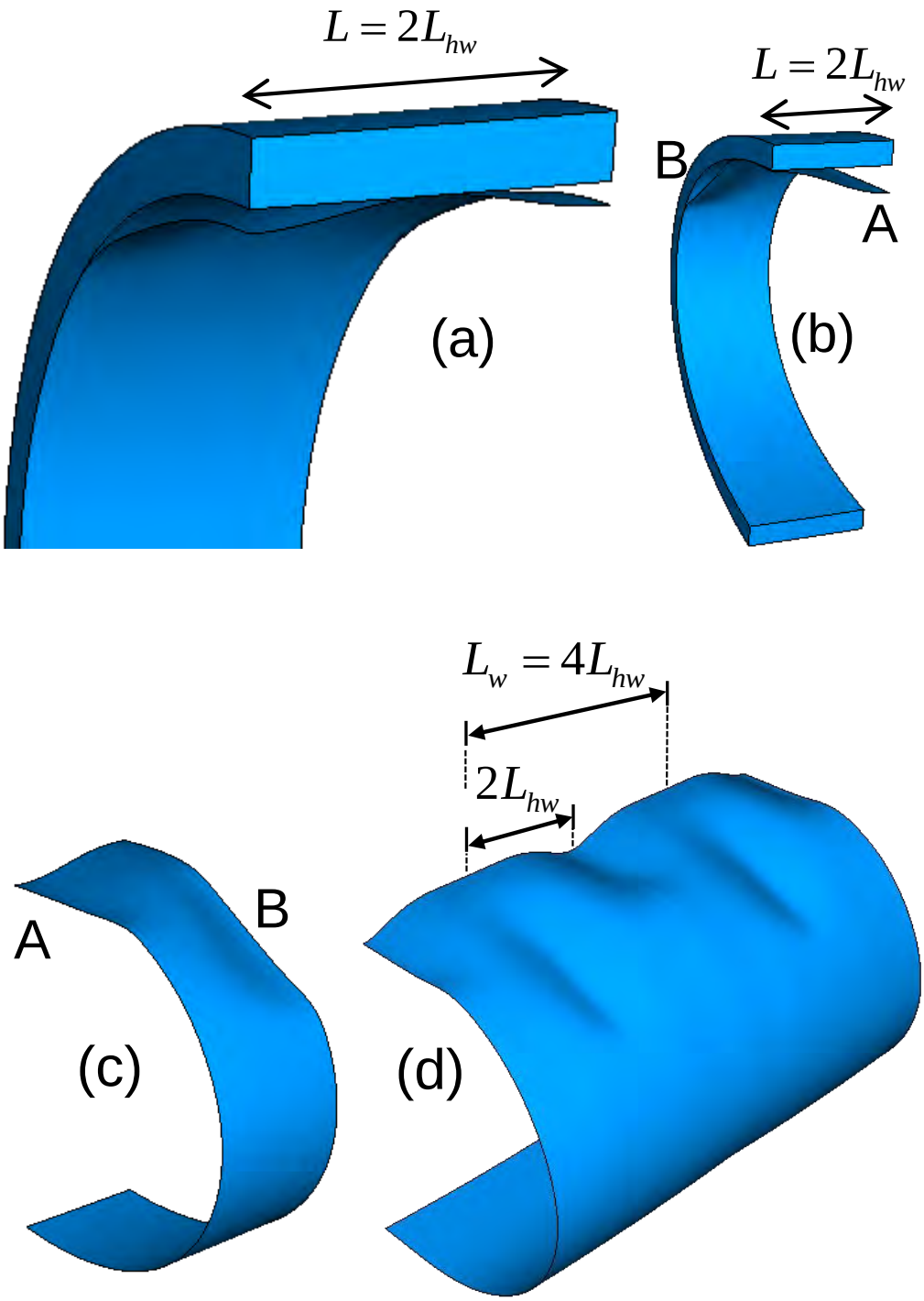

Figures 95: *(a) Initial configuration with liner wavy imperfection and (b),(c),(d) Deformed (buckled) configuration of lined pipe after secondary bifurcation.*

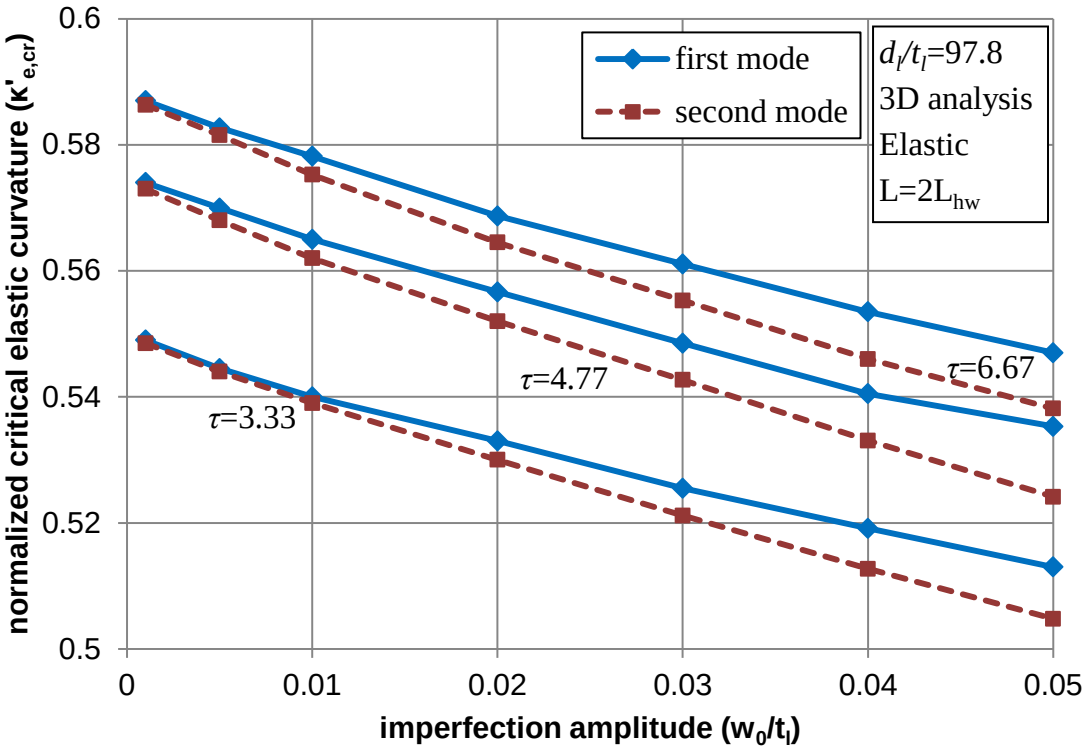

Figure 96: *Normalized critical elastic curvature with respect to the imperfection amplitudes for different values of τ ; imperfections are assumed in the form of first and second buckling mode.*

3.4 Buckling of lined steel pipes

The mechanical behavior of lined steel pipes is examined extensively in the present section. The outer pipe is made of carbon steel (API 5L Grade X65), whereas stainless steel (AISI 316L) is used for the thin-walled liner. The nominal stress – engineering strain curve for the carbon steel X65 material of the outer pipe obtained from a uniaxial tensile test is shown in Figure 97, with elastic modulus $E_o = 210{,}000$ MPa, Poisson's ratio $\nu = 0.3$, yield stress $\sigma_{Y,o} = 566$ MPa, a plastic plateau up to 2% engineering strain, and ultimate nominal stress $\sigma_{u,o} = 614$ MPa at 9% elongation. The corresponding stress-strain curve of the liner pipe 316L material is also shown in Figure 97, with parameters $E_l = 193{,}000$ MPa, $\nu = 0.3$, proportional limit $\sigma_{pr} = 250$ MPa at 0.13%, and yield stress $\sigma_{Y,l} = 298$ MPa, corresponding to a 0.2% residual (plastic) strain. In particular, after the proportional limit, the Young's modulus of the liner pipe material is gradually decreased up to the value of 0.9% of the strain, while after that value, the post-yield modulus is equal to 1524 MPa. In Table 5, the material properties of the outer and liner pipe are summarized.

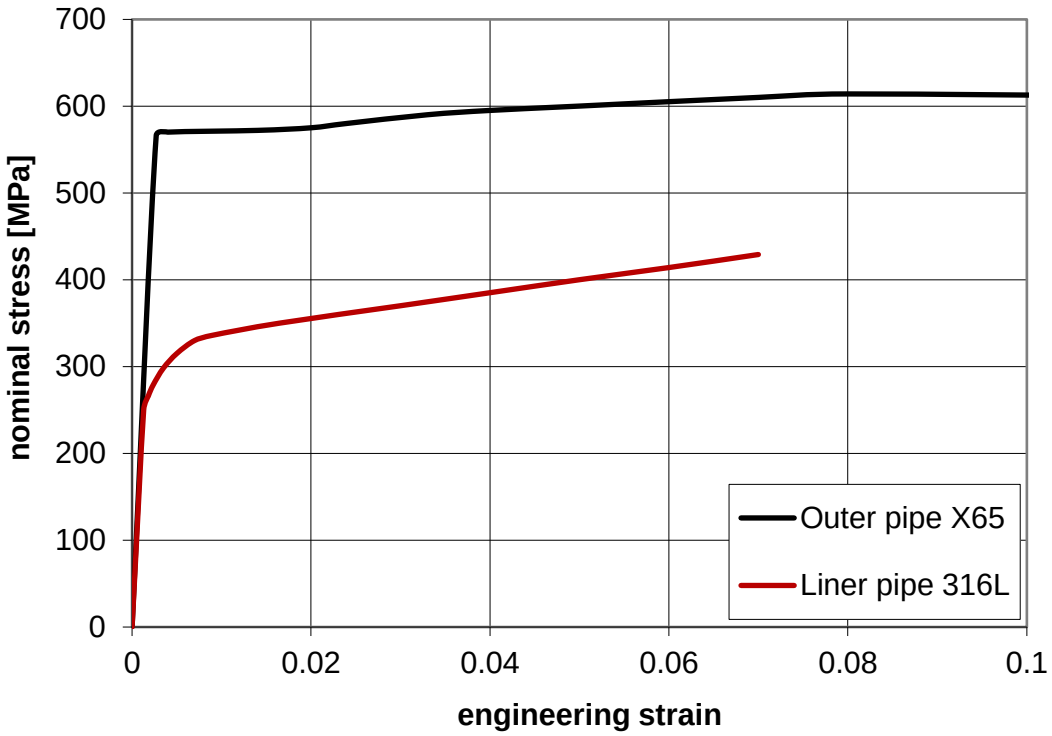

Figure 97: *Stress-strain curves of the outer pipe and liner pipe materials.*

	Outer pipe	**Liner pipe**
Material	API 5L Grade X65	AISI 316L
Yield stress	$\sigma_{Y,o} = 566$ MPa	$\sigma_{Y,l} = 298$ MPa
Young's modulus	$E_o = 210000$ MPa	$E_l = 193000$ MPa
Poisson's ratio	$\nu = 0.3$	$\nu = 0.3$

Table 5: *Material properties of outer and liner pipe.*

The present analysis focuses on three pipes of 12-inch nominal diameter, which are candidates for deep offshore pipeline applications. The first lined pipe, referred to as Pipe A, has outside diameter equal to 325 mm, the thickness of the outer and the liner pipe are 14.3 mm and 3 mm respectively, and has been tested experimentally under reel-bending conditions [11]. The outer diameter of the second pipe, denoted as Pipe B, is 335.4 mm, the thickness of the outer and the liner pipe equal to 19.5 mm and 3 mm respectively, and it has been tested experimentally under four-point bending [13]. Both pipes, A and B, have the same diameter and thickness for the liner pipe; 296.4 mm and 3 mm respectively. The third pipe considered in the present analysis, referred to as Pipe C, has outside diameter equal to 325 mm and the thickness of the outer pipe is 14.3 mm (similar to Pipe A), while the thickness of the liner pipe is 2.5 mm. In Table 6, the geometrical properties of the used Lined Pipes are summarized.

	Lined Pipe A	**Lined Pipe B**	**Lined Pipe C**
External diameter of outer pipe D_o	325 mm	335.4 mm	325 mm
Thickness of outer pipe t_o	14.3 mm	19.5 mm	14.3 mm
External diameter of liner pipe D_l	296.4 mm	296.4 mm	296.4 mm
Thickness of liner pipe t_l	3 mm	3 mm	2.5 mm
Residual hoop stress of liner σ_{res}	166 MPa	172 MPa	170 MPa

Table 6: *Geometrical properties of the used lined pipes.*

In each case, the liner and the outer pipe are initially in frictionless contact. The lined pipe is considered either stress-free (referred to as snug-fit pipe, SFP) or with an initial stress (referred to as tight-fit pipe, TFP). In the case of TF Pipes, an initial hoop stress of

magnitude of 200 MPa (67.1% of the liner material yield stress) is applied initially on the liner pipe followed by an unloading step, resulting in a final (residual) hoop stress for the liner pipe σ_{res}, equal to 166 MPa, 172 MPa, and 170 MPa for TFP A, B, and C respectively. This level of prestress is equal to 55.7%, 57.7%, and 57% of the liner material yield stress for TFP A, B, and C respectively. Residual stress measurements of the pipes tested in [11] and [13] indicated that the residual compressive hoop stress in the liner can vary from 50 MPa to 200 MPa, depending on the parameters of the manufacturing process, as discussed in Appendix B. In the followings, using the numerical tools described previously in the section 3.2, an ovalization analysis is conducted first, followed by an investigation of liner pipe wrinkling and comparison with test results.

In the following results for lined steel pipes, the values of curvature are normalized by $k_I = t_o / d_o^2$ (also adopted in [2]) where t_o, d_o are the thickness and the mean diameter of the outer pipe, so that $\kappa = k/k_I$. The detachment is normalized by the liner thickness t_l and the ovalization ζ of the liner is defined as $\left(d_{h,l} - d_{v,l}\right)/2d_l$ where $d_{h,l}$ is the current (deformed) mean diameter in the horizontal direction of the liner, $d_{v,l}$ is the current mean diameter in the vertical direction, and d_l is the initial mean diameter of the liner. The value of bending moment M is normalized by $M_0 = \sigma_{Y,o} d_o^2 t_o$, so that $m = M/M_0$, where $\sigma_{Y,o}$ is the yield stress of the outer pipe. The local hoop curvature ($1/r_{\theta 0}$), and the axial stress (σ_{x0}) or hoop stress ($\sigma_{\theta 0}$) of the liner, both measured at $\theta = 0$ (maximum compression point), are normalized by the initial hoop curvature of the liner $1/r_l$ and the yield stress $\sigma_{Y,l}$ of the liner material respectively.

3.4.1 Ovalization analysis

To understand the mechanical response of the lined steel pipe, an ovalization analysis is conducted first and the results are shown in Figures 98, Figures 99, and Figures 100, in terms of the normalized values of detachment (Δ) between the liner and the outer pipe at $\theta = 0$, liner ovalization (ζ), and bending moment (m) respectively, plotted against the normalized value of applied bending curvature (κ). Furthermore, in Figures 101, Figures 102, and Figures 103, local hoop curvature $(1/r_{\theta 0})$, axial stress (σ_{x0}), and hoop

(circumferential) stress $(\sigma_{\theta 0})$ at $\theta = 0$ (maximum compression point) are plotted in terms of κ. An important observation from the ovalization analysis in Figures 98 is the detachment growth between the liner and the outer pipe. In the case of SF Pipes, the detachment occurs as soon as bending is applied, whereas for the TF Pipes, the detachment initiates at a later stage due to the effect of prestressing. On the other hand, Figures 99, Figures 101, and Figures 102, indicate that liner prestressing has a rather negligible effect on liner ovalization, local hoop curvature, and longitudinal stress. Furthermore, the development of hoop stress at the critical location $(\theta = 0)$ indicates that after the first stages of deformation, hoop prestressing is practically lost, so that the hoop stress values from SFP and TFP are very similar, as shown in Figures 103. In addition, it is observed that the liner detachment of TFP (Figures 98) occurs at the bending curvature that hoop prestressing is practically lost (Figures 103). Finally, it is interesting to note that the normalized curves $\zeta - \kappa$, $m - \kappa$, $1/r_{\theta 0} - \kappa$, $\sigma_{x0} - \kappa$, and $\sigma_{\theta 0} - \kappa$ for TF Pipes A, B, and C are quite similar.

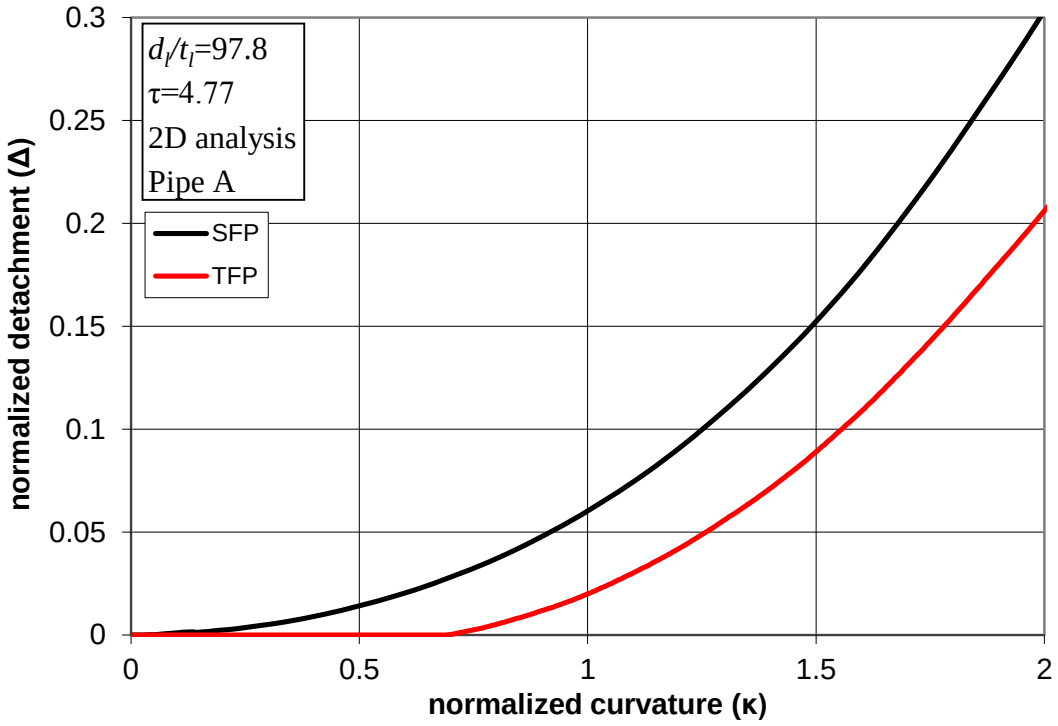

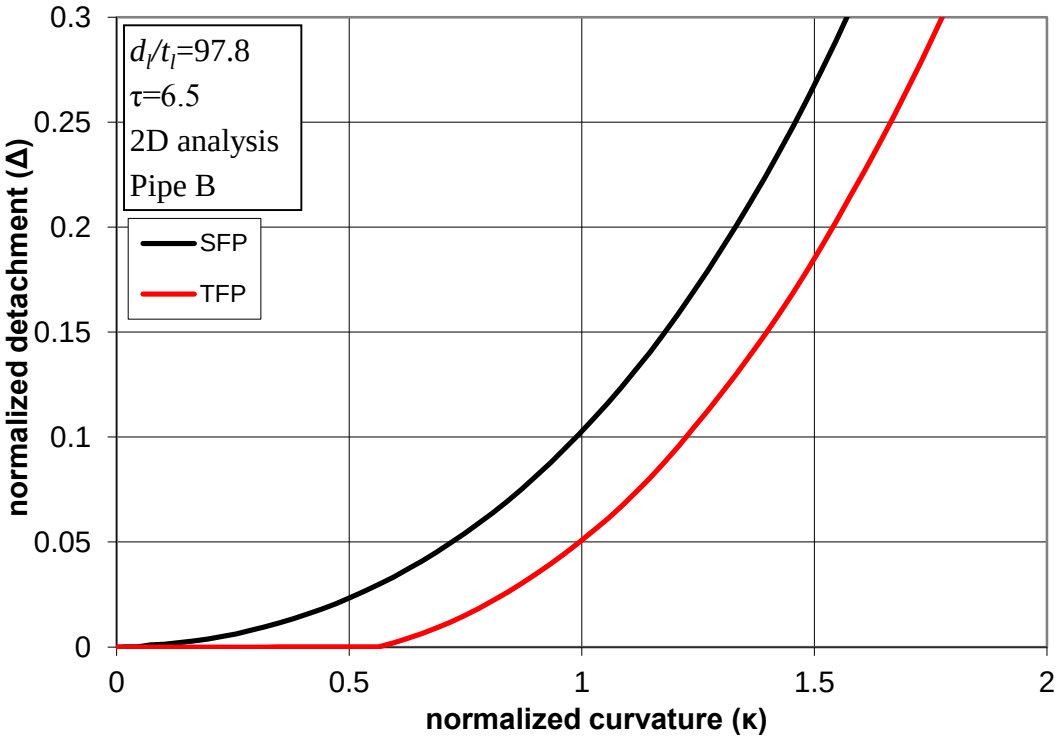

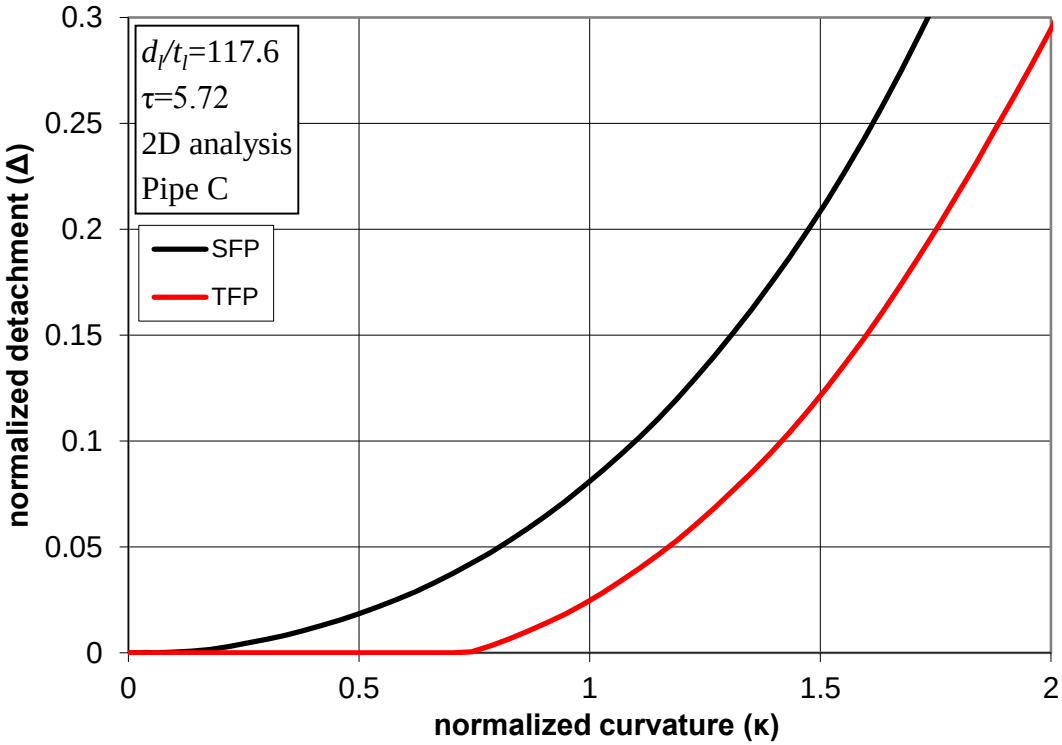

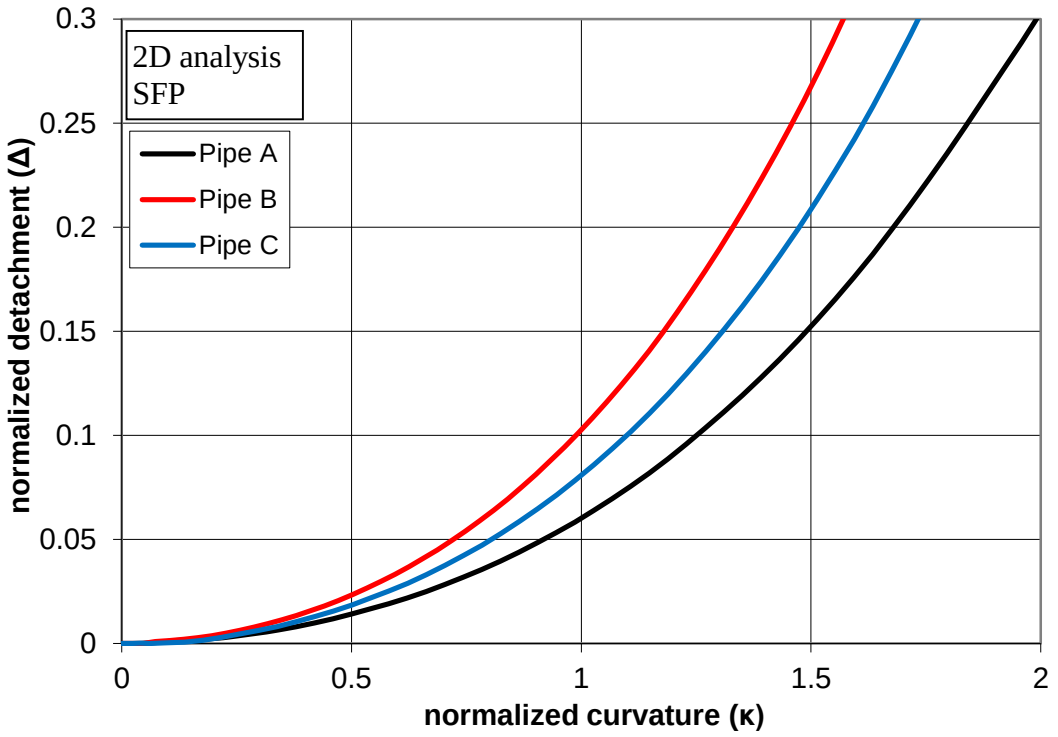

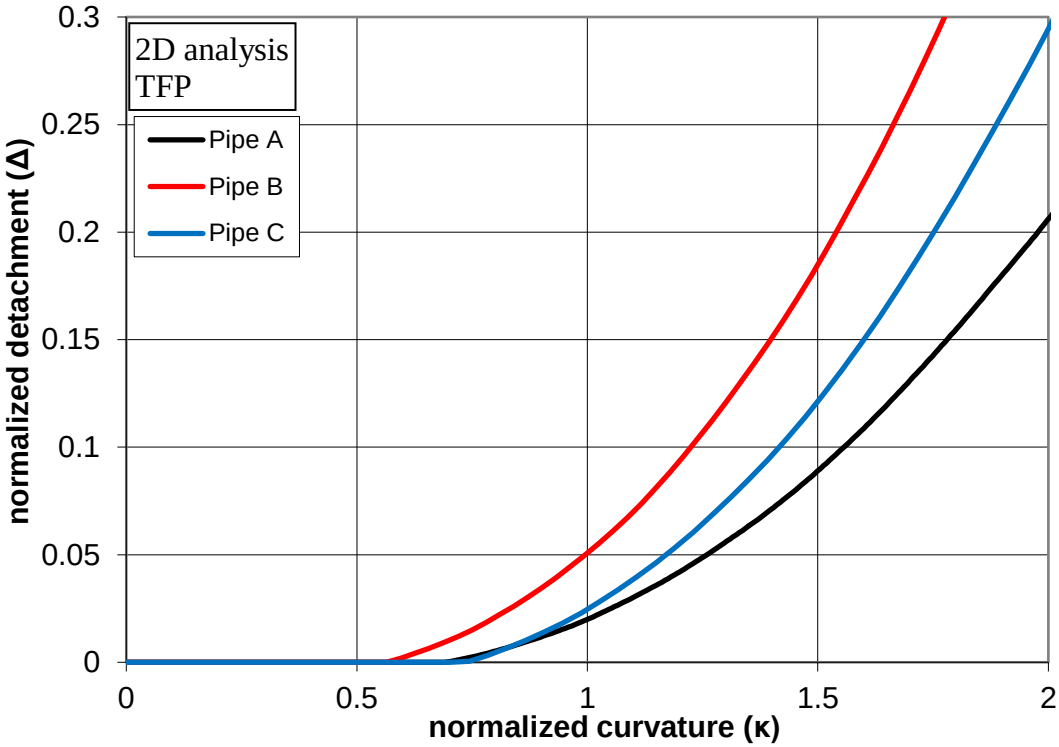

Figures 98: *(a),(b),(c) Detachment between liner and outer pipe in terms of bending curvature for Lined Pipes A, B and C, (d),(e) Comparison of detachment in Lined Pipes A, B and C for Snug-Fit Pipes and Tight-Fit Pipes; ovalization (2D) analysis.*

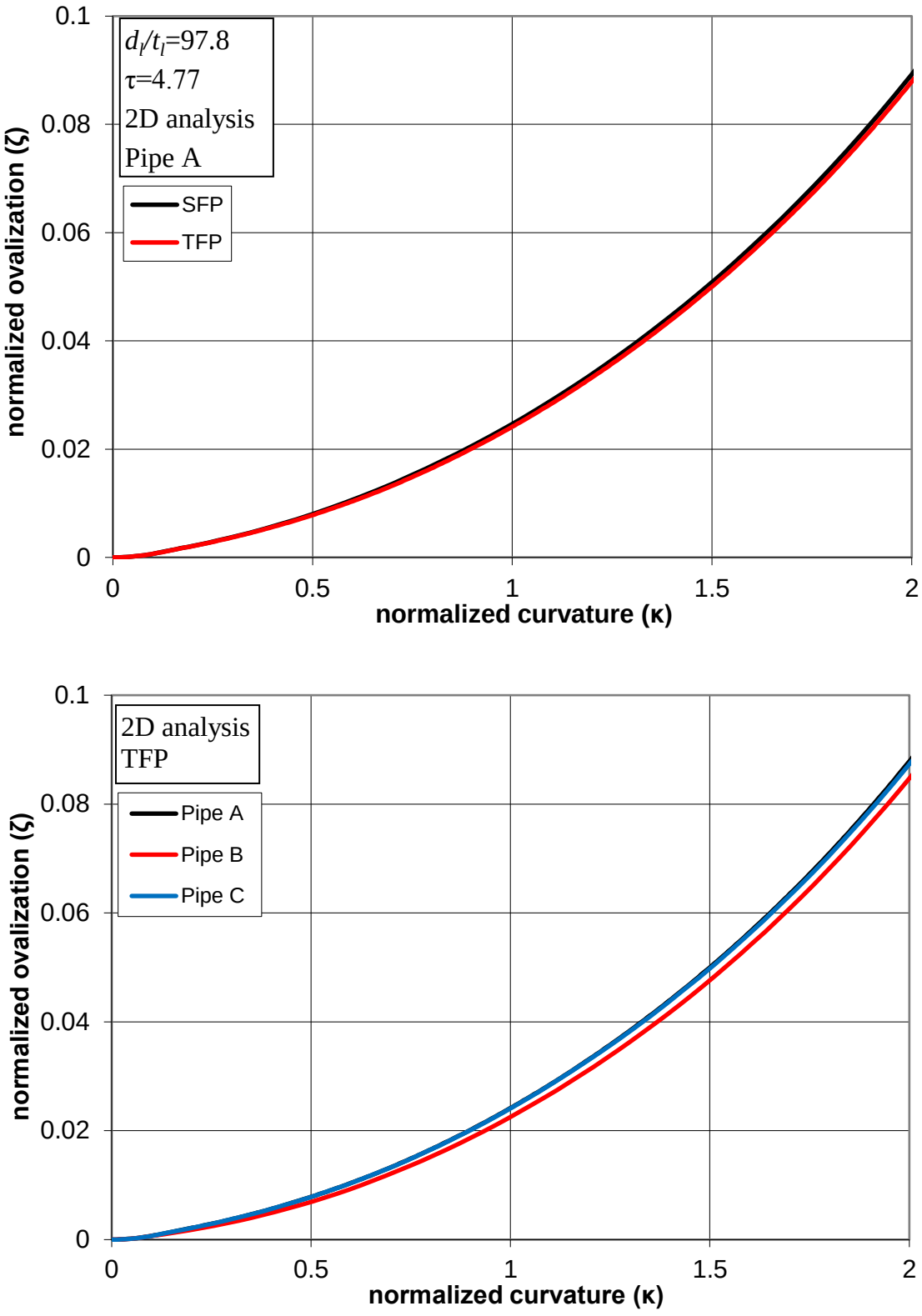

Figures 99: *(a) Ovalization of liner pipe in terms of bending curvature for Pipe A, (b) Comparison of ovalization in Tight-Fit Pipes A, B and C; ovalization (2D) analysis.*

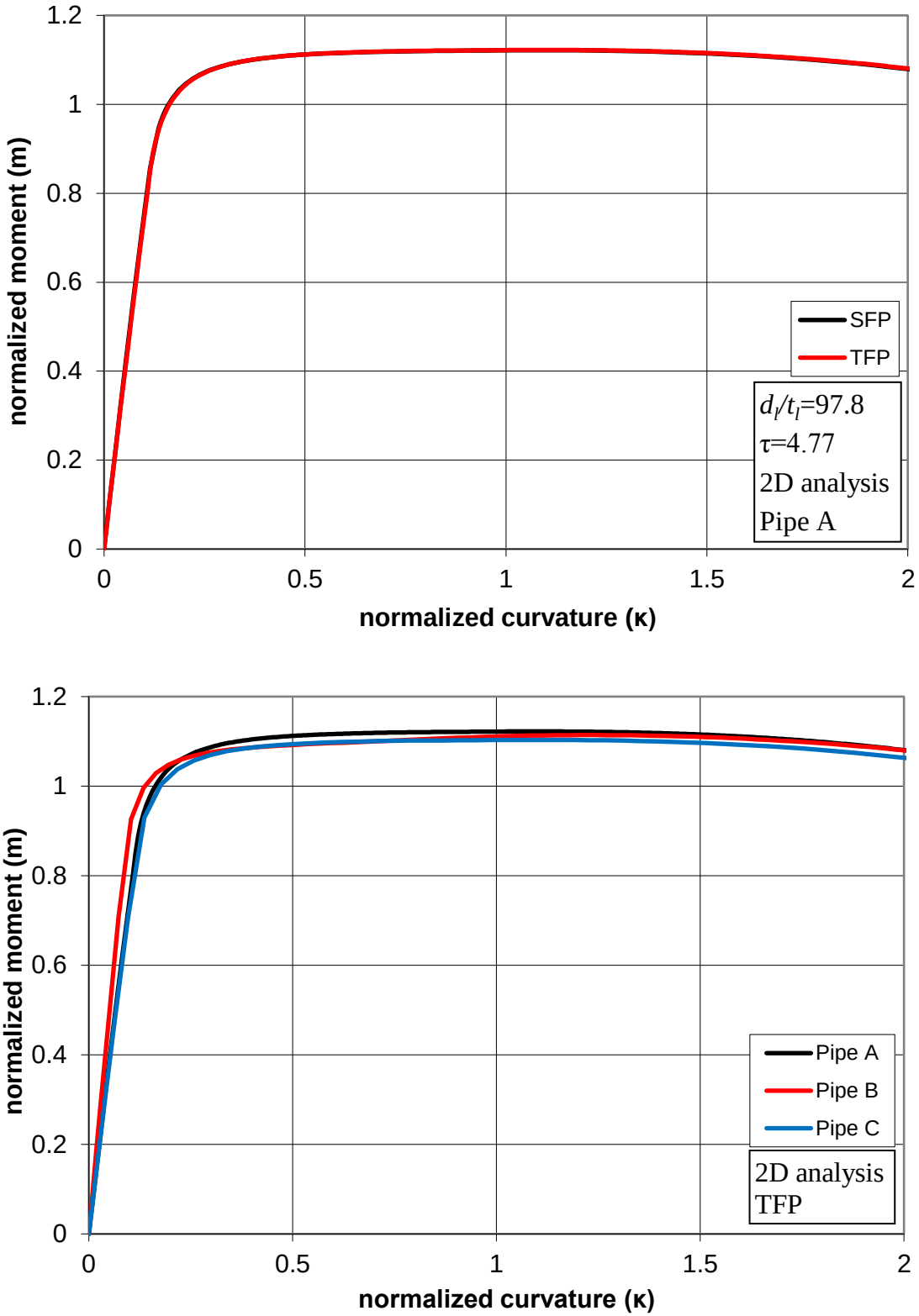

Figures 100: *(a) Bending moment in terms of bending curvature for Pipe A, (b) Comparison of applied bending moment in Tight-Fit Pipes A, B and C; ovalization (2D) analysis.*

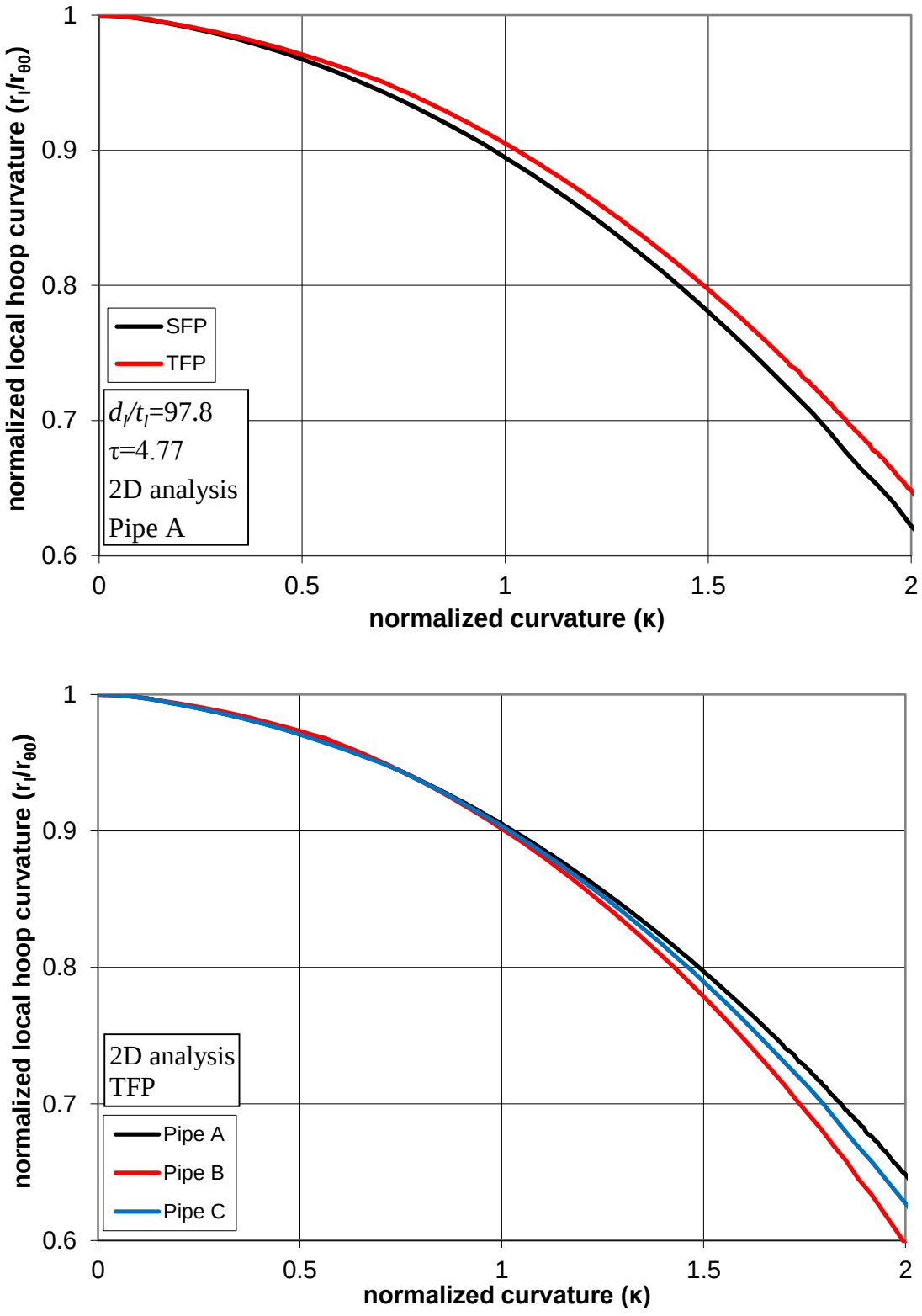

Figures 101: *(a) Local hoop curvature at* $\theta = 0$ *in terms of bending curvature for Pipe A, (b) Comparison of local hoop curvature at* $\theta = 0$ *in Tight-Fit Pipes A, B and C; ovalization (2D) analysis.*

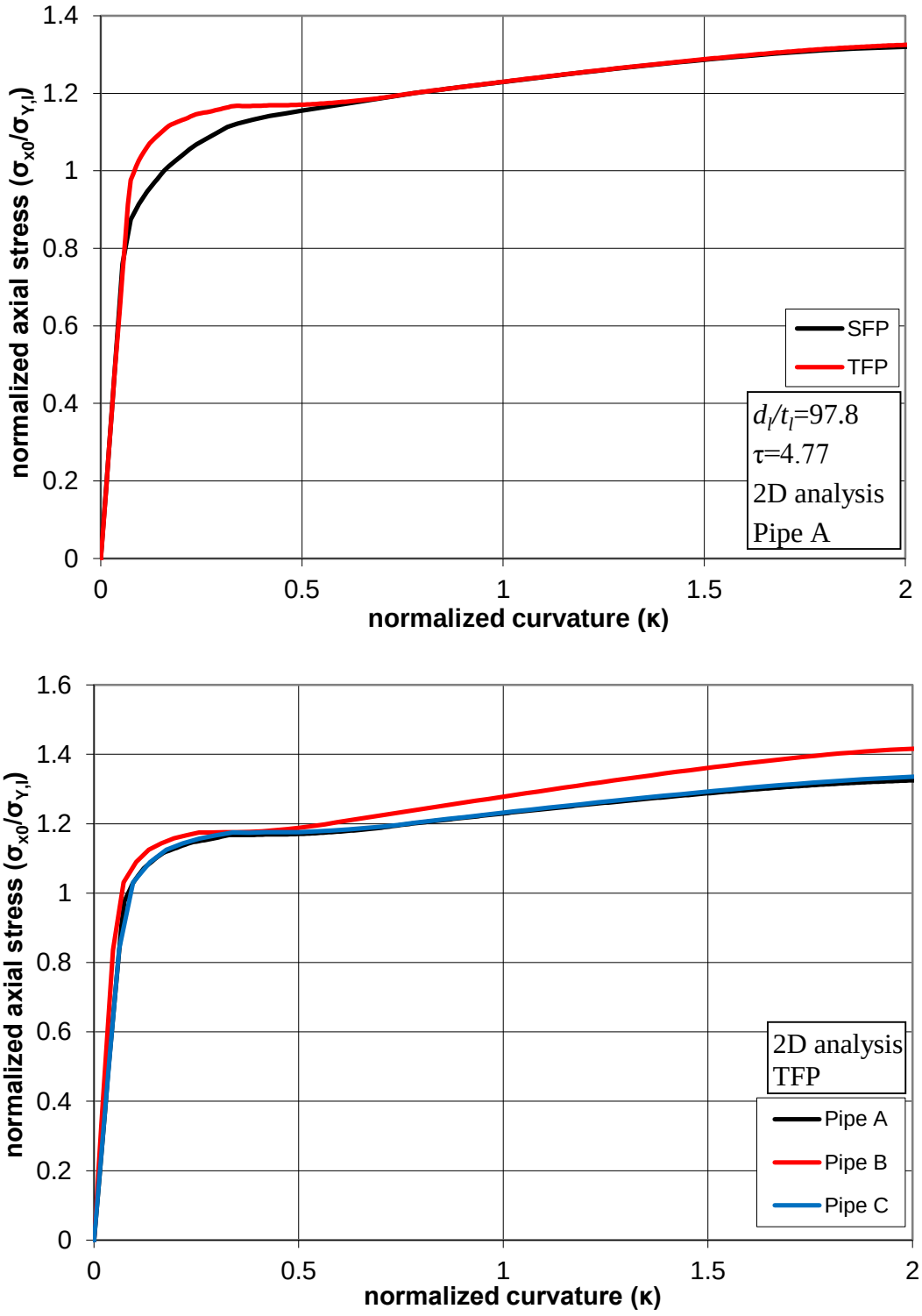

Figures 102: *(a) Axial (Longitudinal) stress at* $\theta = 0$ *in terms of bending curvature for Pipe A, (b) Comparison of axial stress at* $\theta = 0$ *in Tight-Fit Pipes A, B and C; ovalization (2D) analysis.*

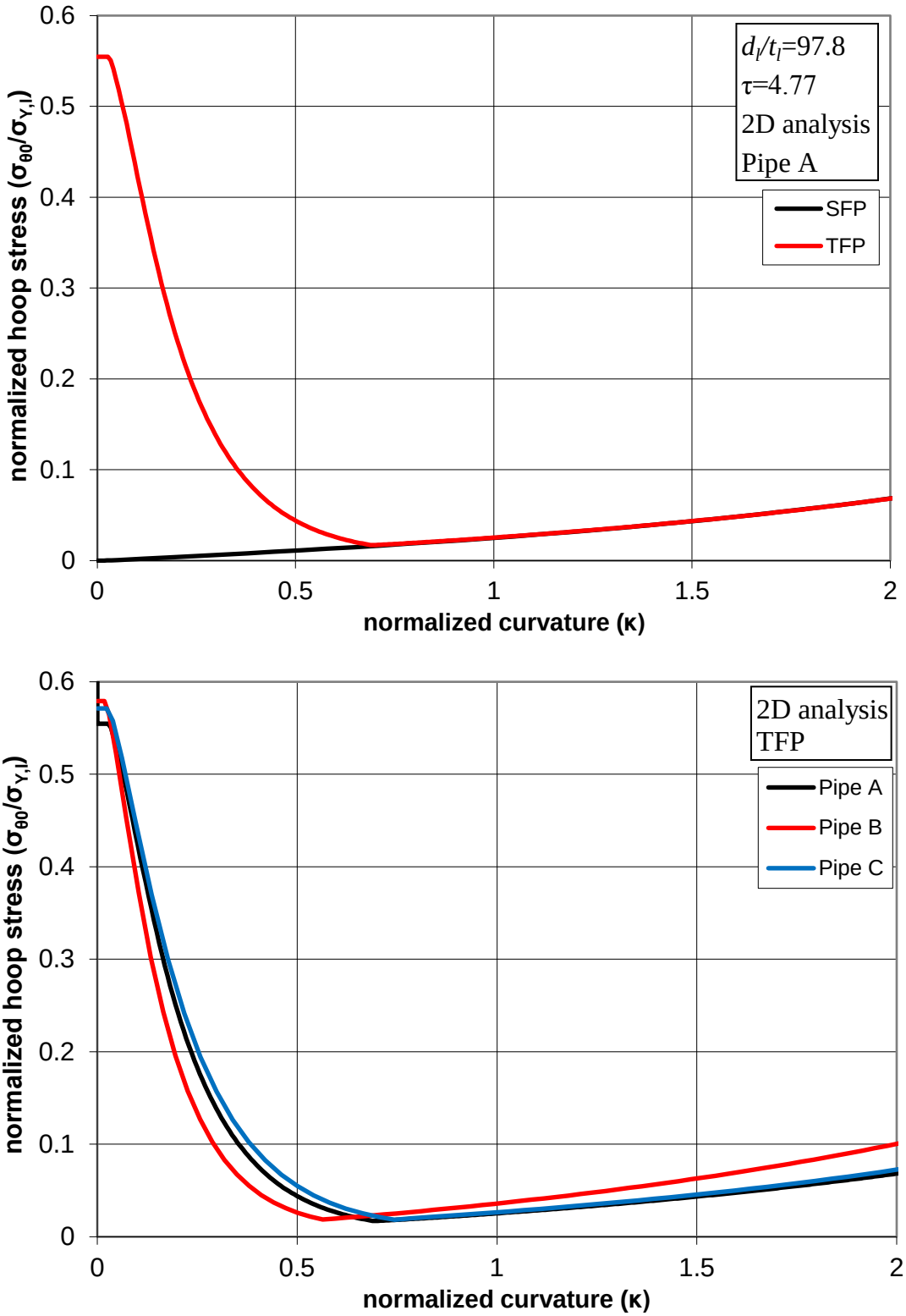

Figures 103: *(a) Hoop (Circumferential) stress at $\theta = 0$ in terms of bending curvature for Pipe A, (b) Comparison of hoop stress at $\theta = 0$ in Tight-Fit Pipes A, B and C; ovalization (2D) analysis.*

For the better understanding of the behavior in terms of the detachment (Δ), the Figures 98d is presented in Figure 104 without normalization of the detachment (Δ) and the curvature (κ). It is observed that the bigger the thickness of the outer pipe, the lower and slower the increase of the detachment during bending. Conversely, with decreasing the thickness of the liner pipe, the higher is the increase of the detachment.

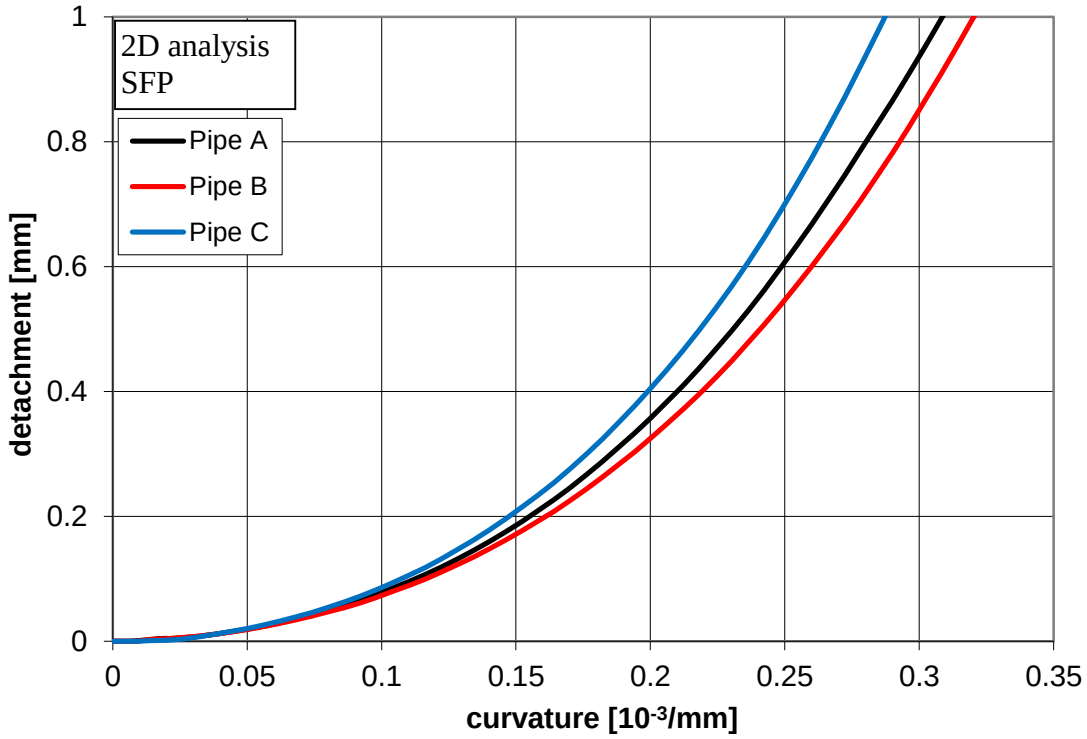

Figure 104: *Detachment between liner and outer pipe in terms of bending curvature for Snug-Fit Pipes A, B and C.*

Correspondingly, the Figures 99b which refers to the ovalization parameter (ζ) is presented in Figure 105 without normalization of the bending curvature (κ). It is observed, that the ovalization parameter of Pipe B, which has bigger thickness of the outer pipe, is smaller than the ovalization parameter of the other two pipes.

Furthermore, the Figures 100b which concerns the bending moment is presented in Figure 106 in a non-normalized form. The main conclusion is that with increasing the thickness of the outer pipe, the higher is the bending strength. In addition, the bigger is the thickness of the outer pipe, the higher is the curvature which corresponds to the maximum bending moment.

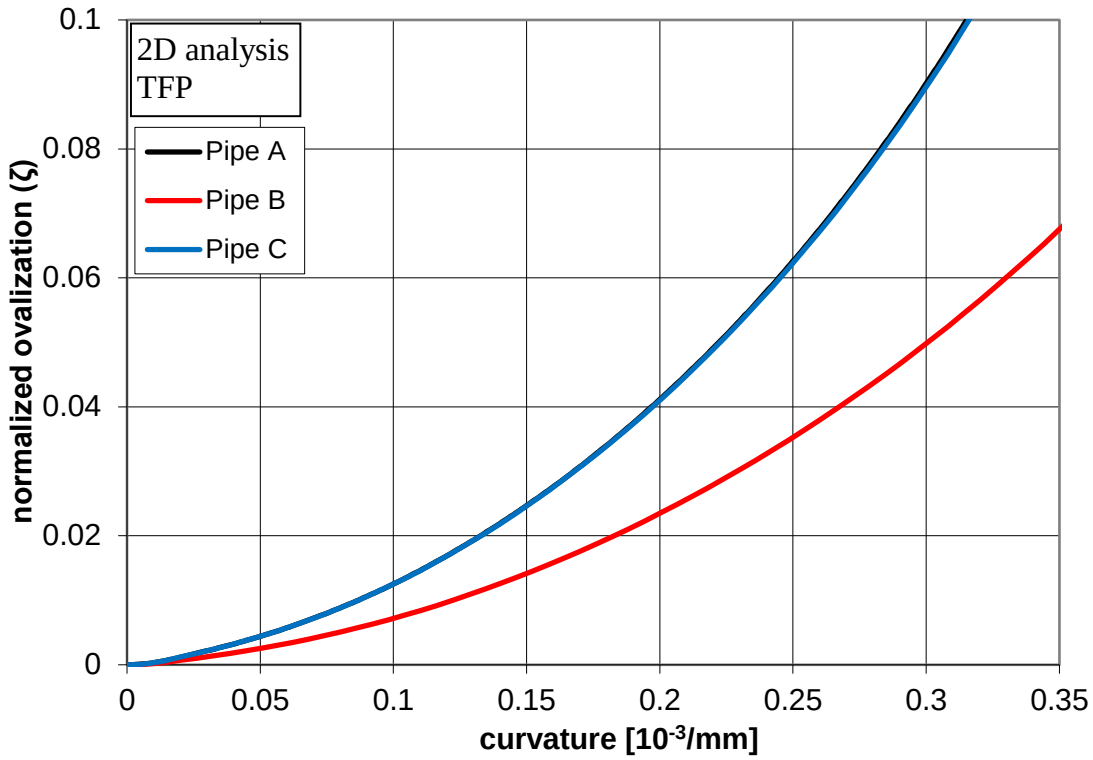

Figure 105: *Ovalization in terms of bending curvature for Snug-Fit Pipes A, B and C.*

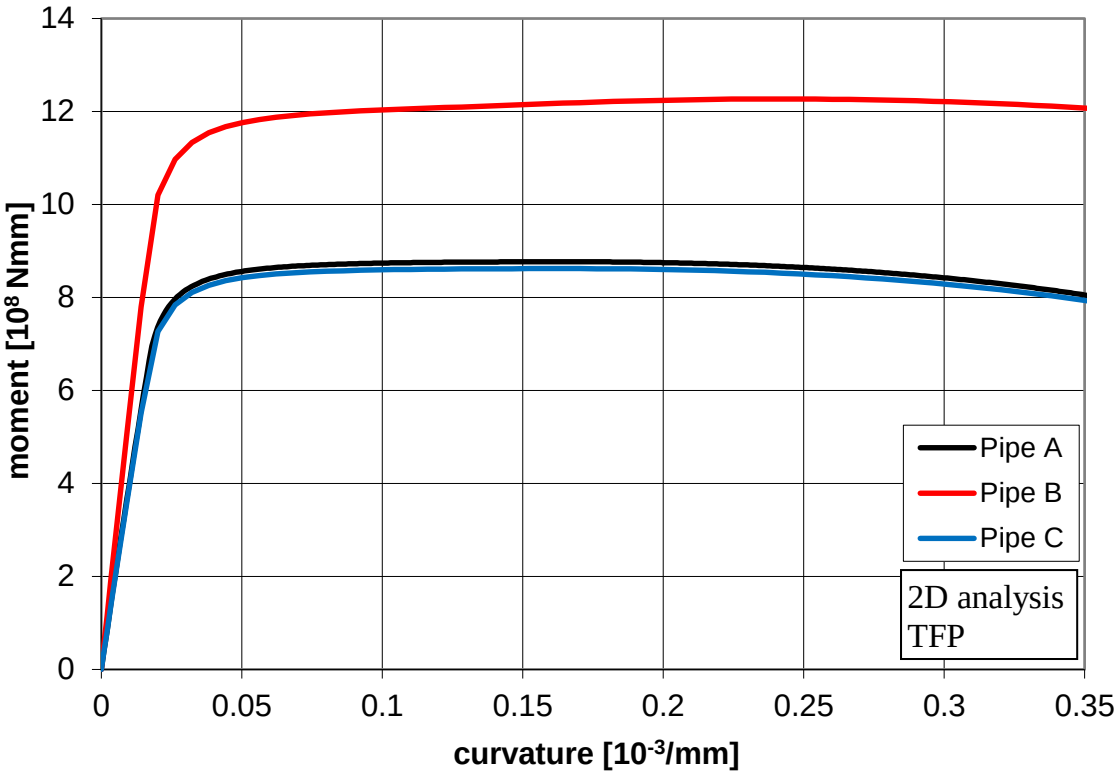

Figure 106: *Bending moment in terms of bending curvature for Snug-Fit Pipes A, B and C.*

The results presented in this subsection verify the conclusion derived from section 3.3 for elastic pipes that the thickness of the outer pipe has a prominent effect on the structural behavior of lined pipe. In particular, that the outer pipe thickness determines the stiffness of the confinement. However, unlike the case of elastic pipes, in case of steel pipes, the increase of axial and hoop stresses (Figures 102 and Figures 103) after the first stages of bending loading results in the development of plastic deformations at the critical location $(\theta = 0)$. Figure 107 depicts the development of the equivalent plastic strain at this location in terms of bending curvature for the Snug-Fit Pipes A, B, and C. It is concluded that the Pipe B, which has bigger outer pipe thickness than Pipes A and C, presents higher increase of plastic strains during bending deformation. This conclusion is expected to affect the buckling behavior of the lined steel pipes.

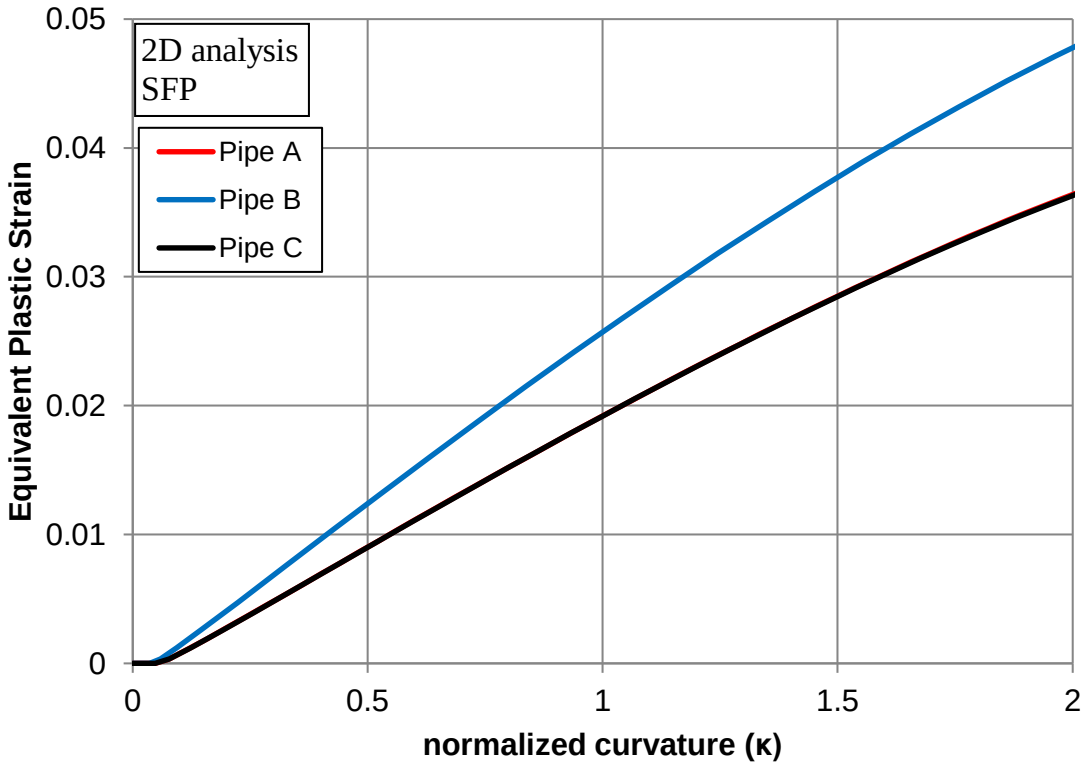

Figure 107: *Equivalent plastic strain of the liner pipe at the critical location* $(\theta = 0)$ *in terms of bending curvature for Snug-Fit Pipes A, B and C.*

After the investigation of the ovalization (2D) mechanical response of the lined steel pipes, a three-dimensional analysis is conducted in the next subsection in order to examine the bifurcation of the liner pipe from a uniform ovalization stage to a uniform (periodic) wrinkling pattern.

3.4.2 Uniform wrinkling

The possibility of transition from a uniform ovalization state along the pipe to a wrinkling pattern of periodic shape is investigated in the present subsection for both SF Pipes and TF Pipes. To simulate this bifurcation in a rigorous manner, a three-dimensional analysis of a pipe segment of length equal to one half-wavelength L_{hw} is considered. As noted in the previous section, the value of L_{hw} is unknown and, therefore, a series of analyses are conducted. The correct (critical) value of L_{hw} is the one that corresponds to the smallest value of buckling curvature κ_{cr}. The results for those series of analyses are shown in Figures 108 with an arrow (↑), where the critical values of normalized half-wavelength $l_{hw} = L_{hw} \big/ \sqrt{d_l t_l}$ are equal to 1.45 for Pipes A and B, and 1.47 for Pipe C in the absence of initial imperfections. It is interesting to note that initial stresses (prestress) in the liner do not affect the value of normalized half-wavelength l_{hw}.

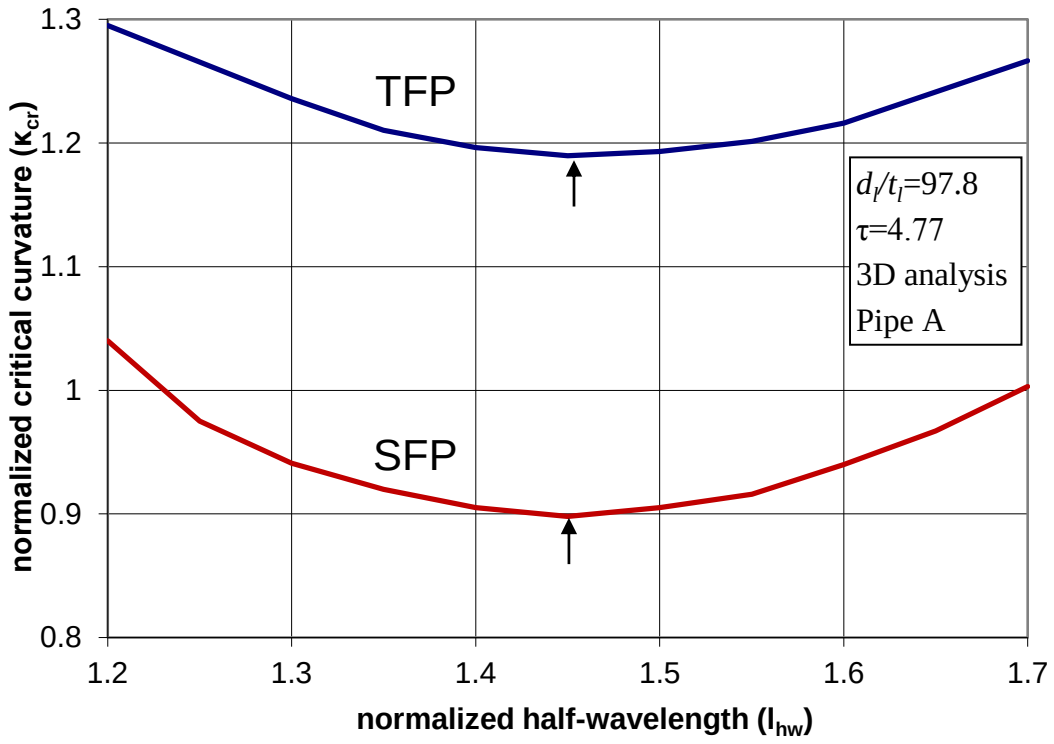

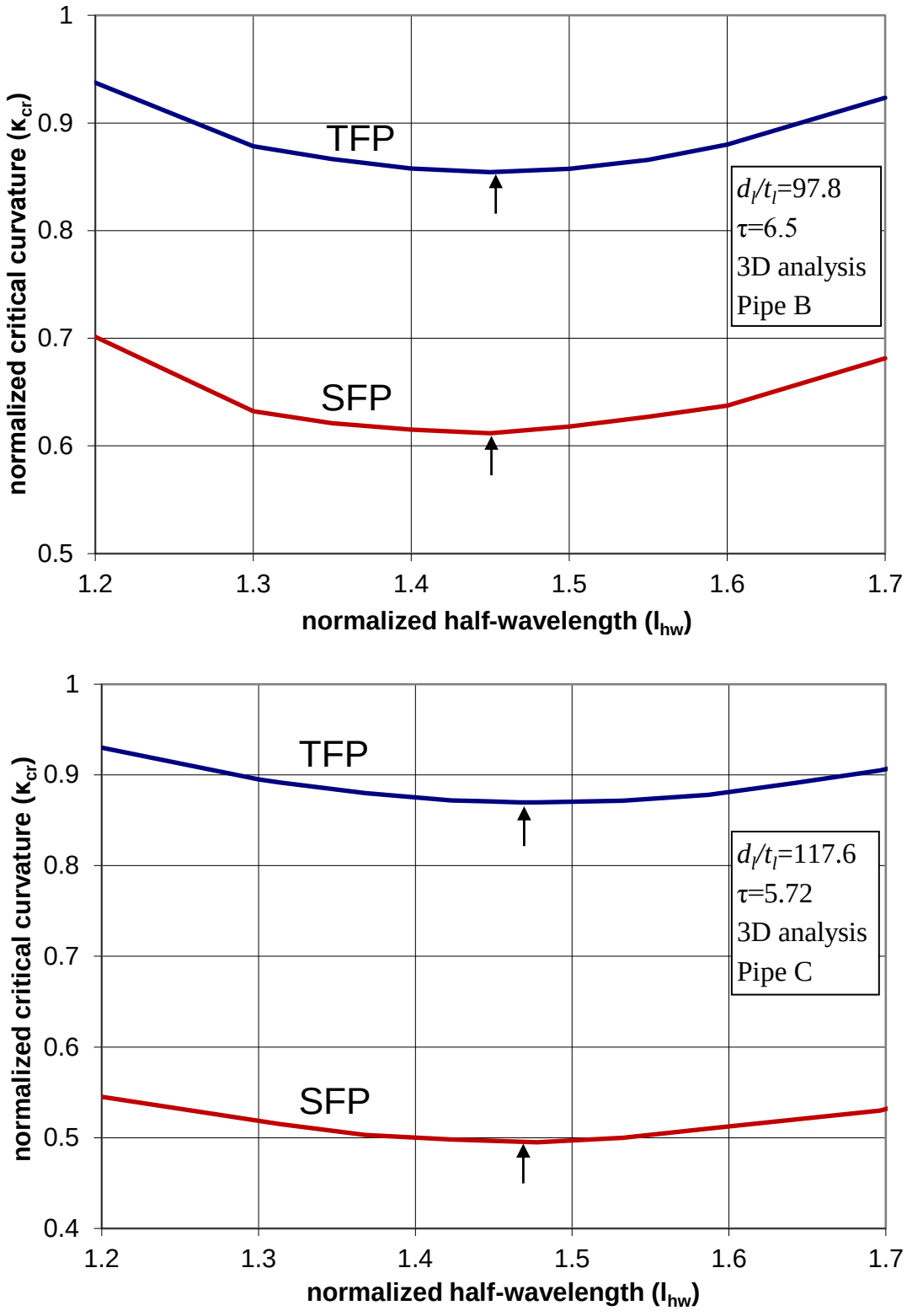

Figures 108: *Variation of buckling curvature* κ_{cr} *with respect to the assumed value of half-wavelength* l_{hw} *in Pipes A, B and C.*

In Figures 109, the detachment of points (1) and (2) are plotted in terms of the applied bending curvature for the lined pipes A, B, and C. The numerical results also indicate that, in contrast with the case of lined elastic pipes, the development of this wavy pattern is not sudden, in the sense that the two curves separate gradually implying a "tangential" type of bifurcation with no distinct point. The smooth transition from pre-buckling to post-buckling in lined steel pipes facilitates its numerical simulation, so that the introduction of a negligible imperfection may not be necessary. The numerical results in Figures 108 and Figures 109 have been obtained without imposing any initial imperfection on the liner pipe and convergence problems have not been observed. Nevertheless, because of this "tangential" bifurcation, the definition of buckling curvature κ_{cr} based on the deviation of the two curves may be rather ambiguous. In the present work, to overcome this ambiguity, the buckling (critical) curvature κ_{cr} is defined as the curvature at which the detachment of point (2) in Figures 109 reaches a maximum value and begins to decrease. Using this definition, the values of κ_{cr} are equal to 0.898 and 1.19 for the SFP and TFP of Pipe A respectively, as shown in Figures 109a. For the Pipe B, the values of critical curvature κ_{cr} are equal to 0.612 and 0.854 for the SFP and TFP respectively (Figures 109b), whereas for the Pipe C, the corresponding κ_{cr} values are equal to 0.495 and 0.870 for the SFP and TFP respectively (Figures 109c). The critical curvature corresponds to a value of detachment (Δ) equal to 4% and 3.4% of the liner wall thickness t_l for SFP A and TFP A respectively. The corresponding values of detachment (Δ) are for SFP B and TFP B equal to 3.1% and 2.4% of t_l respectively and to a value of detachment (Δ) equal to 1.65% and 1.13% of t_l for SFP C and TFP C respectively. These values of detachment are less than 5% of the liner pipe thickness t_l, implying that the wave height corresponding to first bifurcation is quite small, and therefore, it is rather difficult to be detected experimentally. The above values of critical curvature κ_{cr} and normalized detachment (Δ) are summarized following in Table 7. The corresponding buckling shape is a uniformly-wave pattern, which is very similar to the shape presented in the previous section for elastic pipes, shown in Figures 92.

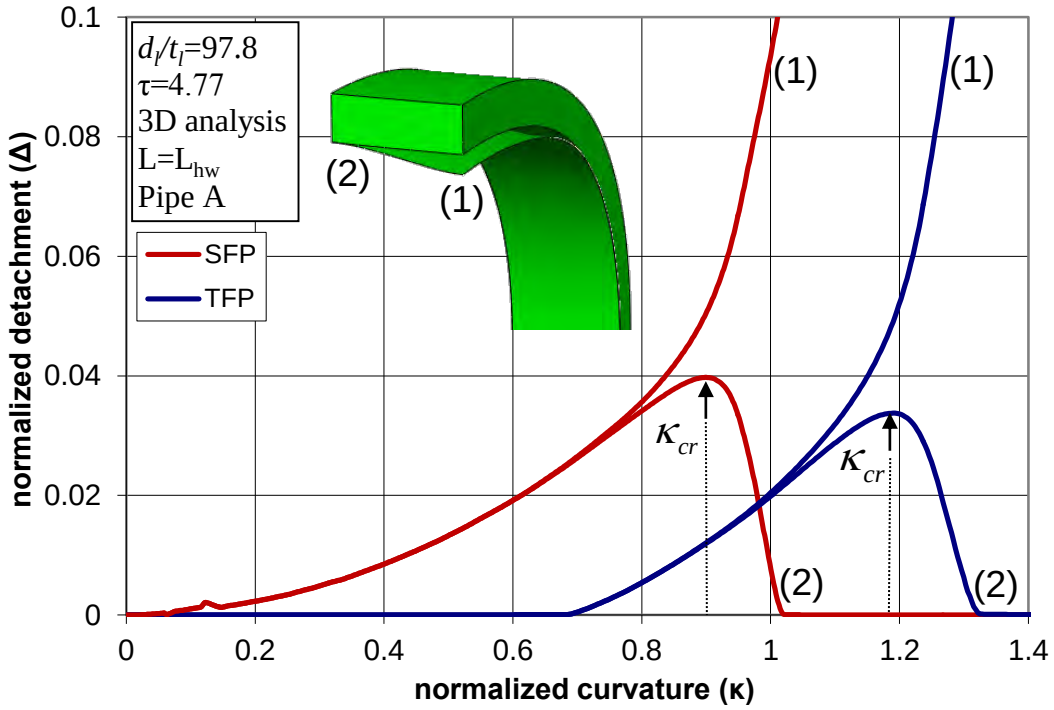

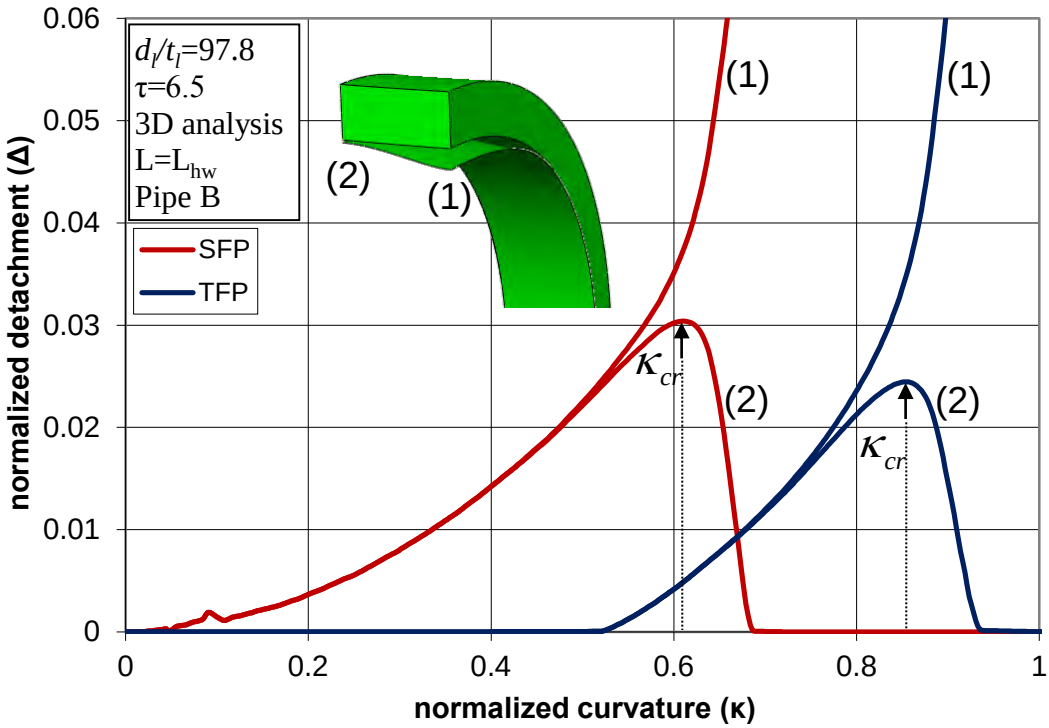

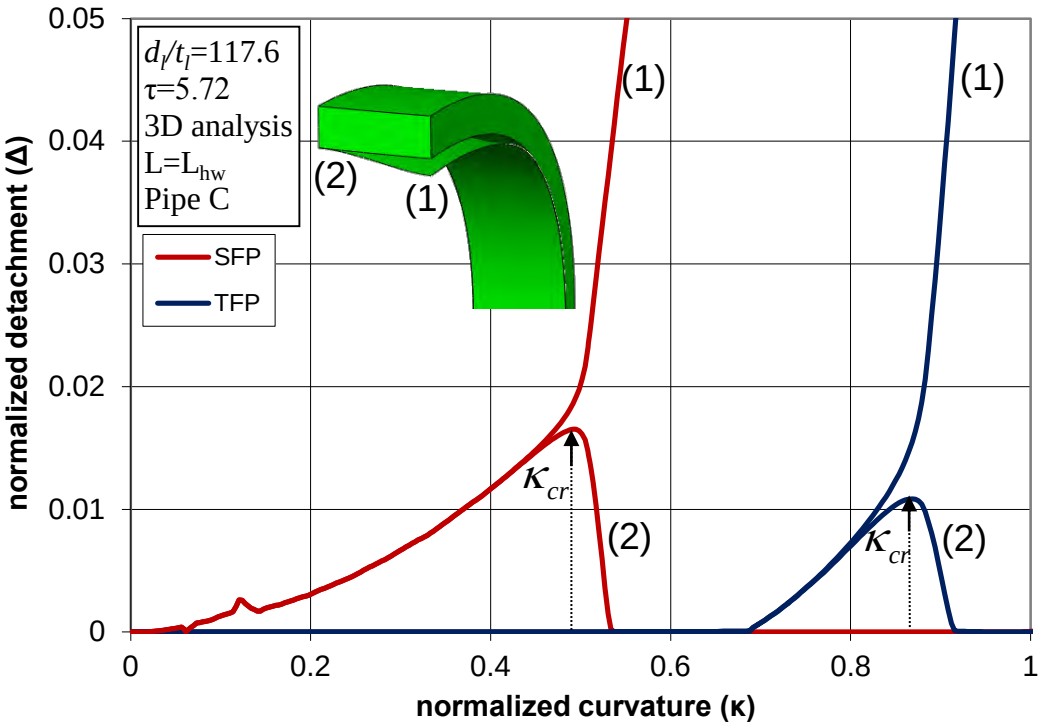

Figures 109: *Detachment development of points (1) and (2) in terms of bending curvature for Pipes A, B and C.*

	Lined Pipe A	**Lined Pipe B**	**Lined Pipe C**
critical curvature κ_{cr} for SFP	0.898	0.612	0.495
normalized detachment (Δ) for SFP	4%	3.1%	1.65%
critical curvature κ_{cr} for TFP	1.19	0.854	0.870
normalized detachment (Δ) for TFP	3.4%	2.4%	1.13%

Table 7: *Critical curvature κ_{cr} and normalized detachment (Δ) for lined pipes A, B and C.*

Comparing the bending behavior of SFP and TFP in terms of uniform wrinkling, an important conclusion is that pipe prestressing has a beneficial effect on the critical curvature κ_{cr} of the liner pipe. On the other hand, the buckling half-wavelength L_{hw} appears to be unaffected by the presence of prestressing.

For the better understanding of the behavior in terms of the detachment (Δ), Figures 109 are presented in Figures 110 without normalization of the detachment and the curvature. It is important to note that although the Pipe A presents bigger development of

detachment than the Pipe B, wrinkling of liner pipe B appears earlier than the one of pipe A. This is justified by the fact that the stresses at the critical location (Figures 102 and Figures 103) for Pipe B are increased in a higher tempo than the ones of Pipe A, resulting in higher plastic strains (Figure 107) which lead to uniform wrinkling of the liner pipe.

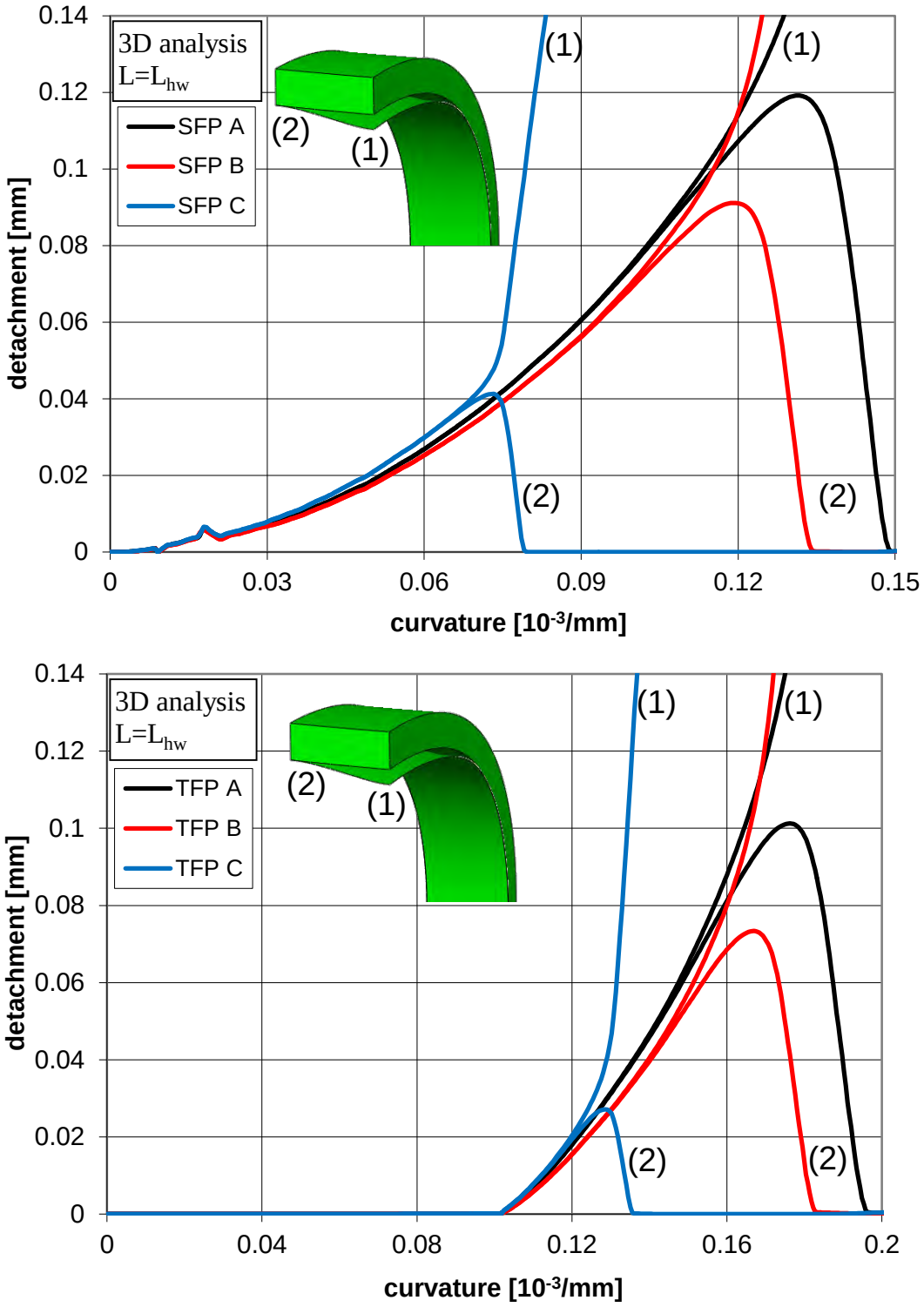

Figures 110: *Detachment development of points (1) and (2) in terms of bending curvature for SFP and TFP. Comparison between Lined Pipes A, B and C.*

The effect of friction in the interface between the liner and the outer pipe on the structural response of lined steel pipes is investigated in this stage for the case of lined pipe A without prestressing (SFP A). The numerical results of the detachment development in terms of bending curvature for different values of the friction coefficient μ are shown in Figure 111. The results demonstrate that the bigger the friction coefficient, the smaller and slower the development of the detachment, which as a consequence results in a higher critical bending curvature κ_{cr}. In other words, the presence of friction in the interface between the liner and the outer pipe has a beneficial effect on the wrinkling response of lined pipes.

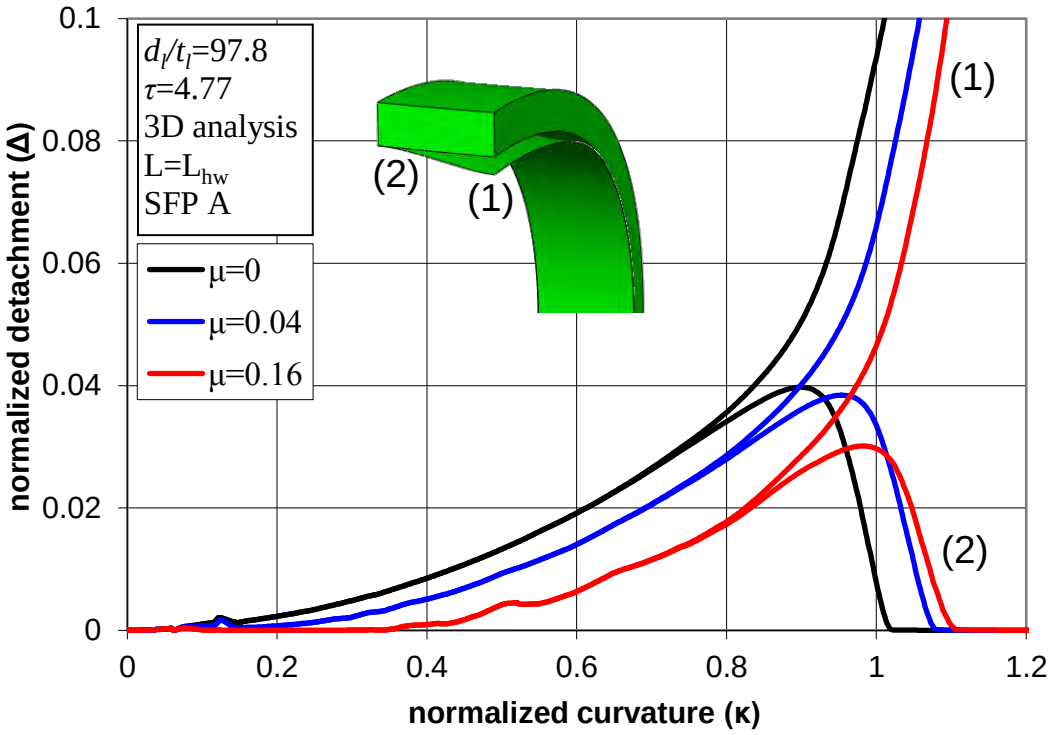

Figure 111: *Detachment development of points (1) and (2) in terms of bending curvature for SFP A for different values of the friction coefficient* μ.

3.4.3 Simplified analytical bifurcation solution

Based on the previous results of ovalization analysis, an attempt is made to develop a simplified formulation for predicting wrinkling of the liner pipe similar to the one proposed in the previous section for elastic pipes. According to the "local buckling hypothesis", buckling will occur at the critical location $(\theta = 0)$ when the axial stress σ_{x0} and hoop curvature $1/r_{\theta 0}$ satisfy the following equation, which is similar to equation (65):

$$\sigma_{x0} = \left[\frac{C_{11}C_{22} - C_{12}^2}{3}\right]^{1/2} \left(\frac{t_l}{r_{\theta 0}}\right), \tag{69}$$

where C_{ij} are the material moduli for elastic-plastic behavior [25]. Assuming J_2–flow theory of plasticity for the C_{ij} moduli and considering uniaxial uniform compression of the liner at the buckling zone,

$$\sigma_{x0} = \frac{E}{\sqrt{3\left[\left(1+4Q\sigma_{x0}^2\right)\left(1+Q\sigma_{x0}^2\right) - \left(\nu + 2Q\sigma_{x0}^2\right)^2\right]}} \left(\frac{t_l}{r_{\theta 0}}\right), \tag{70}$$

where

$$Q = \frac{1}{4\sigma_{x0}^2}\left(\frac{E}{E_T} - 1\right), \tag{71}$$

where E_T is the tangent modulus, and the local hoop curvature $1/r_{\theta 0}$ at the critical point is a function of the axial stress σ_{x0} obtained by the combination of results depicted in Figures 101 and Figures 102. Correspondingly, assuming J_2–deformation theory of plasticity for the C_{ij} moduli, the equation (69) takes the following form:

$$\sigma_{x0} = \frac{E_S}{\sqrt{3\left[\left(1+4q\sigma_{x0}^2\right)\left(1+q\sigma_{x0}^2\right) - \left(\hat{\nu}_s + 2q\sigma_{x0}^2\right)^2\right]}} \left(\frac{t_l}{r_{\theta 0}}\right), \tag{72}$$

where

$$q = \frac{1}{4\sigma_{x0}^2}\left(\frac{E_S}{E_T} - 1\right), \tag{73}$$

and

$$\hat{\nu}_s = \frac{1}{2} + \frac{E_S}{E}\left(\nu - \frac{1}{2}\right), \tag{74}$$

where E_S is the secant modulus. Equations (70) and (72) are solved using a standard iterative numerical scheme.

Furthermore, the corresponding buckling half-wavelength L_{hw} is estimated by the following equation, which is similar to equation (67), and refers to axisymmetric buckling of a uniformly compressed cylinder with radius $r_{\theta 0}$ [25]:

$$L_{hw} = \pi \left[\frac{C_{11}^2}{12\left(C_{11}C_{22} - C_{12}^2\right)} \right]^{1/4} \sqrt{r_{\theta 0} t_l} \,. \tag{75}$$

Assuming J_2–flow theory of plasticity for the C_{ij} moduli, one can write:

$$L_{hw,f} = \sqrt[4]{\frac{\pi^4 (1+Q\sigma_{x0}^2)^2}{12\left[\left(1+4Q\sigma_{x0}^2\right)\left(1+Q\sigma_{x0}^2\right) - \left(\nu + 2Q\sigma_{x0}^2\right)^2\right]}} \sqrt{r_{\theta 0} t_l} \,, \tag{76}$$

whereas, assuming the J_2–deformation theory moduli, the corresponding half-wavelength can be computed as follows:

$$L_{hw,d} = \sqrt[4]{\frac{\pi^4 (1+q\sigma_{x0}^2)^2}{12\left[\left(1+4q\sigma_{x0}^2\right)\left(1+q\sigma_{x0}^2\right) - \left(\hat{\nu}_s + 2q\sigma_{x0}^2\right)^2\right]}} \sqrt{r_{\theta 0} t_l} \,. \tag{77}$$

The buckling curvature of SF Pipes A, B, and C predicted by equation (70) for J_2–flow theory are equal to 0.3, 0.23, and 0.26 for SF Pipes A, B, and C respectively. Correspondingly, the buckling curvature predicted by equation (72) for J_2–deformation theory, are equal to 0.22, 0.17, and 0.20 for SF Pipes A, B, and C respectively, indicating a rather poor prediction of wrinkling initiation. On the other hand, the half-wavelength $L_{hw,f}$ predicted from equation (76) for J_2–flow theory is equal to 49 mm for both SF Pipe A and SF Pipe B, and corresponds to a normalized value of $l_{hw,f}$ equal to 1.65, which is in fairly good agreement with the one obtained by the three-dimensional numerical analysis (l_{hw} = 1.45) for both pipes. For SF Pipe C, the predicted value of $l_{hw,f}$ is equal to 1.55 ($L_{hw,f}$ = 41.9 mm), which also compares fairly well with the three-dimensional analysis prediction ($l_{hw} = 1.47$). Correspondingly, the half-wavelength $L_{hw,d}$ predicted from equation (77) for J_2–deformation moduli is equal to 37.2 mm for both SF Pipe A and SF Pipe B, corresponding to a normalized value of $l_{hw,d}$ equal to 1.25, whereas for SF Pipe C, the predicted value of $l_{hw,d}$ is equal to 1.24 ($L_{hw,d} = 33.5$ mm). The J_2–flow theory predictions for the half-wavelength value $L_{hw,f}$ are higher than the corresponding numerical values L_{hw}, whereas the J_2–deformation theory predictions $L_{hw,d}$ are lower than the numerical results. In general, assuming either J_2–flow moduli or J_2–deformation moduli, the analytical

equations (76) and (77) provide reasonable estimates for the buckling wavelength. The above analytical values for buckling curvature and half-wavelength are summarized and compared with the numerical results in Table 8.

	SFP A	**SFP B**	**SFP C**
buckling curvature κ_{cr} for J_2–flow	0.30	0.23	0.26
buckling curvature κ_{cr} for J_2–deformation	0.22	0.17	0.20
numerical value for buckling curvature	0.898	0.612	0.495
half-wavelength $L_{hw,f}$ for J_2–flow normalized half-wavelength $l_{hw,f}$	49 mm 1.65	49 mm 1.65	41.9 mm 1.55
half-wavelength $L_{hw,d}$ for J_2–deformation normalized half-wavelength $l_{hw,d}$	37.2 mm 1.25	37.2 mm 1.25	33.5 mm 1.24
numerical value for half-wavelength L_{hw} normalized half-wavelength l_{hw}	43.02 mm 1.45	43.02 mm 1.45	40.05 mm 1.47

Table 8: *Buckling curvature and half-wavelength for snug-fit pipes A, B and C.*

3.4.4 Second bifurcation

Upon first wrinkling, the height of the wrinkled pattern increases rapidly, as shown in Figures 109, due to the inward displacement of point (1), whereas point (2) is in contact with the outer pipe. Similar to the case of lined elastic pipes, the possibility of this wavy pattern to exhibit a second bifurcation is also examined, considering a pipe segment of length equal to $2L_{hw}$, where L_{hw} is the half-wavelength determined above. This consideration stems from experimental observations [11], where upon formation of uniform wrinkling ("wrinkling area 1" in Figure 75), one wrinkle is further developed to form the central (main) buckle, which is symmetric with respect to the plane of bending and denoted as A in Figure 75, and the adjacent wrinkles for the four lateral (minor) buckles, denoted as B ("wrinkling area 2"). The liner response is shown in Figures 112, Figures 113, and Figures 114, for Pipes A, B, and C respectively, in terms of the detachment of points (1), (2) and (3). In those Figures, the numerical results have been obtained without imposing any initial imperfections on the liner pipe. Initially, the response follows exactly the path obtained for uniform wrinkling, as shown in Figures 109, and the curves for points (1) and (3) coincide. After a certain level of bending curvature, the curves for points (1) and (3)

deviate, and transition from a uniform wavy pattern of Figures 92 to a new wavy shape is obtained, similar to the one shown in Figures 95 for elastic pipes, which is also similar to the experimental shape of Figure 75.

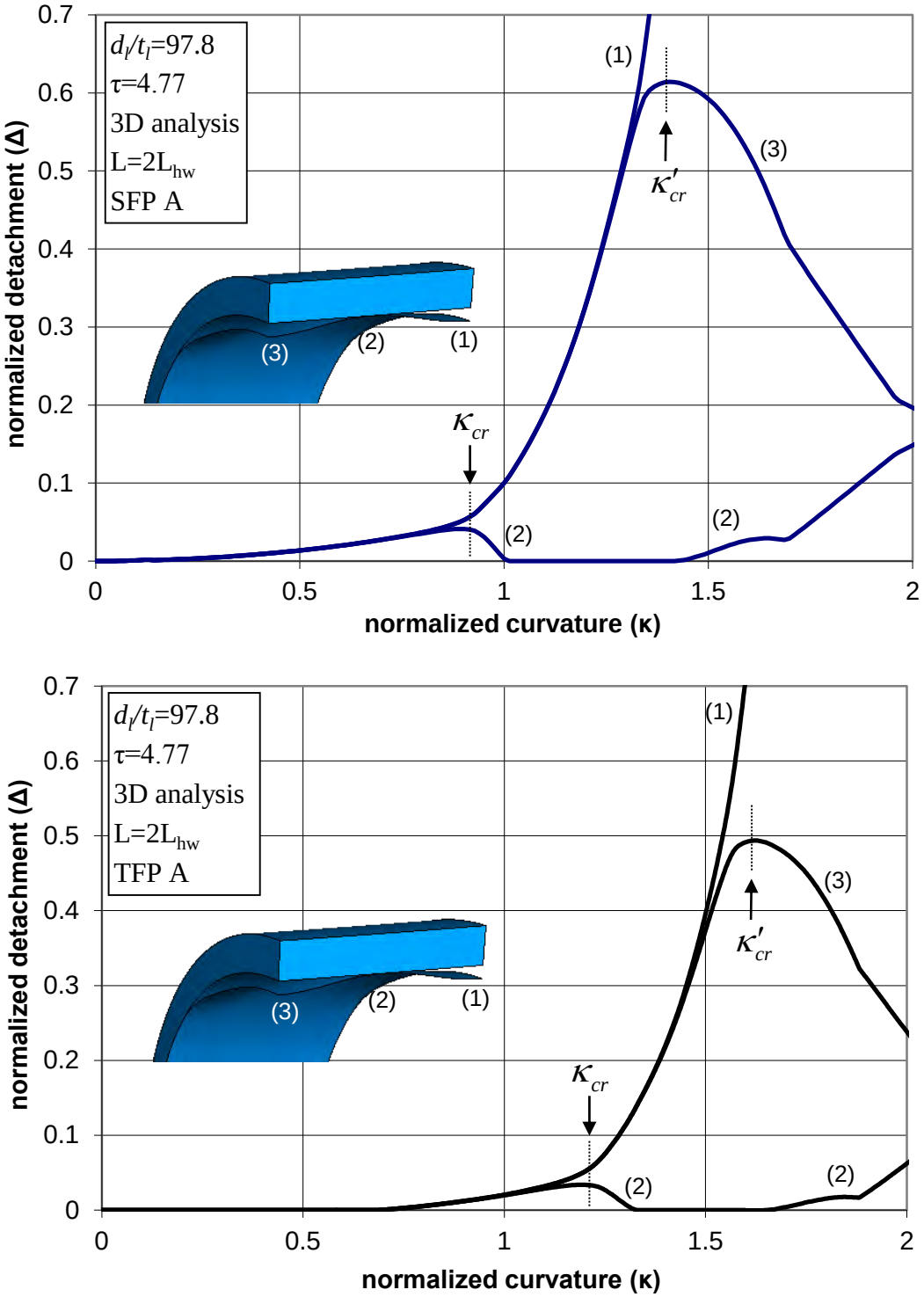

Figures 112: *Detachment of points (1), (2) and (3) in terms of bending curvature; (a) SF Pipe A and (b) TF Pipe A.*

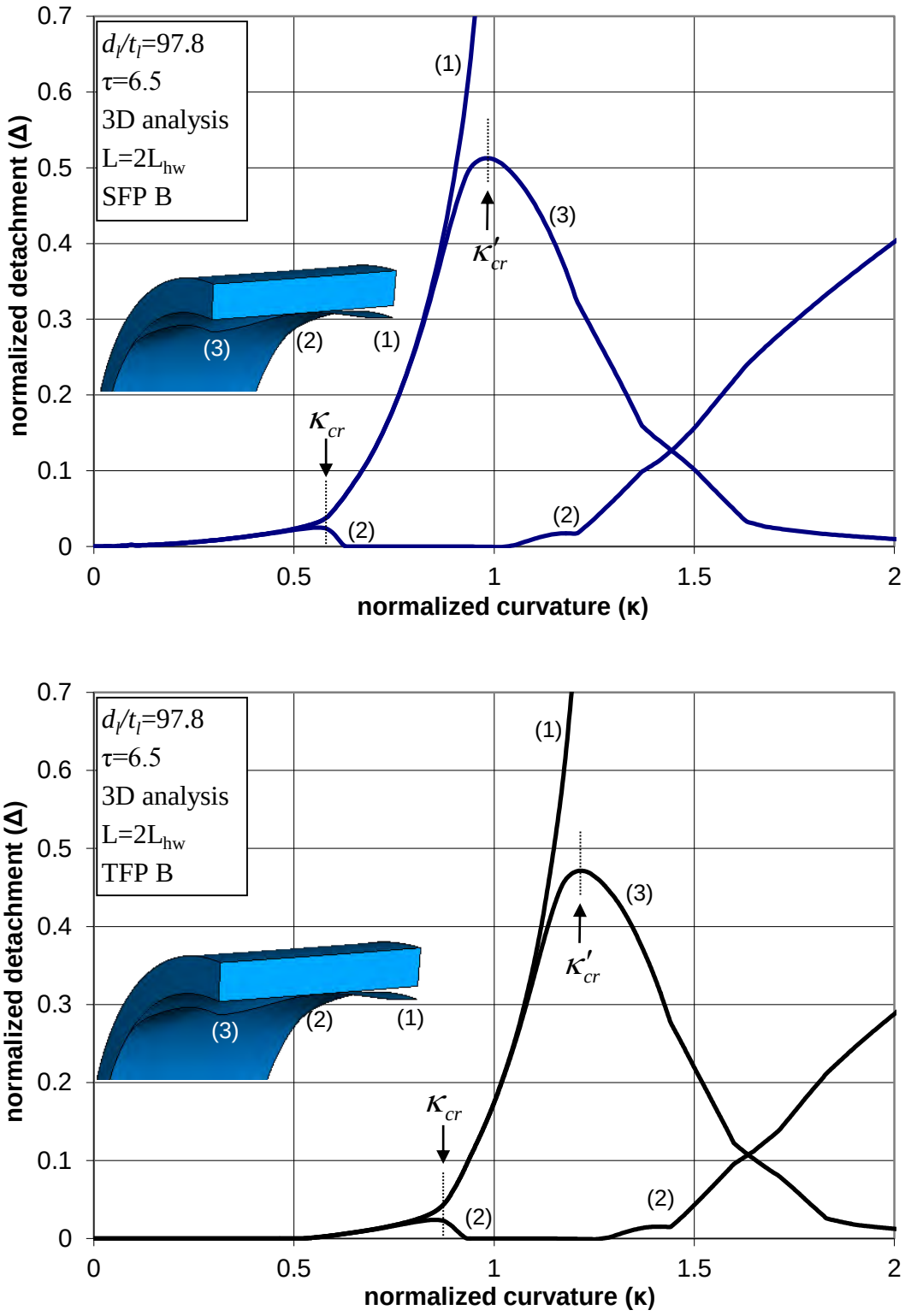

Figures 113: *Detachment of points (1), (2) and (3) in terms of bending curvature; (a) SF Pipe B and (b) TF Pipe B.*

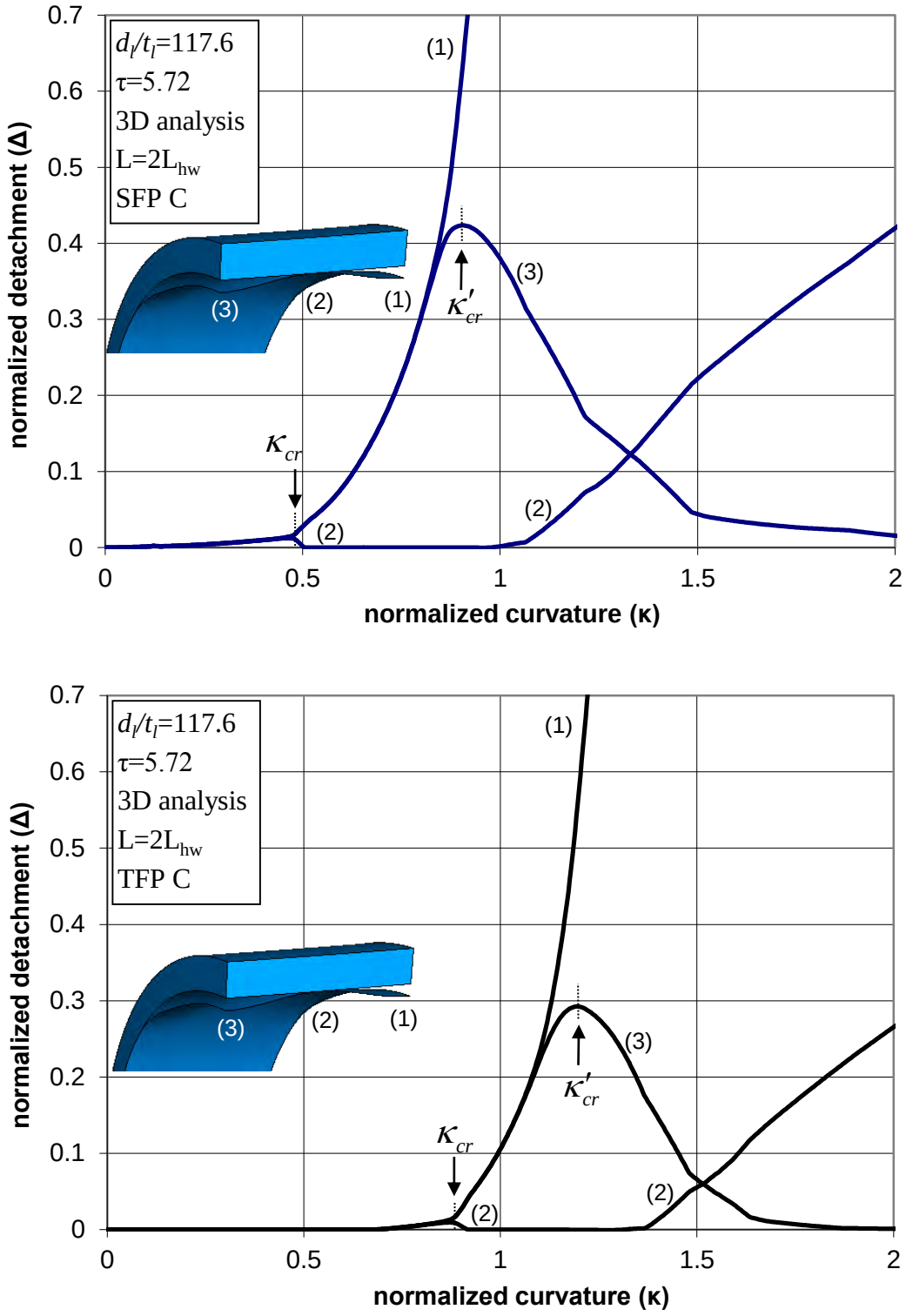

Figures 114: *Detachment of points (1), (2) and (3) in terms of bending curvature; (a) SF Pipe C and (b) TF Pipe C.*

Similar to the first bifurcation, this second bifurcation is quite gradual, also indicating a "tangential" bifurcation, with no distinct point at which the two curves for points (1) and (3) begin to deviate in Figures 112, Figures 113 and Figures 114, and implying ambiguity in the determination of the corresponding buckling curvature κ'_{cr}. Similar to the first bifurcation, the buckling curvature κ'_{cr} is defined as the curvature at which the detachment of point (3) reaches a maximum value and begins to decrease. The κ'_{cr} values are equal to 1.424 for SFP A and 1.625 for TFP A. Furthermore, for Pipe B, the values of κ'_{cr} are equal to 0.983 and 1.216 for SFP B and TFP B respectively, whereas for Pipe C, the values of κ'_{cr} are equal to 0.904 and 1.197 for SFP C and TFP C respectively. These numerical values for the buckling curvature κ'_{cr} are summarized in Table 9. The numerical results demonstrate clearly the beneficial effects of prestressing on the value of buckling curvature; the prestressing level considered in the present analysis results in a 14.1%, 23.7%, and 32.4% increase of the κ'_{cr} value for Pipe A, Pipe B, and Pipe C respectively. Also note that κ'_{cr} is associated with wrinkle heights which are significantly higher than those corresponding to uniform wrinkling bifurcation (κ_{cr}). Therefore, it is reasonable to consider liner failure to occur when the second bifurcation takes place (i.e. when $\kappa = \kappa'_{cr}$).

	Lined Pipe A	**Lined Pipe B**	**Lined Pipe C**
buckling curvature κ'_{cr} for SFP	1.424	0.983	0.904
buckling curvature κ'_{cr} for TFP	1.625	1.216	1.197

Table 9: *Buckling curvature κ'_{cr} for lined pipes A, B and C.*

For the better understanding of the behavior in terms of the detachment (Δ), Figures 112, Figures 113 and Figures 114 are presented in Figures 115 without normalization of the detachment and the curvature. It is observed that the critical curvature of Pipe C is significantly lower than the one of Pipe A. This means that the lower is thickness of the liner pipe, the lower the critical curvature is. Correspondingly, the critical curvature of Pipe B is a little lower than the one of Pipe A. This happens due to the bigger outer pipe thickness of Pipe B, that causes higher stress concentration and as a consequence faster collapse.

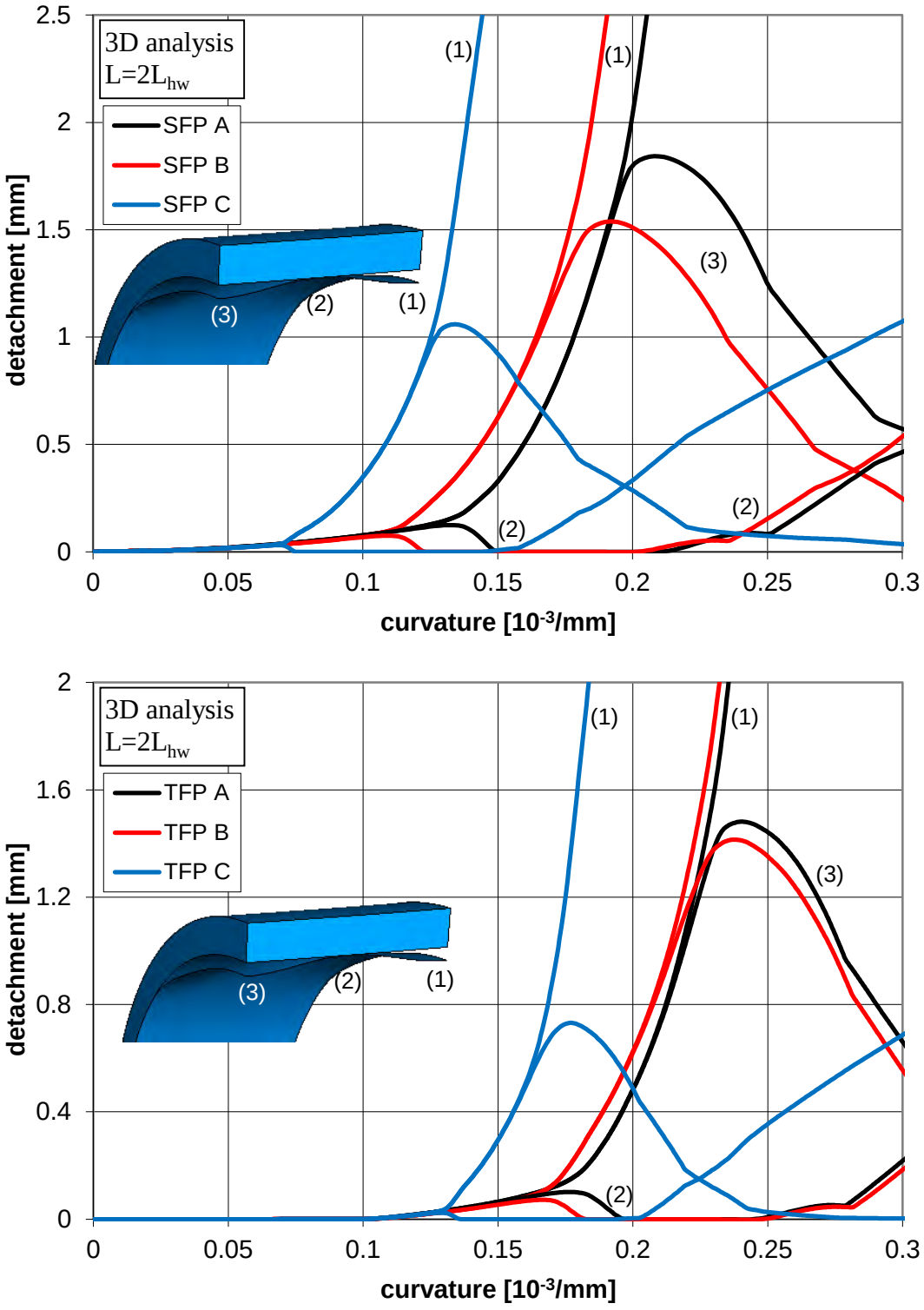

Figures 115: *Detachment of points (1), (2) and (3) in terms of bending curvature; (a) SF Pipes and (b) TF Pipes. Comparison between Lined Pipes A, B and C.*

The liner failure has a non significant effect on the bending strength of the lined pipe as shown in Figure 116. This figure verifies also the small contribution (about 10%) of the liner pipe on the total bending moment of the lined pipe.

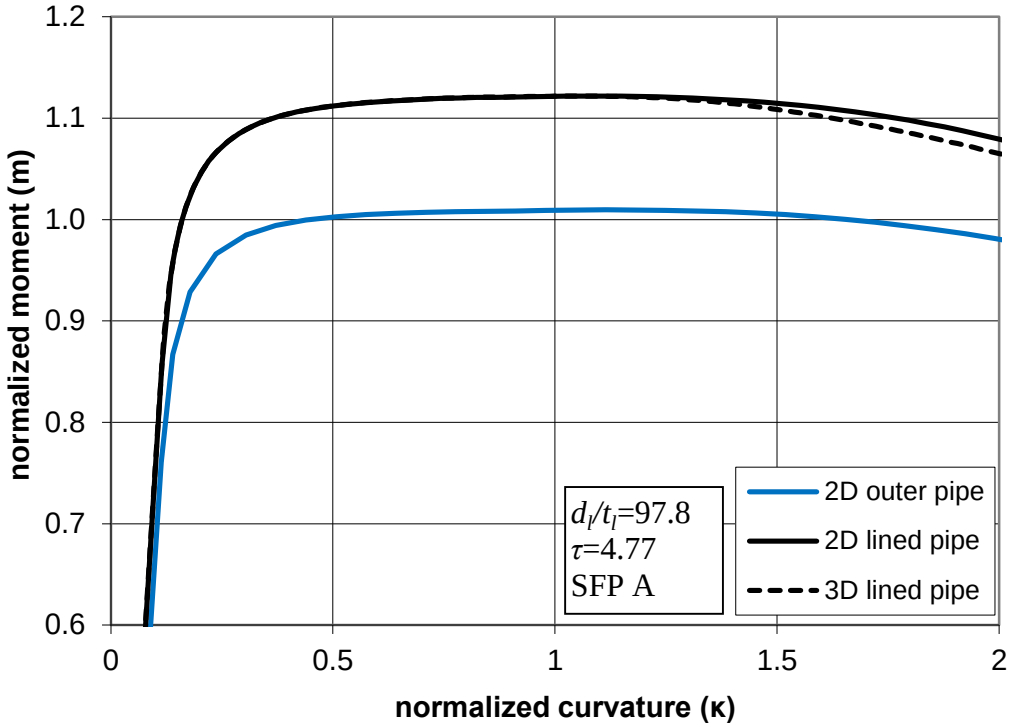

Figure 116: *Bending moment in terms of bending curvature for outer pipe and lined pipe. Effect of liner failure on the bending strength of lined pipe.*

Figure 117 depicts the equivalent plastic strain of the liner pipe at the critical location $(\theta = 0)$ in terms of the bending curvature for the ovalization analysis (2D) and the secondary buckling analysis (3D). This figure demonstrates that the plastification of the liner pipe at the critical location initiates at a quite low curvature and that after the liner uniform wrinkling, the liner pipe sustains a significant increase of the plastic strain.

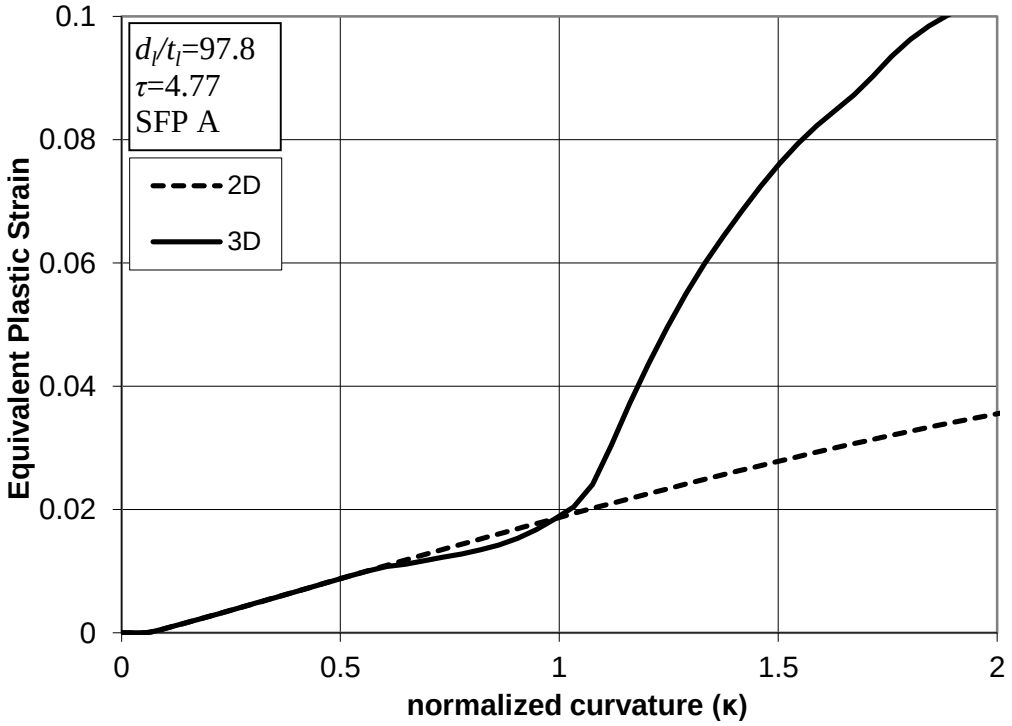

Figure 117: *Equivalent plastic strain of the liner pipe at the critical location* $(\theta = 0)$ *in terms of bending curvature; Effect of liner failure.*

The variation of hoop (circumferential) stress $(\sigma_{\theta 0})$ and axial (longitudinal) stress (σ_{x0}) for the liner pipe of TFP A at the critical location $(\theta = 0)$ during bending in terms of the bending curvature is depicted in Figure 118 and Figure 119 respectively for the inner, middle and outer surface of the liner pipe. It is observed the increase of the stresses after the uniform wrinkling $(\kappa_{cr} = 1.19)$ as well as the abrupt change of the slope after the secondary bifurcation $(\kappa'_{cr} = 1.625)$. Furthermore, in Figure 120, it is shown the variation of hoop and axial strain at the middle surface of the liner pipe. It is noted that the axial stresses and strains at the critical location are always compressive.

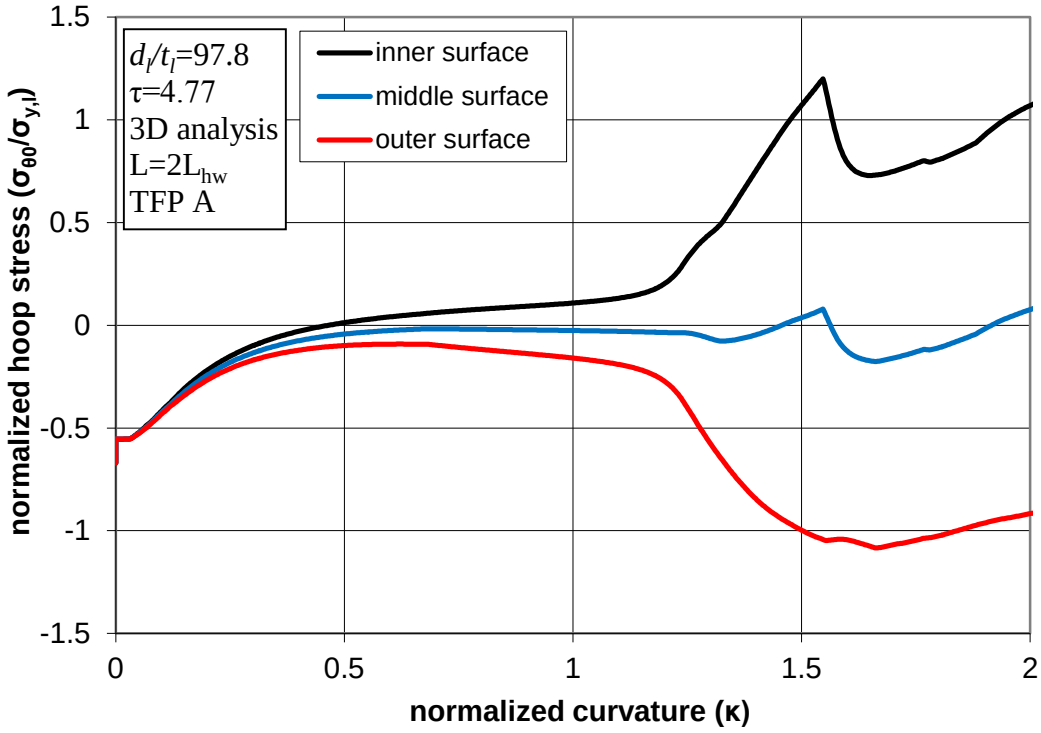

Figure 118: *Variation of hoop stress of the liner pipe at the critical location* $(\theta = 0)$ *in terms of bending curvature for the inner, middle and outer surface of the liner pipe.*

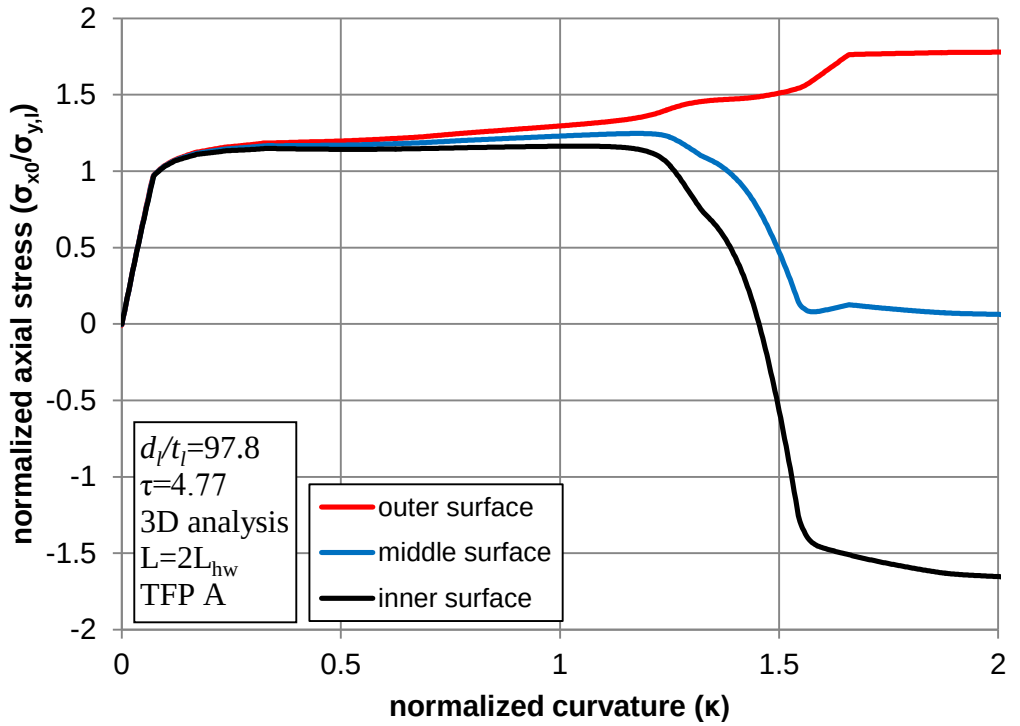

Figure 119: *Variation of axial stress of the liner pipe at the critical location* $(\theta = 0)$ *in terms of bending curvature for the inner, middle and outer surface of the liner pipe.*

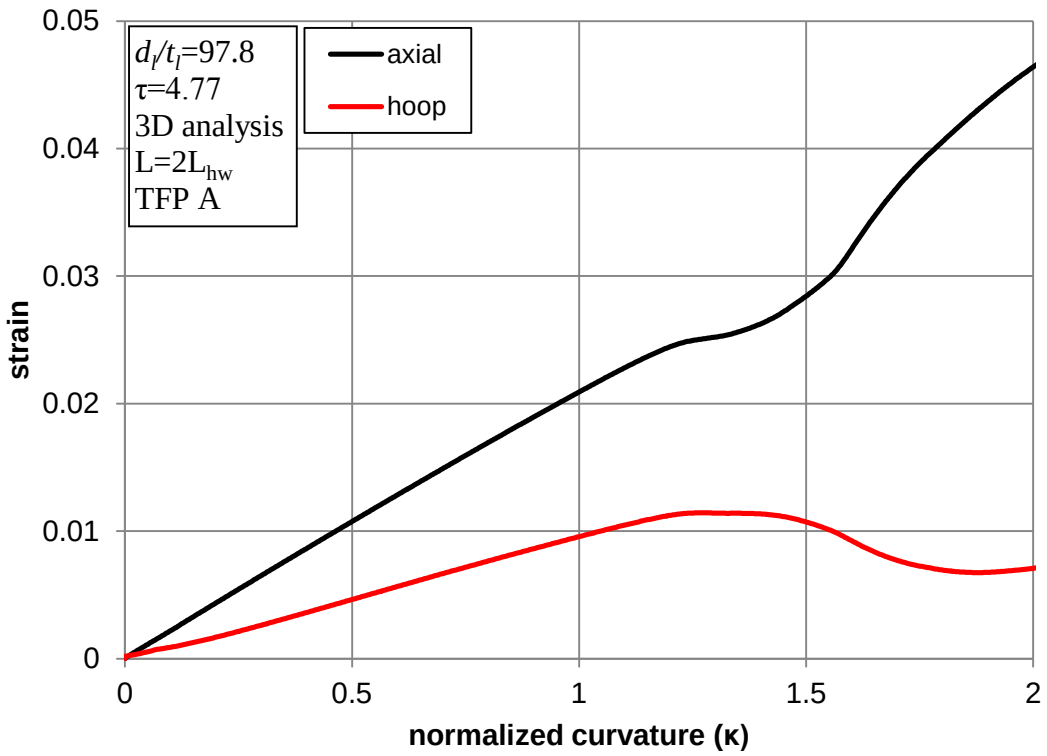

Figure 120: *Variation of axial (compressive) and hoop strain of the liner pipe at the critical location in terms of bending curvature for the middle surface of the liner pipe.*

The above numerical results for obtaining the value of κ'_{cr} refer to imperfection-free (perfect) pipes. The effects of an initial uniformly-wrinkled configuration of the liner over the length of $2L_{hw}$ (Figures 95a or equivalently Figures 92d) are presented in Figures 121 for SF Pipe A and TF Pipe A, where the detachment magnitude is plotted in terms of normalized applied curvature. In the case of Tight-Fit Pipes, the reported imperfection amplitude w_0 is imposed geometrically before initial prestressing is applied. Upon application of prestress and completion of the unloading step, the residual imperfection amplitude w'_0 is quite smaller than the one considered initially. In Figures 122, the effects of initial wrinkling imperfection on the value of secondary bifurcation curvature κ'_{cr} for Pipes A, B and C are plotted with solid lines, where the κ'_{cr} value is plotted with respect to initial wrinkling amplitude w_0, normalized by the liner wall thickness t_l. The results show that the response of lined pipes under bending is sensitive to initial imperfections. For both SF and TF Pipes, the reduction of κ'_{cr} is very abrupt for values of normalized imperfection amplitude at the order of 10^{-3}. Furthermore, for imperfection amplitude equal to 10% of the

liner thickness (i.e. about 0.3 mm), the value of critical curvature κ'_{cr} may be reduced by an amount of about 50% with respect to the critical curvature of the corresponding imperfection-free pipe.

In addition, the sensitivity of response on the presence of initial imperfections in the form of the secondary buckling mode is shown in Figures 123 for SFP and TFP, and in Figures 122a with dotted lines, where the value of κ'_{cr} is plotted against the imperfection amplitude. The results indicate that this shape of imperfection has a somewhat more pronounced effect on the value of κ'_{cr} than the effect of an imperfection in the form of the first mode. The results are compatible with those obtained for elastic cylinders in Figure 96.

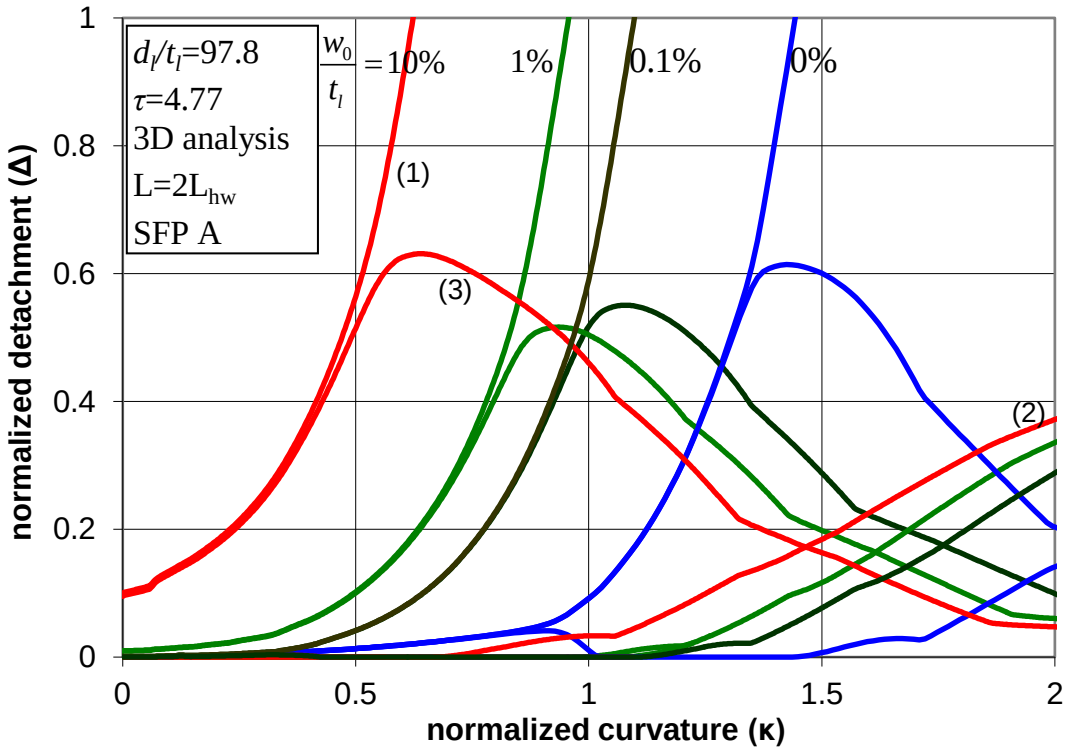

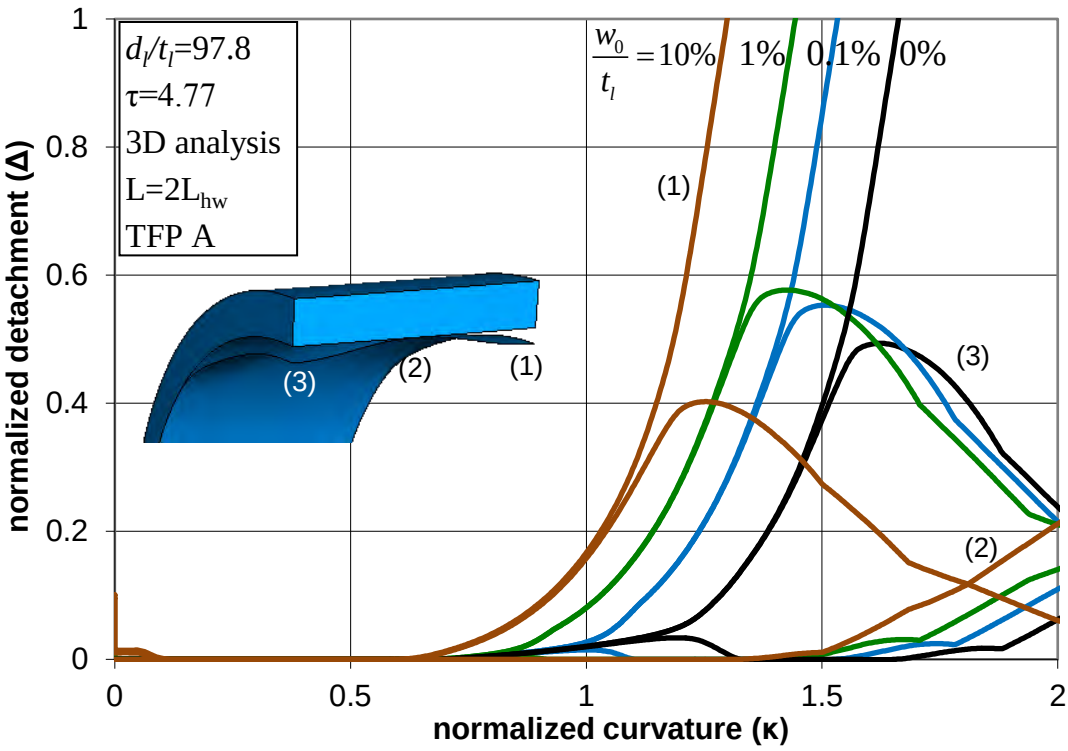

Figures 121: *Detachment development of SF Pipe A and TF Pipe A for different values of the first mode imperfection amplitude.*

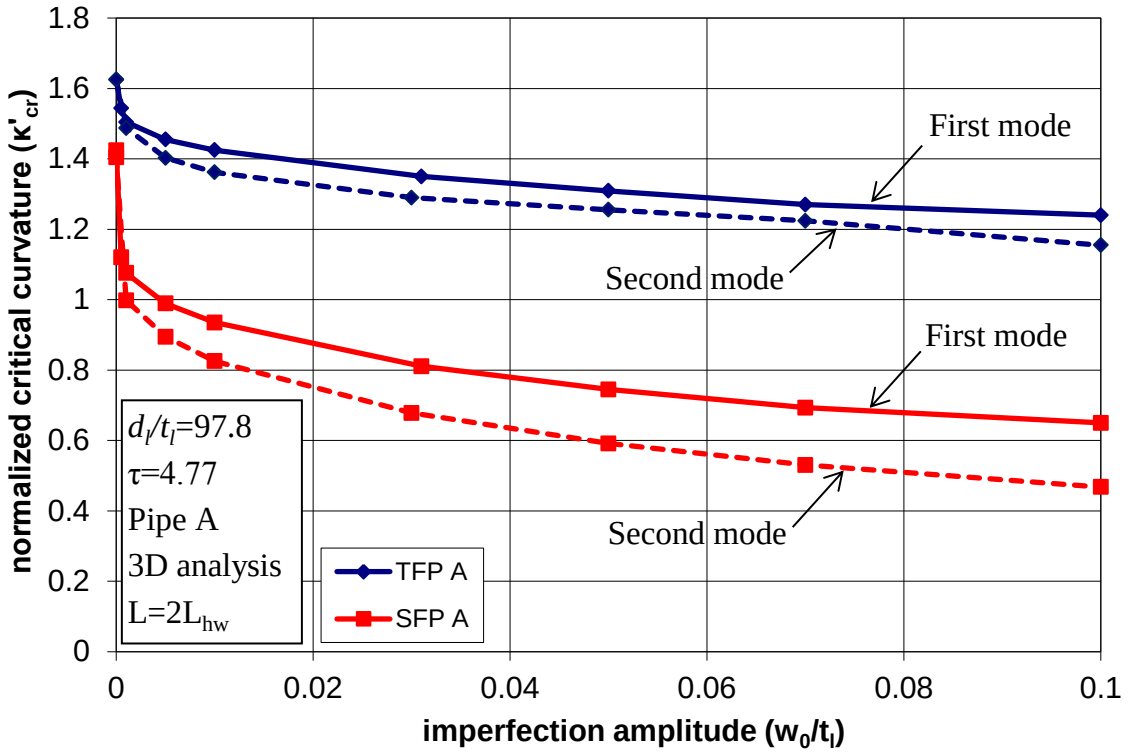

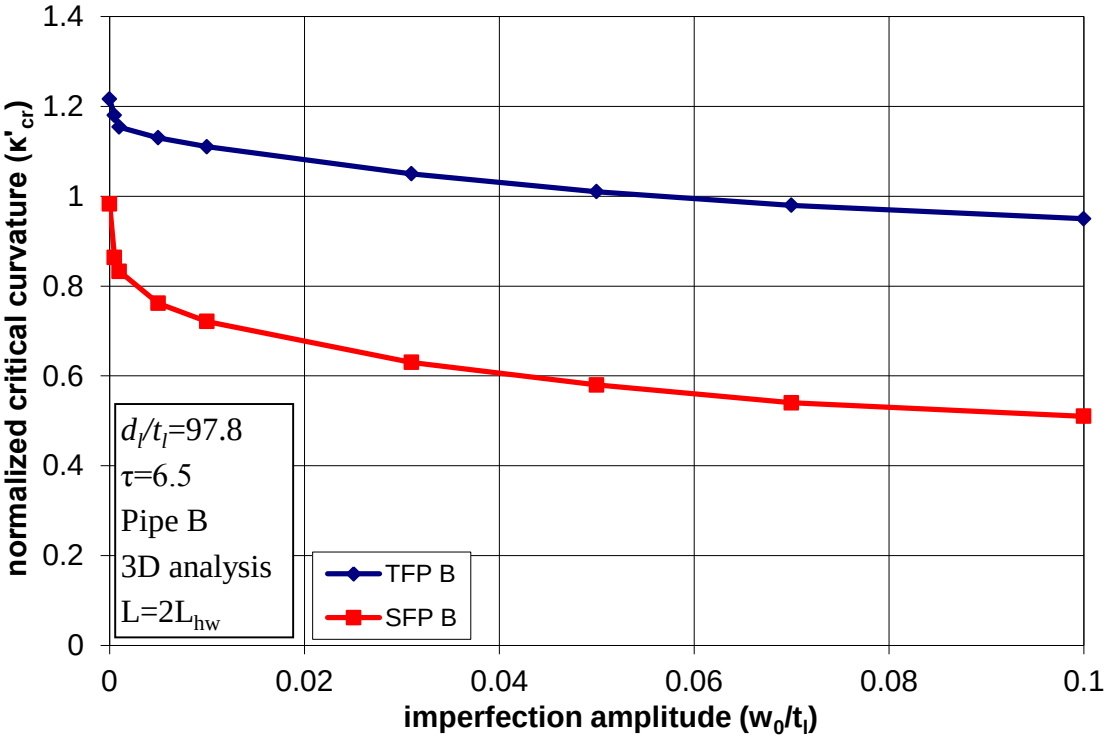

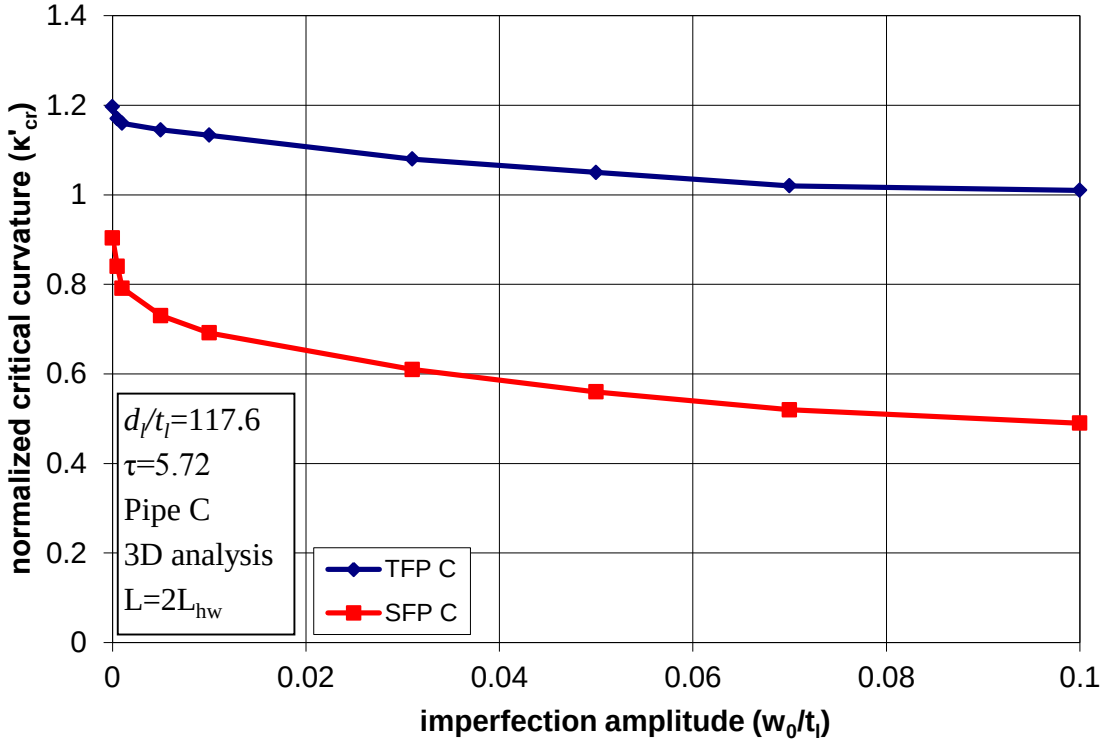

Figures 122: *Effects of initial wrinkling imperfections on the value of secondary bifurcation curvature for Pipes A, B and C. In Pipes B, C, imperfections are assumed in the form of the first bifurcation mode.*

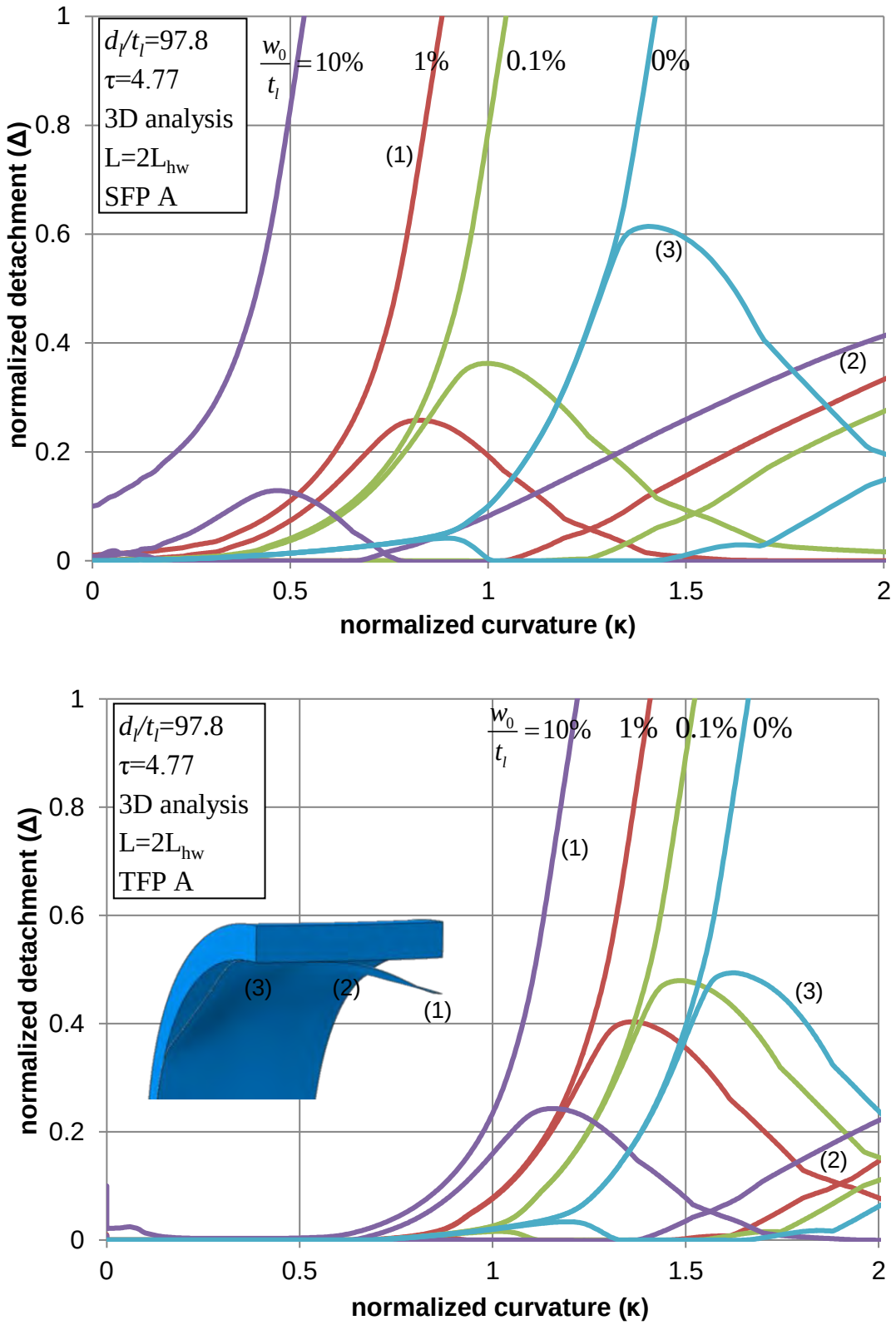

Figures 123: *Detachment development of SF Pipe A and TF Pipe A for different values of secondary mode imperfection amplitude.*

3.5 Comparison with experimental data

In the present section, numerical results for TFP A are compared with experimental data of lined pipes tested under pure bending, as reported by Focke [11] and Hilberink [13]. The material and geometric characteristics of Lined Pipe A are similar with lined pipes OR-2, GR-1, GR-2, WT-1, and WT-2 tested in [11] and P01KA pipe in [13]. The residual liner pipe hoop stresses σ_{res} for the tested pipes has been measured equal to 178 MPa for OR-2 pipe, 199 MPa for both GR-1 and GR-2 pipes, and 185 MPa for the P01KA pipe, which are comparable with the residual stress of the TFP A (166 MPa) considered in the present analysis. Furthermore, the residual stress for tested pipes WT-1 and WT-2 has been measured equal to 53 MPa.

3.5.1 Buckling shape

In Figure 124, the photo of the wrinkled specimen is depicted at the plane of bending together with an image from numerical simulation, demonstrating that the wrinkled shape from experimental data is very similar to the one from the numerical analysis.

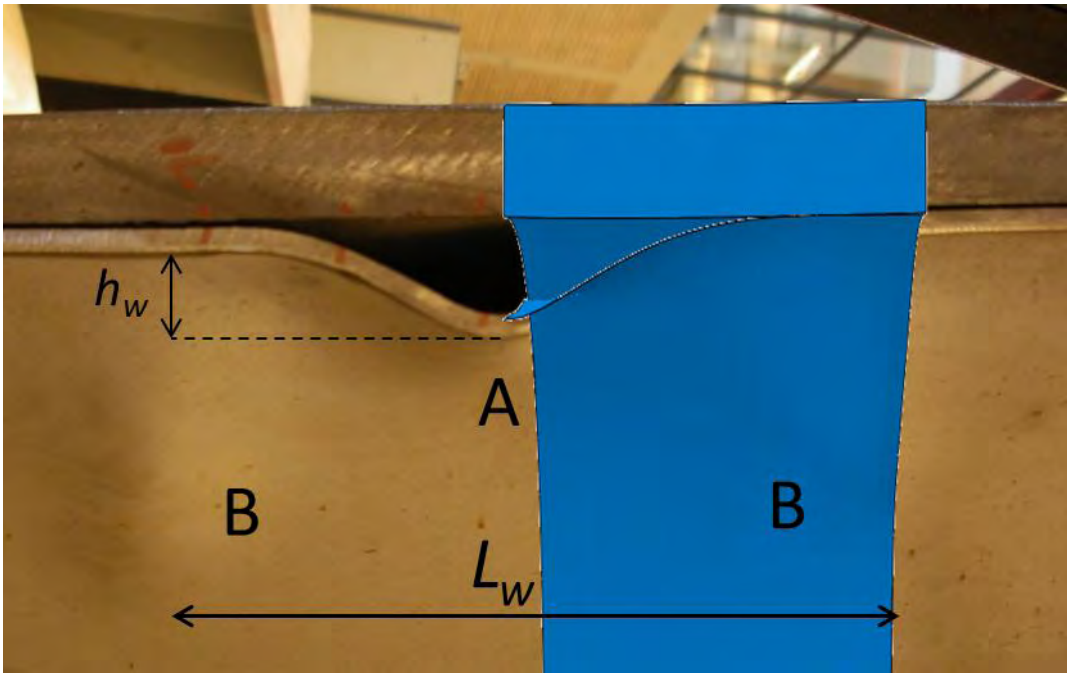

Figure 124: *Photo of wrinkled specimen after experimental testing with image from finite element simulation.*

3.5.2 Wrinkle wavelength

Experimental measurements [11],[13] obtained for the wrinkle wavelength (L_w), shown in Figure 124, are depicted in Figure 125, normalized by the value of $\sqrt{d_l t_l}$ and indicate a significant scatter. Similar scatter has also been reported in buckling wavelength measurements of single-walled pipes subjected to bending [26],[27],[28]. The wavelength L_w of Figure 124 corresponds to the secondary buckling mode (shown in Figures 95) where A denotes the main buckle and B denote the two minor buckles, also depicted in Figure 75. In the same Figure, the experimental measurements for the wrinkle wavelength are compared with the corresponding numerical prediction, where the numerical value of L_w is taken equal to $4L_{hw}$, where L_{hw} is the half-wave length value of the first bifurcation mode, shown in Figures 92. The relationship between L_{hw} and L_w is also shown in Figures 95d. The comparison in Figure 125 shows that the measured values of L_w are in fairly good agreement with the numerical prediction. It is interesting to note that based on the experimental results, the level of the prestressing does not affect significantly the buckling wavelength, verifying the corresponding numerical results in Figure 91 and Figures 108.

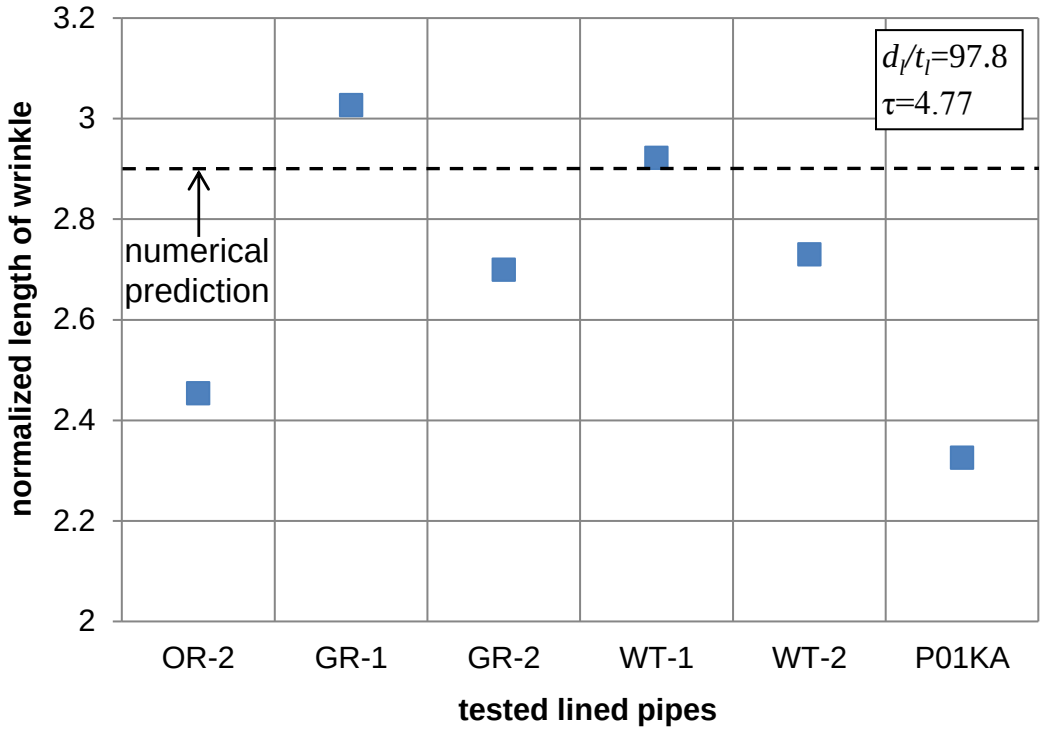

Figure 125: *Comparison between numerical and experimental values of the wavelength.*

3.5.3 Wrinkle height

In Figure 126, numerical results for the evolution of liner pipe wrinkle height h_w, normalized by the liner thickness t_l, are plotted for different values of residual imperfection amplitude $\left(w_0'/t_l\right)$ and compared with relevant experimental data [11],[13]. The values of residual imperfection amplitude $\left(w_0'/t_l\right)$ used in the analyses of Figure 126 are consistent with the range of initial wrinkling measurements reported in specimen locations OR-2 W4, OR-2 W5, GR-2 W4, and GR-2 W5. The comparison indicates that the numerical results for the gradual increase of wrinkling height are in very good agreement with the experimental measurements.

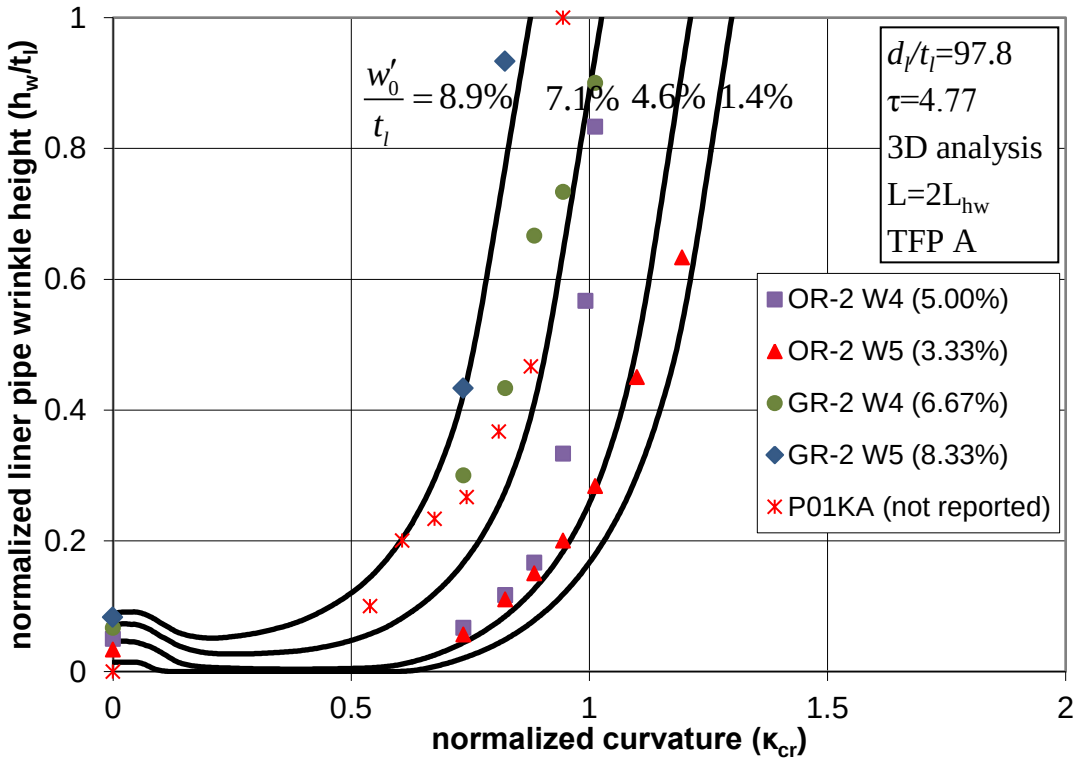

Figure 126: *Evolution of liner pipe wrinkle height for TF Pipe A for different values of initial imperfection; comparison between numerical and experimental results.*

3.6 Effects of external pressure on lined pipe bending behavior

An important issue regarding the structural integrity of offshore pipelines during the installation procedure is the determination of maximum (ultimate) bending curvature $\kappa_{\max}$ beyond which pipeline failure occurs [1]. Extensive experimental and numerical work on pressurized bending of single-wall steel pipes has demonstrated that for thick-walled pipes with diameter-to-thickness ratio less than 30, which are candidates for deep offshore pipeline applications, ovalization instability governs the bending response of the pipe, in the sense that the pipe exhibits a limit (maximum) moment due to excessive cross-sectional ovalization before local wrinkling of the pipe wall occurs [2],[3]. The dominance of ovalization instability over pipe wall local buckling becomes more pronounced when the pipe is bent in the presence of external pressure due to the significant contribution of external pressure on the ovalization process and the curvature $\kappa_{\max}$ decreases substantially with increasing external pressure. Therefore, the curvature corresponding to the maximum moment ($\kappa_{\max}$), calculated from an ovalization (two-dimensional) analysis, as described in sections 3.3.1 and 3.4.1, considering pressurized bending conditions, is representative for the deformation capacity of thick walled pipes [2],[3].

In the case of lined pipes, a similar ovalization analysis can used to obtain $\kappa_{\max}$ which is considered as the maximum allowable bending curvature. The $\kappa_{\max}$ value depends mainly on the load-bearing outer pipe, whereas the contribution of the liner is rather small. In Figures 127, the response of lined pipes under pressurized bending conditions is shown in terms of the moment-curvature equilibrium paths for different levels of external pressure p for the SF and the TF Pipe A. The values of pressure p are normalized by the yield pressure of the outer pipe $p_{Y,o} = 2\sigma_{Y,o} t_o / d_o$, so that $q = p / p_{Y,o}$. The curves with $q = 0$ (zero pressure) are identical to those presented in Figures 100 for pipe A. In all those analyses, external pressure is first raised and, subsequently, keeping the pressure constant, bending is applied until a limit (maximum) moment is reached.

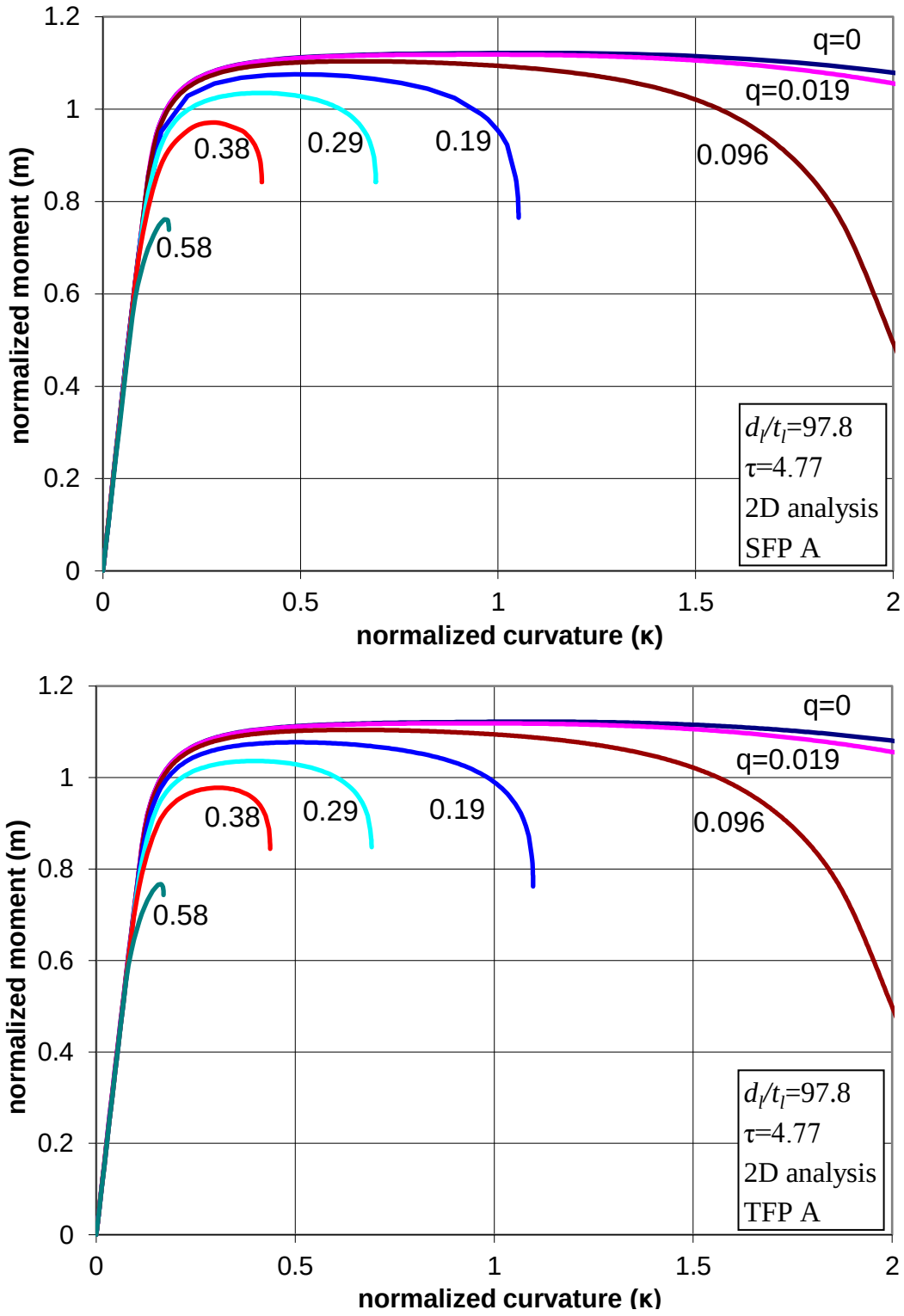

Figures 127: *Moment-curvature diagrams for pressurized bending response of lined pipes; (a) SF Pipe A and (b) TF Pipe A.*

In Figure 128, the corresponding pressure-curvature interaction diagram is plotted depicting the values of $\kappa_{\max}$ for different values of pressure level. The solid lines in Figure 128 represent the curvature $\kappa_{\max}$ for different values of normalized pressure q corresponding this limit moment for the SF and TF pipes. In the same figure, an empirical interaction equation [1] proposed by Shell Oil Company for pressure-curvature interaction is also plotted, considering only the strength of the outer pipe (dashed line). Shell interaction equation is given by the following formula:

$$\frac{k}{k_c}+\frac{p}{p_c}=1, \tag{78}$$

where $k_c=\frac{t_o}{d_o^2}$, $p_c=\frac{p_{Y,o}p_{e,o}}{\sqrt{p_{Y,o}^2+p_{e,o}^2}}$, $p_{Y,o}=2\sigma_{Y,o}\frac{t_o}{d_o}$, and $p_{e,o}=\frac{2E}{1-\nu^2}\left(\frac{t_o}{d_o}\right)^3$.

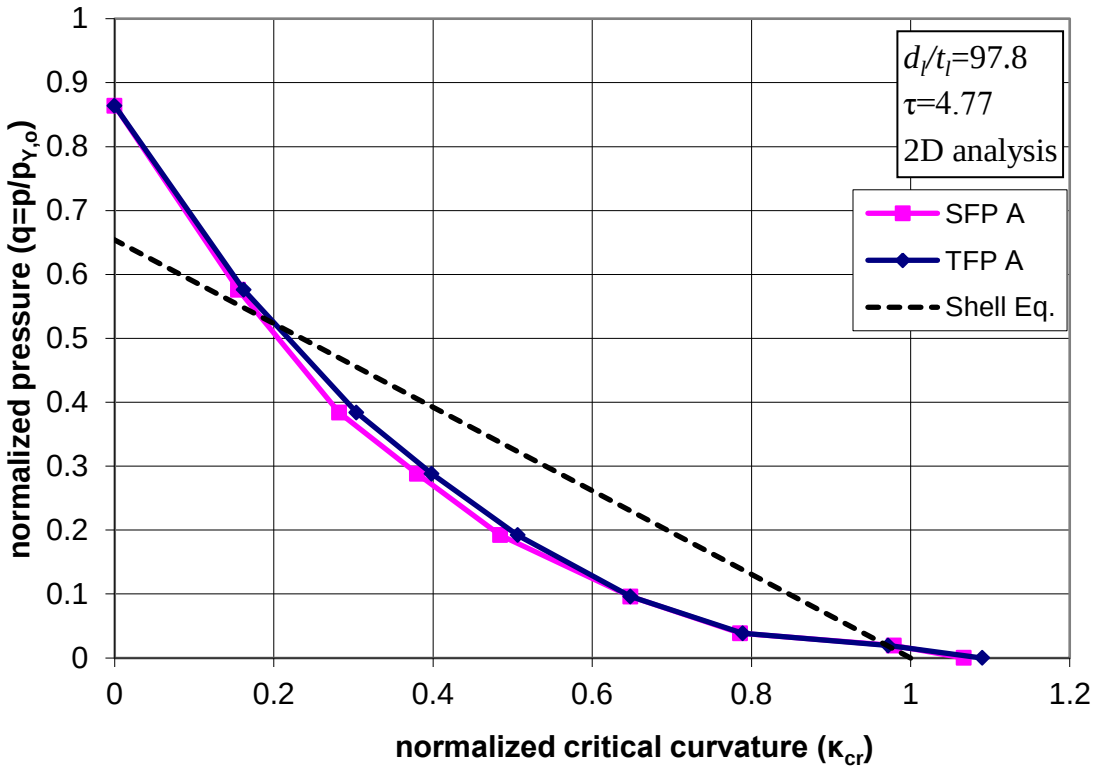

Figure 128: *Pressure-curvature interaction diagram for pressurized bending response of lined pipes; numerical results.*

The previous numerical results for pressurized pipes referred to the entire lined pipe system. The behavior of liner pipe during pressurized bending of SF and TF Pipes is shown in Figures 129 and in Figures 130 in terms of their ovalization and their detachment from the outer pipe respectively. The results indicate that, for both SFP and TFP, external pressure has a prominent effect on the liner response; detachment is significantly delayed, even for very low levels of pressure. Furthermore, for higher values of pressure, the liner is always in contact with the outer pipe, until the value of $\kappa_{\max}$ is reached. Three-dimensional analyses of lined pipes under pressurized bending for levels q greater than 0.05 indicated no wrinkling up to the bending curvature $\kappa_{\max}$. Upon reaching the value of $\kappa_{\max}$, the system becomes very unstable and rapidly collapses due to excessive ovalization. Therefore, liner wrinkling does not occur for bent lined pipes in the presence of external pressure that exceeds 5% of the yield pressure of the outer pipe $p_{Y,o}$.

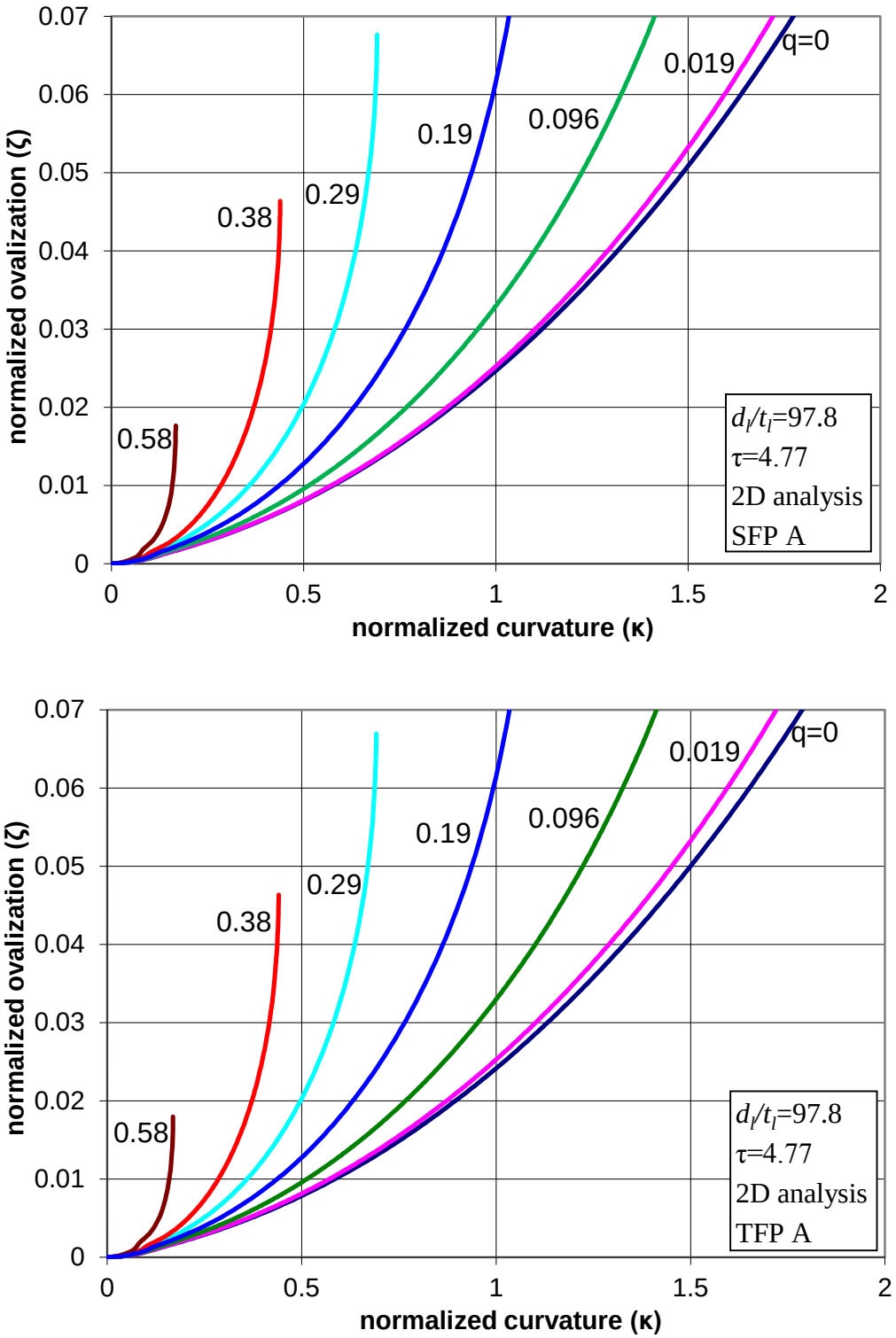

Figures 129: *Liner ovalization during pressurized bending response of lined pipes; (a) SF Pipe A and (b) TF Pipe A.*

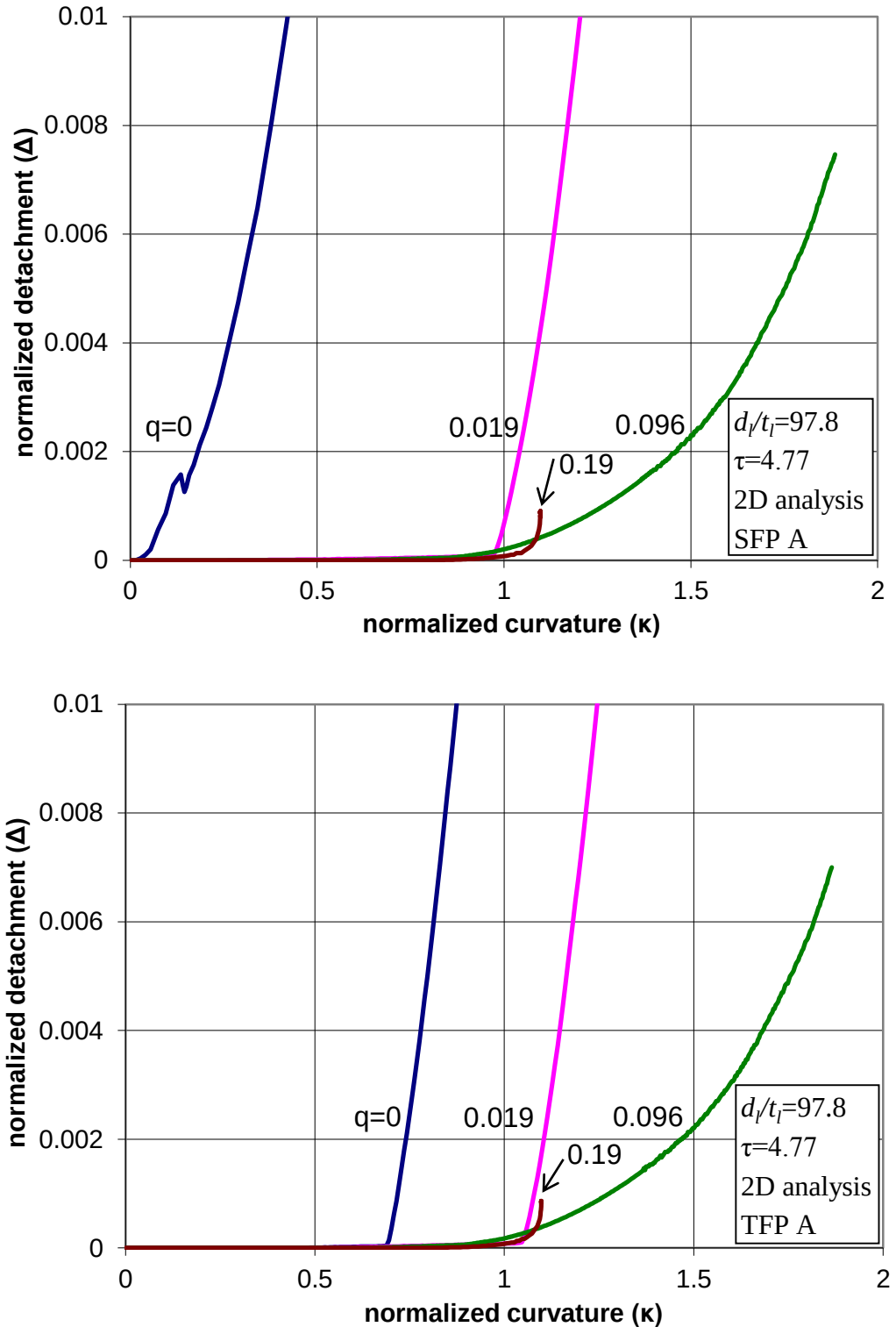

Figures 130: *Liner detachment from outer pipe during pressurized bending response of lined pipes; (a) SF Pipe A and (b) TF Pipe A.*

3.7 Conclusions

The mechanical behavior of lined elastic and steel pipes under bending loading and external pressure has been investigated. The investigation is computational using nonlinear two- and three-dimensional models through the employment of the general-purpose finite element program ABAQUS.

Numerical results indicate that separation (detachment) between the liner and the outer pipe occurs at the compression zone, and a cylindrical panel is formed, leading to liner buckling in the form of wrinkling. Results from three-dimensional analysis in both elastic and steel lined pipes indicate that a first bifurcation occurs at curvature κ_{cr} that leads to a uniform wrinkling pattern, associated with small values of detachment and of buckle wave-height. Subsequently, a second bifurcation occurs at a bending curvature κ'_{cr}, which is higher than the value of κ_{cr}. This secondary bifurcation is associated with larger values of wrinkling amplitude and more visible deformations with respect to the first bifurcation and therefore can be considered as the wrinkling limit state of liner failure due to bending. The numerical results from lined steel pipes show that liner prestressing due to the manufacturing process has a beneficial effect on the values of critical curvature κ_{cr} and κ'_{cr}, whereas both κ_{cr} and κ'_{cr} are sensitive to the presence of initial wrinkling imperfections. Furthermore, the numerical results indicate that the lateral confinement of the liner pipe due to the deformable outer pipe and its interaction with the outer pipe has a decisive influence on the wrinkling behaviour of the lined pipe.

In contrast with the case of lined elastic pipes, the development of the wavy pattern in case of lined steel pipes is not sudden, indicating a “tangential” type of bifurcation with no distinct point. The smooth transition from pre-buckling to post-buckling in lined steel pipes facilitates its numerical simulation, so that the introduction of a negligible imperfection may not be necessary. Because of this “tangential” bifurcation, the definition of buckling curvature κ_{cr} may be rather ambiguous. In the present work, to overcome this ambiguity, the buckling (critical) curvature κ_{cr} is defined as the curvature at which the detachment of the end cross-section (point (2) in the equilibrium paths of detachment-curvature figures) reaches a maximum value and begins to decrease.

Two types of lined steel pipes are considered; stress-free lined pipes (referred to as snug-fit pipes, SFP) and lined pipes with an initial prestress (referred to as tight-fit pipes, TFP). In the case of SF Pipes, the detachment occurs as soon as bending is applied, whereas

for the TF Pipes, the detachment initiates at a later stage due to prestressing. On the other hand, numerical results indicate that liner prestressing has a rather negligible effect on liner ovalization, local hoop curvature, and longitudinal stress. Furthermore, the development of hoop stress at the critical location $(\theta = 0)$ indicates that after the first stages of deformation, hoop prestressing is practically lost. Moreover, from the series of analyses that conducted to define the critical value of half-wavelength (L_{hw}), it is concluded that prestressing do not affect the half-wavelength value. Similar effect on the wrinkling response of lined pipes has the presence of friction in the interface between the liner and the outer pipe. In particular, friction delays the initiation of detachment, so that wrinkling occurs in a higher bending curvature.

Regarding the influence of liner and outer pipe thickness, numerical results indicate that the bigger is the thickness of the outer pipe, the lower and slower is the increase of the detachment and ovalization during bending. On the other hand, with decreasing the thickness of the liner pipe, the higher is the increase of the detachment. In general, the thickness of the outer pipe determines the confinement stiffness. Therefore, a thicker outer pipe results in higher stresses at the critical location, leading to plastic strains (for a steel pipe) and finally to wrinkling of the liner pipe. Furthermore, with increasing the thickness of the outer pipe, the higher is the bending strength, and the curvature that corresponds to the maximum bending moment.

Comparison of the present numerical results with available experimental data has demonstrated that the buckled shapes obtained numerically are very similar to the shapes observed experimentally. In addition, the numerical values of wavelength and evolution of wrinkling height are compared very well with relevant test measurements.

Finally, the effects of external pressure on the bending response of lined pipes have been investigated and numerical results from ovalization analysis indicate that the external pressure affects the liner response at rather low pressure levels. In particular, when the level of external pressure exceeds a rather low value, the liner pipe does not detach from the outer pipe, while the entire lined pipe collapses due to excessive ovalization, and liner wrinkling does not occurs.

3.8 References

[1] Murphy, C.E., Langner, C.G. (1985). "Ultimate Pipe Strength Under Bending, Collapse and Fatigue", *Proceedings of the 4th International Conference on Offshore Mechanics and Arctic Engineering (OMAE)*, Dallas, USA.

[2] Corona, E., Kyriakides, S. (1988). "On the Collapse of Inelastic Tubes under Combined Bending and Pressure", *International Journal of Solids and Structures*, Vol. 24, No. 5, pp. 505-535.

[3] Karamanos, S.A., Tassoulas, J.L. (1991). "Stability of Inelastic Tubes under External Pressure and Bending", *Journal of Engineering Mechanics*, ASCE, Vol. 117, No. 12, pp. 2845-2861.

[4] Kyriakides, S., Babcock, C.D., Elyada, D. (1984). "Initiation of Propagating Buckles From Local Pipeline Damages", *Journal of Energy Resource Technology*, Vol. 106, No. 1, pp. 79-87.

[5] Nogueira, A.C., Tassoulas, J.L. (1994). "Buckle Propagation: Steady-State Finite Element Analysis" *Journal of Engineering Mechanics*, ASCE, Vol. 120, No. 9, pp. 1931-1944.

[6] API PR 1111 (1999). Design, Construction, Operation, and Maintenance of Offshore Hydrocarbon Pipelines (Limit State Design), Third Edition, American Petroleum Institute.

[7] Det Norske Veritas (2010). Offshore Standard DNV-OS-F101: Sub-marine Pipeline Systems.

[8] Kyriakides, S., Corona, E. (2007). *Mechanics of Offshore Pipelines. Vol. 1: Buckling and Collapse.* Elsevier, Oxford, UK.

[9] Karamanos, S.A. (2002). "Bending Instabilities of Elastic Tubes", *International Journal of Solids and Structures*, Vol. 39, No. 8, pp. 2059-2085.

[10] Dama, E., Karamanos, S.A., Gresnigt, A.M. (2007), "Failure of Locally Buckled Pipelines", *Journal of Pressure Vessel Technology*, ASME, Vol. 129, No. 2, pp. 272-279.

[11] Focke, E. (2007). *Reeling of Tight Fit Pipe*, Ph.D. Thesis, Delft Univ. of Technology, The Netherlands.

[12] de Koning, A.C., Nakasugi, H., Ping, L. (2004), "TFP and TFT Back in Town (Tight Fit CRA Lined Pipe and Tubing)", *Stainless Steel World*, p.53-61.

[13] Hilberink, A. (2011). *Mechanical Behaviour of Lined Pipe*, Ph.D. Thesis, Delft Univ. of Technology, The Netherlands.

[14] Tkaczyk, T., Pepin, A., Denniel, S. (2011). "Integrity of Mechanically Lined Pipes Subjected to Multi-Cycle Plastic Bending", *Proceedings of International Conference on Ocean, Offshore and Arctic Engineering (OMAE)*, Rotterdam, The Netherlands.

[15] Peek, R., Hilberink, A. (2012). "Axisymmetric Wrinkling of Snug-Fit Lined Pipe", *Shell Global Solutions International B.V.*, Rijswijk, The Netherlands.

[16] Wang, C.Y., Ru, C.Q., Mioduchowski, A. (2004). "Applicability and Limitations of Simplified Elastic Shells Equations for Carbon Nanotubes", *Journal of Applied Mechanics*, ASME, Vol. 71, pp. 622-631.

[17] Vodenitcharova, T., Zhang, L.C. (2006). "Bending and Local Buckling of a Nanocomposite Beam Reinforced by a Single-Walled Carbon Nanotube", *International Journal of Solid and Structures*, Vol. 43, pp. 3006-3024.

[18] Lourie, O., Cox, D.M., Wagner, H.D. (1998). "Buckling and Collapse of Embedded Carbon Nanotubes", *The American Physical Society*, Vol. 81, No. 8, pp. 1638-1641.

[19] Hibbit, H.D., Karlsson, B.I., Sorensen, P. (2007). *Theory Manual*, ABAQUS, version 6.7, Providence, RI, USA.

[20] Houliara, S., Karamanos, S.A. (2006). "Buckling and Post-Buckling of Long Pressurized Elastic Thin-Walled Tubes under In-Plane Bending", *International Journal of Non-Linear Mechanics*, Vol. 41, No. 4, pp. 491-511.

[21] Houliara, S., Karamanos, S.A. (2010). "Stability of Long Transversely-Isotropic Elastic Cylinders under Bending", *International Journal of Solids and Structures*, Vol. 47, No. 1, pp. 10-24.

[22] Axelrad, E.L. (1965). "Refinement of buckling-load analysis for tube flexure by way of considering precritical deformation" [in Russian]. *Izvestiya Akademii Nauk SSSR, Otdelenie Tekhnicheskikh Nauk, Mekhanika i Mashinostroenie*, Vol. 4, pp. 133-139.

[23] Timoshenko, S., Gere, J.M. (1961). *Theory of Elastic Stability*, 2nd Ed., McGraw Hill, New York, NY.

[24] Koiter, W.T. (1963). "The Effect of Axisymmetric Imperfections on the Buckling of Cylindrical Shells under Axial Compression", *Proceedings of Koninklijke Nederlandse Akademie Van Wetenschappen*, Amsterdam, Series B, Vol. 66, pp. 265–279.

[25] Bardi, F.C., Kyriakides, S. (2006). "Plastic buckling of circular tubes under axial compression-part I: Experiments", *International Journal of Mechanical Sciences*, Vol. 48, pp. 830-841.

[26] Kyriakides, S., Ju, G.T. (1992). "Bifurcation and Localization Instabilities in Cylindrical Shells under Bending I: Experiments", *International Journal of Solids and Structures*, Vol. 29, pp. 1117-1142.

[27] Ju, G.T., Kyriakides, S. (1992). "Bifurcation and Localization Instabilities in Cylindrical Shells under Bending II: Predictions", *International Journal of Solids and Structures*, Vol. 29, pp. 1143-1171.

[28] Corona, E., Lee, L.H., Kyriakides, S. (2006). "Yield anisotropy effects on buckling of circular tubes under bending", *International Journal of Solids and Structures,* Vol. 43, pp. 7099-7118.

4. Summary and conclusions of the study

4.1 Summary

The main objective of this study is the investigation of the mechanical behavior of thin-walled elastic and steel cylindrical shells confined within a surrounding medium or another shell in terms of their structural stability under two principal types of loading, namely external pressure and longitudinal bending. The work has been motivated by practical engineering applications, as well as by the need for better understanding and accurate predictions of bifurcation, and post-buckling response of confined thin-walled cylindrical shells. The first issue, examined in Chapter 2 of the present dissertation, refers to the structural behavior and stability of confined cylinders under external pressure with direct reference to thin-walled buried pipelines. The second problem is examined in Chapter 3 and concerns the mechanical behavior and wrinkling of confined cylindrical shells, motivated by the need of investigating the response of lined pipes under bending and external pressure. The investigation is computational using advanced finite element tools through the employment of a general-purpose finite element program. The numerical simulation methodology is similar for the two problems, where the shell under consideration and the corresponding confinement are simulated with nonlinear finite elements that account for both geometric nonlinearity and inelastic material behavior. The numerical simulation is verified by comparison of the numerical results with available analytical solutions and experimental data. Special emphasis is given on structural stability in terms of post-buckling and imperfection sensitivity.

For the case of externally-pressurized confined cylinders, the numerical results are presented in the form of pressure-deformation equilibrium paths, and show an unstable post-buckling response beyond the point of ultimate pressure capacity. The sensitivity of response on the presence of initial imperfections, in the form of both initial out-of-roundness of the cylinder cross-section and the presence of initial gap between the cylinder and the surrounding medium, is examined. The effects of the ratio D/t, the yield stress, the friction, the medium deformability, and the vertical preloading on the ultimate pressure are investigated. Based on the numerical results, a simplified and efficient methodology is developed, which is compatible with the recent general provisions of European design recommendations for shell buckling, and could be used for design purposes. Finally, a comparison with the similar problem of “shrink buckling” is attempted and the differences

between those two problems are pin-pointed, emphasizing the significantly different response with respect to the presence of initial imperfections.

For the case of lined pipes under longitudinal bending, the stresses and deformations in the compression zone are monitored, with emphasis on possible detachment of the liner from the outer pipe. The possibility of bifurcation in a wrinkling pattern, including the possibility for a secondary bifurcation is examined. Furthermore, the liner ovalization, bending moment, local hoop curvature, axial stress, and hoop stress are investigated. The effects of liner pipe thickness, outer pipe thickness, friction, and liner prestressing due to manufacturing process on the buckling curvature and wavelength are examined. The sensitivity of response on the presence of initial wrinkling imperfections is investigated. Finally, the effect of external pressure on the mechanical response is discussed.

4.2 Conclusions

A detailed description of conclusions on each of the two subjects has been presented separately at the end of the corresponding chapter, and the reader is referred to sections 2.7 and 3.7 for the two problems respectively. An attempt to summarize those conclusions is offered below.

For the case of externally-pressurized confined cylinders, the numerical results of elastic and steel cylinders compared successfully with available closed-form analytical predictions and supported by available experimental data. The numerical results showed an unstable post-buckling response beyond the point of maximum capacity due to development of a plastic collapse mechanism, indicating significant imperfection sensitivity. A three-hinge plastic collapse mechanism with one stationary and two moving plastic hinges was developed that results in a closed-form expression and illustrates the post-buckling response of the cylinder in an approximate yet very representative manner. The numerical results showed a significant sensitivity of the ultimate pressure in terms of initial imperfections, in the form of both initial out-of-roundness of the cylinder cross-section and initial gap between the cylinder and the surrounding medium, on the value of the maximum pressure. Reduction of the medium modulus results in a substantial reduction of the pressure capacity of the cylinder. The simplified and efficient methodology that was developed, is compatible with the recent general provisions of European design recommendations for shell buckling, quite close to and on the conservative side of the present numerical results, and could be used for the prediction of buckling pressure of

buried pipelines and other rigidly encased steel cylinders. Experimental results are compared very well with the numerical results, as well as with the predictions of the proposed design methodology. The main differences of the shrink buckling problem with the hydrostatic buckling problem were pin-pointed, emphasizing the significantly different response of the two problems with respect to the presence of initial imperfections.

For the case of lined pipes under longitudinal bending, the numerical results indicate that separation (detachment) between the liner and the outer pipe occurs at the compression zone, leading to liner buckling in the form of wrinkling. A first bifurcation occurs at curvature κ_{cr} that leads to a uniform wrinkling pattern, associated with small values of detachment and of buckle wave-height. Subsequently, a second bifurcation occurs at a bending curvature κ'_{cr}, which is higher than the value of κ_{cr}. This secondary bifurcation is associated with larger values of wrinkling amplitude and more visible deformations with respect to the first bifurcation and therefore can be considered as the wrinkling limit state of liner failure due to bending. The liner prestressing due to the manufacturing process has a beneficial effect on the value of critical curvature, whereas the critical curvature is sensitive to the presence of initial wrinkling imperfections. Comparison of the present numerical results with available experimental data has demonstrated that the buckled shapes obtained numerically are very similar to the shapes observed experimentally. In addition, the numerical values of wavelength and evolution of wrinkling height are compared very well with relevant test measurements. The external pressure affects the liner response at rather low pressure levels; when the level of external pressure exceeds a rather low value, the liner pipe does not detach from the outer pipe, while the entire lined pipe collapses due to excessive ovalization, and liner wrinkling does not occurs.

It can be generally concluded that the lateral confinement of the shell, either is a surrounding medium or another shell, characterizes the structural behavior of the shell-confinement system. In particular, the lateral confinement has a positive influence on the maximum (pressure or bending) capacity of the shell. Furthermore, the interaction of the steel shell with the lateral confinement results in the development of a plastic collapse mechanism which accelerates the failure of the shell. The stiffness of the confinement is controlled either through the elastic modulus of the surrounding medium or through the thickness of the confining shell (in the case of double-wall pipes). Particularly, the increase of the confinement stiffness decreases the ovalization and the detachment of the shell and as a consequence increases resistance to buckling.

The above problems of structural mechanics often occur to numerous technological/engineering applications. The dissertation contributes to the numerical investigation of the buckling of cylindrical shells within a confinement medium and its sensitivity on imperfections, as well as to the better understanding of their mechanical behavior. Up to date, it constitutes the most rigorous numerical simulation of confined cylindrical shells under structural loading and pressure. For the problem of externally-pressurized cylinders, with direct application to buried steel pipelines, it was demonstrated that buckling occurs well below the plastic pressure level, improving existing design practice. Furthermore, a new design methodology is proposed, compatible with the recent general provisions of European design recommendations for shell buckling. In addition, results of this research have been already adopted in two ASCE Manual of Practice for buried steel pipeline design; MoP No.79 for steel penstocks and Mop No. 119 for buried flexible steel pipes. Finally, the structural behavior of an innovative steel pipeline product, referred to as "lined pipe", is numerically investigated and the mechanism of liner wrinkling is examined in detail, allowing for its efficient use in practical applications for hydrocarbon transportation. This offers the theoretical background for the safer application of lined pipes in offshore pipeline construction, an issue of significant technological interest.

4.3 Recommendations for further study

Based on the present results for the mechanical and structural behavior of confined cylindrical steel shells, several engineering problems, relevant with the present investigation, are recommended for further study.

For the case of externally-pressurized confined cylinders, the buckling and post-buckling behavior of a three-dimensional problem is an open issue with particular emphasis on possible occurrence of buckle propagation of the steel cylinders in confined conditions, considering the effect of deformable medium.

In addition, several issues related to the bending buckling of confined cylinders could be proposed for further study, given the fact that lined pipes constitute a promising technological application. The research could be continued towards defining a wrinkle acceptability criterion. In addition, the present study could be extended investigating the cyclic loading response, including fatigue/ratcheting phenomena at the wrinkled area, motivated by the offshore installation of such pipes with the reeling installation method.

Furthermore, the design, set-up and implementation of experimental testing on structural behavior of lined pipes under various types of loading (e.g. longitudinal bending with or without internal/external pressure, cyclic loading), constitutes a challenge, and will give significant value to the numerical simulations towards progress on understanding better the problem. Finally, an ultimate goal of the above research issues could be the development of relevant design guidelines for lined pipes concerning both their manufacturing and their construction.

Finally, the structural stability of cylindrical shells with lateral confinement under primarily bending loading conditions may be of interest to nano-composite tubes reinforced by an inner single-walled carbon nanotube. The simulation of the mechanical behavior of carbon nanotubes using structural (shell) models, as an alternative to molecular dynamics models, has gained quite some attention lately. In particular, the structural stability and the definition of the buckling load for such confined cylindrical shells are of particular interest and remain an open issue for further investigation.

Appendix A: Proposal for EDR chapter on confined cylinders under external pressure

A proposed chapter for the design of confined steel cylinders, within the framework of the European Design Recommendations (EDR), is developed and presented in this Appendix, for possible inclusion of the present work in future editions of the EDR.

A Confined steel cylinders under uniform external pressure

Principal authors: D. Vasilikis, S. A. Karamanos

A.1 General

This chapter is concerned with the structural stability of long steel cylinders, surrounded by an elastic medium, subjected to uniform external pressure on the steel cylinder directly.

The rules of this chapter are based on extensive numerical parametric studies using GNA, GMNA and GMNIA analyses (Vasilikis & Karamanos, 2009, 2011). Special emphasis is given on the effects of initial imperfections; those are considered in the form of initial out-of-roundness of the cylinder and as an initial gap between the cylinder and the medium. Furthermore, the effects of the deformability of the surrounding medium are discussed. A simple and efficient design methodology, which is compatible with the recent general provisions of European Design Recommendations for shell buckling is developed. These provisions differ from those for steel cylinders under hoop compression described in Chapter 10.2.3 of these Recommendations, which focus on unconfined lateral conditions only. The results indicate significant imperfection sensitivity and a strong dependency on the medium stiffness.

In numerous applications, externally-pressurized steel cylinders are confined within a rigid or deformable cavity. Typical examples are buried steel pipelines in various soil conditions or encased in concrete, steel liners for the rehabilitation of damaged buried pipelines, steel tunnels and ducts used in power plants, and steel casing employed in oil and gas production wells. In those applications, hydrostatic pressure conditions may develop because of the presence of ground water and the permeability of the surrounding medium, and may cause significant hoop stresses in the cylinder, which may cause cylinder buckling. Due to the confining effect of the cavity, the steel cylinder usually does not ovalize, and buckling occurs in the form of an “inward lobe”, as shown in Figure A.1.

The design rules of the present chapter refer mainly to steel cylinders surrounded by a stiff (undeformable) medium. The geometrical properties and imperfections are stated in section A.2, whereas buckling design rules are stated in section A.3. In section A.4, the design methodology is illustrated in a design example.

A.2 Geometrical properties, boundary conditions and imperfections

A.2.1 Geometrical properties

(1) Description of system: The following rules are applicable to steel cylinders confined by a rigid (non-deformable) medium with diameter-to-thickness ratio ranging between 100 and 300.

The cylinders are relatively thin-walled with diameter-to-thickness D/t ratio that ranges between 100 and 300, which is typical for water transmission pipelines or rehabilitation liners.

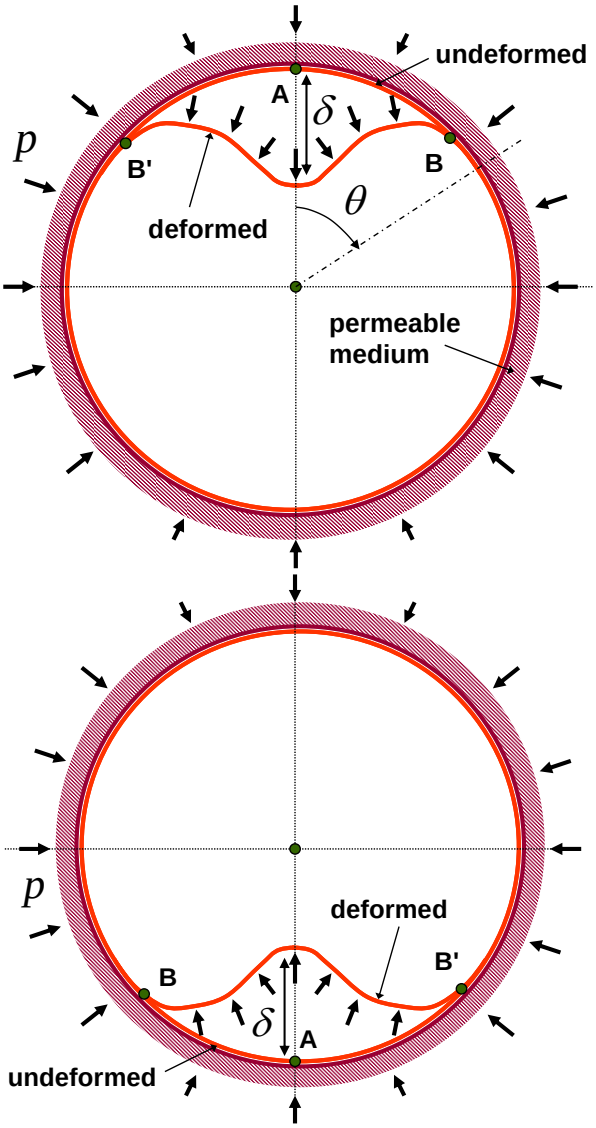

Figure A.131. Schematic representation of the buckling problem of an externally-pressurized cylinder confined by the permeable surrounding medium. (a) lobe on the top and (b) buckling lobe at the bottom due to buoyancy

D	diameter of the cylinder
r	radius of the cylinder
t	thickness of the cylinder
θ	hoop coordinate
δ	vertical displacement
p	uniform external pressure

(2) Loading: The rules only apply to uniform external pressure loading p around the cylinder, see Figure A.131.

A.2.2 Boundary and symmetry conditions

(1) Boundary conditions: For the structural system considered in this problem, no variation of loading and deformation is assumed along the cylinder axis. In consequence, plane-strain conditions are considered. Furthermore, symmetry is considered with respect to the $\theta = 0$ plane.

A.2.3 Imperfections

(1) Imperfections: Two types of initial imperfections are considered in the present study.

(2) The first type of imperfection is an initial gap between the confining medium and the cylinder. The gap is introduced assuming that the circular cavity of the medium has a radius slightly larger than the circular cylinder radius, and that the cylinder and the cavity are initially in contact at one location (e.g. $\theta = \pi$), so that the maximum gap between the cylinder and the medium occurs at $\theta = 0$. The amplitude of the gap is denoted as g (see Figure A.132a).

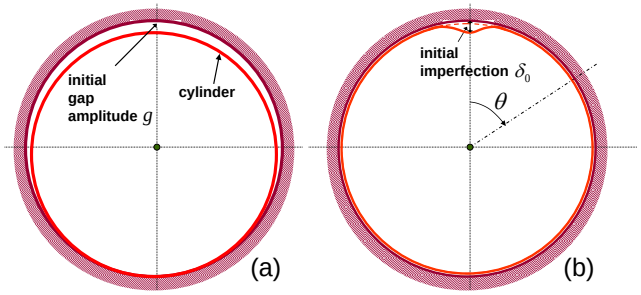

Figure A.132. Schematic representation of a confined ring with (a) gap-type initial imperfection and (b) "out-of-roundness" initial imperfection

(3) The second type of imperfection is a small initial "out-of-roundness" imperfection on the steel cylinder in the form of a small localized ("single-lobe") inward displacement pattern at the vicinity of the $\theta = 0$ location (see Figure A.132b). The size of the out-of-roundness is denoted by δ_0.

A.2.4 Range of applicability

(1) The rules of this chapter are applicable for cylindrical shells within the ranges given by

$$100 \le \frac{D}{t} \le 300 \qquad \text{(A.1)}$$

Equation (A.1) represents the range of D/t values used in the numerical parametric studies for determining the buckling parameters given in paragraph A.3 (see also Vasilikis & Karamanos, 2009, 2011).

A.3 Buckling Design

The rules refer to cylinders confined by a stiff (undeformable) medium.

A.3.1 Elastic critical buckling resistance

(1) The elastic critical buckling pressure p_{Rcr} is given by

$$p_{Rcr} = \frac{E}{1-\nu^2}\left(\frac{t}{D}\right)^{2.2} \qquad \text{(A.2)}$$

The equation for the elastic critical buckling resistance is taken from the paper by Glock (1977).

A.3.2 Plastic reference resistance

(1) The plastic reference resistance may be taken as

$$p_{Rpl} = 2\frac{\sigma_y}{\sqrt{1-\nu+\nu^2}}\left(\frac{t}{D}\right) \qquad \text{(A.3)}$$

where ν is Poisson's ratio ($\nu = 0.3$ for metals)

Equation A.3 is the fully plastic limit load of a ring based on small displacement theory and ideal plastic behaviour obtained by simple statics and considering plane strain conditions of the ring in the out-of-plane direction.

A.3.3 Characteristic buckling resistance

(1) The characteristic buckling pressure p_{Rk} should be determined as

$$p_{Rk} = \chi p_{Rpl} \qquad \text{(A.4)}$$

The determination of the characteristic buckling resistance follows procedure of EN 1993-1-6 (see Section 8.2) and uses the parameters set out in A.3.4.

in which

p_{Rpl} = plastic reference resistance (Eq. (A.3))

χ = buckling reduction factor for elastic- plastic buckling (see below)

(2) The buckling reduction factor should be determined from

$$\chi = f(\lambda)$$

where λ is the relative slenderness

The parameter χ is taken from Chapter 9 of these Recommendations, where $\chi = f(\lambda)$ is presented in the form of Eqs 9.3 to 9.5, is identical to section 8.5.2 of EN 1993-1-6. The three ranges of λ refer to the following

parameter

$$\lambda = \sqrt{\frac{p_{Rpl}}{p_{Rcr}}} = \sqrt{\frac{2.26\,\sigma_y(1-\nu^2)}{E}\left(\frac{D}{t}\right)^{1.2}} \quad \text{(A.6)}$$

and where the function $\chi = f(\lambda)$ is to be taken from EN 1993-1-6 or Chapter 9 of these Recommendations, using the buckling parameters which are given below.

values of p_{Rk}

$\lambda \le \lambda_0$: $p_{Rk} = p_{Rpl}$ *(plastic)*

$\lambda_0 < \lambda \le \lambda_p$: *elastic-plastic interaction*

$$\frac{p_{Rk}}{p_{Rpl}} = 1 - \beta\left(\frac{\lambda - \lambda_0}{\lambda_p - \lambda_0}\right)^{\eta}$$

$\lambda_p < \lambda$: $p_{Rk} = \alpha \cdot p_{Rcr}$ *(elastic)*

A.3.4 Buckling parameters

(1) The squash limit relative slenderness λ_0 should be taken as

$$\lambda_0 = 0.25 \quad \text{(A.7)}$$

The two reference slenderness parameters λ_0 *and* λ_p *define the three parts of the buckling curve:*

a) plastic plateau to λ_0

b) elastic-plastic interaction between λ_0 *and* λ_p *,*

c) elastic buckling beyond λ_p *.*

The buckling parameters are repeated here to simplify the usage of the equations.

(2) The plastic limit relative slenderness λ_p should be determined as

$$\lambda_p = 2.2 \quad \text{(A.8)}$$

(3) The elastic imperfection reduction factor should be obtained from

$$\alpha = \frac{0.15}{\Delta^{0.7}} \quad \text{(A.9)}$$

where Δ is the characteristic imperfection amplitude

$$\Delta = \left(\frac{\delta_0 + 3g}{r}\right)\sqrt{\left(\frac{D}{t}\right)} \quad \text{(A.10)}$$

(4) The interaction exponent η should be taken as

$$\eta = 0.6 - 3\Delta \quad \text{(A.11)}$$

but always $\eta \ge 0.3$

(5) The plastic range factor β should be determined as

$$\beta = 1 - \frac{\alpha}{\lambda_p^2} \quad \text{(A.12)}$$

The plastic range factor governs the load level at which plasticity first begins to affect the buckling strength significantly.

A.3.5 Buckling strength verification

(1) The design buckling resistance p_{Rd} should be obtained from

$$p_{Rd} = \frac{p_{Rk}}{\gamma_M} \qquad \text{(A.13)}$$

where the safety factor γ_M should be taken from the other relevant application standard. If none exists, the default value (EN 1993-1-1) is

$$\gamma_M = 1{,}1 \qquad \text{(A.14)}$$

(2) It should be verified that

$$p_{Ed} \le p_{Rd} \qquad \text{(A.15)}$$

A.4 Design example

Design of a steel pipe under a dam encased in concrete.

A steel pipe under a dam with diameter-to-thickness (ring flexibility parameter) $D/t = 180$ is encased in concrete. The steel material has yield stress $\sigma_y = 300MPa$. Over time, pressure builds up on the pipe. Assuming a gap equal to 0.1% of the pipe radius (and neglecting localized out-of-roundness δ_0), is the pipe safe against wall buckling?

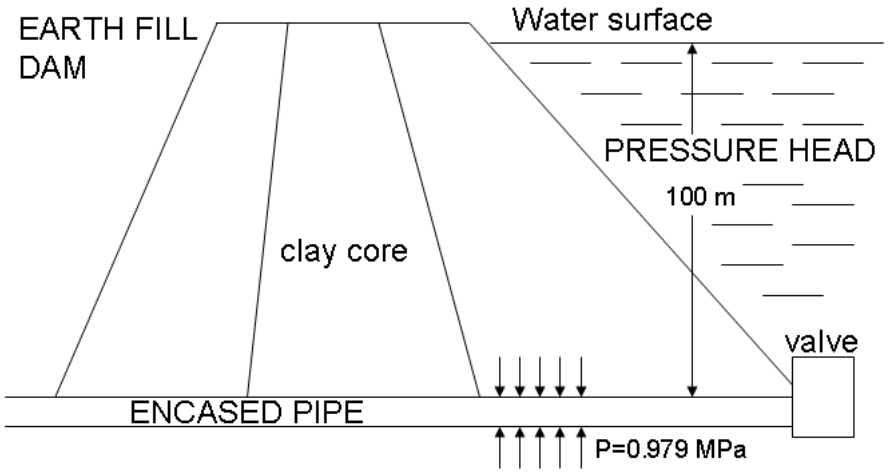

Figure A.133 Encased pipe in dam

Technical data

$D = 1530mm,\ t = 8.5mm$

Material: $\sigma_y = 300MPa,\ E = 210{,}000MPa,\ v = 0.3$

Pressure on the pipe: $p = 0.979MPa$

Design values of loads

The partial factor on loads is $\gamma_F = 1.35$

Design pressure on the pipe: $p_{Ed} = 0.979 \times 1.35 = 1.322 MPa$

Range of applicability

$D/t = 180$

The buckling resistance is within our range ($100 \le D/t \le 300$) and can be checked with the present provisions.

Elastic critical buckling resistance

$$p_{Rcr} = \frac{E}{1-\nu^2}\left(\frac{t}{D}\right)^{2.2} = \frac{210,000}{1-0.3^2}\left(\frac{8.5}{1530}\right)^{2.2} = 2.52 MPa \quad \text{(Eq. A.2)}$$

Plastic reference resistance

$$p_{Rpl} = 2\frac{\sigma_y}{\sqrt{1-\nu+\nu^2}}\left(\frac{t}{D}\right) = 2\frac{300}{\sqrt{1-0.3+0.3^2}}\left(\frac{8.5}{1530}\right) = 3.75 MPa \quad \text{(Eq. A.3)}$$

Buckling parameters

The characteristic imperfection amplitude Δ is

$$\Delta = \left(\frac{\delta_0 + 3g}{r}\right)\sqrt{\left(\frac{D}{t}\right)} = \left(0 + 3 \times 0.001\right)\sqrt{180} = 0.04 \quad \text{(Eq. A.10)}$$

Thus, the elastic imperfection reduction factor a is

$$\alpha = \frac{0.15}{\Delta^{0.7}} = \frac{0.15}{0.04^{0.7}} = 1.43 \quad \text{(Eq. A.9)}$$

The squash limit relative slenderness λ_0 is

$$\lambda_0 = 0.25 \quad \text{(Eq. A.7)}$$

The plastic limit relative slenderness λ_p is

$$\lambda_p = 2.2 \quad \text{(Eq. A.8)}$$

The interaction exponent η is

$$\eta = 0.6 - 3\Delta = 0.6 - 3 \times 0.04 = 0.48 \quad \text{(Eq. A.11)}$$

The plastic range factor β is

$$\beta = 1 - \frac{\alpha}{\lambda_p^2} = 1 - \frac{1.43}{2.2^2} = 0.704 \quad \text{(Eq. A.12)}$$

Characteristic buckling resistance is calculating as follows:

The shell slenderness is

$$\lambda = \sqrt{\frac{p_{Rpl}}{p_{Rcr}}} = \sqrt{\frac{2.26\,\sigma_y(1-\nu^2)}{E}\left(\frac{D}{t}\right)^{1.2}} = \sqrt{\frac{2.26 \times 300(1-0.3^2)}{210000}\left(180\right)^{1.2}} = 1.22 \quad \text{(Eq. A.6)}$$

or

$$\lambda = \sqrt{\frac{p_{Rpl}}{p_{Rcr}}} = \sqrt{\frac{3.75}{2.52}} = 1.22 \qquad \text{(Eq. A.6)}$$

Therefore, $\lambda_0 < \lambda \le \lambda_p$ and the design is controlled by elastic-plastic interaction buckling. Consequently,

$$\frac{p_{Rk}}{p_{Rpl}} = 1 - \beta\left(\frac{\lambda - \lambda_0}{\lambda_p - \lambda_0}\right)^{\eta} \Rightarrow p_{Rk} = 3.75\left[1 - 0.704\left(\frac{1.22 - 0.25}{2.2 - 0.25}\right)^{0.48}\right] = 1.862MPa$$

Design buckling resistance

$$p_{Rd} = \frac{p_{Rk}}{\gamma_M} = \frac{1.862}{1.1} = 1.693MPa \qquad \text{(Eq. A.13)}$$

$$p_{Ed} = 1.322MPa \le 1.693MPa = p_{Rd} \quad \checkmark$$

A.6 References

Glock, D. (1977). "Überkritisches Verhalten eines Starr Ummantelten Kreisrohres bei Wasserdrunck von Aussen und Temperaturdehnung." (Post-Critical Behavior of a Rigidly Encased Circular Pipe Subject to External Water Pressure and Thermal Extension), *Der Stahlbau*, Vol. 7, pp. 212-217.

Vasilikis, D. and Karamanos, S. A. (2009), "Stability of Confined Thin-Walled Steel Cylinders under External Pressure", *International Journal of Mechanical Sciences,* Vol. 51, No. 1, pp. 21-32.

Vasilikis, D. and Karamanos, S. A. (2011), "Buckling Design of Confined Steel Cylinders under External Pressure", *Journal of Pressure Vessel Technology*, Vol. 133, No. 1, Paper Number: 011205.

Comité Européen de Normalization (2007), *Strength and Stability of Shell Structures*, EN 1993-1-6, Eurocode 3, part 1-6, Brussels, Belgium.

European Convention for Constructional Steelwork (2008), *Buckling of Steel Shells, European Design Recommendations*, 5th Edition, ECCS Publication No. 125, J. M. Rotter and H. Schmidt Eds., Brussels, Belgium.

Buried Flexible Steel Pipe, Design and Structural Analysis, (2009), ASCE Manuals and Reports on Engineering Practice No. 119, USA

Appendix B: Numerical simulation of lined pipe manufacturing process

In the present chapter, the manufacturing process of lined pipes is simulated in order to determine the liner residual hoop stress at the end of the process. This residual stress is inserted in the steel liner as initial condition (prestressing) before the application of the bending curvature.

In general, pipe producers provide two types of clad (or lined) pipes: metallurgical clad pipes and mechanical clad pipes. In manufacturing metallurgical clad pipes, the bonding process for joining the corrosion-resistant internal sleeve to the strong external carbon steel can be performed by weld cladding, centrifugal casting, extrusion, or rolling laminated plates. However, during this metallurgical process a single heat treatment is used for both the ferritic external layer and the austenitic internal layer, and some material combinations may not be technically feasible. In any case, regardless of the manufacturing process, the main characteristic of metallurgically clad pipes is that the two materials become a single mass. On the other hand, mechanically clad (or lined) pipe consists of a corrosion-resistant liner inserted into an external carbon steel pipe. The nature of the mechanical bond depends on the manufacturing process, but regardless of the method, the bond is purely mechanical, in the sense that the materials of the outer pipe and the liner pipe remain two distinct materials in the sense that they do not fuse together to become a single mass as metallurgically bonded pipes do.

Two types of mechanical lined pipes are considered in the section of lined steel pipes; the Snug-Fit Pipe (SFP) in which the liner is stress-free, and the Tight-Fit Pipe (TFP) where the liner has an initial hoop compressive stress due to the manufacturing process. More specifically, in TF Pipes, the liner is fitted inside the carbon steel outer pipe through a thermo-hydraulic manufacturing process, resulting in a tightly-bonded lined pipe, where the outer pipe “compresses” the liner pipe, introducing a significant hoop compressive stress in the liner, which is often called “residual stress” or “prestressing” and the two pipes are mechanically bonded together. During this process (Figure 134), the outer pipe is heated first. Subsequently, the liner pipe is inserted inside the outer pipe and pressurized internally so that it is expands and it is in good contact with the outer pipe. Finally, the outer pipe is cooled and the internal pressure of the liner pipe is removed, so that the two pipes are mechanically bonded together. The heating temperature of the outer pipe and the level of internal pressure are important parameters of the above manufacturing process. In addition, when the two pipes are in contact, there is an amount of heat transferred from the outer pipe

to the liner, depending on the duration of contact. Furthermore, the sequence of outer pipe cooling and depressurization could influence the final amount of residual stress. The manufacturing process follows the following steps:

Step 1: the outer pipe is heated up to a prescribed temperature.

Step 2: the liner is internally pressurized until it is in contact with the outer pipe, and further pressurized, expanding the double-wall pipe system, until the maximum prescribed pressure is reached.

Step 3: the temperature of the liner pipe is increased up a certain level, as a result of liner-outer pipe contact and heat transfer from the outer pipe to the liner (it depends on the time duration of liner-outer pipe contact during manufacturing).

Step 4: the liner is depressurized.

Step 5: the outer pipe is cooled.

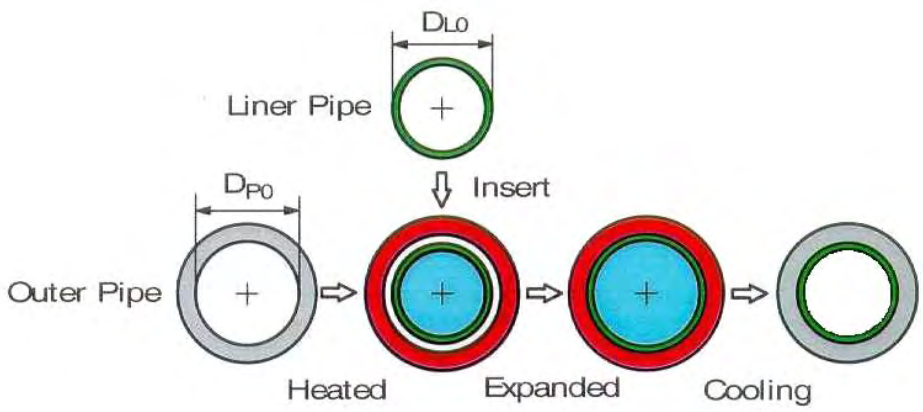

***Figure 134**: Schematic representation of the manufacturing process [1],[2].*

There are several parameters determining the final value of the residual stress, namely (a) the heating temperature of the outer pipe ΔT, (b) the level of pressure applied for liner expansion P_{int}, (c) the heating temperature $\Delta T'$ of the liner pipe due to partial or complete heating, (d) whether step 5 (cooling) occurs simultaneously or after step 4 (depressurization).

The above described manufacturing process is simulated through the finite element modeling procedure presented in section 3.2 and the parameters that influence the manufacturing process of TFP are investigated. Specifically, an ovalization analysis is conducted using a two-dimensional finite element model with appropriate symmetry conditions. In the present numerical simulation, the two pipes are assumed initially stress-

free and an initial very small gap of 0.2 mm is assumed between the two pipes [1],[2]. Following the dimensions of pipes examined in chapter 3, the considered external diameter D_o and thickness t_o of the outer pipe is 325 mm and 14.3 mm respectively. The outside diameter of the liner pipe D_l is considered equal to 296 mm, whereas the thickness t_l of the liner pipe is equal to 3 mm.-The material properties of the two pipes are described in detail in the section 3.4 of the dissertation. The thermal expansion coefficient for both liner and outer pipe is $\alpha = 1.16 \times 10^{-5} / {}^{o}C$, whereas the reference temperature is considered equal to 25^{o}C.

The variation of the external radius of the liner and the internal radius of the outer pipe during the manufacturing process is depicted in Figure 135. The outer pipe temperature increase ΔT is 350^{o}C and the internal pressure P_{int} of the liner is 15 MPa. The temperature increase $\Delta T'$ of the liner due to the contact with the heat outer pipe is 175^{o}C (i.e. the half of the outer pipe temperature increase). In the first step, it is observed the increase of the outer pipe radius Δr due to the heating of the pipe. The amount of the radius increase can be calculated, assuming plain strain conditions, by the following formula: $\Delta r = \alpha \cdot \Delta T (1+v) \cdot r$. During the second step of internal pressure, it is shown that the liner radius increases due to expansion until it touches the outer pipe in order to expand together as a single pipe. It is noted that the full plastification pressure P_y of the liner cross-section, given by equation $P_y = 2\sigma_y \frac{t}{D}$ is equal to 6 MPa, quite lower than internal pressure P_{int}. Therefore, at that pressure level (i.e. $P = P_y$), the increase of the liner radius loses the linearity as shown in Figure 135, and the contact of the liner with the outer pipe occurs a little later in a pressure level equal to 7.42 MPa. In the third step, the system continues to expand due to liner pipe heating. Next, during the two final steps of unloading (depressurization and cooling), it is observed that the two pipes remain in contact.

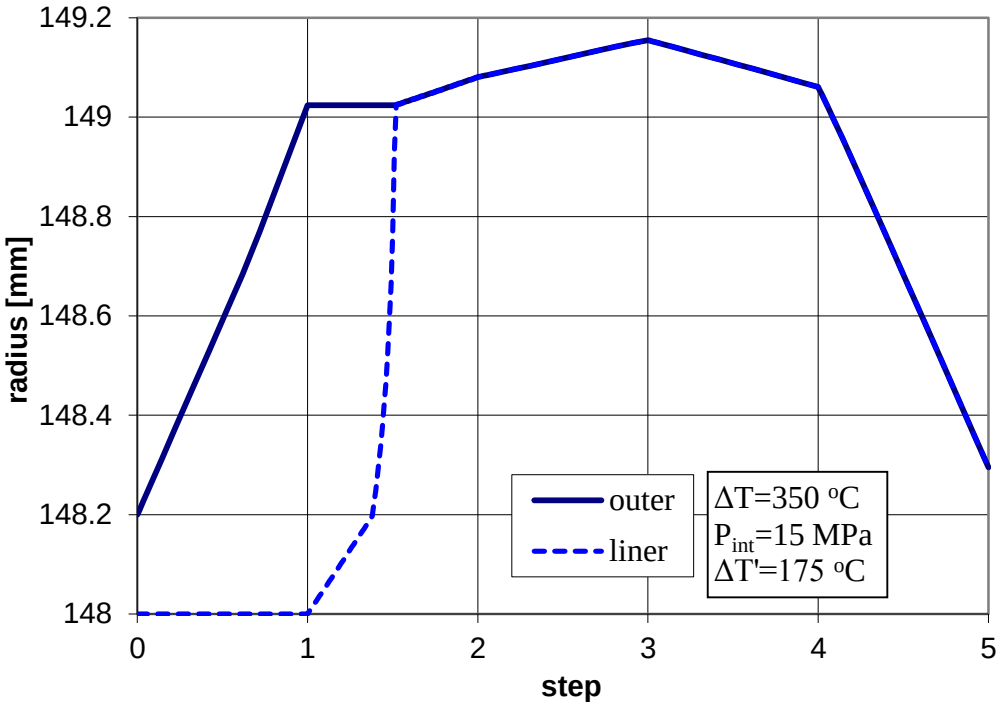

***Figure 135**: Variation of the external radius of the liner and the internal radius of the outer pipe during the manufacturing process.*

One of the parameter that affects the manufacturing procedure is the amount of heat that transferred from the outer pipe to the liner, which depends on the duration of contact of the liner with the heat outer pipe in the third step. In most cases, partial heating $(\Delta T' < \Delta T)$ of the liner is considered, but if the two pipes are in contact for a long time, complete heating $(\Delta T' = \Delta T)$ of the liner should be taking into account. In Figure 136, the displacement of the liner radius is depicted in terms of manufacturing steps for partial and complete heating.

Another parameter that also affects the manufacturing procedure concerns the two final steps of the procedure, and specifically whether the step 4 (depressurization) and step 5 (cooling) applied simultaneously in one unloading step or step 5 occurs after the step 4. In Figure 137, the displacement of the liner radius is depicted in terms of manufacturing steps for these two cases (i.e. two unloading steps or simultaneous unloading).

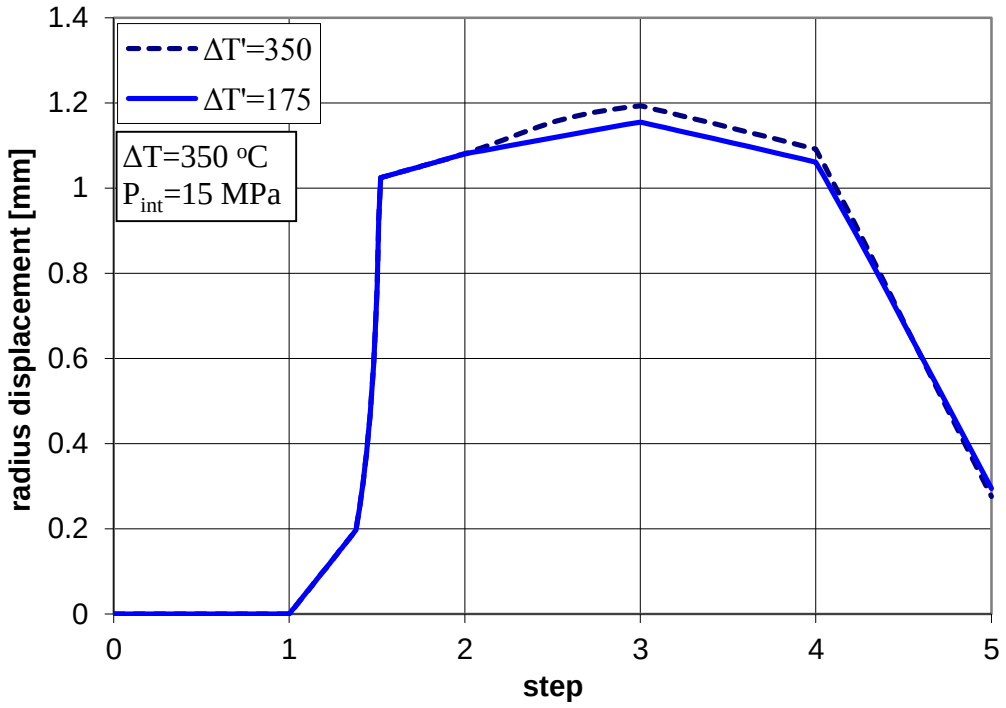

***Figure 136**: Effect of the partial and complete heating of the liner on the variation of the external radius of the liner pipe.*

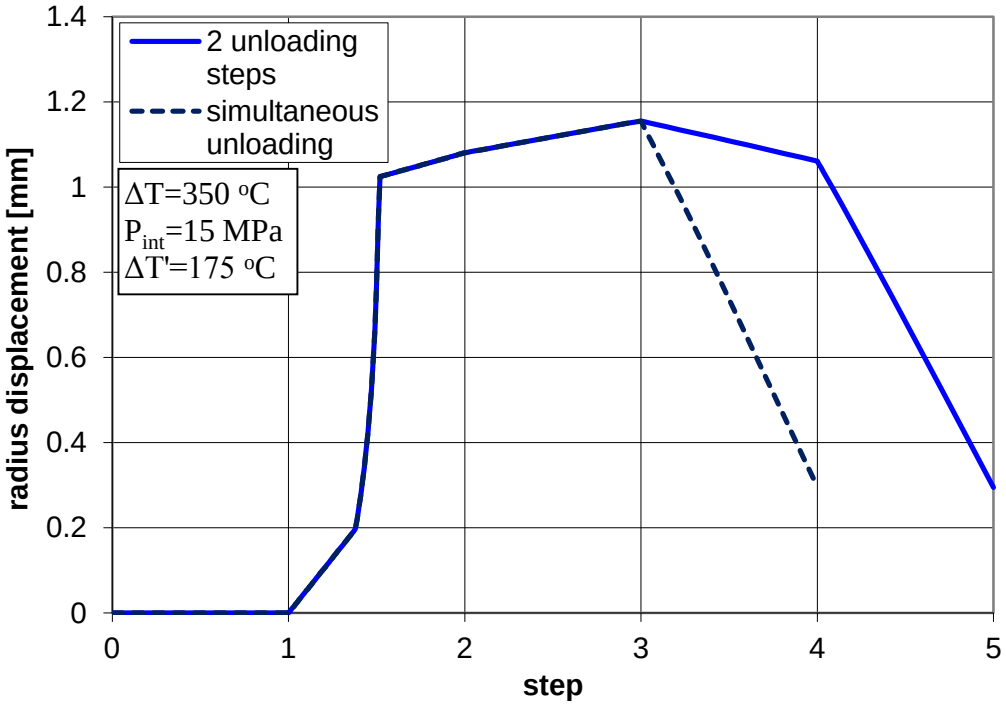

***Figure 137**: Effect of the simultaneous application of step 4 and 5 on the variation of the external radius of the liner and the internal radius of the outer pipe.*

The variation of mises, hoop and axial stresses for liner and outer pipe during the manufacturing process is shown in Figure 138. It is shown that the compression of the liner from the outer pipe in the two final steps of unloading, results in a residual hoop compressive stress of the liner pipe.

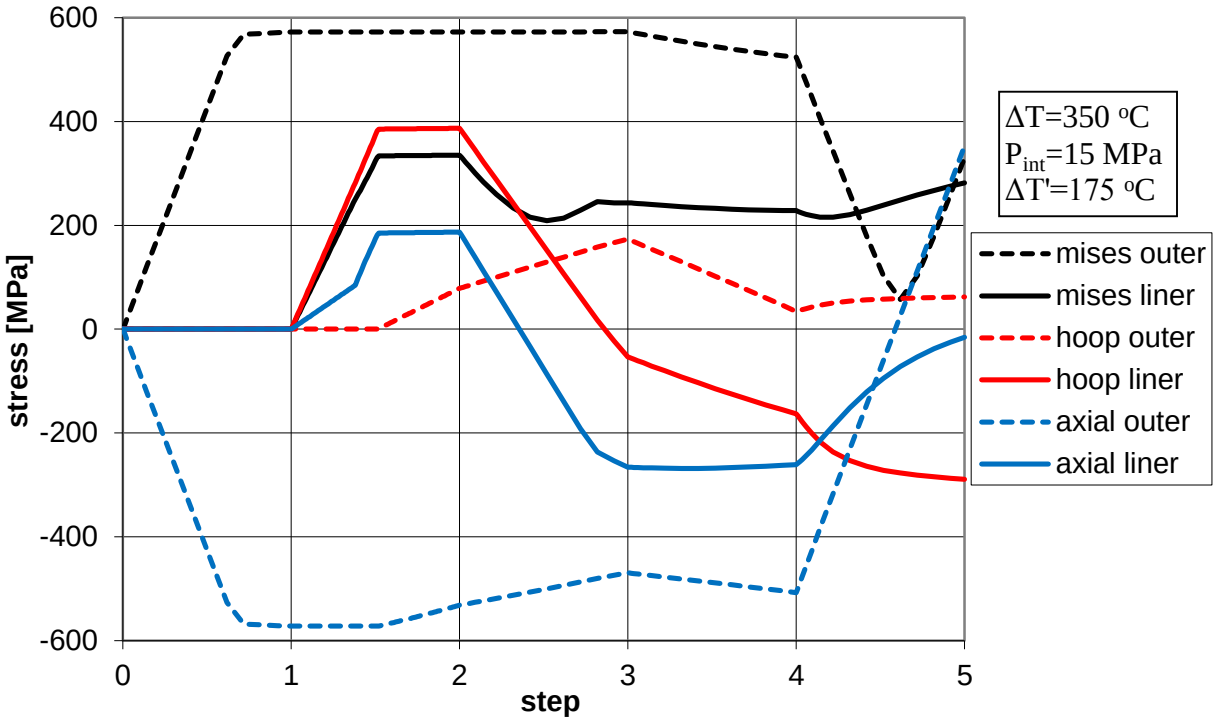

***Figure 138**: Variation of mises, hoop and axial stresses for liner and outer pipe during the manufacturing process.*

Figures 139 depict the variation of hoop stress of the liner pipe during the manufacturing process for different values of the liner temperature increase $\Delta T'$, (a) for two separate unloading steps (firstly depressurization and then cooling) and (b) for one unloading step (simultaneous cooling/depressurization). It is concluded that for both cases, the higher temperature increase for the liner pipe (i.e. long time contact with the hot outer pipe), the smaller the residual hoop compressive stress of the liner pipe.

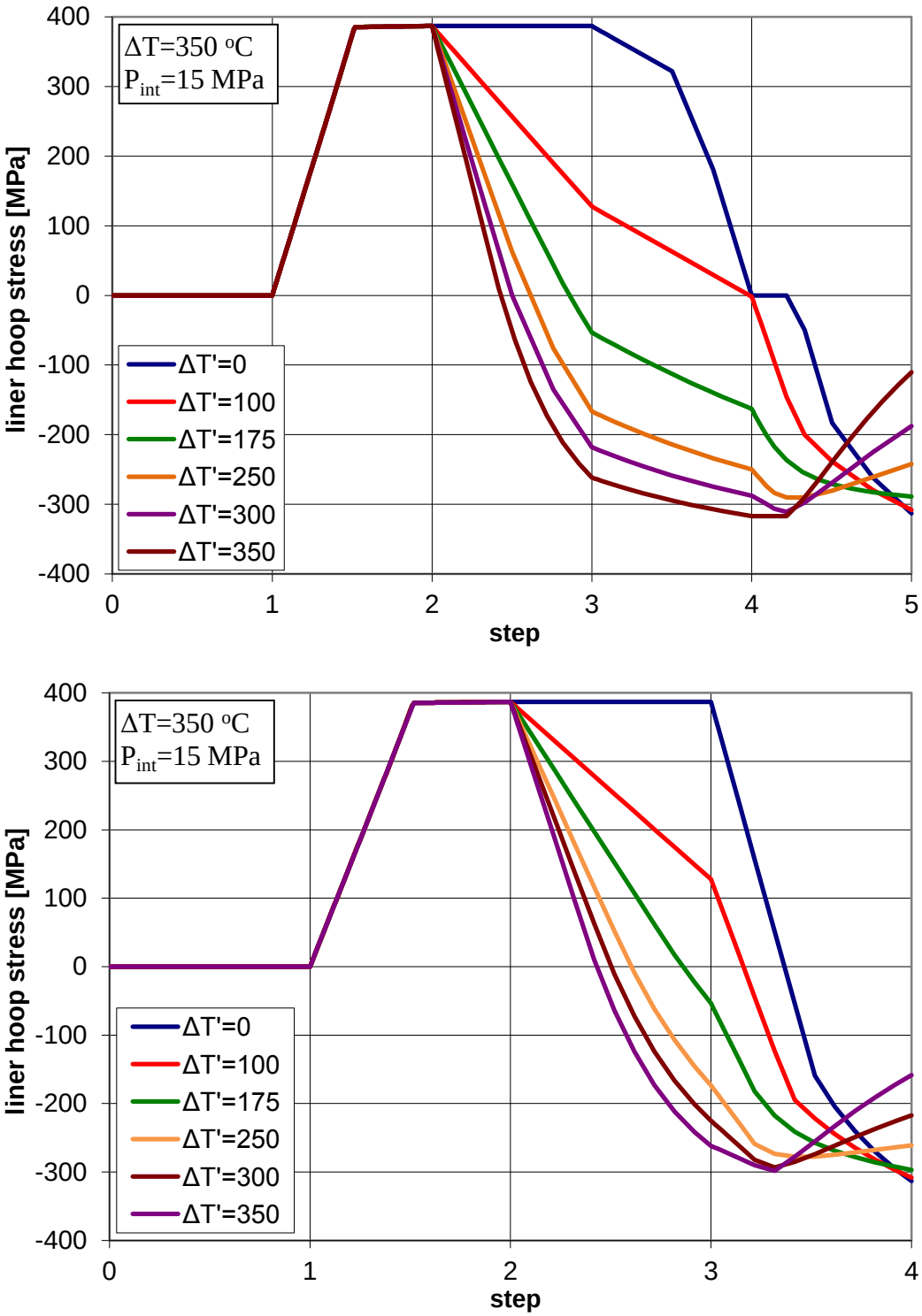

***Figures 139**: Variation of liner hoop stress during the manufacturing process for different values of liner temperature increase; (a) two unloading steps, (b) one unloading step.*

Figure 140 shows the effect of simultaneous cooling/depressurization in terms of the liner pipe temperature increase on the residual hoop stress of the liner. The sequence of cooling/depressurization is important only when the liner pipe is significantly heated. Finally, one can readily notice that one specific value of residual stress may correspond to several combinations of the manufacturing parameters.

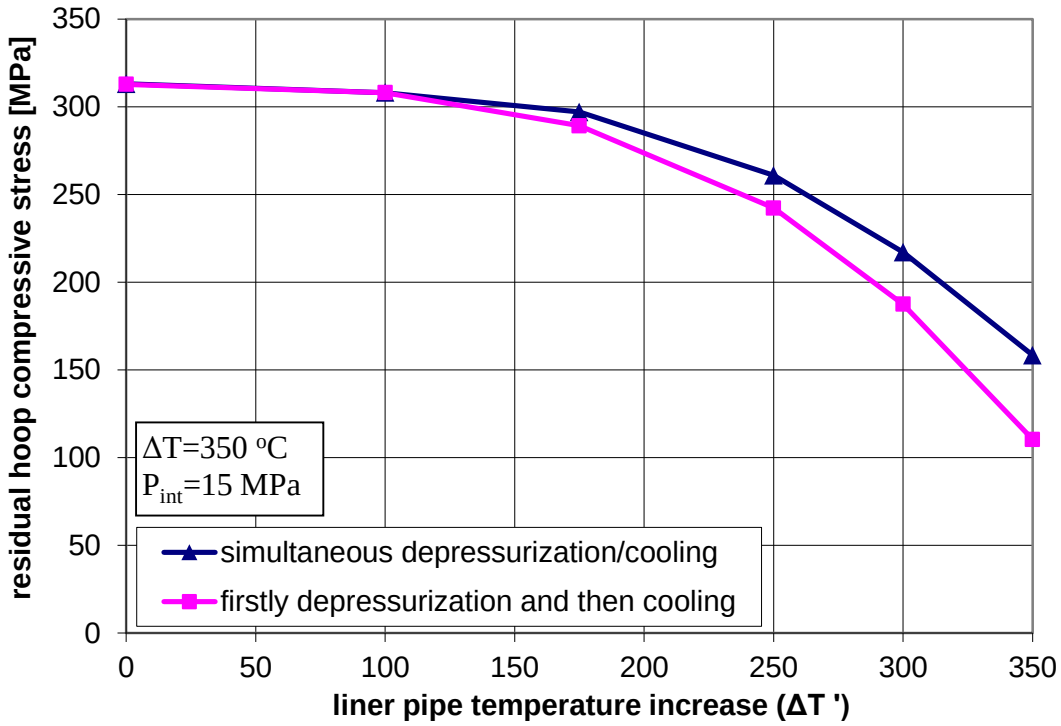

***Figure 140**: Variation of residual liner hoop stress in terms of heating temperature of liner pipe.*

Figure 141 shows the variation of residual hoop stress of the liner with respect to the heating temperature $\Delta T'$ of the liner pipe, when the internal pressure P_{int} in the second step is either 15 or 25 MPa. The numerical results show that the level of internal pressure does not have significant effect on the final value of residual stress.

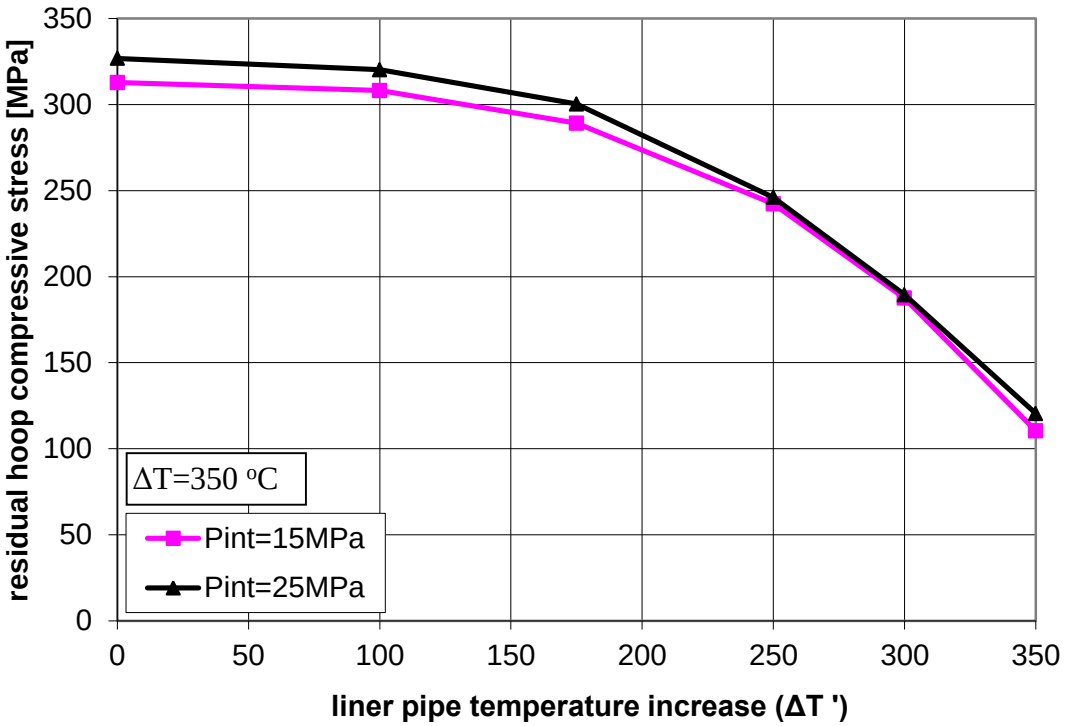

***Figure 141**: Variation of residual hoop stress in terms of liner pipe temperature increase.*

References

[1] Focke, E. (2007). *Reeling of Tight Fit Pipe*, Ph.D. Thesis, Delft Univ. of Technology, The Netherlands.

[2] de Koning, A.C., Nakasugi, H., Ping, L. (2004), "TFP and TFT Back in Town (Tight Fit CRA Lined Pipe and Tubing)", *Stainless Steel World*, p.53-61.